A Study on the Synthesis and Properties of NaSICON Solid Electrolyte

Zur Erlangung des akademischen Grades eines

Doktors der INGENIEURWISSENSCHAFTEN (Dr.-Ing.)

von der KIT-Fakultät für MASCHINENBAU
des Karlsruher Instituts für Technologie (KIT)

genehmigte

Dissertation

von

M. Sc. Asma'u Ibrahim Gebi

Tag der mündlichen Prüfung: 17.12.2024
Erster Gutachter: Prof. Dr. rer. nat Helmut Ehrenberg
Zweiter Gutachter: Prof. Dr. rer. nat Michael J. Hoffmann
Dritter Gutachter: Prof. Dr. rer. nat Wilhelm Pfleging

Kurzfassung

In den letzten Jahren hat das Interesse an der Entwicklung von Festelektrolyten aufgrund von Sicherheitsaspekten, hoher Energiedichte, relativ langer Lebensdauer und eines breiten Betriebsbereichs zugenommen, was sie zu einem Schlüssel für die Zukunft der Batterietechnik macht. Die Verfügbarkeit kostengünstiger Synthesewege ist jedoch eine Voraussetzung für Fortschritte bei der Herstellung und Verwendung solcher Elektrolyte. Der superionische Natriumleiter $Na_3Zr_2Si_2PO_{12}$ mit einer so genannten NaSICON-Struktur ist ein vielversprechender Natrium-Festkörperelektrolyt mit hoher Ionenleitfähigkeit und guter thermischer, chemischer und elektrochemischer Stabilität. Die bekannten Synthesemethoden für dieses Material sind jedoch zeit- und energieaufwändig. Um dieses Problem anzugehen, zielt diese Arbeit darauf ab, einen einfachen, zeitsparenden alternativen Prozessweg für die Synthese von Natrium-Festkörperelektrolyten zu entwickeln. Es wurde eine vergleichende Studie zwischen der entwickelten alternativen Methode und allgemein bekannten Methoden durchgeführt, um ein besseres Verständnis des Bildungsmechanismus der NaSICON-Struktur zu erhalten. Die Ergebnisse zeigten, dass durch die Verwendung von Vorläufern mit großer Oberfläche und Hochenergiemahlung (HEM) der Umwandlungsprozess verbessert und die benötigte Verarbeitungszeit und -energie reduziert werden konnte.

Anschließend wurden die Synthesebedingungen der High Energy Mill (HEM)-Vorstufen bestimmt. Es wurde ein stabiler Zyklus des erhaltenen Festkörperelektrolyten mit Na vs. Na bei 1 $mAcm^{-2}$ beobachtet und eine Raumtemperaturleitfähigkeit von 1,8 $mScm^{-1}$ bei einer reduzierten Gesamtbearbeitungszeit und -energie erreicht. Dies stellt einen neuen alternativen Weg für die Synthese von NaSICON-Natrium-Festkörperelektrolyten dar.

Um den Prozess zu vereinfachen, wurde die Verarbeitung optimiert und eine kombinierte zweistufige Wärmebehandlung (ohne Mahlung und Re-Pelletierung zwischen Kalzinierung und Sintern) untersucht. Die Auswirkungen unterschiedlicher Prozessparameter auf die mikrostrukturelle Entwicklung, die Ionenleitfähigkeit, die Dotierung und die Zyklen wurden untersucht. Es wurde festgestellt, dass die Variation der Heiz-/Kühlrate, der Sinterumgebung, des Abschreckens und der Partikelgröße die Mikrostruktur beeinflusst. Die vielversprechendste Korrelation zwischen Mikrostruktur und Eigenschaften (2,2 $mScm^{-1}$) wurde durch die Verringerung des chemischen Potentialgradienten des HEM-Pulvers durch Sieben beobachtet, was zu einer verbesserten Sinterung und einem normalen Kornwachstum mit guten Leitfähigkeiten führte. Die Wirkung von Mg und Mo auf die Struktur, das Gefüge und die Leitfähigkeit wurde bewertet. Mg ging in ein sekundäres Na_3PO_4 über, während Mo zu einer Kornverfeinerung führte. ES hat eine begrenzte Löslichkeit in der NaSICON-Struktur und erhöhte die Leitfähigkeit geringfügig.

Schließlich werden in der Studie die Auswirkungen der Verarbeitungsmethode/Zusammensetzung auf die Struktur und Dynamik von $Na_3Zr_2Si_2PO_{12}$ and $Na_{3.4}Zr_2Si_{2.4}P_{0.6}O_{12}$ untersucht. Hochtemperatur-Röntgenbeugung (HT-XRD), kernmagnetische Resonanz (NMR) und elektrochemische Impedanzspektroskopie (EIS) wurden zur Untersuchung der Struktur und Ionendynamik eingesetzt. Zwei monokline NaSICON-Modelle mit 3Na- und 4Na-Natrium-Untergittern und ein

rhomboedrisches 3Na-Natrium-Untergittermodell wurden für die FullProf-Rietveld-Strukturverfeinerung verwendet. Es wurde versucht, eine Korrelation zwischen der Verfeinerung der Strukturdaten und den mittels NMR beobachteten Bewegungen zu ermitteln. Die durch NMR beobachtete langsame Grenzbewegung wurde auf die langsame Bewegung von Na an der Na2-Stelle aufgrund seiner hohen Energie in der monoklinen Phase und den Unterschied in der potentiellen Gitterenergie aufgrund der Kräfte, die die Verteilung vohn P und Si im Gitter bestimmen sowie auf lokale Unterschiede in der Zusammensetzung zurückgeführt.

Abstract

In recent years, there has been a growing interest in developing solid electrolytes due to safety considerations, high energy density, relatively long lifetime, and wide operating range, all of which make them a key to the future of battery technology. However, the availability of cost-effective synthesis routes is a prerequisite to driving progress in the manufacturing and use of such electrolytes. The sodium superionic conductor $Na_3Zr_2Si_2PO_{12}$ a so-called NaSICON structure, is a promising solid-state sodium electrolyte with high ionic conductivity and good thermal, chemical, and electrochemical stability. However, the reported synthesis methods for this material are time-consuming and energy-intensive. To address this issue, this work aims to develop a simple, time-efficient alternative processing route for the synthesis of solid-state sodium electrolytes. A comparative study was carried out between the developed alternative and commonly reported methods to understand the NaSICON structure's formation mechanism better. The results showed that using precursors with a large surface area together with high-energy milling (HEM) improved the conversion process, and the required processing time and energy was reduced. Subsequently, the synthesis conditions of the High Energy Mill (HEM) precursors were determined. Stable cycling of the obtained solid-state electrolyte was observed with Na vs. Na at 1 mA/cm^2 and a room temperature conductivity of 1.8 mS/cm was achieved at a reduced total processing time and energy. This marks a new alternative route for the synthesis of NaSICON solid-state sodium electrolytes.

Furthermore, to pursue process simplification, the processing was optimized, combined (without an intermediate grinding and re-pelletizing step between calcination and sintering) two-step heat treatment were studied. The effect of varying process parameters on microstructural evolution, ionic conductivity, doping, and cycling was investigated. Varying the heating/cooling rate, sintering environment, quenching, and particle size were found to affect the microstructure. The most promising microstructure-property correlation was observed by reducing the chemical potential gradient of the HEM powder by sieving, leading to improved sintering and normal grain growth with good conductivities. The effect of Mg and Mo on the structure, microstructure and conductivity was evaluated, Mg went into a secondary Na_3PO_4 phase while Mo led to grain growth it has limited solubility in the NaSICON structure, and marginally increased the conductivity.

Finally, the study explores the effects of processing route/composition on the structure and dynamics of $Na_3Zr_2Si_2PO_{12}$ and $Na_{3.4}Zr_2Si_{2.4}P_{0.6}O_{12}$. High temperature x-ray diffraction (HT-XRD), nuclear magnetic resonance (NMR), and electrochemical impedance spectroscopy (EIS) were employed to investigate the structure and ion dynamics. Two monoclinic NaSICON models with 3Na and 4Na sodium position sub-lattices and a 3Na sodium sublattice rhombohedral model were used for the FullProf Rietveld refinement of the high-temperature structure. An attempt was made to determine a correlation between the refinement data and observed motions using NMR. Two migration paths were identified, slow hopping motion observed by NMR was attributed to the

slow motion of Na at sites other than the Na3(8f) site in the monoclinic phase and the difference in lattice potential energy due to the forces governing the distribution of P and Si in the lattice, as well as local compositional variation.

Table of Contents

List of Figures

List of Tables

Abbreviations

ASSBs	All-Solid-State Batteries
CE	Coulombic efficiency
CIF	Crystallographic information file
DEC	Diethyl carbonate
DEMETFSIb	N-diethyl-N methoxyethylammoniumbis(trifluoromethanesulfonyl) imide
DMC	Dimethyl carbonate
EC	Ethylene carbonate
EMC	Methyl ethyl carbonate
EMImFSI	1-ethyl-3-methylimidazolium bis(fluoromethanesulfonyl)imide
FEC	Flouroethylenecarbonate
HC	Hard carbon
HEM	High energy milling
LIBs	lithium-ion batteries
NaFSI	Sodium bis(fluorosulfonyl)imide
NaODFB	Sodium difluoroxalateborate
NaSICON	Sodium super ion conductors
NaTFSI	Sodium bis(trifluoromethylsulfonyl)imide
PBA	Prussian blue analogues
PC	Propylene carbonate
PMMA	Polymethyl methacrylate
PVdF-HFP	Poly(vinylidenfluorid-co-hexafluorpropylen)
SE	Solid electrolyte
SEI	Solid electrolyte interface

SIBs	Sodium-ion batteries
TM	Transition metal

Declaration of Authorship

I hereby declare that this PhD thesis is my independent work. All sources and tools used in this work are specified and all citations labelled as references. This thesis was not presented to another examination board, and it has not been published before.

Karlsruhe, im Dezember, 2024

Asma'u Gebi

To Sulaiman, Abulkhayr, and Abdulmajeed, though our journey has been marked by physical distance and limited communication, your presence in my heart and thoughts has never wavered.

To the strength and resilience of women and children who have endured separation during critical phases of their lives, may we embrace the lessons learned and inspire hope in others who find themselves in similar circumstances.

With love and unwavering determination.

Acknowledgement

First, I express my deepest gratitude to Allah for granting me the strength, perseverance, and wisdom to complete this thesis.

I am immensely thankful to DAAD and PTDF Nigeria for their generous scholarship that made my studies and research possible. Their support has been a pillar in shaping my academic and personal growth.

I am eternally grateful to my supervisor Prof. Dr. rer. nat Helmut Ehrenberg, for the invaluable opportunity to work under his guidance. His lab's expertise, encouragement, and support have shaped my research and personal development. Deep appreciation goes to my reviewer Prof. Dr. rer. nat Michel Hoffmann, for kindly serving as my reviewer during his retirement, and to Prof. Dr. rer. nat Wilhelm Pfleging for taking the time to review my work despite his demanding schedule. I sincerely and deeply appreciate my group leader, Dr. Michael Knapp, for introducing me to Powder XRD and FullProf Rietveld refinement, and for his continuous support, guidance, and patience throughout the dissertation.

A special vote of thanks and immense gratitude goes to Dr. Oleksandr Dolotko for introducing me to high-energy milling and guiding me through synthesis, to Dr. Sylvio Indris for his insights and guidance, to Dr. Mareen Schaller for taking the time to do NMR measurements and analysis of the data and for patiently guiding me through many other things, to Dr. Anna-Lena Hansen for introducing me to PDF analysis and for her insights, to Dr. Angelina Sarapulova for all the PDF and synchrotron measurements and for being there to respond to my many questions, to Udo Geckle for the SEM/EDX measurements, to Dr. Hannes Radinger for the XPS measurement and analysis, and for his kindness and willingness to support, to Dr. Arseniy Bokov for his constructive review and feedback, to Dr. Charlotte Fristch, Dr. Ruth Schlenker, and Dr. Heike Stoffler for introducing me to solid electrolytes. Their knowledge, guidance, dedication, and willingness to share their expertise and mentorship have been instrumental in introducing me to certain topics and providing invaluable insights at different points of my research, significantly enriching my work.

Heartfelt appreciation is extended to Liuda Merecrea for the DTA/TGA/DSC measurement and her warmth, support, kindness, expertise, guidance, and friendship. Her presence and unwavering encouragement created a positive and supportive environment that contributed to my overall well-being.

I am grateful to the administrative/technical team, Almut, Heinz, Phillip and Luis for their support. To Dr Asmaa Marchoud, Eliana Fuentes, Bijian Deng, Dr. Sani Sabo, Dr. Umma Aliyu Musa, Qasim Sani, office mates, and the students and scientists at the IAM/ESS. Their presence and willingness to offer help and share experiences have been truly invaluable.

To my dear friend Madiya Umar Alka, who has stood by me through thick and thin, I am sincerely thankful. Your companionship and encouragement have been a source of strength throughout this journey. Together, we have walked through hills and valleys, and I am deeply grateful for the bond we share.

To my neighbours, the Jonatzke family, whose warmth and generosity have made us feel at home in a foreign land, I am truly thankful. You opened your hearts to us and became like grandparents to my son, offering friendship and care that have meant more than words can express.

My heartfelt gratitude goes to my family, especially my mother, Hajiya, for her constant love, prayers, and support. Amina Gebi (Maman Haida), you have been both a sister and a friend; your unwavering presence and strength have carried me through my most difficult moments. Anti Ladi, Muni, Rukayya, Hassana, each of you, in your own way, has shared in my struggles and triumphs; your calls, prayers, and words of encouragement have sustained me when the road was hardest. Dr Usman Gebi (Baban Khaleel), I remember telling you of my intention to embark on this journey, and your words, '*Go for it, I'll support you*' meant the world. Thank you so much for being there in our times of need.

I also honour the memory of my late father, whose legacy of learning continues to guide me. His belief in the power of education and the values he instilled in us remain the foundation of my perseverance and purpose.

And to my little son, Al'ameen, you have been my quiet strength and my greatest blessing. Though you may not yet understand this work, your laughter and innocence gave me courage and joy in the toughest of days.

To those whose challenges tested my resolve, thank you for giving me the motivation, courage, and strength I needed to pursue this endeavour. Ya Allah, I am grateful for every blessing in disguise.

As I look back, I am humbled by the love, kindness, and support that surrounded me on this journey. Each person mentioned here—and many others not named—has left an indelible mark on my heart and on the path that led me here.

1 Introduction

1.1 Motivation

Reducing reliance on non-renewable energy sources is vital to meet the rising global energy demand while protecting the environment[1]. The capacity of humanity to efficiently transform, store, transport and access energy in numerous ways will be at the heart of this endeavour. Batteries are a crucial part of energy transition because they enable efficient management of energy demand and storage of renewable energy produced by solar and wind energy[2]. The use of flammable liquid electrolytes in conventional sodium-ion batteries (SIBs) and lithium-ion batteries (LIBs) poses challenges to safety[3]. Therefore, all-solid-state batteries (ASSBs) with non-flammable solid-state electrolytes should overcome this obstacle. Due to a high theoretical energy density, secure operation and extended lifespan, solid electrolytes also present the prospect of metal anode (Li or Na) solid-state batteries, which are promising for producing the next generation of energy-storage devices[3].

Research and development of various types of solid-state electrolytes has been going on for decades[4], such as oxide-, polymer-, sulphide-based electrolytes and, recently halides. However, each type has its own benefits and drawbacks[4]. Ceramic electrolytes, such as NaSICON and Na-β″/β-Al_2O_3, are highly conductive at room temperature, but they require a high-temperature synthesis process and show high interface impedance[5]. Polymer electrolytes, such as PEO-based ones, have poor ionic conductivity while demonstrating good mechanical stability and adhesive properties [6]. Gel polymer electrolytes, such as those based on PVdF-HFP and PMMA, have good conductivity; however, their mechanical properties need to be improved and the issue of sodium dendrite formation should be tackled[6]. Sulphide-based electrolytes need a low-temperature synthesis process, show good conductivity, and low grain boundary resistance, but cannot be used in oxygen-rich environments[7]. In contrast, halides offer better electrochemical stability than sulphides, but they provide lower ionic conductivity[8]. Overall, numerous efforts have been made to improve the performance of solid-state electrolytes in battery applications. Nonetheless, practical applications of sodium-based solid-state electrolytes have still not been possible.

1.2 Aim and Objectives

This study aims to develop and optimise a method for NaSICON ($Na_3Zr_2Si_2PO_{12}$) solid-state electrolytes' synthesis. It seeks to provide an understanding of the material phase evolution during solid-state electrolytes' fabrication and the effect of the processing conditions on the Na-conductor. In addition, it attempts to evaluate the impact of the synthesis method on the structure, ionic conductivity, lattice dynamics, morphology and electrochemical performance of the electrolyte. Hence, this research work is focused on the following topics:

- Synthesizing NaSICON solid electrolyte by a simple, time-efficient high-energy milling (HEM) route and comparing this method with those reported in the literature.
- Optimizing the selection of precursors for the new synthesis method.
- Understanding the morphological evolution of NaSICON solid electrolytes.
- Investigating the effect of Mg and Mo doping on structure, morphology and performance of the electrolyte.
- Assessing and evaluating the effect of the process on ionic conductivity and lattice dynamics of the electrolyte.

1.3 Scope of the Dissertation

The research findings obtained in this dissertation shed light on several important aspects related to sodium super-ionic conductor solid electrolytes for solid-state sodium batteries. The investigation focused on improving the synthesis methods, understanding the structure and dynamics, exploring the influence of processing conditions and doping strategies, and optimizing the microstructure and electrical performance of NaSICON electrolytes.

Regarding the synthesis methods, a novel and cost-effective processing technology that could enhance the fabrication of the electrolytes was explored. Through systematic experiments and analysis, it was determined that modifying the precursor composition and adjusting the sintering parameters results in improved crystallinity, purity, and uniformity of the synthesized materials. These findings contribute to the development of more efficient and scalable synthesis routes for NaSICON solid electrolytes.

In terms of the structure and dynamics of NaSICON electrolytes, the research employed advanced characterization techniques to investigate the crystal structure and ion transport of $Na_3Zr_2Si_2PO_{12}$-based compositions. The results provided valuable insights into the relationship between the crystal structure and ionic conductivity of the materials. It was observed that certain crystallographic features, such as grain boundaries and defects, significantly influence the ionic conductivity, highlighting the importance of microstructure optimization to enhance the overall performance of NaSICON electrolytes.

Furthermore, the effects of processing strategies and doping conditions on the microstructure and properties of NaSICON electrolytes were thoroughly examined. The research demonstrated that varying the synthesis temperature, heating rate, and sintering atmosphere had a profound impact on the grain size, density, and phase purity of NaSICON materials. Additionally, the introduction of specific dopants, such as Mo or Mg, was found to enhance the ionic conductivity and stability of the electrolytes. These findings offer valuable insights into tailoring the properties of NaSICON electrolytes through precise control of processing parameters and targeted doping approaches.

Lastly, the research focused on optimizing the synthesis and sintering conditions to control the microstructure and electrical performance of NaSICON electrolytes. By systematically exploring

different synthesis and sintering parameters, it was possible to achieve a desirable microstructure characterized by uniform grain size, enhanced densification, and improved intergranular connectivity. This optimization resulted in a significantly enhanced ionic conductivity and electrochemical stability of the NaSICON electrolytes, leading to improved battery performance.

In conclusion, the research findings presented in this dissertation contribute to the understanding and advancement of NaSICON solid electrolytes for solid-state sodium batteries. The improved synthesis methods, insights into structure and dynamics, understanding of processing conditions and doping strategies, and optimization of microstructure and electrical performance provide a solid foundation for further research and development in the field of NaSICON-based solid-state sodium batteries

2 Fundamentals

2.1 Background

The use of carbon-based fossil fuels has caused disastrous climate change effects in recent years, posing a serious threat to the ecosystem, human health and global economy. As shown Fig. 2.1, the future world energy demand is projected to witness a consistent rise. Therefore, making a switch to cleaner energy sources is crucial[2], because intermittent renewable clean energy sources such as wind and solar require a balance between high and low generation times. Electric energy storage systems could balance the supply and demand of energy by storing energy produced at one time and releasing it later[9]. Numerous energy storage technologies exist, including flow batteries, supercapacitors, compressed air, flywheels, thermal energy storage and electrochemical batteries[10]. Other cutting-edge storage technologies include superconducting magnetic energy storage and pumped hydroelectric power.

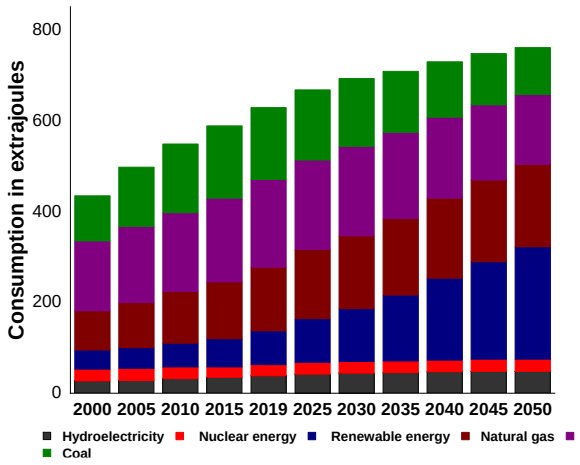

Fig. 2.1: World energy consumption prediction by source for the past, present and future (adapted using data from Ref [11]).

2.2 Batteries

A battery is an electro-chemical energy device made up of one or more galvanic cells that utilize redox processes to convert chemical energy into electrical energy or vice versa[11]. It is composed of one or more galvanic cells, which consist of an anode and cathode that undergo oxidation and reduction, respectively. The anode undergoes oxidation, while the cathode undergoes reduction, and a separator and electrolyte are used to conduct ions and physically separate the two electrodes. A current **I** and voltage **V** applied to the cell reverses the chemical process, completing the cycle.

Batteries are divided into the following two categories: primary batteries, which are non-rechargeable and become unusable after one discharge, and secondary batteries, which are rechargeable and reusable. Among these, lithium-ion batteries (LIBs) have the highest energy density, largest operational voltage, highest capacity, lightest weight and longest cycle lifespan[12].

2.3 Performance Metrics for Batteries

The common terms that are used frequently in the evaluation of cells are as follows:

2.3.1 Cell potential

Cell potential refers to the electric potential difference between two electrodes of a battery or electrochemical cell, it is divided into following two categories: theoretical and practical[13]. The equilibrium cell potential ($E^0(x)$) is the theoretical voltage of an electrochemical cell based on the difference between the standard potential of anode and cathode materials. This potential is equal to the open circuit voltage (OCV) when no current flows through the external circuit. The Nernst equation expressed in eq. (2.1) determines the equilibrium cell potential and provides the driving force for ions to travel through the electrolyte and electrons in the external circuits[14].

$$\Delta E^{0}_{(cell)} = \Delta E_{cathode} - \Delta E_{anode} \tag{2.1}$$

$$E^{0}(x) = -\frac{1}{F}.\left(\frac{\partial \Delta G(x)}{\partial x}\right)_{T,P} = -\frac{\mu^{cathode}_{Na(x)} - \mu^{anode}_{Na}}{zF} = -\frac{RT}{zF}\ln\frac{a^{cathode}_{Na}}{a^{anode}_{Na}} \tag{2.2}$$

Where $\Delta_{(x)}$ is the Gibbs free energy change for the cell reaction:

$$MeO_2 + x\text{Na} \rightarrow \text{Na}_x\text{MeO}_2 \tag{2.3}$$

and $E^0(x)$ is the open circuit voltage at x state of charge (sodium content in the cathode); μ_{Na} and a_{Na} are the chemical potentials and activity of sodium, respectively, in the relevant electrode. F is the Faraday constant (96500 $Cmol^{-1}$ = 26.8 $Ahmol^{-1}$), R is the universal gas constant (8.314 $JK^{-1}mol^{-1}$) and z is the charge (in moles of electrons) transferred by sodium in the electrolyte during the cell reaction.

For sodium intercalation in most non-electronically conducting electrolytes, z = 1. For a half-cell configuration with pure metallic sodium as anode material, $a_{Na}{}^{anode} = 1$. The operating voltage ($E^0(x)$) or the closed-circuit voltage is the output voltage at which the battery operates during charge and discharge in its actual use. This voltage is a function of the state of charge. In most cases, it is different from the equilibrium voltage due to various kinetic factors.

2.3.2 Voltage Window

The range of potential between the upper limit of charging and the lower limit of discharging is a crucial factor to consider[14]. A standard procedure exists to determine this value, although it is recommended that the discharging lower limit voltage for the cathode be set at 1.5-2.0 volts and

the charging upper limit for the anode be set below 1.5 volts. Furthermore, the cell voltage should remain within electrochemical stability window throughout the process.

2.3.3 Charge Capacity

This is the amount of electric charge stored in a battery, which is measured in mAh or Ah[13,14]. The maximum charge capacity of a battery is determined by the amount of material it contains and its chemical makeup. Faraday's law can be used to calculate theoretical capacity (Q_{th}) in Ah, as given by:

$$Q_{th=} \frac{z.F.m}{3600.M} \tag{2.4}$$

Where M is the molar weight of the cathode materials in $gmol^{-1}$, m is the mass of the active material in the cathode used in the cell in grams, and F is 96500 $Cmol^{-1}$. The practical capacity in Ah is calculated as follows:

$$Q_{p=} \int_{t_1}^{t_2} I(t)dt \tag{2.5}$$

Where I(t) in Amperes is the current as a function of time and t_1 and t_2 are the beginning and end of the considered interval in hours, respectively.

2.3.4 Charge Density or Specific Charge

Is the amount of theoretical (Q_{th}) or practical (Q_p) charge that can be stored or delivered per unit weight of the active material, expressed in Ampere hours per gram $Ah \cdot g^{-1}$[13,14].

2.3.5 Current Density (J)

Current density (j) is the ratio of the total current from an electrode (I) to its surface area (A):

$$J = \frac{I}{A} \tag{2.6}$$

2.3.6 State of Charge

State of charge is the fraction of the maximum capacity of a battery that remains available at a given time.

2.3.7 Energy Density or Specific Energy (W)

The energy density is determined by the electrochemical voltage (V) between the utilized redox couples and the specific capacity (C) of the electroactive materials in the electrodes[13,14]. It is the energy per unit weight (or volume) of the material or system measured in $Whkg^{-1}$ or WhL^{-1}. The

practical energy contained in an electro-chemical cell in Whg^{-1} is the integral of the voltage multiplied by the charge capacity.

$$W = \int E_x \, dq \tag{2.7}$$

$$W = \frac{C_c \times C_a}{(C_c + C_a)} \times (V_c - V_a) \tag{2.8}$$

Where q is the amount of practical charge density in Ahg^{-1} and E_x is the cell's voltage in volts, Cc, Ca are the specific capacities of cathode and anode, respectively, and V_c, V_a is the electrochemical potential of cathode and anode, respectively. Clearly, from the equation, the energy density can be increased by increasing the operating voltage, the charge-storage capacity and the mass loading alone or in combination[13,14].

2.3.8 Active Mass Loading

Active mass loading is the weight of the electrode active material on the current collector per unit area[13,14]. In laboratory cells, electrodes are coated with low mass loading to reduce electrical pathways and maximize performance. However, as the loading increases, the electrodes become thicker and more challenging to produce. High mass loading is a key factor in achieving this high energy density. In current LIBs, electrodes are prepared with high mass loadings to achieve an aerial capacity of 3–4 $mAhcm^{-2}$. To reach the goal of high energy density, the areal capacity must increase.

2.3.9 Cycling Stability

Cyclability indicates the longevity of an electrode material, which can be measured by the number of times it can maintain its initial capacity when cycled. Galvanostatic charge/discharge is a common test for evaluating its stability. For excellent cyclability, the electrode material must be structurally stable against electrochemical strain and volume fluctuation, and the interface between the electrolyte and the electrode should be stable and enable reversible ion transfer in each cycle without sodium loss. The nature of the active material's crystalline structure influences the former, while Coulombic efficiency (CE) affects the latter[13,14].

2.3.10 Coulombic Efficiency

The charge efficiency of a battery is the ratio of the total charge extracted from the battery to the total charge put into the battery over a full cycle. Ideally, the charge efficiency should be 100%; however, in reality, some charge is lost due to side reactions. To ensure a long battery life and commercialization, the charge efficiency should be at least 99.96% for 500 cycles.

2.3.11 Transference Number

The transference number is defined as the ratio of the electric current derived from the cation to the total electric current. If the transference number is close to 1, it implies that the ion conducting

performance in the electrolyte is mainly accomplished by the cation[15]. A high transference number equal or close to one can reduce the concentration polarization of electrolytes during charge–discharge steps, and thus produce higher power density. It is highly desirable that the transference number of ions approaches 1 in an electrolyte system. However, many existing electrolyte systems, either liquid or polymeric, have transference numbers less than 0.5[16].

2.4 Sodium vs Lithium Batteries: Beyond Energy Densities

Secondary battery technologies are the most widely used electrical energy storage systems due to their good energy conversion ability, adaptability and manageable maintenance[15]. LIBs have high energy density and a long-life span, and they are used for electric vehicles, laptops, phones, etc[16]. Prior to 2020, the key success factors for battery development have primarily centred on theoretical energy density, power density, lifetime, safety, and costs per kWh. Consequently, there is significant anticipation surrounding energy storage systems like lithium-air (Li-O_2) and lithium-sulphur (Li-S) systems, particularly for mobile applications[3]. These systems boast high theoretical specific energy densities compared to conventional Li-ion systems. If the challenges of practical implementation, low energy efficiency, and cycle life can be addressed, these systems could offer an interesting energy source for EVs. However, the increasing demand for raw materials, particularly metallic lithium, is a concern. The growing market for batteries is driving an absolute increase in lithium demand, and many lithium sources are not environmentally sustainable. Due to limited obtainable lithium resources, predictions have been made that lithium supplies may run out in the future[17,18,19].

High cost of transition metals used in electrodes also makes LIBs generally expensive. As a result, there is growing interest in alternative technologies like Na-ion batteries. Sodium exhibits chemical properties similar to those of lithium and is abundant (Fig. 2.2), making SIBs a potential alternative to LIBs[19,20]. Lithium has a smaller ionic radius, a lower atomic weight, and a larger electro-chemical potential than sodium. This affects the host materials' interphase formation, transport characteristics and phase stability during intercalation and de-intercalation[17]. Due to its lower ionisation potential, Li is expected to intercalate more easily than Na. NIBs have an electrochemical mechanism similar to that of LIBs but with different ion carriers, and though they offer lower energy density than LIBs, they are a low-cost option, and might be easier for recycling compared to Li. Consequently, SIBs have been developed for different applications with less demanding weight requirements, such as storing fluctuating renewable energies and releasing energy into the grid [18].

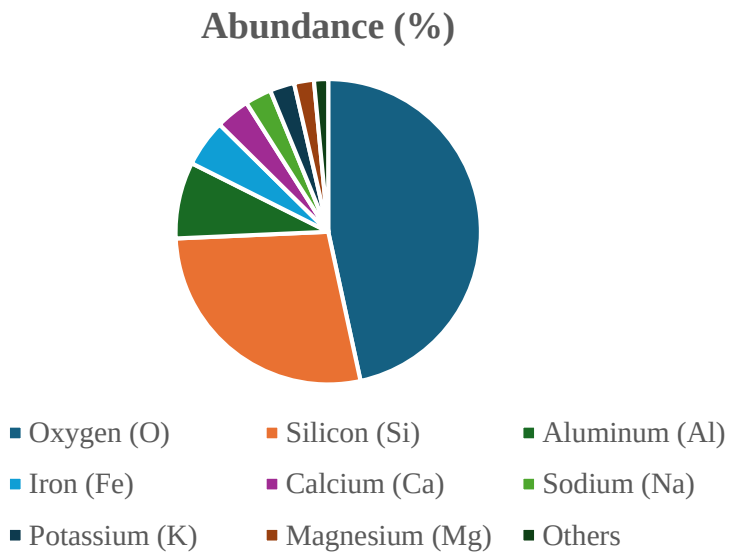

Fig. 2.2: Abundance of elements in the Earth's crust adapted with permission from[18]

2.5 Developmental History of Sodium Battery

In 1839, Faraday discovered ionic conductivity in the solid-state material, which inspired many researchers to contribute to the field of solid-state ionics[19]. Warburg and Nernst (1884) demonstrated Na conductivity in Thuringia glasses and doped zirconia. In the first part of the 20th century, Frenkel, Kruger, Wagner and Schottky made significant contributions to the basis of solid-state electrochemistry[19]. Kummer and Yao of Ford Motor's discovery of high Na^+ conductivity at intermediate temperatures in beta-alumina allowed for the integration of these materials in new applications[19]. Ford developed the sodium–sulphur (Na–S) battery with beta-alumina for use in electric vehicles in the 1960s due to its low cost, high capacity, less damaging environmental impact and high operating temperature (300–350°C)[20]. However, researchers are exploring corrosion-resistant materials and low-temperature cells that can function just below 100°C. Despite its limitations, the Na–S battery has been used worldwide for grid stabilization applications, with a few reported accidents[21].

Coetzer *et al.* has developed a ZEBRA battery in South Africa, which is similar to the Na–S battery. It operates between 270°C and 350°C and uses $NiCl_2$ instead of sulphur[22]. Its anode is Na metal, while Fe is added to increase the power response. NaCl and $AlCl_3$ are added to the positive electrode, forming $NaAlCl_4$ in liquid form and facilitating Na conduction. The cell voltage is 2.6 V, which is higher than that of the Na–S cell, and the batteries are manufactured in a discharged state for safety[19]. Several SIBs have been commercialized or are at an advanced level of research (Fig. 2.3), such as Aquion Energy (2008–2017) with sodium titanium phosphate negative electrodes, manganese dioxide positive electrodes and sodium perchlorate electrolyte[23,24]. Faradion Limited (2011) has pouch cells with energy densities comparable to LIBs (140–160 $Whkg^{-1}$) and good rate performance (3C) and cycle life (1000 cycles, 80% depth of discharge) [23,24]. TIAMAT (2017 France) focuses on 18650 cylindrical cells (100–120 $Whkg^{-1}$, 5000+ cycle lives, 80% capacity) [23,24]. HiNa (2017) uses Na-Fe-Mn-Cu oxide cathodes and anthracite carbon

anode (120 Whkg^{-1}) [23,24]. Natron Energy uses Prussian blue analogues for both cathode and anode with an aqueous electrolyte. Altris AB (Angstrom Advanced Battery Centre) uses an iron-based Prussian blue analogue for positive electrodes in non-aqueous sodium-ion cells with a hard carbon anode[23,24]. CATL (Chinese LIB manufacturer) has a SIB with a Prussian blue analogue positive electrode and porous carbon negative electrode, with a specific energy density of 160 Wh/kg[24]. Northvolt (2023) announced sodium batteries with capacity of over 160 Whkg^{-1} based on hard carbon anode and Prussian white cathode[25].

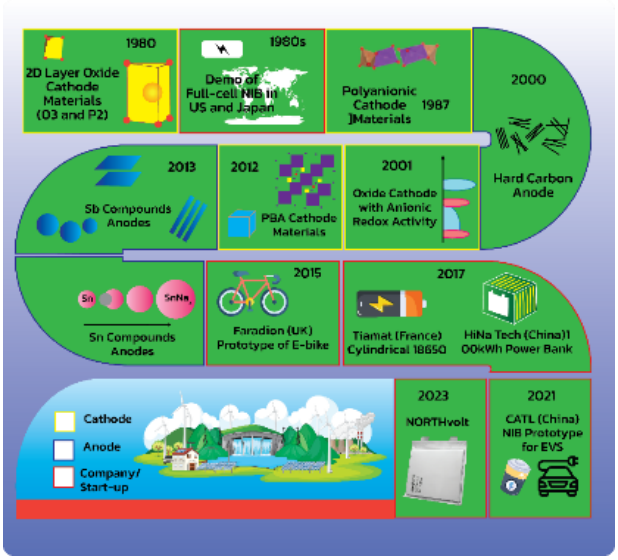

Fig. 2.3: Schematic roadmap of sodium-ion batteries over the years, highlighting the discovery of key ma-terials (adapted with permission from ref[23])

2.6 Mechanism of Operation and Components of Sodium ion Batteries

SIBs also called NIBs, are energy storage devices that work in a way similar to LIBs, using a 'rocking chair mechanism' to shuttle ions between electrodes. A reversible chemical reaction (redox reaction) occurs at the interface of the two electrodes and electrolyte, where oxidation and reduction take place at anode and cathode, respectively. This allows the conversion of electrical energy into chemical energy, and vice versa[26] (illustrated in Fig. 2.4).

Anodes and cathodes are defined on the basis of their behaviour when a cell is discharged[3]. Sodium ions are transferred between the electrodes with the help of an electrolyte, and released electrons are not allowed to pass through the electrolyte; they instead have to go through an external electrical circuit[18]. As a result, upon discharge, the output is current I at a voltage V for a time period Δt. When two or more galvanic cells are connected in series or parallel, a battery is formed[27]. In reversible electrochemical cells, switches between anode and cathode occurs, depending on the flow of the current. As a result, instead of using the terms anode and cathode, the electrodes are usually labelled negative and positive. However, due to convention, the negative electrode is known as the anode, and the positive electrode is known as the cathode. In sodium-

ion batteries, the positive electrode contains transferable sodium ions, while the negative electrode is sodium-free[28]. Initially, electrical energy is utilized to cause the migration of sodium ions from the positive electrode to the negative electrode through an external circuit. At the same time, the positive electrode releases sodium ions into the electrolyte to maintain a balanced charge[26]. The ions are transferred to the negative electrodes via the electrolyte and are embedded in the active material. This results in oxidation at the positive electrode and reduction at the negative electrode. As the cell is charged, the voltage increases[3]. Commonly used cathode materials are sodium transition metal oxides, Prussian blue analogues and poly-anion materials, while anodes are typically made of disordered carbon (hard carbon)[29].

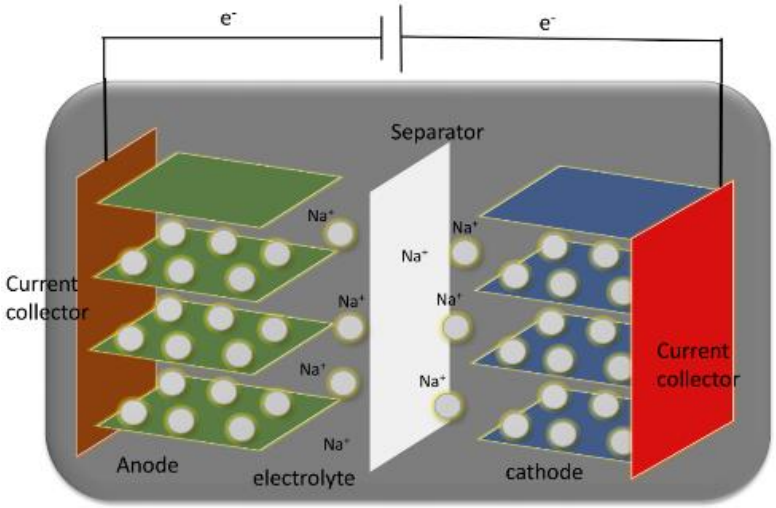

Fig. 2.4: Cell configurations of a sodium-ion battery

Lithium-layered transition metal oxides ($LiTMO_2$) serve as effective cathode materials in lithium-ion batteries (LIBs)[9,11,30]. Similarly, sodium-layered transition metal(TM) oxides Na_xTMO_2 show promise for sodium-ion batteries (SIBs) due to their high specific capacity and possibility of adapting to established LIB synthesis processes[31]. However, sodium-layered oxides face challenges, such as irreversible phase changes, limited air stability, complex charge-compensation mechanisms, and higher cell costs compared to phosphate-based SIBs[31,32]. Alternative cathode materials for SIBs include polyanionic compounds and Prussian blue analogues (PBA)[29,31,33]. Polyanion-type materials, particularly vanadium(V)-based compounds are increasingly attractive[34,35]. They display high operating potentials, unlike the layered oxides their 3D structure promotes cycling stability by reducing structural changes during cycling, the strong covalent bond with oxygen in the structure prevents oxygen release, they possess high operating potential because of the inductive effects of the polyanion group and redox activity of the TM such as with Vanadium[33]. Nonetheless, limitations in electronic conductivity and capacity persist[31]. PBA, is another cathode material known for cost-effectiveness, easy synthesis, and low toxicity[29,31,36].

Graphite (Gr) is the most common primary active material for anodes in LIBs [37]. However, its suitability for SIB is limited due to sodium's constrained ability to intercalate into graphite, resulting in significantly reduced capacities[31]. Similarly, sodium metal is unsuitable for use as an

anode due to issues like dendrite formation, high reactivity with the electrolyte, and a low melting point of 97.7 °C, compared to lithium's 180.5 °C, which poses safety concerns[38]. Consequently, various alternative materials are being explored as anodes for SIBs. These materials fall into categories such as carbon-based materials, conversion materials, conversion/alloying materials, alloying compounds, and organic compounds[38]. Particularly amorphous carbon materials such as hard carbon (HC) owing to their cost-effectiveness and favourable electrochemical performance are widely researched[39]. HC produced primarily through the pyrolysis of biomass or synthetic organic materials, stands as the current benchmark anode for SIBs in terms of energy density[40,41]. The inability of the precursors of these carbon materials to graphitize is attributed to their high oxygen content and disordered structure[42], making HC retain its disordered structure alongside randomly oriented pseudo graphitic domains, thereby featuring larger interlayer spacing compared to graphitic carbon[43]. This unique characteristic facilitates the intercalation of Na+ ions. Furthermore, HC comprises micro and mesopores, together with residual heteroatoms (such as N, S, P, B, etc.), providing additional storage sites for sodium and pathways for rapid Na+ ion transport[31,43]. To tailor HC for SIBs, it becomes essential to adjust pertinent properties such as interlayer spacing, pore structure, and the presence of defects and heteroatoms[31].

The electrolyte comprises a solvent (organic), solute (salts), and additives, collectively influencing the characteristics of the electrolyte[30]. The solvent is a crucial component of organic liquid electrolytes, requiring attributes such as stability, non-toxicity, and cost-effectiveness[44]. Essential features include a wide electrochemical stability window, sufficient sodium salt solubility, high dielectric constant, low viscosity, and a broad liquid range[45,46]. Balancing these requirements within a single solvent is challenging, leading to the common use of combinations[47]. Ester and ether solvents are prominent choices in sodium-ion batteries, exhibiting excellent performance. The ester solvents, notably cyclic ones such as propylene carbonate (PC) and ethylene carbonate (EC), as well as chain solvents like dimethyl carbonate (DMC), diethyl carbonate (DEC), and methyl ethyl carbonate (EMC), are widely employed[18,44]. The electrolytes composed of carbonate solvents typically exhibit enhanced ionic conductivity and favourable oxidation resistance[30]. The organic liquid electrolytes for sodium ion batteries are categorized based on sodium salts, encompassing sodium perchlorate ($NaClO_4$), sodium hexafluorophosphate ($NaPF_6$), sodium bis(fluorosulfonyl)imide (NaFSI), sodium bis(trifluoromethylsulfonyl)imide (NaTFSI), and sodium difluoroxalateborate (NaODFB)[18,28,30,48]. The $NaClO_4$-based organic liquid electrolytes have gained widespread usage as a well-established electrolyte for sodium ion batteries, contributing to enhanced energy density alongside stability and oxidation resistance, particularly with high-voltage cathode materials[30]. However, challenges exist in terms of compatibility with certain positive and negative electrodes, potentially leading to issues such as dissolution of transition metal ions and the formation of thick solid electrolyte interface (SEI) films[30]. The $NaPF_6$-based organic electrolytes are commercially available and exhibit favourable compatibility with common cathode and anode materials, demonstrating superior performance in ether solvents compared to other sodium salts. The NaFSI electrolytes, when dissolved in carbonate esters and ionic liquids, showcase improved electrochemical performance and compatibility with hard carbon electrodes and sodium metal electrodes compared to other sodium salt electrolytes[30]. The NaTFSI ionic liquid electrolytes demonstrate promising electrochemical performance, yet challenges such as aluminium foil corrosion, capacity decay, and inherent disadvantages of ionic liquid elec-

trolytes (e.g., high viscosity, poor wettability to electrodes) necessitate ongoing efforts for improvement[30]. The NaODFB exhibits high compatibility with various solvents used for sodium-ion batteries (NIBs), indicating its potential effectiveness with diverse electrode materials[30,49]. However, current research primarily focuses on its application as an additive, and further exploration is needed to expand its utility in SIBs[30].

Additives, constituting the third primary element in organic liquid electrolytes, are present in minimal quantities (less than 5%)[30]. Characterized by high specificity and low dosage, additives play a crucial role in rectifying inherent electrolyte shortcomings and substantially enhancing battery performance. This optimization can be achieved without augmenting production costs or altering manufacturing processes[50,51]. Additives serve diverse functions, including film-forming, flame retardant properties, overcharge protection, and other specific roles[52]. The film-forming additives, notably the most extensively studied, are typically readily consumed[30]. In the initial activation cycle, they actively contribute to forming the interface between the electrode and the electrolyte, leaving a chemical signature only at the interface rather than in the electrolyte itself[47]. Ideal film-forming additives should possess a higher Fermi energy (Eg) than solvents and electrolyte salts, facilitating preferential oxidation or reduction. This enhances the quality and efficiency of the solid electrolyte interface (SEI) film, thereby improving the cell's electrochemical performance[47,53,54]. Additional additives, such as acidity enhancers, impurity scavengers, viscosity reducers, and free radical scavengers, also hold potential applications in sodium ion batteries[55]. The examples include 1-ethyl-3-methylimidazolium bis(fluoromethanesulfonyl)imide (EMImFSI)[56], N-N-diethyl-N-methoxyethylammonium bis(trifluoromethanesulfonyl)imide (DEMETFSI)[57], and flouroethylenecarbonate (FEC)[58].

2.7 Why Solid Electrolytes?

The development of sustainable batteries requires technology tailored to ecological and environmental factors[59]. Conventional sodium-ion batteries can be unsafe due to flammable liquid electrolytes, whereas all-solid-state sodium batteries (ASSBs) are non-flammable and have higher thermal stability. Replacing liquid electrolytes with solid electrolytes (SE) can address safety issues, and using high-voltage cathodes and Na-metal anodes can increase energy density[60]. These promising improvements in ASSBs have great potential for large-scale energy storage systems (Fig. 2.5).

Solid electrolytes have the potential to create safer and more efficient rechargeable batteries with high energy densities[59]. These electrolytes must be stable against reactive metals to perform well in solid-state batteries. In the 1960s, β-alumina electrolytes were used in high-temperature sodium–sulphur batteries[45]. Beta Alumina, established since the 1930s, represents a non-stoichiometric compound within the compositional range (5.3 Al_2O_3, Na_2O–8.5 Al_2O_3, Na_2O)[19]. Numerous studies have been conducted to comprehend its structure, the Na^+ diffusion process, material optimization, and the exploration of novel substances exhibiting elevated ionic conductivity[19]. The hexagonal system governs its structure, featuring two spinel blocks separated by a mirror plane housing one oxygen and one vacancy. This non-compact plane, characterized by "BR" (Beevers-Ross) and "aBR" (anti-Beevers-Ross) nomenclature, facilitates Na^+ ion delocalization

at elevated temperatures resembling a bidimensional liquid. Depending on composition and reaction synthesis temperature, an alternative structural variant known as β″-Al_2O_3 may be obtained, crystallizing in the rhombohedral system with three spinel blocks separated by a conduction plane akin to the β phase. Both materials exhibit comparable ionic conductivities, with potential enhancement through cationic substitution. The electrolyte derived from β-Al_2O_3 found application in the sodium–sulfur battery (NaS), developed by Ford Company for electric vehicles in the late 1960s[19].

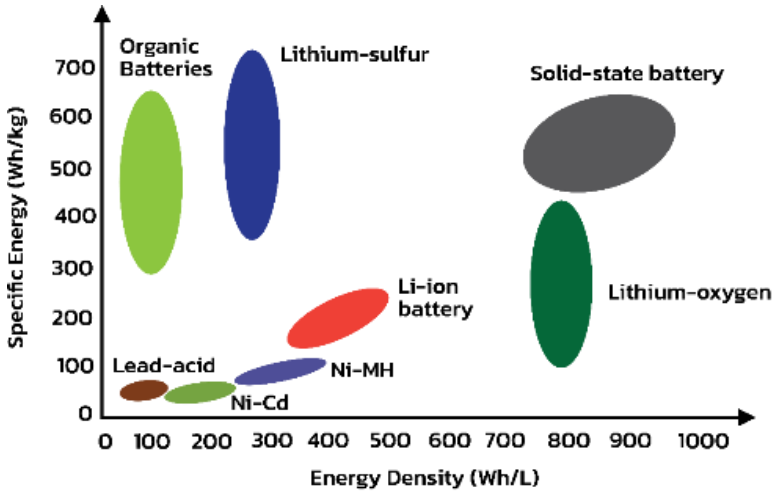

Fig. 2.5: Energy density versus specific capacity for different batteries (adapted with permission from ref[62])

However, the use of these batteries was limited due to extreme operating conditions[10]. Over the past decade, various solid electrolytes have been developed to meet the requirements of room-temperature solid-state batteries[61]. Fig. 2.6 shows the study trends in sodium based ASSB research.

The ASSBs comprise a cathode, an anode and a solid electrolyte (SE)[62]. The SEs are necessary for practical applications of ASSBs but have a low stability, low ionic conductivity and poor electrode/electrolyte compatibility when used at room temperature. The SEs can be divided into solid polymer electrolytes, inorganic solid electrolytes and their combinations[63]. The most widely studied inorganic SEs are oxides, sulphides, boron hydrides and halides[45]. Inorganic solid electrolytes have good thermal and chemical stabilities; however, they may have insufficient physical contact with the Na anode and electrode materials. Solid polymer electrolytes offer better interfacial contact; however, they have poor thermal and chemical stabilities and low ionic conductivity. Difficulties in controlling cathode/electrolyte and anode/electrolyte interfacial reactions also hinder the practical applications of ASSBs[64]. Solid electrolytes are closely linked with the performance of all-solid sodium batteries (ASSBs). To be effective, they must have good sodium-ion conductivity, low interfacial resistance, a wide and stable electrochemical window, a good thermal stability window and good mechanical properties[65]. In addition, electronic conductivity must be lower than 10^{-12} Scm^{-1} to minimize self-discharge[66]. Despite previous efforts, the majority of solid electrolytes work only at high temperatures and fail to conduct sodium ions at room temperature. Developing a highly conductive and electrochemically stable solid-state sodium-ion

electrolyte is a difficult research area to overcome. To compete with liquid electrolytes, a solid electrolyte must have an ionic conductivity of 10^{-3} Scm^{-1} at room temperature[67].

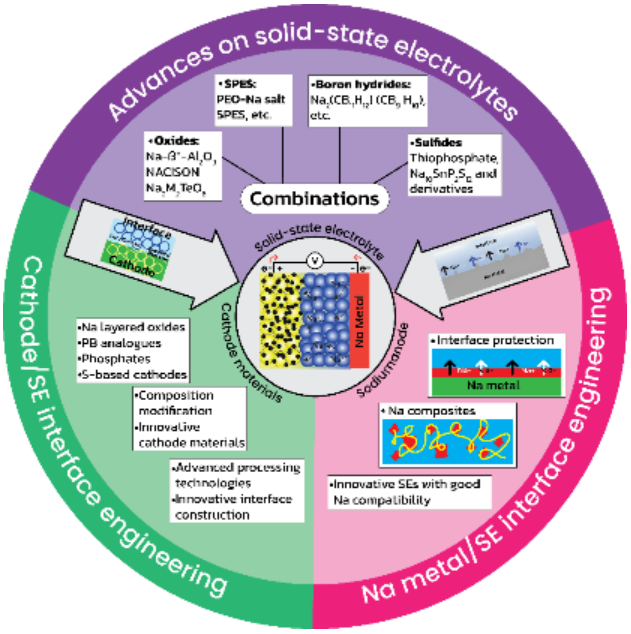

Fig. 2.6: Schematic diagram of study trends in ASSBs (adapted with permission from ref[64])

2.8 Polymer Solid Electrolytes

A polymer electrolyte is a type of membrane composed of a high-molecular-weight polymer matrix and dissolved sodium salt[68]. Such electrolyte has the advantage of being flexible, safe, dimensionally stable, easily processed and extremely effective in preventing the formation of sodium dendrites. Fig. 2.7 depicts advantages and disadvantages of some polymer electrolytes. There are following two forms of polymer electrolytes: solid and gel. The solid polymer electrolytes consist of a polymer host and sodium salts. In contrast, the gel polymer electrolytes consist of a polymer host, sodium salts and a plasticizer, giving the polymer gel-like consistency[69]. The solid polymer electrolytes have been extensively researched for decades due to their advantageous mechanical properties, fabrication and handling in thin films and capacity to foster effective electrode–electrolyte contact.

The most common host polymers include polyethylene oxide PEO, poly(vinylidene fluoride) (PVdF), poly(vinylidenefluoridehexafluoropropylene) (PVdF-HFP), poly(methyl methacrylate) (PMMA), poly(vinyl alcohol) (PVA), poly(vinyl chloride) (PVC), poly(acrylonitrile) (PAN), poly(acrylic acid) (PAA) and poly(ethyl methacrylate) (PEMA), with PEO being the most popular one due to its electrochemical stability. Common sodium salts include $NaPF_6$, $NaClO_4$, NaTFSI, NaFSI, Na_2SO_4, $NaCF_3SO_3$ and $NaPO_3$[6]. The solution-casting technique using methanol as a solvent is commonly used to make solid polymer electrolytes. Research has found that the ionic conductivity of these electrolytes can be affected by the ratio of PEO:NaTFSI, the amount of $NaClO_4$ and other types of sodium salts such as NaX (X: TFSI, FSI). For instance, increasing the

ratio of PEO:NaTFSI from 6:1 to 20:1 increases ionic conductivity, while the conductivity of the PEO30:NaTFSI composition drops to the lowest values[70]. In addition, raising the content of $NaClO_4$ from 0% to 30% can slightly increase the conductivity of PVP-based solid polymer electrolytes[6,56]. A study showed that as the content of sodium salt $NaFeF_4$ increases, the ionic conductivity of solid polymer increases and the activation energy both in the amorphous and crystalline state decreases[71].

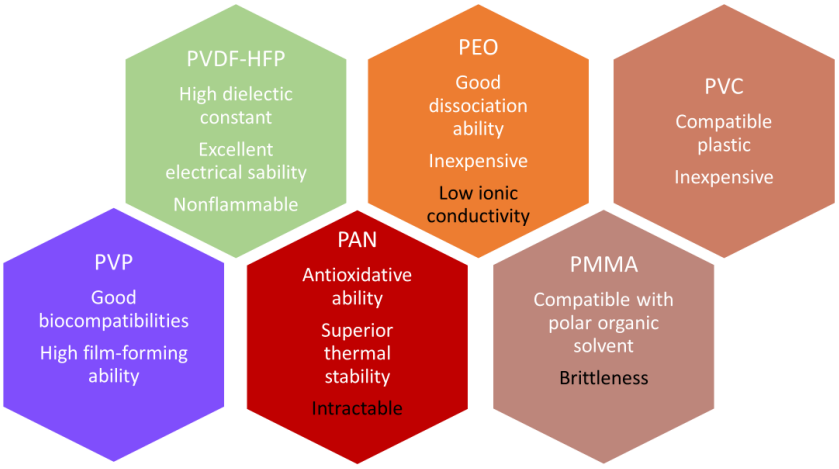

Fig. 2.7: Typical polymer electrolyte matrices with their advantages (in white fonts) and disadvantages (in black fonts) adapted with permission from ref[73]

This leads to an increased transference number of sodium ions. Nonetheless, at room temperature, the ionic conductivity of most materials is below 10^{-6} Scm^{-1}, making the performance of solid polymers unsatisfactory[72–74]. Ceramic fillers such as ZrO_2, SiO_2 and Al_2O_3 could be added to the polymer matrix to enhance the ionic conductivity of the polymer electrolytes. These fillers can reduce the equilibrium glass-transition temperature and suppress the degree of crystallinity, thus allowing faster ionic transport within the amorphous region than within the crystalline region[72–74]. The low sodium ionic conductivity of solid polymer electrolyte cells results in unsatisfactory capacity performance, with cycling capacity typically below 100 $mAhg^{-1}$. Nevertheless, it displays good cycle stability. To maximize the performance of these cells, further improvement of ionic conductivity is necessary[72–74].

2.9 Halides Solid Electrolyte

In recent years, the halide SEs have been attracting research attention for their wide electrochemical stability window and compatibility with high-voltage cathodes[8,75]. The Li-based ternary chlorides, Li_3MCl_6, offer high chemical stability and ionic conductivity of 0.5–3.0 $mScm^{-1}$. In contrast, the Na halides have only been reported with low ionic conductivity below 10^{-4} Scm^{-1} and crystal structures of P31c, P21/n and R3[8,75]. The size of Na ion (102 pm) is larger than Li ion (76 pm) and has lower ionic conductivity than Li_3MCl_6, whose crystal structures are C2/m and P3. Theoretical studies have predicted the phase-dependent ionic conductivities of Na_3YBr_6

and Na_3YI_6; however, few studies have reported on the phases of Na bromides and iodides, Na_3MX_6 (X = Br and I)[8,75].

2.10 Sulphide Solid Electrolytes

Compared to conventional electrolytes, sulphide-based materials have great potential because they undergo synthesis at lower temperatures, with high room-temperature ionic conductivity, low grain boundary resistance and a good contact with electrodes[76–80]. In recent years, great advances have been made in the development of lithium-sulphide electrolytes, and ionic conductivity as high as 10mScm^{-1} has been achieved[78]. This has led to further research into sodium-ion sulphide-based electrolytes. The Na_3PS_4 sulphide electrolyte has the following two known structures: cubic and tetragonal. In 2012, Hayashi et al. initially observed the ionic conductivity of cubic Na_3PS_4 to be 0.2 mScm^{-1}[77]. Subsequent studies attempted to investigate the effects of synthesis conditions on phase change and ionic conductivity of sodium-ion sulphide-based electrolytes to enhance their ionic conductivity and improve their air stability. This highlighted Na_3PS_4 as a potential solid-state electrolyte for sodium-ion battery applications, prompting many research efforts to further increase its ionic conductivity. To obtain an even higher conductivity, various elements have been doped, for instance, Si, Cl, Sb, Se and As were tested in Na_3PS_4 with some success[76–80].

2.11 Oxide Solid Electrolytes (NaSICON)

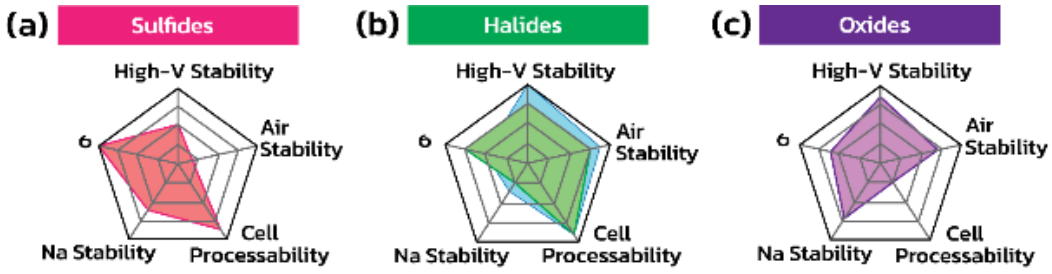

Fig. 2.8: Radar plot showing level of progress of properties for (a) sulphides, (b) halides and (c) oxides inorganic solid electrolytes. Adapted with permission from ref [78].

The NaSICON compounds are promising solid electrolyte materials with a unique 3D conduction network that endows the structure with superior ion-conducting property[60]. The NaSICON compounds of the general formula $Na_{1+x}Zr_2Si_xP_{3-x}O_{12}$ (with $0 \leq x \leq 3$) were first proposed in 1976 by Goodenough and Hong[81]. The high room-temperature ionic conductivity, 0.67 mScm^{-1} of NaSICON compounds has been achieved at $x = 2$ ($Na_3Zr_2Si_2PO_{12}$). They exhibit high thermal and superior chemical stability e.t.c as compared in Fig. 2.8. This family of materials is one of the groups of SEs that simultaneously possess high ionic conductivity and chemical/electrochemical stability.

2.11.1 Structure of NaSICON Solid Electrolyte

The original NaSICON solid solution has been derived from $NaZr_2(PO_4)_3$ by partial substitution of Si for P with the addition of Na to balance the negative charge[81]. The 3D framework of NaSICON compounds is formed by corner-sharing $(Si,P)O_4$ tetrahedra with ZrO_6 octahedra, and it can be characterized by structural building units (SBUs)[81,82]. This comprises two ZrO_6 octahedra and three $(Si,P)O_4$ tetrahedra each[83]. The SBUs are linked by $(Si,P)O_4$ tetrahedra to form infinite ribbons along the c-axis. The SBU is composed of interconnected framework cavities through which Na ions can move easily[81,82]. The general formula $Na_{1+x}Zr_2Si_xP_{3-x}O_{12}$ allows for a variety of compositions, with x values ranging from 0 to 3. At room temperature and with $0 < x < 1.8$, NaSICON crystallizes in a rhombohedral space group (R-3c). When Si content increases to $1.8 \leq x \leq 2.3$, it undergoes transition to a monoclinic C2/c symmetry. With a further increase in the Si content, it transforms back to the rhombohedral R-3c form[81,82]. The monoclinic version can also become rhombohedral at temperatures of 420–450 K due to the shear deformation of the unit cell. Maximum ionic conductivity of 0.67 $m{\cdot}Scm^{-1}$ at room temperature is achieved when $x = 2$ ($Na_3Zr_2Si_2PO_{12}$). The atomic coordinates for the $[Zr_2Si_2PO_{12}]^3$ frame were confirmed by diffraction studies of monoclinic $Na_{1+x}Zr_2Si_xP_{3-x}O_{12}$; however, discrepancies exist in the description of the Na sub-lattice[81,82].

In recent years, some models with different numbers of Na sites (3 or 4) and positions/occupancies have been proposed[82,84,85]. A recent study combining the bond valence energy landscape approach, the maximum entropy method and Rietveld neutron powder diffraction data analysis identified five distinct Na sites in the monoclinic phase and three in the rhombohedral phase. When the rhombohedral phase transforms to the monoclinic phase, the Na2 site (18e) splits into Na2' (4e) and Na3' (8f) sites, while the Na3 site (36f) splits into Na4' (8f) and Na5' (8f). The rhombohedral phase has a higher symmetry than the distorted monoclinic phase and thus a lower activation energy[86]. The NaSICON electrolytes possess high ionic conductivity and good chemical and thermal stability, and they remain stable in humid air and aqueous solutions. This characteristic makes them a promising option for Na ion SE[87]. However, ZrO_2 impurity, which is formed due to the volatilization of Na and P elements during high-temperature sintering, can hinder ion conduction at the grain boundary. Adding an excess of Na and P to the raw materials can prevent the formation of impurity and yield phase-pure NaSICON materials[88]. Research has focused on improving ionic conductivity, exploring the ion conduction mechanism and forming a stable interface with electrode materials[89].

The ionic conductivity of a crystalline material is influenced by the bottleneck size, which is determined by the skeleton structure[90]. Chemical modification is an effective way to increase ionic conductivity by changing lattice parameters and bottleneck sizes. Substituting the Zr^{4+} site with isovalent or heterovalent ions, such as Hf^{4+}, Sn^{4+}, Mg^{2+}, Ca^{2+}, Sr^{2+} and Ba^{2+}, has led to a notable increase in the bulk conductivity of NaSICONs[83,91–93].

The highest conductivity of 3.5 $mScm^{-1}$ was achieved when 2.5% of the Zr^{4+} was substituted with Mg^{2+}[94]. The enhanced conductivity was attributed to the enlarged bottleneck that Na ions use to migrate between sites. Substituting Zr^{4+} with Zn^{2+}, which has a similar ionic radius, resulted in a conductivity of 5.3 $mScm^{-1}$[83,95]. However, replacing Zr^{4+} with smaller ions, such as Co^{2+} and

Al^{3+}, causes the bulk conductivity to decrease slightly. The incorporation of Al^{3+} densifies ceramics, increasing grain boundary conductivity, while increasing Si/P ratio enlarges the bottleneck for Na ion transport, resulting in a dramatic enhancement of bulk conductivity (2.1 $mScm^{-1}$ at RT)[96].

The substitution of trivalent lanthanide ions (Sc^{3+}, Pr^{3+}, Eu^{3+}, Lu^{3+}, Y^{3+}, Yb^{3+}) for Zr^{4+} forms a wide range of solid solutions; however, the only difference between monoclinic and rhombohedral phases is a slight twist of the unit cell structure caused by a shear deformation of the unit cell[83]. The lattice parameters of Sc-doped NaSICON samples vary based on Na^+-ion concentration in the formula unit, yielding RT ionic conductivities up to 4.0 $mScm^{-1}$ with 20 at% Sc^{3+}[89,97]. The Pr and Eu elements have limited solubility due to the great difference in them and the host in terms of ionic radius. Evidently, dopants effectively enhance Na^+-ion diffusion properties, with low valence-doped ions, increasing Na ion concentration and radii that in turn broaden the migration channel, resulting in improved bulk conductivity[83]. The dopants also increase ceramic density, facilitating Na-ion transport at the grain boundaries. Pr^{3+} has the lowest electronegativity and the largest ionic radius, resulting in the highest ionic conductivity of 1.27 $mScm^{-1}$. Eu- and Lu-doped systems have conductivities of 1.08 and 0.83 $mScm^{-1}$, respectively. Substituting Zr^{4+} with lower electronegativity elements reduces the electronic conductivity ion conduction mechanism[98].

Early models related the ion conduction mechanism to the size of the bottleneck and thermal displacement[81,82,84,99]. For instance, Park *et al.*[100] revealed that incorporating excess Na into the NaSICON system can significantly affect grain conductivity (σ_G), increasing it at both low and high temperatures. Measurements showed σ_{ion} value from the Na-excess sample at 300°C to be 92% higher than that from the bare sample. They related the mechanism to the bottleneck size based on structural changes observed, such as an increase of ∼2.7 % in the smallest bottleneck area of the Na1–Na2 channel. This was corroborated by ab initio DFT computations, which also predicted a rise in the size of the smallest bottleneck in the Na1–Na2 diffusion channels with the addition of excess Na[100].

In a recent study, Zhang *et al.*[86] investigated ion conduction mechanisms in two NaSICON polymorphs. Bond valence energy landscape (BVEL) calculations suggested that Na5 has the lowest occupation (0.12/12%) and relatively high energy; however, the energy barrier for jumps to neighbouring local minima is low (≈0.47 eV), enabling its participation in ion transport. BVEL and ab initio molecular dynamics (AIMD) simulations revealed that Na^+ ions at all five sites take part in 3D network diffusion. The Na5 is the major pathway and cross-over site, climbing image nudged elastic band method (CI-NEB) revealed that correlated migration has a lower energy barrier than single-ion diffusion, suggesting that the former is the preferred conduction in $Na_3Zr_2Si_2PO_{12}$. An experimental substitution revealed that increasing the Na ion concentration is a more effective approach to enhancing ion conductivity than simply expanding the framework while keeping the Na ion concentration unchanged. The best conductivity was obtained at an optimum Na content of 3.3–3.55 mol per formula unit[86].

In another recent study, Morgan *et al.*[101] used variable temperature neutron diffraction, NMR spectroscopy and DFT calculations to investigate the thermal behaviour of $NaZr_2(PO_4)_3$. The results showed an increase in Na–O bond distances and rotations of the PO_4 and ZrO_6 polyhedra, leading to changes in lattice parameters. The NMR experiments and DFT calculations were used

to elucidate the trends in chemical shifts; however, empirically derived predictions were found to be unsuccessful. The 3rd Model, which incorporated finite temperature effects, provided values for NMR parameters that matched all trends. This study highlights the sensitivity of solid-state NMR to local dynamics, the utility of phonon calculations in predicting atomic displacement parameters and the importance of finite temperature effects in DFT calculations of NMR parameters[101]. Clearly, an insufficient understanding remains of the mechanism of conduction in this important class of materials.

2.11.2 Processing of NaSICON Solid Electrolytes

The NaSICON oxide powders are commonly synthesized using the following methods: sol–gel and solid-state reaction processes, as well as other processes, such as hydrothermal, co-precipitation, mechano-chemical synthesis and combustion synthesis[102–104]. The solid-state reaction involves mixing powder reactants in the correct proportions, grinding, calcining, and then pressing into green pellets and sintering at >1200°C to achieve high densification. This method is simple and cost-effective, but high temperatures may result in the volatilization of elements such as Na and P and the formation of secondary phases[105].

Sol–gel processing facilitates low-temperature processing, precise morphological control and improved chemical homogeneity. However, it is costly and complex, especially for large-scale production[106,107]. The hydrolysis of Zr and Si precursors, followed by the addition of P and Na salts, creates a colloidal solution that is heated to form a gel network and then crystallized at 700–1000°C. To create bulk samples, the nanosized powder is pressed and sintered at 1000–1250°C, with the processing parameters such as calcination temperature, sintering temperature and pH of the sol being important for stabilizing NaSICON phases[106,107]. The excess of P and Na must be added to compensate for evaporation during synthesis[106,107]. The sintering temperature should not be too high, as this could cause impurities from phase segregation/decomposition.

Synthesizing nanosized powders via wet chemistry has the benefit of producing dense specimens at low temperatures; however, these processes are expensive and difficult to scale up. An alternative material processing method is needed to lower sintering temperatures while avoiding the formation of impurity phases that impede sodium-ion conduction. This solution should be cost-effective and suitable for large-scale production.

A novel solution-assisted solid-state reaction (SA-SSR) method was developed by Naqash *et al.* to produce NaSICON compounds[108]. The procedure involves dissolving nitrates of Na and Zr in water, followed by the addition of tetraethyl orthosilicate (TEOS), nitric acid and $NH_4H_2PO_4$. After the solution is heated to 100°C and cooled, the powder is calcined at 800–1000°C. The resulting product is chemically homogeneous and contains ultrafine particles of size 0.1–0.2 μm with low secondary ZrO_2 phase. This process is cost-effective, uses low-cost raw materials and is easily scalable compared to wet-chemistry approaches. Furthermore, a 48-h milling step was recently added before sintering. This makes the method more time consuming.

The addition of sintering aids to fabricate dense bulk NaSICON ceramics has been effective; Na_3BO_3, Bi_2O_3 and $60Na_2O$-$10Nb_2O_5$-$30P_2O_5$ reduce sintering temperatures and notably improve ionic conductivity[40]. For instance, NZSP with 9.1wt% Na_3BO_3 sintered at 700°C has a conductivity of 0.1 $mScm^{-1}$ at room temperature, which is a three-fold increase compared to samples

without Na_3BO_3[109]. Advanced sintering techniques, such as microwave, spark plasma and cold sintering, have been applied to promote densification at low temperatures (down to 140°C). However, these[110], [111] extensive processes can be energy intensive, increasing the cost of commercial NaSICON synthesis. Further investigations are needed to understand the sintering process, because the future of solid-state batteries depends on cost-effective processing technologies.

2.12 Analytical Techniques used in this Study.

Below, the backgrounds of the techniques used in the study are discussed.

2.12.1 X-ray Diffraction

The X-ray Powder Diffraction (XRD) is a non-destructive technique that can be used to determine the atomic and molecular structures of crystal materials[112]. This is done by having X-rays (electromagnetic waves) scatter off the electrons of atoms in the crystal, creating a regular array of secondary spherical waves that can constructively interfere in certain directions (Fig. 2.9). These directions are established laue equation and simplified by Bragg's law that states that:

$$n\lambda = 2d\ sin\ \theta \tag{2.9}$$

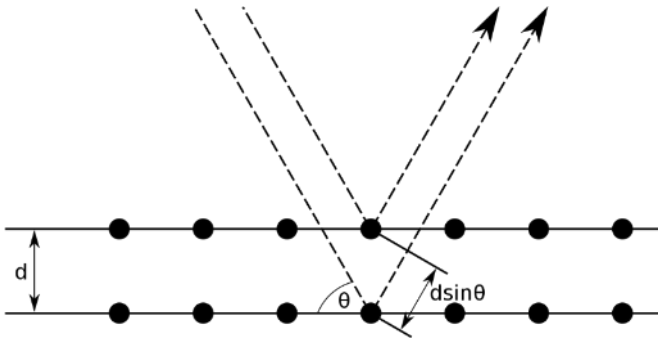

Fig. 2.9: Schematic illustration of Bragg's law

Where d is the spacing between diffracting planes, θ is the diffraction angle, n is an integer and λ is the X-ray wavelength. A powdered sample can be used to represent an isotropic case in which all possible crystalline orientations are equally represented[112]. This allows the use of angles and intensities of the diffracted beams to uncover crystallographic information about the powdered crystal material[112]. An X-ray diffractometer is employed in transmission, reflection and Debye-Scherrer modes to measure this information; the sample is typically put on one axis of the diffractometer while a detector rotates around it to form a 2θ angle with the X-ray tube[112].

2.12.2 High-Temperature X-ray Diffraction (HT_XRD)

The High-Temperature X-ray Diffraction (HTXRD) technique involves placing a fine powder into a quartz capillary and then either keeping it open to air or sealing it under inert gas (e.g., Ar).

Afterwards, the capillary is heated in a ceramic heater equipped with a cooling system that can control the temperature range from 20°C to 900°C. While the sample is heated, XRD is conducted at set temperatures, allowing the monitoring of temperature-related phase transitions and thermal expansion of the sample.

2.12.3 Rietveld Method

To analyse the average structure of a material in reciprocal space, the FullProf Suite software package[113] was used to implement the Rietveld full-profile fitting method[114]. This method involves a least-squares approach to extract crystal structural information from X-ray and neutron powder diffraction data by minimizing the weighted sum of point-by-point differences squared between a measured and calculated powder diffraction pattern. The experimental parameters and sample-dependent parameters are taken into account, such as instrumental parameters, background intensities, absorption, unit cell parameters, atomic fractional coordinates, atomic occupancy of each crystallographic site, Debye–Waller factors and background[12]. The Minimisation is defined by:

$$\text{Minimisation} = \sum_{i=0}^{N-1}\left(w_i(Y_{obs}\text{-}Y_{calc})\right) \tag{2.10}$$

The equation is the summation of ($w_i(Y_{obsi} - Y_{calc})$). The statistical weight, represented by w_i, is determined by the of the observed intensity, σ_i^2, where $wi = 1/\sigma_i^2$. Yobsi represents the observed value, and Ycalci represents the calculated value. The standard deviation is represented by σ, and the total number of points in the pattern used for refinement are represented by N. Constraints can be applied to the set of equations that need to be solved to reduce the degree of freedom. The Rietveld method is capable of refining multiple parameters simultaneously, such as unit cell dimensions, atomic coordinates, profile parameters, atomic site occupancies, temperature factors and background parameters. The equation is used for minimisation in the Rietveld full profile fitting method to obtain the optimal values of the parameters. The powder pattern information can be divided into four groups, as shown in Table 2.1.

Table 2.1 Relationship between powder diffraction pattern, sample, crystal structure and instrument parameter.

Peak intensity	**Atomic positions, temperature factor, structure factors, occupancy, texture, absorption, and geometrical contributions (e.g. polarization)**
Peak position	dimension of unit cell, symmetry, and instrumental contributions
Background	diffuse scattering (e.g. local structure, amorphous fraction etc.), Compton scattering, and scattering from sample container or air
Peak shape	Micro-structural parameters (e.g. micro-strain and crystallite size) and instrument profile

Residual functions are used to assess the accuracy of the Rietveld refinement, as shown below. The profile R-factor is a discrepancy index that indicates the level of agreement between the calculated and observed profiles and is the most commonly used measure of refinement quality.

$$\text{Profile factor:} \quad R_p = 100 \frac{\sum_{i=0}^{n=1} w_i |Y_{obs} - Y_{calc}|}{\sum_{i=0}^{n=1} w_i Y_{obs}} \tag{2.11}$$

$$\text{Weighted profile factor:} \quad R_{wp} = 100 \sqrt{\frac{\sum_{i=0}^{n=1} w_i |Y_{obs} - Y_{calc}|^2}{\sum_{i=0}^{n=1} w_i Y_{obs}^2}} \tag{2.12}$$

The R_{wp} considers the statistical uncertainty of each data point by incorporating a weighting scheme.

$$\text{Expected weighted} \quad R_{exp} = 100 \sqrt{\frac{N\text{-}P}{\sum_{i=0}^{n=1} w_i Y_{obs}^2}} \tag{2.13}$$

The expected weighted profile factor is the optimal statistically possible value for R_{wp}, determined by the number of data points (N) and refined parameters (P). R_{exp} indicates the precision of the data (i.e. counting statistics). The reduced chi-squared is a reliable measure of refinement quality and is calculated as the square of the ratio between the weighted profile R-value and the expected R-value.

$$\chi^2 = \left[\frac{R_{wp}}{R_{exp}}\right]^2 = \frac{\sum_{i=0}^{n} wi |Y_{obs} - Y_{calc}|^2}{N\text{-}P} \tag{2.14}$$

Some constraints can be introduced into the refinement process to minimize the number of free parameters. In crystalline materials, groups of atoms, molecules or coordination polyhedral have a predefined structure and are not completely independent. The constraints are typically placed on the coordinates of sites with specific local symmetries. The combination of Rietveld refinement with restraints has been shown to have a positive effect on the refinement process. Examples of restraints include linear constraints, which are used for chemistry and crystallographic site occupancy, as well as interatomic distances and angles. The use of restraints in refinement stabilizes the process, avoids false minima and accelerates convergence[12].

2.12.4 Nuclear Magnetic Resonance Relaxometry

The superionic conductors experience spin–lattice relaxation (SLR) caused by variations in the magnetic field that result from the movement of ions. In particular, quadrupolar relaxation occurs due to oscillations of the electric field gradient (EFG) within the ion's local environment[115]. The relaxation rate T_1^{-1} in these materials can be described by an exponential correlation function G(t) according to the Bloembergen, Purcell and Pound (BPP)[116] model for random jump diffusion in three dimensions.

In superionic conductors, which are materials that conduct ions, there is a phenomenon called spin–lattice relaxation (SLR) that happens due to the fluctuating electric field generated by the

movement of ions within the material[115]. In quadrupolar relaxation, these fluctuations are specifically caused by oscillations in the electric field gradient (EFG) within the local environment of the ion. This means that the EFG in the ion's immediate surroundings is not static; rather, it oscillates over time[115].

The relaxation rate T_1^{-1}, which refers to how quickly the magnetic spin system of the material returns to its equilibrium state after being perturbed, can be described by an exponential correlation function called G(t). This model was first introduced by Bloembergen, Purcell and Pound[116] in the context of random jump diffusion in three dimensions, and it has since been applied to various systems and phenomena, including the spin–lattice relaxation in superionic conductors.

$$G(t) = G(0)\exp(-1|\tau) \tag{2.15}$$

The G(t) equation is Fourier transformed to obtain the spectral density function J(w) that characterizes the frequency distribution in the system and is proportional to the relaxation rate T_1^{-1}[115]. In the case of quadrupolar relaxation, the relationship between the Zeeman relaxation rate T_1^{-1} and J(w) can be described as follows:

$$T_1^{-1} = K[J_1(w) + 4J_2(2\omega)] \tag{2.16}$$

$$T_1^{-1} = K\left[\frac{\tau}{1+(\omega\tau)^2} + \frac{4\tau}{1+(2\omega\tau)^2}\right] \tag{2.17}$$

$$K = \frac{1}{100}\left(\frac{e^2qQ}{h^2}\right)^2 \frac{1+\eta^2}{3} \tag{2.18}$$

The efficiency of Spin Lattice Relaxation is apparent when J displays intensities at or above twice the Larmor frequency[115]. The temperature dependence of SLR is typically given by an Arrhenius relationship, where $\tau = \tau_0 \exp^{(-EA/kBT)}$, where τ_0 is the pre-exponential factor and E_A is the average activation energy for the diffusion process. The Boltzmann constant is represented by k_B, and T represents the absolute temperature. The diffusion relaxation rate can be separated into following two temperature regimes: the high-temperature regime with $\omega t << 1$ and the low-temperature regime with $\omega t >> 1$. Between these two regimes, the relaxation rate reaches a maximum at a specific temperature, T_{max}. Considering the frequency dependence of SLR, T_1^{-1} can be described by the following equations[117],[118]:

For a high T regime

$$T_1^{-1} \propto \omega^{-\beta_{high}} \exp\left(E_A/k_B T\right) \tag{2.19}$$

For low T regimes

$$T_1^{-1} \propto \omega^{-\beta_{low}} \exp\left(-E_A/k_B T\right) \tag{2.20}$$

To apply the BPP model for 'uncorrelated' motion, which refers to isotropic single-ion jumps, the parameters $\beta_{low} = 2$ and $\beta_{high} = 0$ are used. The BPP model assumes that there is always a local motional correlation in the low-temperature regime, as the spins perform numerous precessions before jumping to the next position. In contrast, correlated motion of several types leads to values

of β_{low} less than or equal to 2, which is supported by different models for disordered ionic conductors, such as the coupling concept, the jump relaxation model, the dynamic structure model, and the model of a distribution of hopping correlation times. Nonetheless, there are some experiments on ionic conductors that do not exhibit any frequency dependence in relaxation measurements, meaning a β_{low} of 0[119]. Richards hypothesized that this could be due to the strongly correlated motion between only two atomic positions[120]. However, it is uncertain whether this relaxation model can account for this phenomenon.

2.12.5 Thermo-Gravimetric Analysis

The Thermo-Gravimetric Analysis (TGA) is a type of thermal analysis that measures the mass of a sample as it undergoes changes in temperature or time[121]. This technique can be used to identify phase transitions, gas absorption and desorption, thermal decomposition, and solid-gas reactions. The main component of a thermo-gravimetric analyser is a thermo-balance that is composed of a balance, a furnace, a temperature control system and a recording system[121]. Furthermore, TGA can be conducted in multiple atmospheres, such as ambient air, vacuum, inert gas, and oxidizing/reducing gases, as well as at different pressures, such as high vacuum, high pressure, constant pressure or controlled pressure[121].

2.12.6 Scanning Electron Microscopy Energy-Dispersive Spectroscopy

The Scanning Electron Microscopy (SEM) is a powerful tool that can provide information on a sample's external morphology and chemical composition[122]. A focused beam of high-energy electrons is used to scan the specimen surface in a raster pattern. Interaction of the electrons with the specimen surface atoms produces different signals, including secondary electrons, reflected or back-scattered electrons, characteristic X-rays and cathode-luminescence light[123]. Secondary electrons are used to produce high-resolution (<1 nm) images of the sample surface, while back-scattered electrons emerge from deeper positions and have a lower resolution. The Energy-dispersive X-ray spectroscopy (EDX) can be used to identify the abundance of elements and map their distribution in specimens. Conductive materials can be scanned without any additional steps; however, non-conductive specimens must be coated with an ultra-thin layer of gold or graphite for imaging[123].

2.12.7 Raman Spectroscopy

The Raman spectroscopy is a technique used to identify and examine a material's structure and chemical makeup[124]. When a material is exposed to light, typically generated by a laser, a portion of the light is scattered in an inelastic manner at either a longer or shorter wavelength than the light source, a phenomenon known as the Raman Effect that was discovered by Sir C.V. Raman in 1928. The Raman Effect is usually weaker than Rayleigh scattering, which is the scattering of light with the same energy and wavelength as the incident light[124,125]. Vibrations of atoms within a solid occur at frequencies between 10^{12} and 10^{13} Hz, which are related to the atom's structure[124,125]. When a laser emits photons of light with a frequency ν_0, the Raman lines of frequency

$\nu_0 \pm \nu_1$ are present in the scattered beam, as the photons cause transitions in the sample and either gain or lose energy through the collective vibrations of the atoms[124,125]. Not all transitions can be seen in the Raman spectrum; for a Raman active transition to take place, the nuclear motion has to cause a change in polarizability. Raman technique uses monochromatic light (visible, near-infrared, or near-ultraviolet) to detect vibrational, rotational and other low-frequency modes in a system. This results in a decrease (Stokes Raman scattering) and an increase (Anti-Stokes Raman scattering) in photon energy, which can be used to determine the molecular structure[124,125]. This effect is determined by the electric dipole– dipole polarizability derivative of a bond. Neutral bonds (e.g., C─C, C─H, C═C) have a strong Raman signal due to the large changes in polarizability during a vibration, while polar bonds (e.g., C─O, N─O, O─H) have a weak Raman signal due to the small effect on polarization from a vibration[124,125].

2.12.8 X-ray Photoelectron Spectroscopy

The x-ray photoelectron spectroscopy (XPS) is an analytical technique that can be used to determine the elemental composition of a sample surface up to a depth of 10 nm[126]. This technique is based on Ernest Rutherford's work that states that the binding energy of an electron is equal to the energy of the incident X-ray photon minus the electron's kinetic energy plus the electron's work function. XPS systems can be used with either monochromatic Al Kα or Mg Kα X-rays or with a synchrotron light source with either soft or hard X-rays. Using different photon energies makes it possible to obtain information from different depths of the sample[126]. Furthermore, XPS can also be performed through line profiling, mapping, and depth profiling to evaluate the uniformity of the elemental composition. For depth profiling, ion beam or cluster etching can be used to analyse deeper layers of the sample[126].

2.12.9 Electrochemical Impedance Spectroscopy

The Electrochemical Impedance Spectroscopy (EIS) is an analytical method used to evaluate an electrochemical system without taking any measurements within the system[127,128]. This technique can be used to measure the internal resistance, the state of charge and the state of ageing of a battery[129]. During the process, a modulated sinusoidal AC potential is applied over a wide range of frequencies (10^6~10^{-2} Hz) to a static potential of an electro-chemical cell, and the response current and its phase are then measured. The signal is usually too miniscule (less than 10 mV in amplitude) to disturb the system's linearity[129]. The EIS data can be displayed in following two ways : Bode plots (log frequency vs. absolute value of the impedance and phase shift) and Nyquist plots (real part impedance vs. imaginary part impedance) [129].

It is possible to perform a qualitative analysis of the plots if the curves depicting certain states of the system are known[129]. Equivalent electrical circuits that model the chemical and physical processes occurring in the system can also be designed and used to fit EIS plots. This requires the use of different circuit elements, such as resistors, capacitors, constant phase elements, Warburg elements and virtual inductors[129].

2.12.10 Galvano-static Cycling with Potential Limitation

The batteries are usually charged or discharged using a constant current or voltage[130]. In the laboratory, the constant current mode is often used to evaluate the energy storage characteristics of electrode material, referred to as galvano-static cycling with potential limitations (GCPL). Specifically, a constant current density (measured in Ag^{-1} or Acm^{-2}) is applied between the working electrode and the counter electrode, and the potential is monitored and recorded between the working electrode and the reference electrode. When the potential reaches either the upper or lower limits, the current direction is reversed[130]. Furthermore, GCPL tests can be used with different current densities to determine the rate capability of electrode materials.

3 Materials and Experiments

3.1 Materials

The following chemical reagents are used for the study, sodium carbonate Na_2CO_3 (VWR chemicals), NaOH (Alfa Aesar, 99%), sodium peroxide, Na_2O_2 (99%, Sigma Aldrich), zirconium dioxide ZrO_2 (15–25 nm, Alfa Aesar, 99.9%), silicon dioxide, SiO_2 (90 m^2/g, Aerosil, 99%), sodium hydrogen phosphate, $NaH_2PO_4 \cdot H_2O$ (99%, Merck), zirconium oxynitrate $ZrO(NO_3)_2$ (99.5% Sigma Aldrich) and $SiO_{2(amorph)}$ (99.9%, Sigma Aldrich) were used. The $SiO_{2(amorph)}$ is the common amorphous SiO_2 that has a small surface area compared to aerosol.

3.1.1 Sample Preparation

In this study, the synthesis of $Na_3Zr_2Si_2PO_{12}$ (NZSP) was accomplished by HEM and two other reaction pathways such as solid-state (SS) and sol–gel (SOL). The solid-state approach as reported by Jolley *et al.*[92], and the sol–gel synthesis based on the method described by Naqashi *et al.*[108] (the reported calcination time was increased to obtain a pure phase at 800°C), were compared with the HEM used in this study.

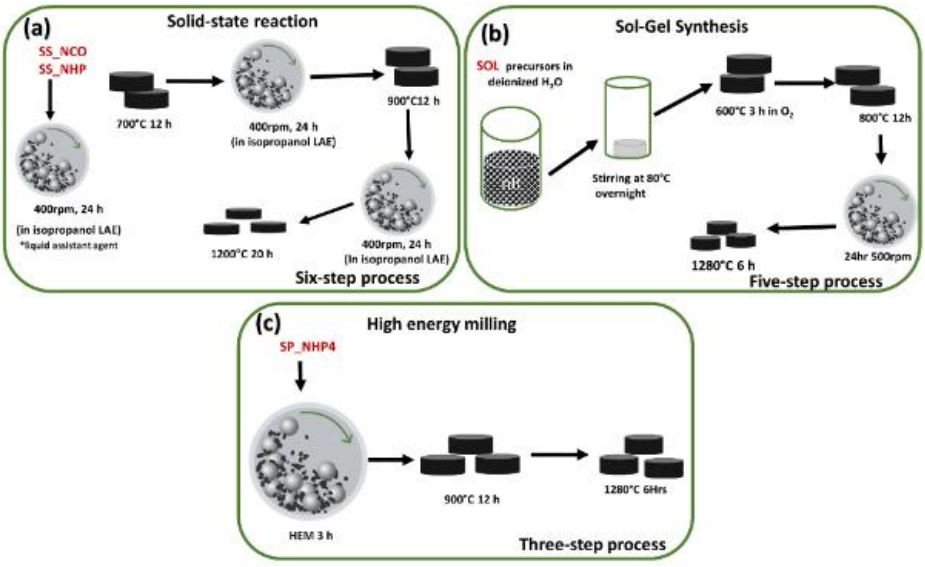

Fig. 3.1: Flow outline of the processing steps of the (a) six-step solid-state reaction, (b) five-step sol–gel and (c) high-energy (HEM) mechano-chemical synthesis

As stated below, two precursor combinations for the solid-state reaction and one for the sol–gel and HEM were used.

Solid-state synthesis:

$$SS\_NCO: Na_2CO_3 + 2ZrO_2 + NH_4H_2PO_4 + SiO_2 \rightarrow Na_3Zr_2Si_2PO_{12} + CO_2 + H_2O \quad (3.1)$$

$$SS\_NHP: Na_2CO_3 + NaH_2PO_4 \cdot H_2O + 2ZrO_2 + 2SiO_2 \longrightarrow Na_3Zr_2Si_2PO_{12} + CO_2 + H_2O \quad (3.2)$$

Sol–gel synthesis:

$$SOL: 3NaNO_3 + 2ZrO(NO_3)_2 + NH_4H_2PO_4 + 2Si(OC_2H_5)_4 \rightarrow Na_3Zr_2Si_2PO_{12} + CO_2 + H_2O \quad (3.3)$$

HEM:

$$SP\_NH4: Na_2O_2 + 2ZrO_2 + NaH_2PO_4 \cdot H_2O + 2SiO_2 \rightarrow Na_3Zr_2Si_2PO_{12} + 2H_2O \quad (3.4)$$

The stoichiometric mixtures of raw materials were taken through the steps outlined in Fig. 3.1 for each processing route. An 8000M SPEX high-energy mill was used for the method developed in this study, and a Fritsch planetary ball mill was used to reproduce the other methods reported in the literature.

In the developed method, the mixture of precursors with a selected molar ratio (total weight of ~2 g) was loaded in a 50 mL hardened-steel vial and ball milled for 3 h in the 8000 M SPEX mill. Steel balls of 20 g (two large balls weighing 8 g each and four small balls weighing 1 g each) were used for ball milling. This was followed by the calcination and sintering step outlined in Fig. 3.1. The SPEX mill delivers more intense and rapid energy input through high-frequency, linear impact motions, making it suitable for fast, aggressive milling, whereas the Fritsch planetary mill offers more controlled, lower-energy milling with circular rotational motion, ideal for gradual grinding and homogenous mixing. Comparing both allows us to understand how milling mechanism and energy input influence the phase formation, microstructure, and ion transport in NaSICON solid electrolytes.

For the optimization of the HEM, the calcination temperature was increased from 900°C to 1100°C; the sintering temperature was not changed. Sodium and zirconium sources were changed to have different precursor combinations (SP_NH4 combination is SP_NO here because of the change in calcination temperature), as listed below:

$$SP\_NCO: Na_2CO_3 + 2ZrO_2 + 2SiO_2 + NaH_2PO_4 \cdot H_2O \rightarrow Na_3Zr_2Si_2PO_{12} + CO_2 + H_2O \quad (3.5)$$

$$SP\_NOH: NaOH + 2ZrO_2 + 2SiO_2 + NaH_2PO_4 \cdot H_2O \rightarrow Na_3Zr_2Si_2PO_{12} + H_2O \quad (3.6)$$

$$SP\_NO: Na_2O_2 + 2ZrO_2 + 2SiO_2 + NaH_2PO_4 \cdot H_2O \rightarrow Na_3Zr_2Si_2PO_{12} + H_2O \quad (3.7)$$

$$SP\_NCO: Na_2CO_3 + ZrO(NO_3)_2 + 2SiO_2 + NaH_2PO_4 \cdot H_2O \rightarrow Na_3Zr_2Si_2PO_{12} + NO_2 + H_2O \quad (3.8)$$

Furthermore, attempt was made to investigate the effect of processing parameters on the structure, conductivity, and microstructure morphology of $Na_3Zr_2Si_2PO_{12}$.

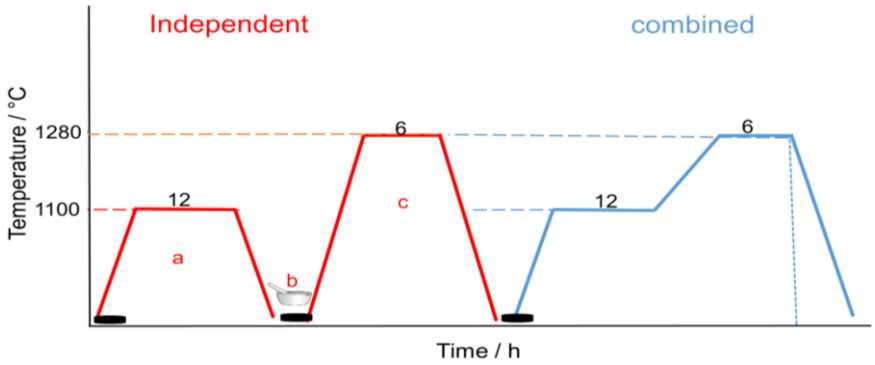

Fig. 3.2: Heat treatment schedule of independent and combined treatment showing three seperate stages a) calcination, b) grinding and repelletizing and c) sintering in the independent schedule and two steps in the combined treatment.

To achieve this, stoichiometric molar ratio of the precursors were processed using high-energy milling. The samples were treated with two schedules namely; independent and combined schedule (Fig. 3.2). The independent treatment involved making pellets with the milled powder in a 12-mm die, followed by calcination at 1100°C for 12 h and grinding in a mortar with a pestle. The ground powder was repelletized and sintered at 1280°C for 6 h at (300°C/h, 240°C/h, 180°C/h, 120°C/h, and 60°C/h heating/cooling rates). In the combined approach, the grinding step after calcination was eliminated, the HEM powder pellets were subjected to a single two-step (1100°C for 12 h, and 1280°C for 6 h) heat treatment at (300°C/h, 240°C/h, 180°C/h, 120°C/h, and 60°C/h°C/h). The study also investigated the effect of N_2, O_2, Ar, sintering environments, quenching in water, air and nitrogen media, as well as the effect powder particle size ranges on the structure, ZrO_2 fraction and morphology of $Na_3Zr_2Si_2PO_{12}$ obtained from the combined treatment.

Table 3.1 Summary of NZSP synthesis routes showing sample codes, synthesis methods, precursor compositions, and notes. The table is divided into compositions adapted from literature and those developed using high-energy milling (SPEX) in this study.

Sample Code	Synthesis Method	Precursors	Reference/Notes
SS_NCO	Solid-state	Na_2CO_3, ZrO_2 (nano), $NH_4H_2PO_2$,SiO_2 (amorph)	Jolley et al.
SS_NHP	Solid-state	Na_2CO_3, $NaH_2PO_4{\cdot}H_2O$, ZrO_2 (nano),SiO_2 (amorph)	Jolley et al.
SOL	Sol–gel	$NaNO_3$, $ZrO(NO_3)_2$, $NH_4H_2PO_4$, $Si(OC_2H_5)_4$	Naqashi et al. with longer calcination
Compositions developed using high-energy milling (SPEX) in this study			
SP_NH4	High-energy milling	Na_2O_2, ZrO_2 (nano), $NaH_2PO_4{\cdot}H_2O$, SiO_2 (Aerosil-90)	Developed in this study using SPEX 8000M

SP_NCO	High-energy milling	Na_2CO_3, ZrO_2, SiO_2, $NaH_2PO_4 \cdot H_2O$	Used for high-temperature optimization
SP_NOH	High-energy milling	NaOH, ZrO_2, SiO_2, $NaH_2PO_4 \cdot H_2O$	Precursor change to NaOH for phase behavior study
SP_NO	High-energy milling	Na_2O_2, ZrO_2, SiO_2, $NaH_2PO_4 \cdot H_2O$	Na_2O_2 used to enhance reactivity
SP_ZNO	High-energy milling	Na_2CO_3 + $ZrO(NO_3)_2$ +SiO_2+$NaH_2PO_4 \cdot H_2O$	Nitrate-based Zr precursor variation

Lastly, the influence of doping on the structure and conductivity was examined. The combined schedule of sample preparation was employed, using MgO and MoO_3 from Sigma Aldrich. A total of four Mg- and seven Mo-doped compositions, outlined in Table 3.1, were evaluated.

Table 3.2 Sample notation for the doped compositions

Sample Notation	**Composition**
$Mg_{0.1}Si_2$	$Na_{3.2}Zr_{1.9}Mg_{0.1}Si_2PO_{12}$
$Mg_{0.1}Si_{2.2}$	$Na_{3.4}Zr_{1.9}Mg_{0.1}Si_{2.2}P_{0.8}O_{12}$
$Mg_{0.2}Si_2$	$Na_{3.4}Zr_{1.8}Mg_{0.2}Si_2PO_{12}$
$Mg_{0.2}Si_{2.2}$	$Na_{3.6}Zr_{1.8}Mg_{0.2}Si_{2.2}P_{0.8}O_{12}$
$Mo_{0.025}$	$Na_{3.1}Zr_2Si_2Mo_{0.025}P_{0.95}O_{12}$
$Mo_{0.05}$	$Na_{3.2}Zr_2Si_2Mo_{0.05}P_{0.9}O_{12}$
$Mo_{0.075}$	$Na_{3.3}Zr_2Si_2Mo_{0.075}P_{0.85}O_{12}$
$Mo_{0.1}$	$Na_{3.4}Zr_2Si_2Mo_{0.1}P_{0.8}O_{12}$
$Mo_{0.2}$	$Na_{3.5}Zr_2Si_2Mo_{0.2}P_{0.6}O_{12}$
$Mo_{0.3}$	$Na_{3.6}Zr_2Si_2Mo_{0.3}P_{0.4}O_{12}$
$Mo_{0.4}$	$Na_{3.7}Zr_2Si_2Mo_{0.4}P_{0.2}O_{12}$

In order to investigate the effect of processing on the structure and ion dynamics, NaSICON ($Na_3Zr_2Si_2PO_{12}$) labelled SS_NCO and (SS_NHP) were prepared using conventional solid-state methods in the comparative study described above and illustrated in Figure 3.1. In addition, $Na_3Zr_2Si_2PO_{12}$ (NZSP) and $Na_{3.4}Zr_2Si_{2.4}P_{0.6}O_{12}$ (NZS24P) were prepared using the high-energy milling process. EIS was performed on the pellets after final sintering, and some of the pellets were crushed for further characterization with HT_XRD, and NMR.

3.2 Characterization

This section complements the broader background discussed in the previous chapter, by providing specific experimental details of the techniques.

The experiments on physical adsorption of N_2 were carried out to determine the surface areas of products; they were performed on a Quantachrome Quadrasorb EVO instrument. The measurement parameters used were a pressure tolerance of 6.6661 Pa, an equilibration time of 60s and an equilibrium time out of 120s. The Brunauer−Emmett−Teller (BET) specific surface area was determined from five data points between a relative pressure (p/p0) of 0.1 and 0.25.

The Laser scattering was used to measure the particle size distribution (PSD) obtained using Horiba LA-950V2 analyser with ethanol as dispersing medium. The Differential Thermal Analysis (DTA coupled with TGA) was used to study the thermochemical changes/phase transitions. It was carried out on an STA 449 C Jupiter instrument (NETZSCH, Germany) from room temperature to 1300°C with a constant heating rate of 5°Cmin^{-1} and an argon flow rate of 312.5 mLmin^{-1}. The data were treated with NETZSCH Proteus thermal analysis software and origin (peak analysis).

Room and high-temperature XRD were used to study the structural evolution and phase purity. The XRD patterns were collected using a STOE Stadi-P powder diffractometer with Mo-$K_{\alpha1}$ radiation (λ = 0.70932 Å) with a linear MYTHEN2 detector module and a focusing Ge111 monochromator from 4 to 70 degree of 2θ. The data collection time was 5hrs for each diffractogram at room temperature and 2hrs for each at elevated temperature in HT_XRD. The Rietveld refinement was applied using the XRD data to determine the lattice parameters and phase fractions of the obtained material using the Fullprof software package[131]. Crystallite size was determined from Scherer equation and W-H relation using HKL refinement output files. Vesta was used for structure visualisation. Raman spectroscopy was used to study vibrational properties, performed with a LabRAM HR evolution spectrometer (HORIBA Scientific) using a ×100 magnification objective and an excitation wavelength of 632.81 nm, using a 600 gmm^{-1} grating. The data were acquired at exposure times of 10s with 15 accumulations over the wavenumber range from 100 to 1300 cm^{-1}.

The scanning electron microscopy and energy-dispersive x-ray spectroscopy were used to study the morphology and elemental composition of the solid electrolyte. Images were recorded on a Zeiss Merlin microscope using 5 kV and 30 kV acceleration voltages, respectively. The x-ray photoelectron spectroscopy (XPS) was used to determine the surface chemical composition of the samples. It was performed using a K-alpha$^+$ spectrometer (Thermo Fisher Scientific) with monochromatic Al-K_α radiation (λ = 1486.6 eV) and a spot size of ~400 μm. Survey spectra were recorded with a pass energy of 200 eV and detailed spectra of 50 eV. The Thermo Avantage software was used for data acquisition and spectra deconvolution, determining a Shirley background with the implemented smart background function. All spectra were binding energy corrected using the C 1 s signal at 285 eV. Normalization of the intensity was achieved using the most intense oxygen O 1 s signal for all core-level data.

The static ^{23}Na relaxometry and lineshape analysis was performed on a Bruker Avance Neo 200 MHz spectrometer at a magnetic field strength of 4.7T. The samples were sealed in 10mm evacuated silica glass tubes. The data were acquired with an inversion-recovery and solid-echo pulse sequence in the temperature range from 260 to 595 K. There cycle delay was set to values between 0.4 and 2s and was always well above 5·T_1. 1M NaCl was used as a reference for the ^{23}Na NMR spectra.

The electrochemical impedance spectroscopy (EIS) was used to estimate ionic conductivities through which the ionic-conducting, semi-conducting, mixed-conducting or dielectric behaviour and the dynamics of bound and mobile charge in the bulk and interfaces can be studied. Two-electrode EIS measurements are typical, as they are experimentally simple and can be applied to a material, cell or pack straightforwardly without modification. EIS of a two-electrode cell using symmetric ion-blocking electrodes was used to extract the ionic conductivity (σ_{ion}) of solid electrolyte, given by:

$$\sigma_{ion} = \frac{l}{R_{total}A} \tag{3.9}$$

Where R_{total} is the total resistance of the electrolyte sample, l is the sample thickness and A is the area. Measurement was done on Au sputtered samples with pellet geometry; 120 mg weight, 1 mm average thickness, 8 mm diameter and was on a VSP-300 Biologic in the frequency range of 3 MHz to 1 Hz. Three samples were measured for each set of conditions. Relaxis software was used for data fitting, and conductivity was calculated from eqn 3.9

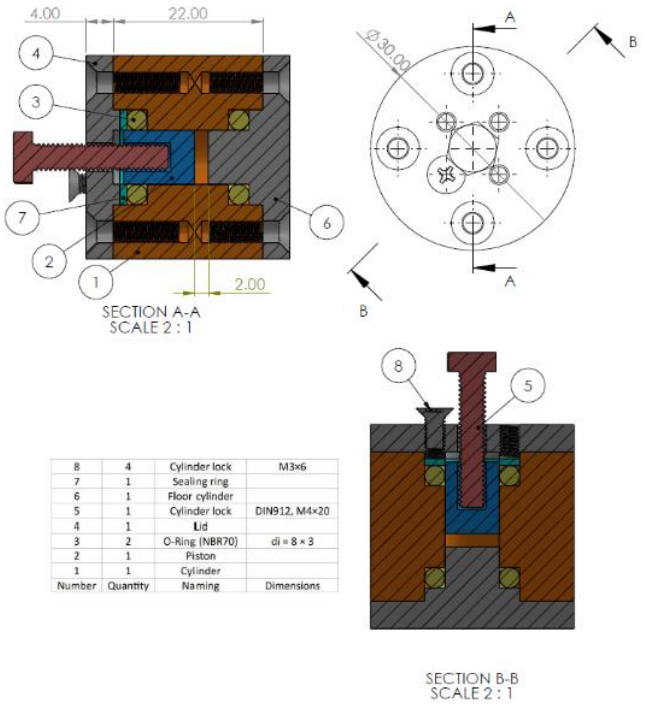

Number	Quantity	Naming	Dimensions
8	4	Cylinder lock	M3×6
7	1	Sealing ring	
6	1	Floor cylinder	
5	1	Cylinder lock	DIN912, M4×20
4	1	Lid	
3	2	O-Ring (NBR70)	di = 8 × 3
2	1	Piston	
1	1	Cylinder	

Fig. 3.3: Schematics of the 8mm PEEK cell used for EIS and GCPL

The galvanostatic coulometry with potential limitations (GCPL) was employed to measure the cycling stability. Symmetric cells were made by placing sodium electrodes on each side of the pellets, the sandwich was placed in an 8 mm diameter cell made of PEEK and a force of 3 kN was applied with a torque screw. 3 samples were measured to ensure data reproducibility. To study stability against Na/NZSP/Na symmetric cells were cycled on a VMP potentiostat at 1 $mAcm^{-2}$ current density. To study stability against active material all-solid state half cells were built with $Na_{0.67}MnO_2$ (NMO). To prepare the cathode of an all-solid-state Na/NZSP/NMO cell,

the active material NMO was mixed with carbon black, PAN, and $NaPF_6$ (65:10:15:10 by weight) and ground in a mortar. The mixture was then dispersed in DMF at 50°C and stirred overnight. The obtained slurry was spread evenly on a carbon coated aluminium foil to produce an electrode film with an active material loading of around 2 $mgcm^{-2}$, which was dried at 60°C for 10 hours under vacuum. The cells were fabricated in an argon-filled glove box with sodium foil as the anode. For the Na/NZSP/NMO-Au the slurry was cast on the pellet to a desired loading and the pellet was dried in vacuum at 60°C, and Au was coated on the cathode side of the pellet. The cycling was done on a VSP potentiostat.

4 Characterization and Comparative Study of Mechano-chemically Induced NaSICON Sodium Solid Electrolyte Synthesis

The majority of the results presented in this chapter have already been published in ChemSusChem[132]

4.1 Particle Size Distribution and Surface Area

The particle size distribution (PSD) of powders is a crucial factor in phase formation and microstructure evolution.

The PSD analysis of samples prepared by different methods and precursor combinations is shown in Fig. 4.1 a,b, in which a log-normal PSD with maxima at approximately 1 and 10 μm was observed in SS_NCO and SS_NHP and 10 and 60 μm in SP_NH4. A bimodal distribution with 10 and 60 μm average sizes was observed in SOL, which agrees with the morphology observed in SEM (Fig. 4.2:). From the results, the HEM after 3 h provided a particle size close to that obtained after 24 h of milling with the planetary ball mill. This effect can be attributed to the higher mechanical energy of the shaker mill.

Upon further investigation of the effects of precursor combinations on the PSD, it was observed (Fig. 4.2: c,d) that even though all combinations show a bimodal PSD, the sizes of SP_ZNO were much larger, averaging 100 and 1500 μm against SP_NC, SP_NO and SP_NOH, which averaged 10 and 60 μm. The SP_ZNO sample showed a high susceptibility to agglomeration. This might be related to a granular texture of the starting precursor and/or some absorption of moisture. These properties lead to a higher tendency for aggregation upon the start of milling, thus reducing milling efficiency.

The results are consistent with the powder morphology observed by SEM (Fig. 4.2:), which showed a range of similarly-sized agglomerates. The BET surface areas are shown in Fig.4.1. In agreement with the trend observed in PSD, SS_NCO, SS_NHP and SP_NH4 had a larger surface area. A similar trend was observed across the precursor combinations, where SP_NC had the largest surface area and SP_ZNO had the smallest surface area, indicating that both processing routes and the precursor combination profoundly affected the PSD, surface area and morphology.

The PSDs and surface areas are in close agreement with what was observed by Jalalian *et al.*[102] and Naqash *et al.*[108].

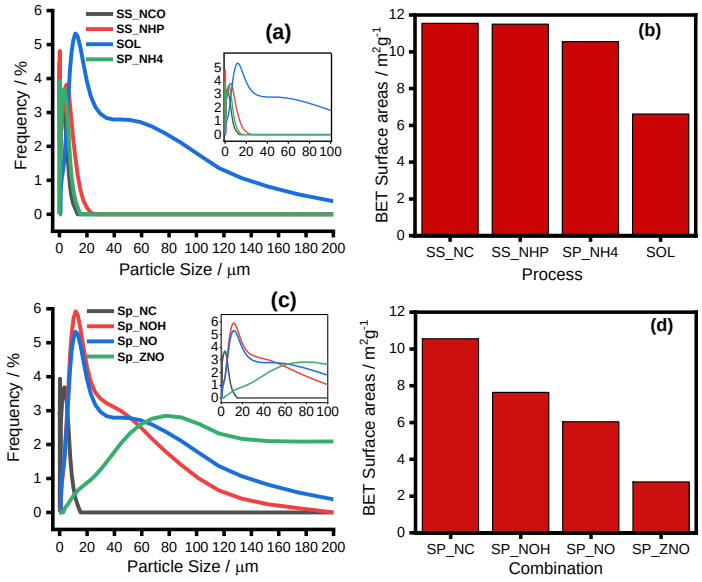

Fig. 4.1: Particle size distribution (PSD) with corresponding surface areas for the processing routes; (a, b) variation of particle size distribution and surface area with processing route; (c, d) effect of precursor combination on the particle size distribution

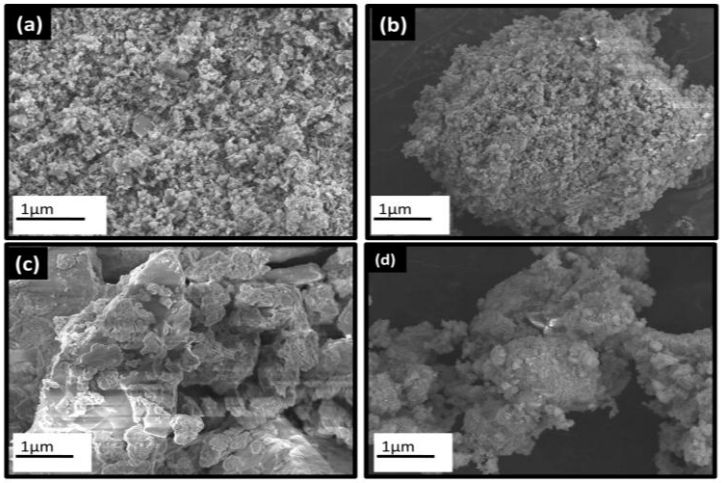

Fig. 4.2: Morphology and distribution of particles after milling for (a) SS_NCO, (b) SS_NHP (c) SOL and (d) SP_NH4

4.2 Phase Transitions/Evolution Through the Processing Steps

To gain insight into different transformations that took place during the conversion of the starting precursor mixtures to the final product, samples from every step of each processing route were

studied. The observations for the different processing routes are shown in Fig. 4.3:, Fig. 4.4:, and Fig. 4.5:. TG and DSC investigated the non-isothermal mass loss process for the mixtures. The weight loss of the mixture during annealing occurs mainly at temperatures below 500°C; this reflects the reactants' thermal decomposition/dehydration and oxidation reaction[133]. Three weight loss regions corresponding to the release of H_2O, CO_2, and NaSICON formation were observed with increasing temperature for SS_NCO (Fig. 4.3:). A corresponding broad peak with two endothermic humps at 820°C and 1050°C was observed on the DSC of the same sample. The hump at 820°C can be attributed to the conversion of low-temperature tetragonal ZrO_2 to monoclinic[104] and the onset of NaSICON conversion. The hump at 1050°C might be correlated with the crystallization of NaSICON[134],[135]. For the SS_NCO XRD patterns (Fig. 4.4a) in different processing steps, it was observed that the reflections after the first mixing in the planetary ball mill were mainly from precursor materials, predominantly ZrO_2, implying that 24 h of grinding with the mill achieved size reduction and mixing but little or no initial reaction. After calcination at 700°C for 12 h, ZrO_2 and intermediate $NaZr_2(PO_4)_3$ reflections were observed. Some low-intensity monoclinic NaSICON $Na_3Zr_2Si_2PO_{12}$ (SG15, *C2/c*, PDF card: 01-070-0234) reflections with monoclinic ZrO_2 evolved after the second calcination at 900°C for 12 h. A narrowing of the NaSICON peaks due to an increase in crystallinity and some monoclinic ZrO_2 secondary phase was observed after the final sintering at 1200 °C.

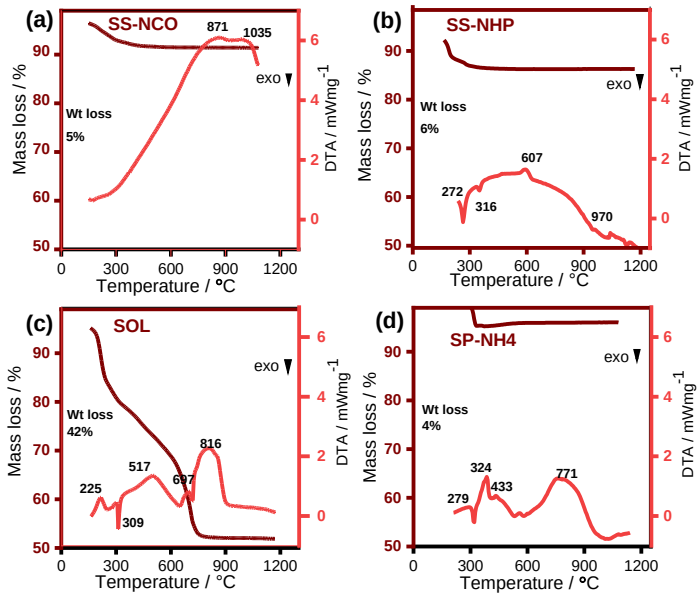

Fig. 4.3: Temperature dependent transitions of the different processing routes (a,b,c,d) Corresponding TGA/DTA curves for SS_NCO, SS_NHP, SOL and SP_NH4 respectively, the brown curve and left axis indicate the thermogravimetric weight loss, while the right axis displayed DTA

The TGA of SS_NHP after the first 24 h of milling showed three weight loss regions between 25–200°C, 200–300°C and 300–400°C and a steady region from 400°C (Fig. 4.3b). This might be ascribed to the decomposition of hydrate, carbonate and phosphate, NaSICON conversion and crystallization. Correspondingly, two exothermic dips at 190°C and 277°C and three endothermic

peaks at 523°C, 970°C and 1075°C were observed in DSC. This is consistent with the TGA results and thus ascribed to similar phenomena.

Furthermore, after different steps, XRD (Fig. 4.4b) revealed that the first 24 h of milling achieved mixing and size reduction without an initial reaction. The reflections are mainly from the starting precursor. This might be related to the high thermodynamic stability of ZrO_2: it transforms from a low-temperature monoclinic to a high-temperature tetragonal structure and participates in the final conversion to NaSICON only at a high temperature. The intermediate $Na_2Zr(PO_4)_2$ phase was observed after calcination at 700°C for 12 h. After 900°C, monoclinic NaSICON was observed. Upon heating to 1200°C, a narrowing of reflections, an increase in intensity indicating increased crystallinity and a reduction in intensity of the second phase was observed.

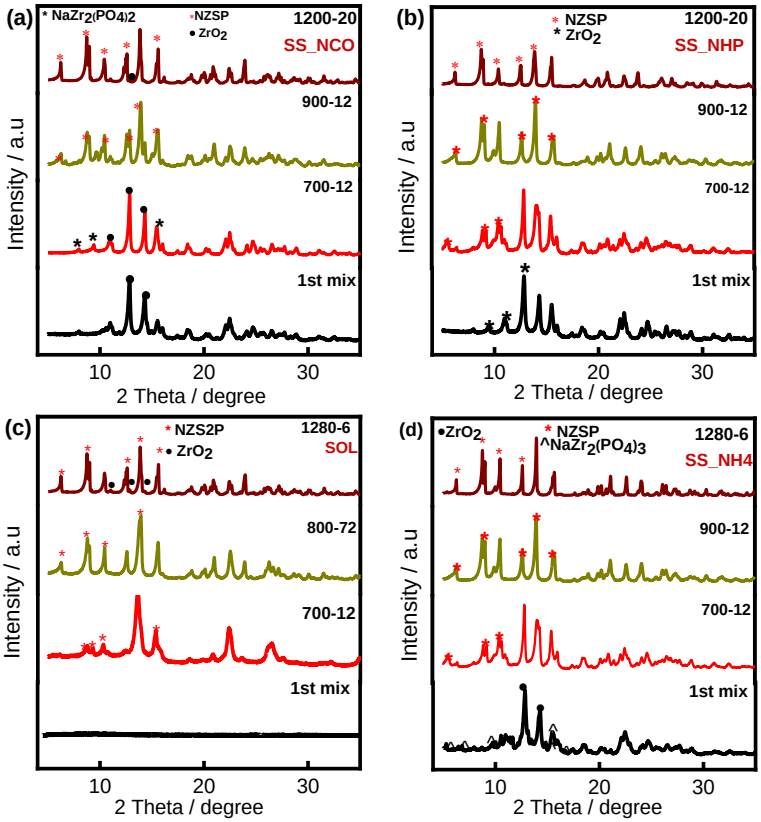

Fig. 4.4: Room temperature XRD λ = 0.70932 after each process step, a,b,c,d) for SS_NCO, SS_NHP, SOL and SP_NH4, respectively.

TGA of SOL samples revealed four main regions of thermal events (Fig. 4.3c). The initial weight loss event occurred between 25°C and 170°C, with a dominant endothermic peak at 167°C. This can be attributed to the loss of physisorbed water. Events of a greater magnitude followed by thermal peaks at 309°C, 493°C, and 717°C corresponding to decomposition of nitrates, carbonates and chemisorbed water, and monoclinic to rhombohedral second-order phase transition[136] resulted in continuous weight loss until the residual mass was stabilized around 800°C. The XRD

pattern of the initial gel was amorphous (Fig. 4.4c). After calcination at 700°C for 12 h, an intermediate $NaZr_2(PO_4)_3$ phase appeared, and the sample crystallized in the monoclinic structure after heating at 800°C.

The TGA of SP_NH4 revealed four main regions (Fig. 4.4d). The initial weight loss occurred in following temperature ranges: 100–200°C, 200–300°C and 300–400°C, with a dominant peak at 189°C, 234°C and 324°C. This can be ascribed to the loss of physiosorbed water, decomposition of chemisorbed water/hydrates, and NaSICON formation/crystallization. A gradual increase in weight from 400°C to 500°C was observed, which might be from the purging gas, as no new phase that could be attributable to oxidation or reaction with the gas environment was observed within that temperature range on XRD. Subsequently, no further heat loss was observed. The XRD (Fig. 4.4d) analysis of the sample after HEM showed reflections of the intermediate $NaZr_2(PO_4)_3$ phase and ZrO_2. Unlike the planetary ball mill treated samples, monoclinic NaSICON (SG15: *C*2/*c*, PDF code:01-070-0234) reflections begin to appear after calcination at 700°C. The sample crystallized to the monoclinic structure after heating to 900°C.

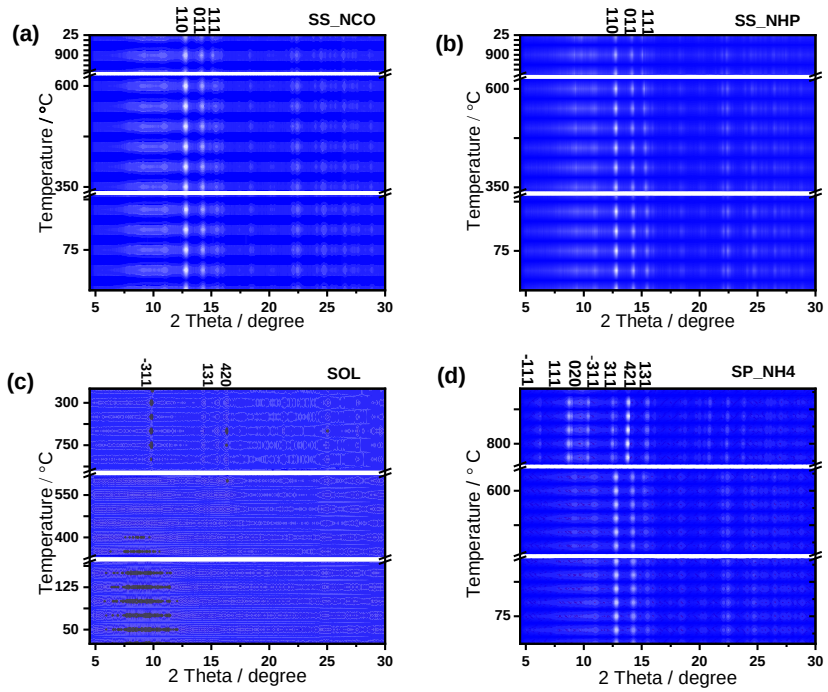

Fig. 4.5: Temperature-dependent structural evolution of the different processing routes. a,b,c,d) High temperature XRD λ = 0.70932 for SS_NCO, SS_NHP (showing ZrO_2 C2/c reflections), SOL, and SP_NH4 (showing NaSICON C2/c reflections) respectively

To further understand the structural evolution of NaSICON in the different methods, HT_XRD was employed (Fig. 4.5 a, b, c, d). A similar trend was observed with DTA/DSC and room-temperature XRD. After the first milling, SS_NCO and SS_NHP samples displayed broad diffraction peaks corresponding to monoclinic ZrO_2 (SG14: $P2_1/c$), no Na-containing phases were identified, likely due to the low scattering contrast of Na or its presence as an amorphous phase. Reflections

of $Na_2Zr(PO_4)_2$ appeared at around 700°C, and around 900°C monoclinic NaSICON reflections were observed.

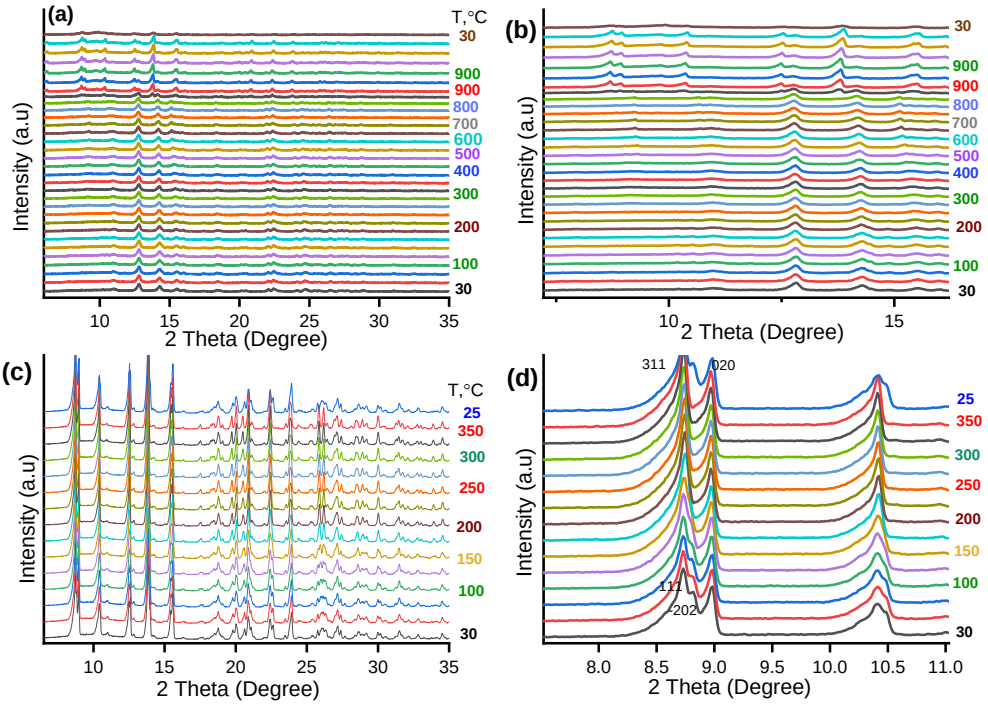

Fig. 4.6: HT-XRD collected on Mo Xrd λ = 0.70932 showing a) formation of HEM NaSICON through the various temperatures, b) a zoomed in image of a) for the selected range from 4 to 17° 2θ and c) the monoclinic to rhombohedral phase transition.

The conversion kinetics was slow in both the SS_NCO and SS_NHP cases (Fig. 4.5a,b) the intermediate phases and targeted NaSICON phase appeared at high temperatures in contrast to SP_NH4(Fig. 4.5d, Fig. 4.6), where some intermediate phases were formed after HEM. This could be attributed to the low mobility of ions and atoms in solids, a key factor that limits the rate of solid-state reactions. Consequently, a high temperature and longer time is required to improve transport and reaction kinetics and complete the conversion of reactants to NaSICON in SS_NCO and SS_NHP. This explains why a final sintering temperature of 1200°C and 20 h of time were reported to allow for complete conversion and crystallization.

In contrast, a gel was obtained for the SOL. Increasing the temperature led to its decomposition, and the onset temperature of the NaSICON conversion was observed around 600°C with the appearance of faint low and weak high angle –311, 131 and 421 reflections. The conversion was completed after increasing the reported calcination time from 12 to 24 h .

In the case of SP_NH4, broad diffraction peaks were identified after milling corresponding to coexistent crystalline phases, such as (i) a C2/*c* structured sodium zirconium phosphate $Na_2Zr(PO_4)_2$, (ii) a *C*2/c -structured ZrO_2, and (iii) a *C*2/*c* phase typical of the NaSICON. Increasing the heat-treatment temperature from 900°C to 1280°C led to peak narrowing, indicating an increase in crystallinity commensurate with the solid-state preparation of NaSICON. To further

understand the evolution of these phases in greater detail, multiphase Rietveld refinement was conducted on the patterns using the following phases: $Na_2Zr(PO_4)_2$, ZrO_2, $Na_3Zr_2Si_2PO_{12}$, etc. (PDF Code: 189 807, 97 546, and 14 585, respectively). The phase ratios at different temperatures are shown in Fig. 4.7. The large uncertainty in the refined phase fraction may be attributed to peak overlap between coexisting phases and limited intensity of minor phase reflections, which affects refinement stability. Generally, for SP_NH4, where fast kinetics were observed, increasing temperature up to 900°C and the duration of heating led to an increase in the NaSICON phase fraction and a decline in phases such as $Na_2Zr(PO_4)_2$ and ZrO_2. The process proceeded according to eq. (4.1) and (4.2) until a phase-pure NaSICON sample was obtained.

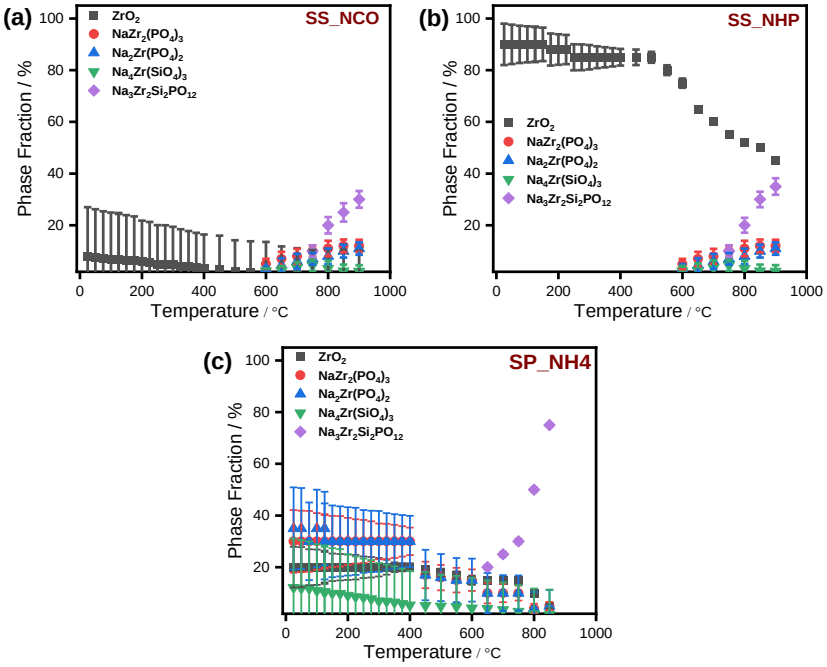

Fig. 4.7: Phase fractions from Rietveld refinement of intermediate and targeted phases at various temperatures (a) SS_NCO (b) SS_NHP (c) SP_NH4

Based on the detected phases, the decomposition reactions for SP_NH4 can be written as follows:

$$Na_2O_2+ZrO_2+NaH_2PO_4{\cdot}H_2O+SiO_2 \rightarrow Na_{1+4x}Zr_{2-x}P_3O_{12} + Na_{1+4x}Zr_2Si_{2-x}O_8 + H_2O \quad (4.1)$$

$$Na_{1+4x}Zr_{2-x}P_3O_{12} + Na_{1+4x}Zr_2Si_{2-x}O_8 \rightarrow Na_{1+x}Zr_2Si_xP_{3-x}O_{12} + ZrO_2 \quad (4.2)$$

Compared to the SS_NCO, SS_NHP and SOL cases, the synthesis of SP_NH4 via a 3h HEM presents a simple alternative route for synthesizing high-purity NaSICON. The effect of impact due to high-energy milling promotes the early initiation of the relevant intermediate reactions necessary for the formation of NaSICON. An increase in temperature further increases the kinetics of the process due to the increased mobility of ions and atoms. Phase-pure (99%) NaSICON was obtained via this route, making it a good alternative for synthesis.

4.3 Effect of High-Energy Milling on Morphology Evolution

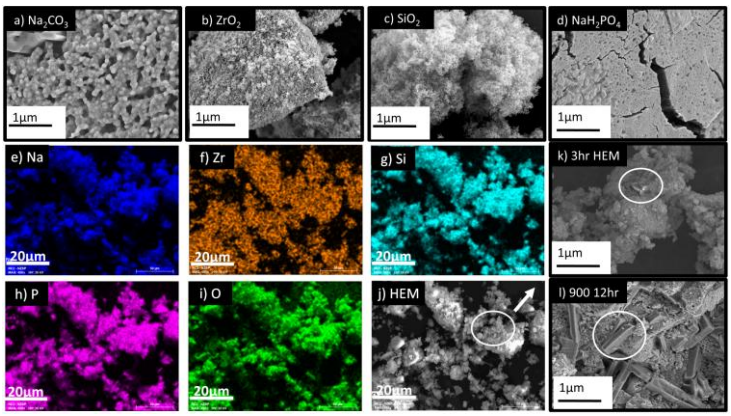

Fig. 4.8: SEM images of precursors and HEM morphological evolution in NaSICON (a) Na_2CO_3 (b) ZrO_2 (c) SiO_2 (d) NaH_2PO_4 (e, f, g, h, i) EDX mapping (Na) showing good distribution of Na, Zr, Si, P, and O in milled matrix (j) Sample after 3 h HEM, (k) Zoomed-in image of j white circle showing grown nuclei (l) More nuclei grow after heating at 900°C for 12 h.

The SEM was employed to gain more insight into the morphology of the solid electrolyte. Upon inspection, the morphology of the starting precursors (Fig. 4.8a–d) showed no indication of preferential growth or underlying particle shape retention from the starting precursor. However, after 3 h HEM, particle shapes (white circle) that indicate the start of NaSICON conversion process were observed. The milled sample comprised packed secondary agglomerates with loosely interconnected porosity. The boundaries between particles were not clearly visible, indicating good neck formation, as evident by the observed particle/grain coarsening (Fig. 4.8k). Apparently, the presence of high mechanical energy during milling and the decomposition of NaH_2PO_4 assisted with particle rearrangement and precipitation of the metastable phase, leading to more efficient NaSICON conversion.

This can be attributed to the potential of the HEM in enabling reactions as supported by Bragg peak reflections obtained after HEM showing the evolution of the intermediate-metastable phase $NaZr_2(PO_4)_3$, which is important for the NaSICON formation of the final structure and is consistent with the monoclinic phase originally reported by Hong[81] The reaction creates a large surface area of interfaces between different phases by the formation and growth of a composite structure in powder particles. The reactions occur in the presence of thermodynamic driving forces for the reactions between the different phases in contact. This increases the efficiency of the HEM for NaSICON processing. Further treatment was carried out at 900°C for 12 h, and phase pure NaSICON was observed on XRD (d). The SEM (Fig. 4.8.) analysis showed substantive growth of the grains. The HEM route not only initiated early conversion but also reduced the temperature.

4.4 Variations in Phase Purity, Lattice Parameters, and Cell Volume During Processing.

Depending on the thermal history, the samples crystallized in a monoclinic or rhombohedral structure. In this study, all samples after final sintering exhibited monoclinic symmetry. The structural parameters of materials prepared by different methods obtained from Rietveld refinement are shown in Fig. 4.9. Hong *et al.* described the structure of $Na_3Zr_2Si_2PO_{12}$ using the C2/c space group ($a = 15.586$ Å, $b = 9.0290$ Å, $c = 9.205$ Å, $\beta = 99.5°$, and $Z = 4$). This structural model was adopted for refinement.

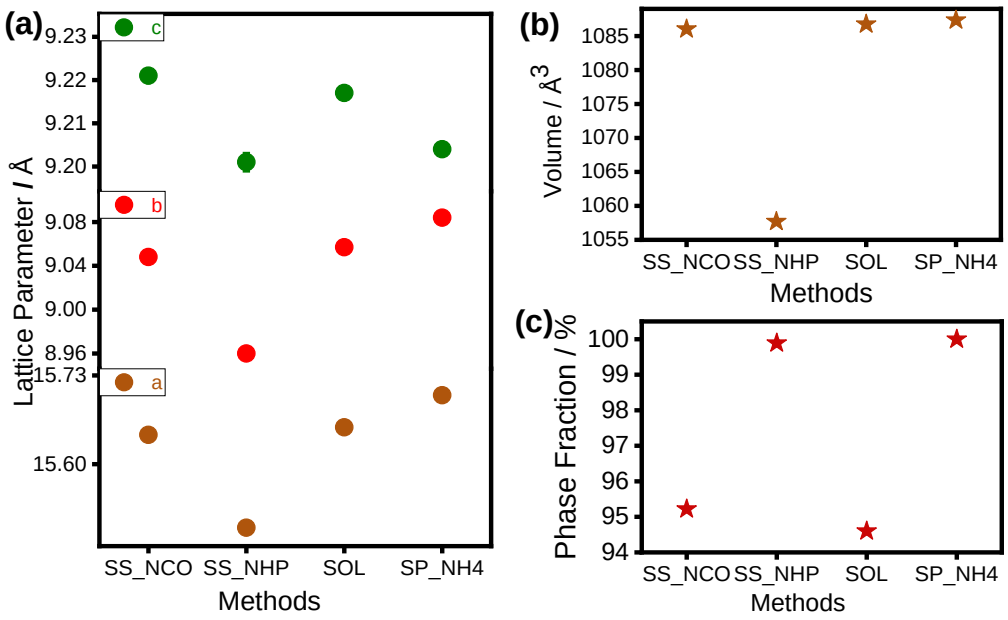

Fig. 4.9: Variations in (a) lattice parameter, (b) unit cell volume, and (c) phase fractions for the different methods.

The lattice parameters, profile parameters, atomic positions, atomic displacement parameter and occupancy were refined using the model proposed by Hong[81] in the monoclinic space group C2/c (no. 15), as shown in Fig. 4.10. The diffraction peaks of the sample were indexed, and the lattice parameters, atomic displacement parameters, atomic coordinates and occupancies are presented in appendix. SP_NH4 and SS_NHP had the highest phase purity of 100% and 98%, respectively. SOL and SS_NCO had 9% and 5% monoclinic ZrO_2 as a secondary phase

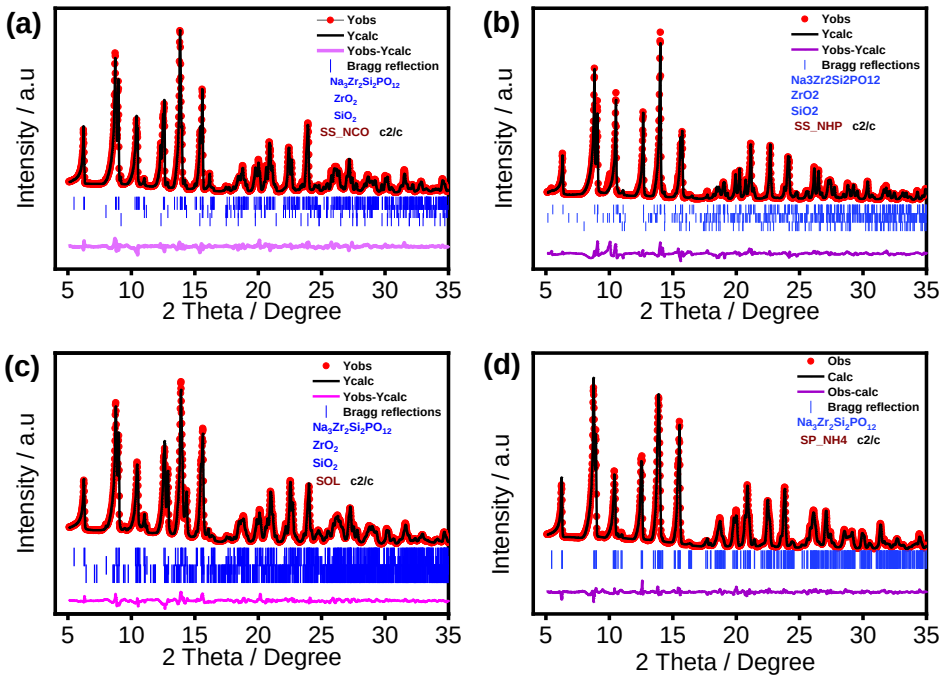

Fig. 4.10: Rietveld refinement pattern of (a) SS_NCO, (b) SS_NHP, (c) SOL and (d) SP_NH4.

4.5 Effect of Processing Route on the Local Microstructure

To investigate the effects of the processing routes on local microstructural disorders, Raman spectroscopy was employed. The Raman band position and shape depend on the shared edges between octahedral/tetrahedral components and the average bond distances[137]. As such, it is a useful tool for investigating short-range disorders in NaSICON[84].

The vibrational modes of the NaSICON lattice (Fig. 4.11) can be assigned to PO_4 tetrahedral internal and external modes and to lattice modes, including the motions of the metallic Zr^{3+} and Na^+ ions in their octahedral cage. The internal modes of the phosphate ions represent the symmetric v_s (PO) and antisymmetric degenerate v_d (PO) stretching of phosphorous to non-bridging oxygen and the symmetric/antisymmetric degenerate δ_d (OPO) bendings. From the modes around 990 cm^{-1}, around 450 cm^{-1}, between 1050–1180 cm^{-1}, and 550–780 cm^{-1} are usually labelled v_1, v_2, v_3, and v_4, respectively. The PO_4 around 180 cm^{-1} and 85 cm^{-1} external modes correspond to the vibrational and translational motions of these groups.

For all processing routes, the spectrum of the monoclinic NaSICON was observed, with marked differences for SOL. Typical for monoclinic symmetry, the band in the range of 900–1000 cm^{-1}, which results from the stretching modes of PO_4 tetrahedra (v_1, v_2), is split into several modes, as observed in all samples. The number of observed bands agrees well with the requirements of the prediction rule for monoclinic symmetry[138]. The 28, 25, 24 and 32 total Raman band components

obtained by fitting the data with CasaXPS were observed in SS_NCO, SS_NHP, SOL and SP_NH4, respectively.

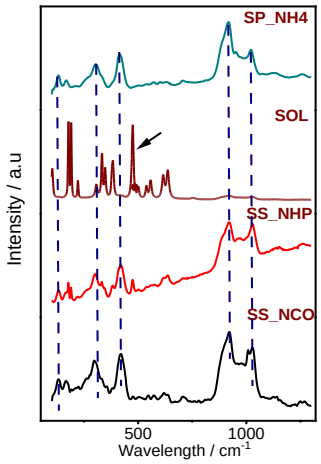

Fig. 4.11: Raman spectra showing; a) bands for the different preparation methods (blue dashed lines NaSICON show bands and black arrow shows ZrO_2).

Reducing the number of vibrational components and observing very broad bands indicate a short-range static disorder. According to Rietveld refinements, SOL has the highest ZrO_2 impurity content, which also has a high Raman sensitivity, as evidenced by the sharp monoclinic ZrO_2 bands at 180, 192 and 476 cm^{-1} and a shift in the Raman bands. Compared to the other processing routes, an increase in the width of the Raman components of the SOL have been noted. There was also a decrease in the number of observed NaSICON bands. This could be correlated with a static short-range disorder (SSRD), essentially associated with the partial occupation of the sodium sites and agrees with the observation of Barj *et al.*[138]. Although, SP_NH4 and SOL enable faster NaSICON conversion, the thermodynamic stability of ZrO_2 in SOL is higher; it also has a high static disorder.

4.6 Effect of Processing Route on Surface Chemistry and Structure

The bonding environment of the composing elements were investigated using XPS. The survey spectrum (Fig. 4.13) reveals the presence of the elements Na, Zr, P, Si, C and O on the surface of the samples. Although the position of all peaks was corrected with respect to the C 1s signal at 285 eV, it can be seen, that all core-level features of SS_NHP and SS_NH4, as well as SS_NCO and SOL, align. These shifts might be related to the internal charging effects which cannot be resolved by normalising to an adsorbed carbonaceous species, whose influence on the underlying chemical states is debatable[139]. In the high-resolution detail spectra of Na 1s (Fig. 4.12a), only one phase was identified for all samples between 1071.2 and 1071.5 eV, and no presence of a

carbonate phase in the $Na_3Zr_2Si_2PO_{12}$ was observed. However, the sodium concentration in the samples was highly different, ranging from 8 at% for SS_NHP to 22 at% for SOL.

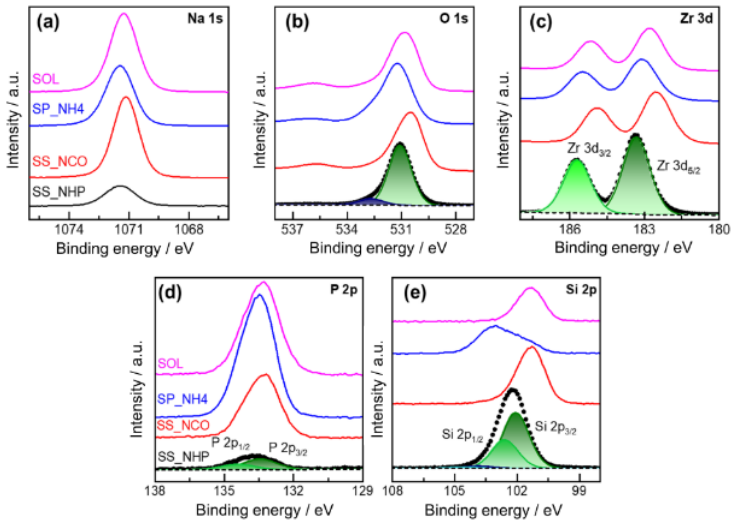

Fig. 4.12: Surface chemical composition studied by X-ray photoelectron spectroscopy. Core-level detail spectra of (a) sodium Na 1s, (b) oxygen O 1s, (c) zirconium Zr 3d, (d) phosphorus P 2p, and (e) silicon Si 2p.

In contrast, all oxygen spectra (Fig. 4.12b) showed two overlapping features, from which the low binding energy peak (530.5 to 531.2 eV) could be assigned to the $(PO_4)^{3-}$ and $(SiO_4)^{4-}$ complexes in the NaSICON lattice[140]. The high binding energy feature at 531.6–532.6 eV can be partially attributed to carbon–oxygen moieties adsorbed due to contact with the atmosphere and slightly differently bonded silicon and phosphorus complexes due to crystal defects and lattice mismatches. The latter assumption is supported by the relatively more intense secondary feature for SP_NH4, which reveals a higher amount of an additional silicon species (compare Fig. 4.12e and Table 4.1). Thus, all samples reveal an oxygen-deficient surface of only 4 and 5.5 at% for SP_NH4 and SOL, but up to 8 and 9.5 at% for SS_NHP and SS_NCO.

All zirconium-related signals (Fig. 4.12c) arose from Zr^{4+} ions (282.5 to 283.4 eV) and were coordinated to silicon and phosphorus oxides[141]. Table 4.1 shows that the zirconium surface concentration for SS_NHP almost doubled compared to the other samples. The inverse evolution is demonstrated for phosphorus (Fig. 4.12d), which is only about 2 at% for this sample. In contrast, almost 90% of the sites in the crystals were occupied by silicon. As mentioned above, the secondary Si-phase, which was found to a minor degree in all samples, was more pronounced in SP_NH4 (Fig. 4.12e). However, this might be related to a different composition of the bulk from the surface, since XRD observed no secondary Si-rich phase. The variation was also observed between the bulk compositions measured with ICP-OES (Table 4.2) and the surface compositions quantified by XPS (Table 4.1). This could be related to the kinetics of the NaSICON formation process, as observed in both DTA/DSC and HT-XRD, which can lead to different decomposition and mass transport during evolution and influence the transport of components to the surface. Specifically, the gradual phase evolution observed in HT-XRD, alongside broad or overlapping thermal events in DTA/DSC, suggests that incomplete or sluggish diffusion of some species may

have occurred during the early stages of calcination. This could result in preferential surface segregation or incomplete incorporation of some elements, particularly under non-equilibrium conditions such as heating or limited mixing. These effects may be further compounded by surface decomposition or volatilization of Na/P at elevated temperatures, leading to the observed surface–bulk compositional mismatch

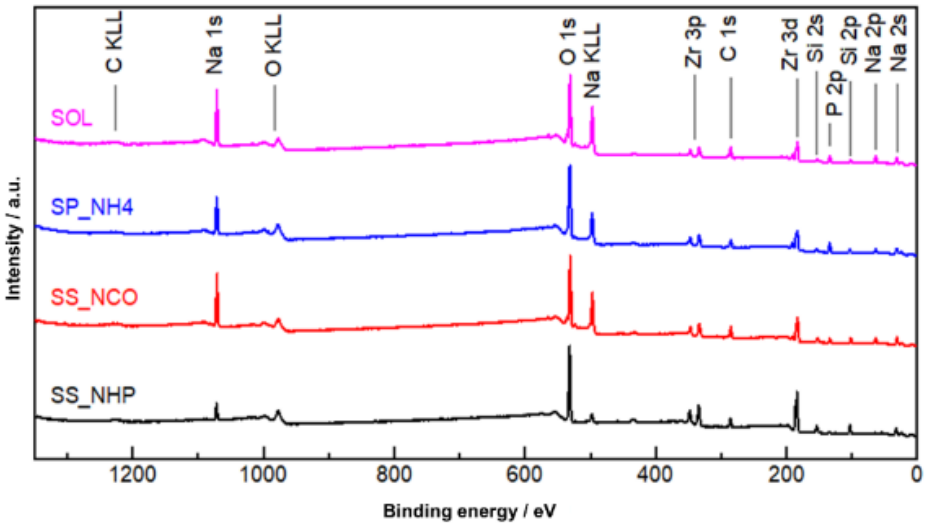

Fig. 4.13: X-ray photoelectron survey spectra of the samples discussed in Fig. 4.12 (All signals in the survey, but adventitious carbon, can be associated with NaSICON.)

Table 4.1 Quantification of the surface chemical composition revealed by XPS

Sample	*Na (at%)*	*O1 (at%)*	*O2 (at%)*	*Zr (at%)*	*P (at%)*	*Si1 (at%)*	*Si2 (at%)*
SS_NHP	8	56	6	11	2	15.5	1.5
SS_NCO	21.5	51.5	5	6.5	6	9.5	1
SP_NH4	16.5	50	12	5	10	2	4.5
SOL	22	54	5.5	5	8	5	0.5

Table 4.2 Quantification of the bulk chemical composition revealed by ICP-OES.

Sample	*Na (at%)*	*O1 (at%)*	*Zr (at%)*	*P (at%)*	*Si (at%)*
S_NHP	14	58.2	9.8	4.7	10.8
SS_NCO	14.7	59	9.7	6	9.5
SP_NH4	15.5	59.9	9.5	5.3	9.8
SOL	14.8	58.5	9.3	4.8	5

4.7 Influence of Processing Route on Microstructure-Morphology

The surface morphology and elemental composition were investigated by SEM/EDX. The micro-morphology of the different processing routes is shown in Fig. 4.14:. The images were obtained without additional polishing or thermal etching. For all samples, SEM showed that the powders were compacted under high-temperature sintering, and the pellets became more densely packed compared to green pellets before sintering. SS_NCO and SS_NHP exhibited a dense, irregular faceted morphology, with relative densities of 90% and 87%, respectively, as determined geometrically and expressed relative to their theoretical densities.

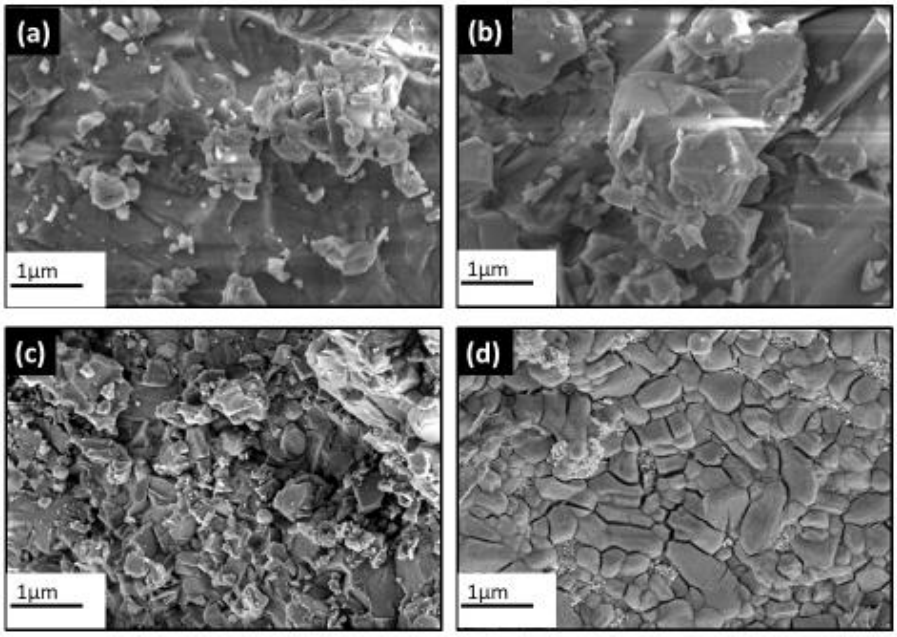

Fig. 4.14: Morphologies investigated by scanning electron microscopy for (a) SS_NCO, (b) SS_NHP, (c) SOL and (d) SP_NH

Samples from SOL process route showed an irregular faceted structure, albeit with a lower density (85%). In the SP_NH4 case, near homogenous grains were seen; however, cleavage fractures occurred between the grains, and the relative density was as low as 79%. SS_NCO, SS_NHP and SOL, all had an embedding glassy/liquid phase. To further check the stoichiometric proportion of all the constituents of elemental mapping and quantification by EDX analysis were performed.

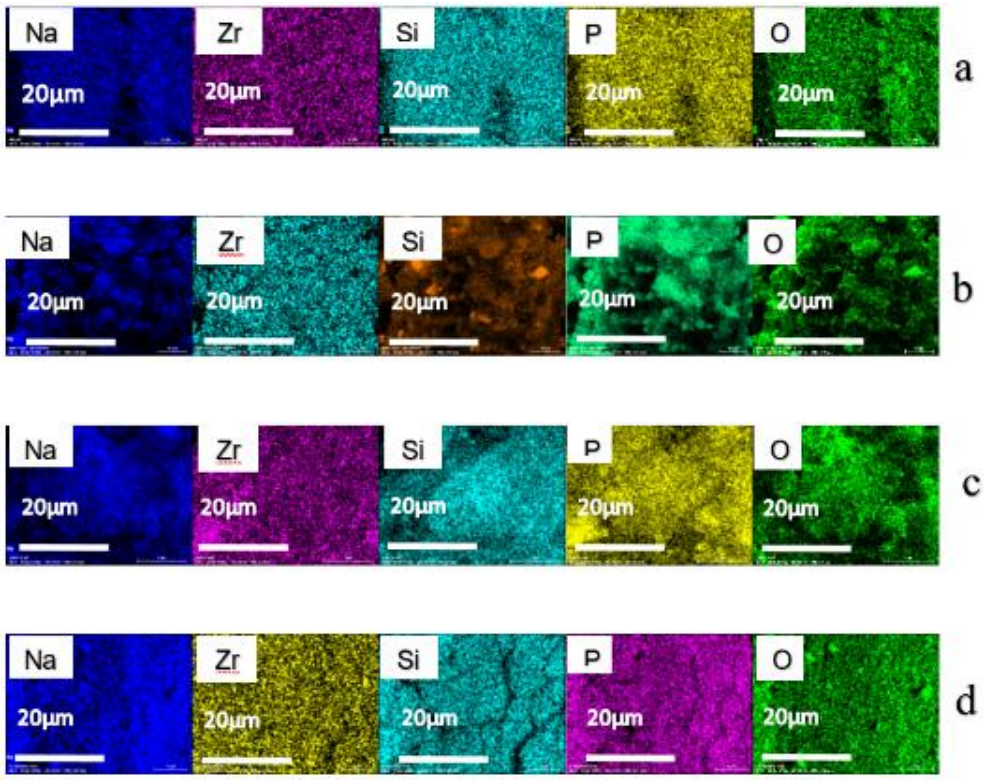

Fig. 4.15: Elemental mapping showing elemental distribution for (a) SS_NCO, (b) SS_NHP, (c) SOL and (d) SS_NH4.

4.8 Variations of Ionic Conductivities and Activation Energy with Processing Route

The conductivity was determined by using AC electrochemical impedance spectroscopy (EIS) in the frequency range of 3 MHz–1 Hz under ambient conditions. The resulting Nyquist plots, conductivities and activation energies are illustrated in Fig. 4.16. Typical impedance patterns, with a semicircle at the higher frequency side and a tail at the lower frequency side, were observed for all cases (the complete semicircle of SP_NH4 is not visible on the plot because the resistance is high and the range of the real impedance was selected to make the other semicircles visible). The semicircle represents the bulk contribution, whereas the tail gives the blocking electrode nature of Au against Na^+ ions. The use of Au, an ion-blocking but electronically conductive contact, prevents charge transfer reactions at the electrode–electrolyte interface. This results in the characteristic capacitive behavior (spike) at low frequencies, confirming ionic transport. Any electronic contribution is expected to be negligible under these conditions[142]. The data was fitted using Fig. 4.16b, fitted quantities are given in Table 4.3. The conductivity of all samples with different sintering times was calculated using equation 3.1. Fig. 4.16 shows that the conductivity of the samples was affected by the processing method. The SS_NCO sample showed the highest ionic conductivity (0.2 $mScm^{-1}$) in the series; while SP_NH4, despite having high purity, delivered the lowest ionic conductivity (0.004 $mScm^{-1}$). This might be attributed to the cleavage fractures observed between grains in the micro-morphology and the low density.

The presence of zirconia as a secondary phase and a much lower density for SOL also affected the conductivity (0.07 $mScm^{-1}$). However, it was slightly lower than reported in the literature (1 $mScm^{-1}$). Generally, morphology and density greatly affect conductivity. It was observed that the relative density (determined geometrically expressed as a percentage of theoretical) increased from SP_NH4 (79%) -SOL (84%)-SS_NHP (87%) -SS_NCO (90%). The highest conductivity and lowest activation energy (0.2 $mScm^{-1}$, 0.32 eV) was achieved for the SS_NCO sample because of its dense microstructure and large grain size (though embedded in an amorphous/ glassy phase). The fitted values of the equivalent circuit components are presented in Table 4.3. Nevertheless, the conductivity obtained for SP_NH4 was within the range of conductivities reported for the same material.

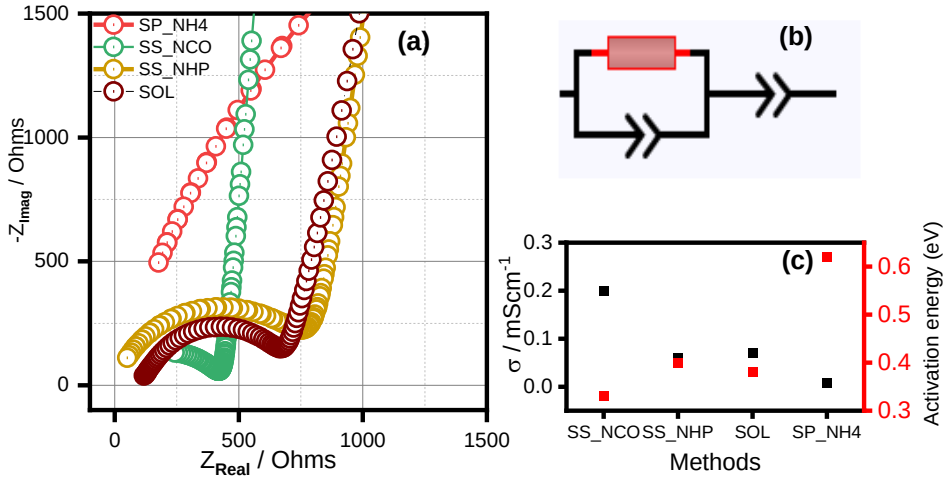

Fig. 4.16: (a) EIS spectra for the different methods, (b) equivalent circuit used for fitting and (c) ionic conductivities and activation energy for the different methods.

Table 4.3 Fitted data for the impedance spectra using the equivalent circuit in Fig. 4.16

	***R*(Ω)**	**C1(F)**	**n1**	**C2(F)**	**N**
SS_NCO	321.15	0.18E-11	0.98	0.51E-7	0.63
SS_NHP	489.32	0.96E-10	0.97	0.63E-7	0.65
SOL	511.31	0.71E-11	0.97	0.41E-7	0.62
SP_NH4	5371.51	0.83E-9	0.82	0.81E-6	0.59
SP_NOH	311.71	0.97E-11	0.98	0.43E-7	0.7
SP_ZNO	1131.81	0.51E-9	0.86	0.78E-6	0.61
SP_NC	187.12	0.99E-11	0.99	0.98E-7	0.73
SP_NO	831	0.55E-10	0.87	0.81E-6	0.75

4.9 Influence of Different Precursors on HEM Milling

Given the potential of HEM at early NaSICON formation and having observed the effect of morphology and density on the ionic conductivities, as well as the fast kinetics of the NaSICON conversion during HEM, as revealed by DTA/DSC and XRD, an attempt was made to optimize the process; different precursor combinations described in Section 3 were used.

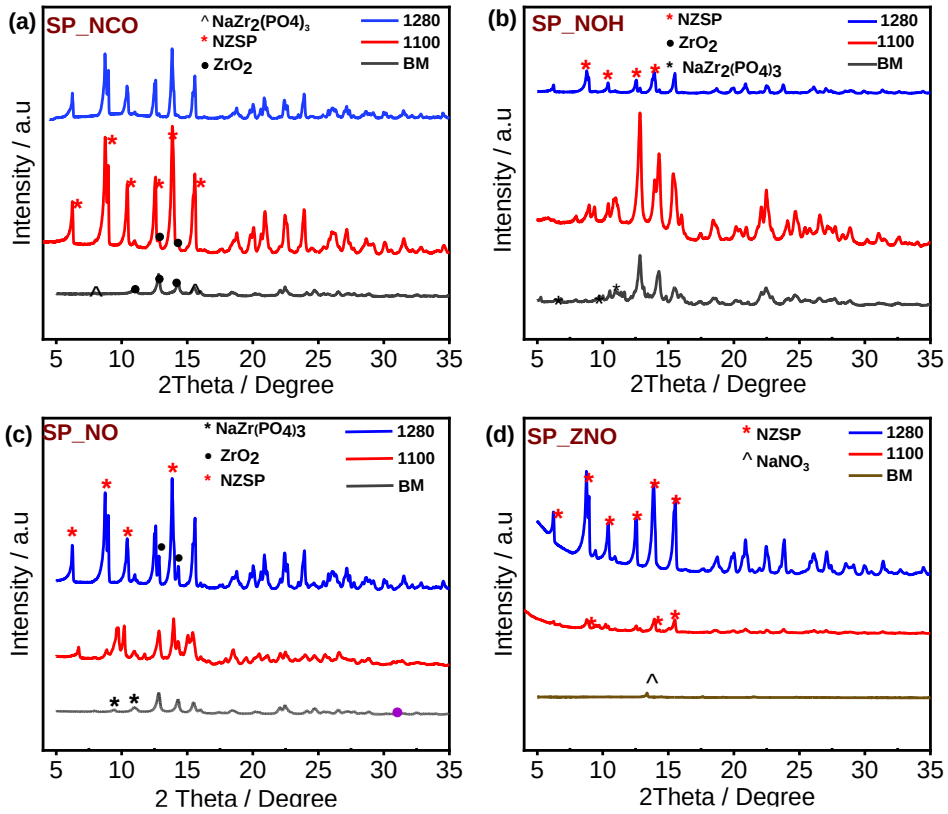

Fig. 4.17: XRD illustrating phase evolution in (a) SP_NCO, (b) SP_NOH, (c) SP_NO and (d) SP_ZNO after different calcination temperatures and ball milling.

Following the earlier observed influence of morphology on conductivity, the calcination temperature was increased from 900°C to 1100˚C, to eliminate trapped pores and increase density after sintering at 1280˚C. The effects of the four sets of precursors on density, morphology and ionic conductivities were analysed.

The XRD patterns in Fig. 4.17 confirmed what was observed earlier: the HEM milling initiated conversion reactions in all combinations, as evidenced by the formation of $NaZr_2(PO_4)_3$ after 3 h of milling in SP_NO, SP_NOH and SP_NCO. For the SP_ZNO sample, formed $NaNO_3$ and an amorphous phase after the first milling. Upon calcination at 1100°C, phase-pure NaSICON was obtained for SP_NCO; the other combinations had some decomposition products. After sintering, dense, well-connected grains averaging 1 µm were obtained for SP_NCO and SP_NOH, as shown

in Fig. S10. SP_NCO had a density of 94%, SP_NOH had 90%, SP_NO had 86%, and SP_ZNO had 84%, the densities were determined geometrically.

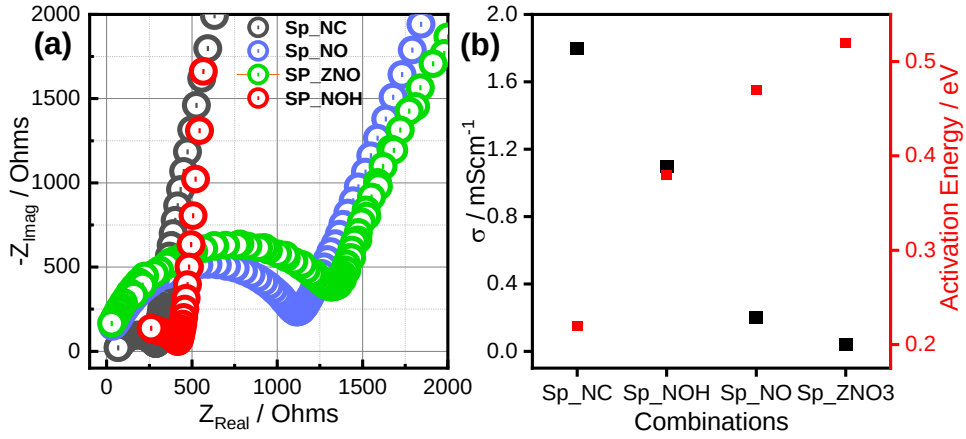

Fig. 4.18: (a) EIS spectra for the SPEX combinations and (b) ionic conductivities and activation energy for the precursor combinations.

The increase in calcination temperature improved the density of sintered samples. Fig. 4.18 shows the precursor combinations' ionic conductivities and activation energies. Conductivities from precursor combinations fell within the range of conductivities reported by more time- and energy-consuming methods. The SP_NCO sample had the highest conductivity and lowest activation energy (1.8 $mScm^{-1}$, 0.22 eV), close to the conductivity reported by Naqashi *et al.*[143] and Jolley *et. al.*[96], as shown in Table 3. Fig. 4.19 shows the morphology in the different samples, all samples had a dense morphology, SP_NOH have cubic and tetragonal grains, and SP_NCO have more homogenous and denser cubic grains which could be attributed to enhanced densification and grain connectivity that led to the higher ionic conductivity. The particle morphology observed in SEM (cubic/tetragonal habit) reflects the external shape of the grains, however, the crystal structure determined from XRD refinement indicates a monoclinic, which describes the internal atomic arrangement. It is not uncommon for particles with low-symmetry structures to exhibit higher-symmetry morphology. The external morphology of particles is often governed by factors such as growth kinetics, surface energy minimization, anisotropic surface energy, and synthesis conditions, rather than directly reflecting the internal crystal symmetry. As a result, materials with lower crystallographic symmetry can still form particles with higher-symmetry shapes, particularly if certain crystallographic planes grow more slowly and dominate the particle surface. This phenomenon has been reported in some oxide systems, particularly under conditions that promote anisotropic grain growth or faceting. Such behavior has been observed in rutile TiO_2, where elongated prismatic grains grow in specific crystallographic directions despite the lower symmetry of the internal structure[144]. Table 4.4 shows a comparison between conductivities measured in the study and literature values. The differences between measured and literature-reported ionic conductivities can arise from variations in synthesis conditions (e.g., Na loss, densification, grain boundaries), phase purity, electrode configuration, and differences in impedance fitting models.

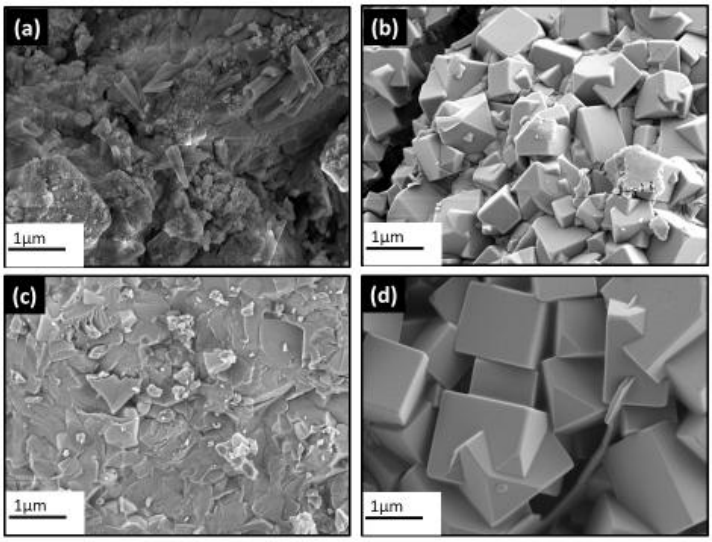

Fig. 4.19: Morphology of HEM NaSICON combinations for (a) SP_NO, (b) SP_NOH, (c) SP_ZNO and (d) SP_NCO after sintering at 1280°C.

Table 4.4 Reference NaSICON conductivities and conductivities from this study

Samples	Ionic Conductivity $mScm^{-1}$ (Present Study)	Compared Adopted Reference	Ionic Conductivity $mScm^{-1}$ (Reference Literature)
SS_NCO	0.2	Naqashi *et al*[108].[143]	1
SS_NHP	0.06	Jolley *et al.*[96]	1.55
SOL	0.04	Other Reported NaSICON Conductivities	
SP_NH4	0.004	Hayashi *et al.*[77]	1.2
SP_NCO	1.8	Narayan *et al.*[145]	1.13
SP_NOH	1.1	Kim *et al.*[134]	1.03
SP_NO	0.1	Ma et al[146].	5
SP_ZNO	0.2	Lee *et al.*[110],[147]	1.8

4.10 Cycling Stability

The cycling performance of Na/SP_NCO/Na (Fig. 4.20) was evaluated at a current density of 1 $mAcm^{-2}$ and capacity loading of 1 $mAhcm^{-2}$ to investigate the stability of the solid electrolyte against sodium anode at room temperature for 100 cycles. The SP_NCO sample was selected for cycling tests based on its relatively higher ionic conductivity and improved microstructure compared to other compositions. A typical flat voltage plateau indicating good stability was obtained in the first eleven cycles. Subsequently, the cells show a slowly increasing slope in the voltage plateau during cycling in both directions (plating and stripping), likely due to polarization. Although an increase in overpotential was observed, it can be seen that this remained stable through the remaining cycling, which might be related to good conductivity and transference number of the solid electrolyte[148].

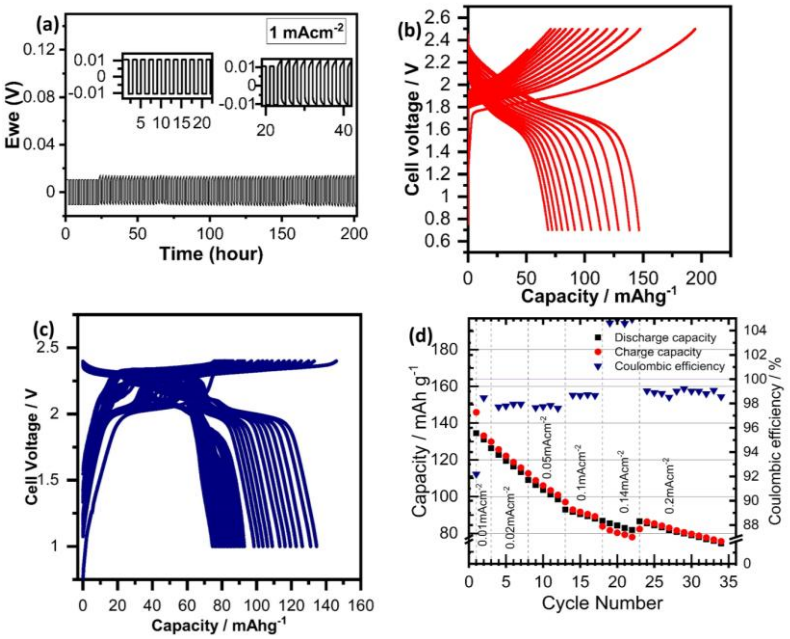

Fig. 4.20: Striping and plating GCPL cycling of Na/NZSP/Na symmetric cells a) galvanostatic charge discharge profile at 1 $mAcm^{-2}$ and 1 $mAhcm^{-2}$ with zoomed in images in inset b) rate capability of Na/NZSP/NMO @ 60°C c) rate capability of Na/NZSP/NMO-Au @ 60°C d) capacity decay and coulombic efficiency profiles with different current densities.

The slow increase in overpotential might also be attributed to the depletion and probable replenishment on the surface during cycling, a similar phenomenon has been described by Lu et al.[148] as partly short circuit. The term 'partly short circuit' describes the primary stage of short circuit, during which the short circuit pauses or terminates subsequently. This could be due to the sodium penetrating partly, not through the whole bulk of the SE. Thus, the slight polarization voltage drop/increase represents the partial reduction of the bulk impedance. Because of the existence of bulk electrolyte impedance, the 'partly short circuit' is not regarded as a failure of a solid-state battery[140]. Qian Li et al.[149] in their study also observed a growth of dendrites on the edges of their NaSICON solid electrode pellet and not through the bulk, which might also contribute to the partly short circuiting behaviour observed in this study.

Furthermore, the observed increase in potential might be attributed to grain boundaries, space charge and other defects. However, the low overpotential observed was in agreement with what was observed for the solid electrolyte in other studies[150],[146],[151]. For the HEM NaSICON, 1 $mAcm^{-2}$ is the critical current density implying that such a solid electrolyte has good stability against Na and thus has promising capabilities with sodium-anode.

Subsequently, the stability of the solid electrolyte with active material was investigated. The NZSP has been tested against NVP[65],[62], FeS_2[152], NTP[150]. Here, we examined the long-term stability of sodium manganese oxide ($Na_{0.67}MnO_2$) as a cathode material when cycled alongside the sodium zirconium phosphate (SP_NCO) solid electrolyte. This investigation was conducted at lower current densities each for 5cycles than those typically used in symmetric sodium cells. The cells with the configuration Na/ SP_NCO /NMO, operating at an elevated temperature of

60°C, displayed a significant capacity decay over cycling. This observation aligns with prior research findings, indicating that NMOs experience capacity fading due to structural degradation and dissolution of active materials during cycling[153].

Significant improvement was attained when coated with a thin gold (Au) layer as a current collector onto the NMO cathode, creating the configuration Na/ SP_NCO /NMO-Au @ 60°C. In this case a notable reduction in the rate of capacity decay was observed. This enhancement in stability can be attributed to the Au-layer's ability to improve the electrical contact between the NMO cathode and the external circuit. By serving as a current collector, the Au-layer mitigates the resistance within the system, reducing the potential for capacity fade and enhancing the overall performance of the battery.

While the energy density in the Na/ SP_NCO /NMO-Au system remains relatively lower than that typically achieved with liquid electrolyte-based sodium-ion batteries, it is crucial to underscore the promising aspects of our solid electrolyte approach. Despite the lower energy density, this system offers competitive performance, especially when considering the good voltage and coulombic efficiencies achieved. These efficiencies are indicative of the minimal loss of charge during cycling, a crucial characteristic for the practical use of sodium-ion batteries in various applications. The incorporation of a thin Au layer as a current collector on the NMO cathode significantly improves the stability of sodium-ion batteries when cycled with the SP_NCO solid electrolyte. While the energy density may be lower compared to typical liquid electrolyte systems, the performance and good efficiencies make this reliable electrolyte approach a viable option for sodium-ion battery technology

5 Influence of Process Conditions and Doping on Morphology, Structure and Properties of High-Energy Milled NaSICON Solid Electrolyte

To optimize the high-energy milling (HEM) fabrication of NaSICON-type solid electrolytes, the effects of different sintering conditions were systematically investigated. The thermal schedules illustrated in Fig. 3.2 were applied, comparing an independent sintering route (red) and a combined sintering route (blue). The independent schedule consists of two sequential thermal treatments: initial calcination at 1100 °C for 12 hours, followed by intermediate manual grinding (~10 minutes using a mortar) and re-pelletizing, and then final sintering at 1280 °C for 6 hours. In contrast, the combined schedule eliminates the intermediate grinding step and proceeds directly to the final sintering temperature after a single heating ramp. In both protocols, the total holding time at 1280 °C was kept constant at 6 hours to ensure comparability. The milling time prior to calcination was 3 hours using high-energy milling. Although crystallite size after intermediate grinding was not directly measured, the absence of significant peak broadening in XRD patterns and the consistent particle morphology observed via SEM suggest that this step primarily served to break up agglomerates rather than refine crystallite domains. The comparison between the two schedules was aimed at assessing the influence of heating rate, cooling rate, and intermediate grinding on the final structure, microstructure, and ionic conductivity of the sintered samples.

Preliminary findings discussed in Fig. 5.1 below indicated that the use of a lower heating/cooling rate for the independent schedule resulted in an enhancement of conductivity. However, the use of slower heating rates (e.g 120 °C/h and 60 °C/h) increases total process time, which contradicts the goal of simplifying the fabrication process. Therefore, a heating/cooling rate of 180 °C/h was selected as a balance between performance and process efficiency.

Under 180 °C/h heating/cooling condition, additional process variables were explored, including sintering atmosphere (Ar, N_2, O_2), quenching methods (air, water, nitrogen), and particle size ranges. The impact of these conditions on the resulting ZrO_2 content, lattice parameter, microstructure morphology, ionic conductivity, and electrochemical stability of the NaSICON electrolyte was analyzed.

5.1 Effect of Heating/Cooling Rate on Independent 2 Step HEM NaSICON

The effects of heating and cooling rates on the grain growth, size and densification of the independent treatment were investigated (Fig. 5.1). With 300°C/h heating and cooling rates, the sample showed irregularly shaped grains averaging 0.2 μm, having low compaction. Using 240°C/h, the average size of the grains increased up to 0.4 μm, roughness reduced, and compactness became better. For 180°C/h, there was an increase in the smoothness and compactness of the grains and an improved surface coverage. With 120°C/h, there was a change in the grain shapes and size domain from irregularly shaped to cubic crystal-like of an average of 0.5 μm size, with a low surface coverage and low compact and rough edges. Reducing the heating and cooling rates to 60°C/h led to an increase in the size of the cubic grains to 1.2 μm and improved coverage and compactness.

A similar trend was observed for the impedance spectra (Fig. 5.1f). A decrease in real impedance and increase in conductivity from 300°C/h to 180°C/h for the irregularly shaped grains, likewise from 120°C/h to 60°C/h for the cubic shaped grains, were observed. The conductivity increased from 0.8 $mScm^{-1}$ to 1.81 $mScm^{-1}$. The studied sintering rates resulted in two irregularly shaped grains (probably deformed tetragonal or cubic). An increase in grain size, density, and conductivity was observed with decreasing heating and cooling rates. Interestingly, similar trends in ionic conductivity values were observed for 60°C/h and 180°C/h, which was attributable to the high density due to the increase in grain size and the reduction in grain boundaries. The density and conductivity increased with a decreasing heating rate likely due to improved grain growth and reduced porosity[154].

The distinct microstructures obtained for the different rates indicate their effect on microstructural evolution. The irregularly shaped grains observed at higher heating/cooling rates (180°C/h and above) could indicate rapid crystallization or incomplete grain growth. This might be attributed to the fact that at higher rates, the nucleation and growth of crystals happen more rapidly, leading to irregularly shaped grains or probable site disorders as was observed by Geutam et al.[155]. The regular grains observed at lower heating/cooling rates imply slower crystallization and more complete grain growth. Slower rates might allow for a more controlled crystal growth, resulting in well-defined regular shapes. The observed increase in density with decreasing heating/cooling rates could be linked to the grain morphology[156]. Slower rates may allow for better packing and arrangement of particles, leading to higher density also they likely contribute to forming a more uniform and interconnected grain structure, reducing barriers to ion migration and resulting in lower impedance. The irregularly shaped grains at higher rates may have more grain boundaries and defects, leading to higher impedance[157]. On the other hand, the cubic-like grains at lower rates may have fewer defects and more favourable crystal orientations, contributing to lower impedance,[158].

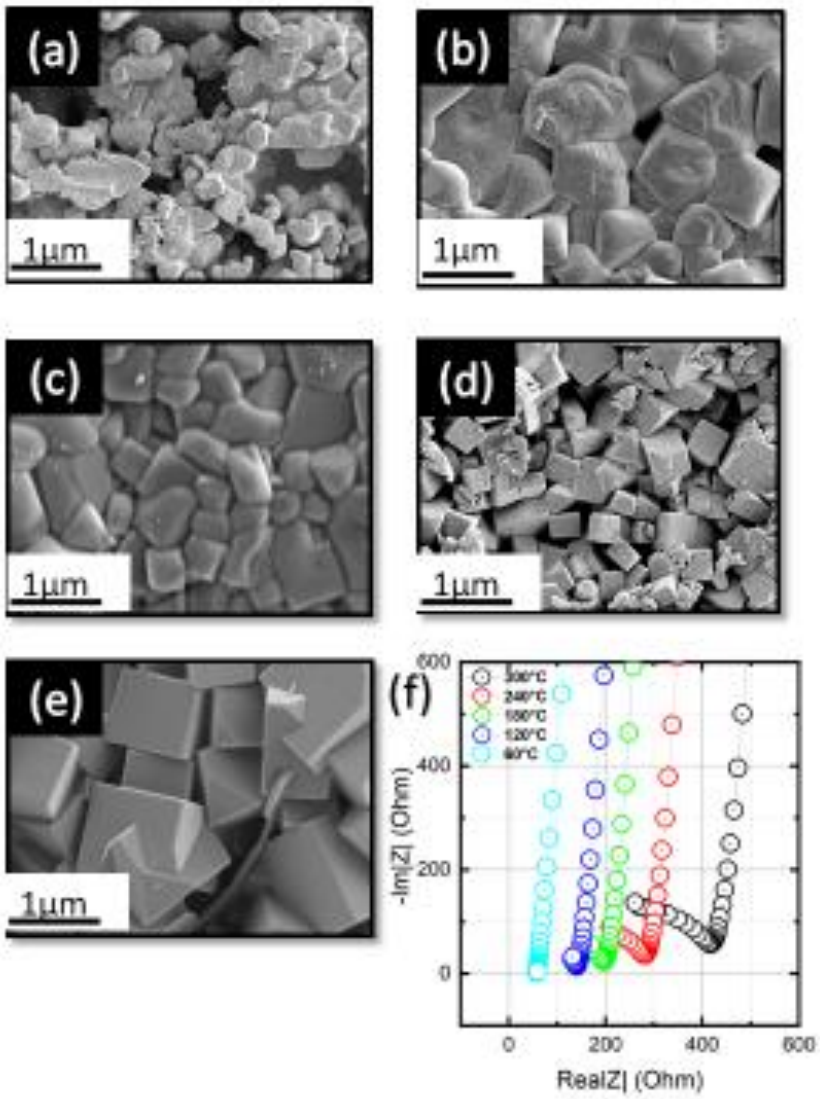

Fig. 5.1: SEM Images at different heating and cooling rates(independent treatment), showing an increase in density and homogenous grain growth (a) 300°C/h, (b) 240°C/h, (c) 180°C/h, (d) 120 °C/h, (e) 60°C/h and (f) EIS spectra for the different heating/cooling rates

5.2 Influence of Sintering Conditions on a Single-Dependent Two-Step Heat Treatment

An investigation of various processing conditions on a combined two-step heat treatment was conducted to study the effect on grain growth. The evolution of microstructure and structure with heating rate was examined to understand the thermal response of NaSICON during synthesis.

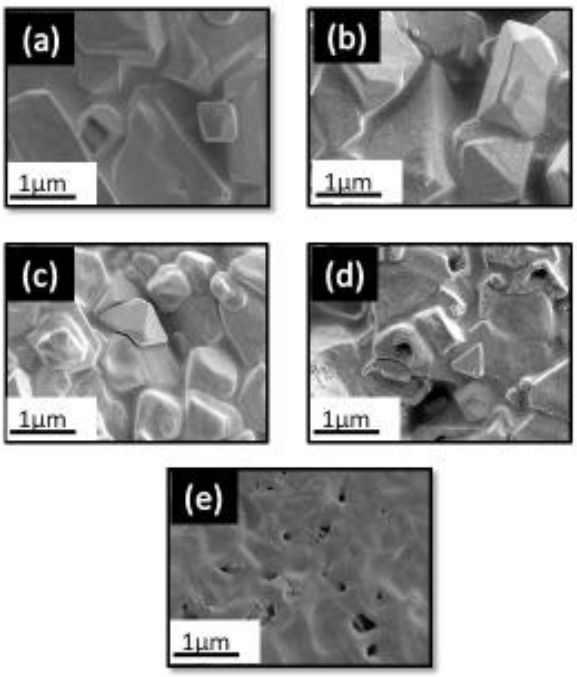

Fig.5.2: Microstructural evolution in the different process conditions of a combined heat treatment for; a) 300°C/h, b) 240°C/h, c) 180°C/h, d) 120°C/h, e) 60°C/h.

SEM images Fig.5.2, shows distinct morphological changes across the combined heating/cooling rate series. At high rates Fig.5.2 a,b (300 °C/h and 240 °C/h), the microstructure consists of irregularly shaped grains surrounded by a lighter background. These features suggest incomplete grain development, possibly due to rapid surface reactions that limit time for reorganization. The lighter regions may represent surface heterogeneity or localized compositional inhomogeneity, though XRD patterns confirm as monoclinic crystal structure across all rates.

At moderate rate of 180 °C/h Fig.5.2 c, grains become more defined and exhibit regular, faceted outlines that resemble tetragonal or cubic morphologies. This visual order reflects improved growth conditions rather than a change in crystal symmetry. Since all samples crystallize to the monoclinic C2/c structure (confirmed by XRD and Rietveld refinement using ICSD 38057), the shape evolution is likely due to anisotropic surface energy effects and kinetically controlled facet development[159]. This intermediate condition also corresponds to the highest refined packing density (3.268 gcm^{-3}), lowest microstrain, and the most distinct microstructure, indicating a well-balanced regime between nucleation and growth.

At lower rates Fig.5.2 d, e, (120 °C/h and 60 °C/h), grain contrast diminishes, and well-defined edges disappear. However, these features cannot be conclusively attributed to amorphous phase formation. XRD patterns (Fig.5.3) show similar intensity and sharpness across all samples, with no significant peak broadening or amorphous background, confirming high crystallinity throughout. Therefore, the diminished grain visibility may result from surface segregation or coalescence

of grains rather than structural disorder. This interpretation is supported by EDX analysis (Appendix Fig. A.3), which reveals local compositional heterogeneity, particularly at lower heating rates.

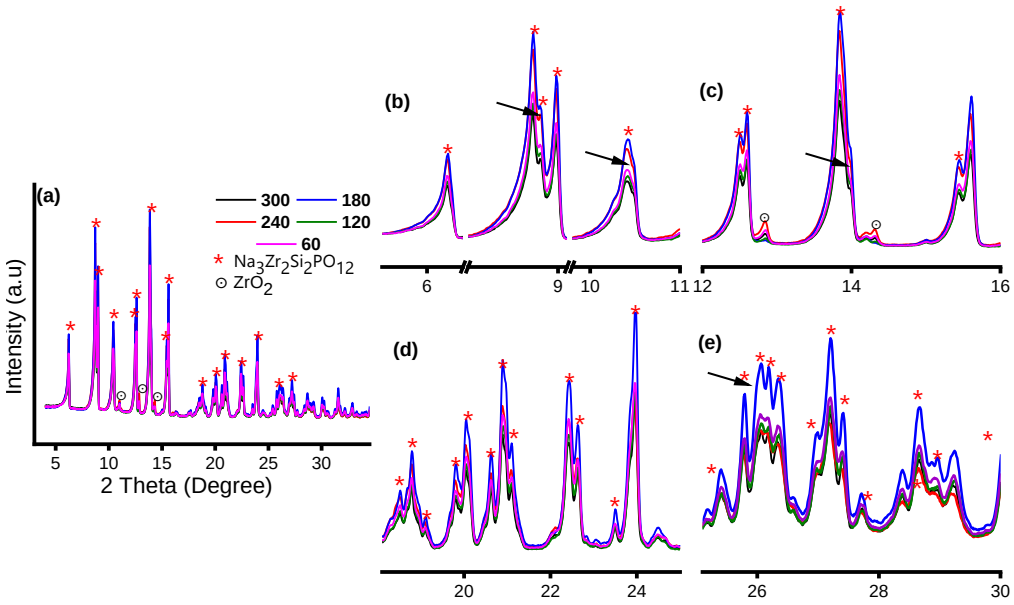

Fig.5.3: Overlapped XRD (λ = 0.70932) patterns at varied heating/cooling rates, b,c,d,e are zoomed in images of a, black arrows indicates reflections with peak splitting.

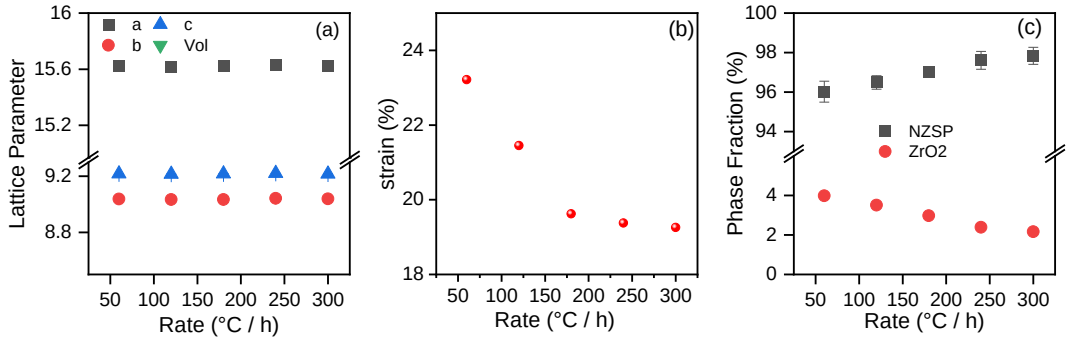

Fig.5.4: Structure modelling parameters at varied heating /cooling rates, a) lattice parameter, b) strain, c) phase fraction.

To understant structural evolution, Rietveld refinement was performed (Fig.5.5), and parameters such as a,b,c, lattice strain, ZrO_2 phase fraction, and density were extracted. Fig.5.4 presents the evolution of structural parameters with heating rate. In Fig.5.4a, the refined lattice parameters (a, b, and c) show only subtle variations across the range of heating rates studied (60–300 °C/h). The values remain relatively stable, indicating that the crystal monoclinic C2/c structure is retained. However, minor changes, particularly in a and c, suggest small distortions in the unit cell that

could reflect local strain relaxation, internal stress redistribution during thermal treatment or compositional fluctuation, possibly arising from localized heterogeneity as indicated by EDX results[160].

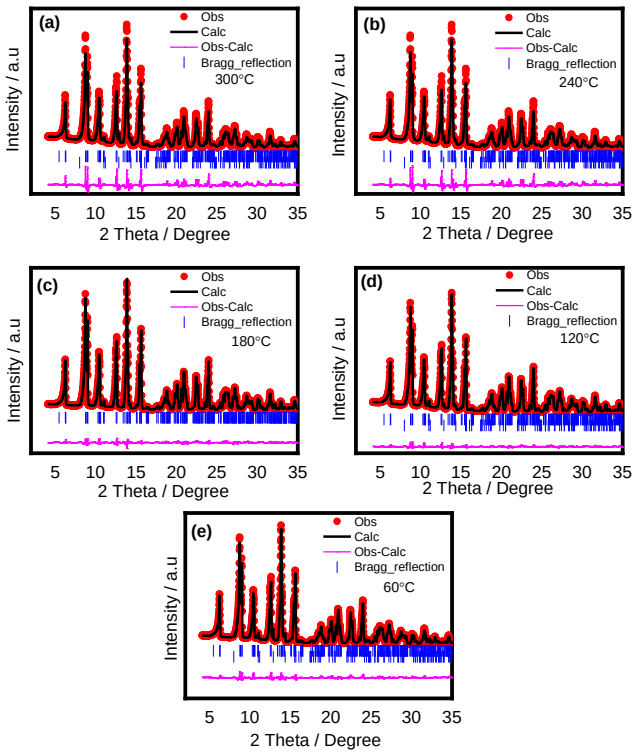

Fig.5.5: Influence of processing conditions on the structure evolution. Rietveld refinement plots for different samples processing conditions (a, b, c, d, e) for the heating rates 300°/h, 240°/h, 180°/h, 120°/h, 60°/h, respectively.

Williamson–Hall (W-H) analysis provided additional insight into crystallite size. It is acknowledged that the W-H method does not distinguish between nucleation and growth processes, but it offers complementary information on the strain relaxation and crystallite domain evolution under different thermal histories.

The slopes of the W–H plots Fig. 5.6 a-e, ecrease with increasing heating rate, indicating a reduction in microstrain from 60 °C/h to 300 °C/h. This trend aligns well with the Rietveld-refined strain values and the observation of sharper, more defined diffraction peaks at higher heating rates. These suggest that faster heating promotes more complete crystallization and relaxation of lattice distortions, likely due to increased reaction kinetics and rapid phase stabilization.

The crystallite sizes extracted from the W-H analysis (Fig. 5.6 f), range from ~250 nm to ~700 nm. These values are above the reliable detection limit of XRD-based line broadening methods, which are generally sensitive only to crystallites smaller than ~100–150 nm[161]; therefore, the absolute values are not precise. However, the relative trend is clear: crystallite size decreases systematically with heating rate. At 60 °C/h, crystallites are largest (~650–700 nm), while at 300 °C/h they

are smallest (~250–300 nm). Consequently, the size values reported here should be interpreted as qualitative indicators rather than precise measurements.

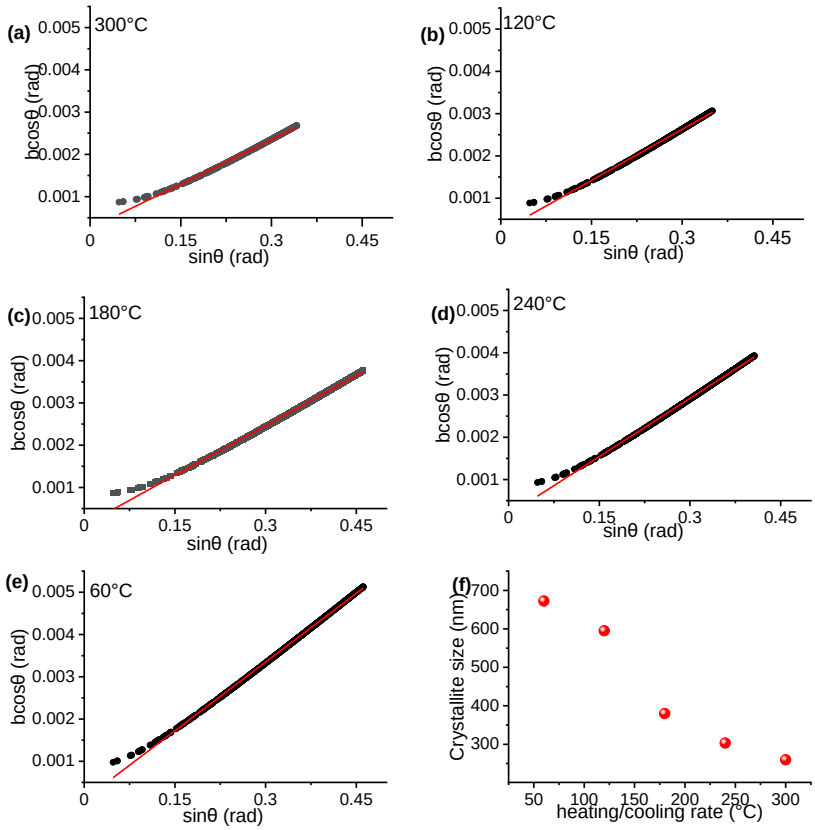

Fig. 5.6: Williamson-Hall plots for NaSICON samples annealed at various temperatures a to e, (60–300 °C). A linear fit to the data was used to estimate the crystallite size and microstrain. As annealing temperature increases, a progressive reduction in slope and increas in intercept indicate reduced strain and larger average crystallite size.

The data reveal an inverse relationship between crystallite size and strain. Slow heating promotes grain coarsening but retains higher strain, while fast heating suppresses grain growth and reduces strain through rapid crystallization and lattice relaxation. SEM observations support this trend: at low heating rates Fig.5.2d–e), grains are larger and often merged, consistent with strain retention. At moderate to high rates (Fig.5.2 a–c), grains are smaller, more distinct, and exhibit well-defined faceting, reflecting reduced strain.

This inverse relation arises from the balance between growth and nucleation. Prolonged residence at intermediate temperatures during slow heating favors grain coarsening but also allows defect accumulation. In contrast, higher heating rates limit thermal dwell, enhancing nucleation over growth and producing smaller, strain-relieved crystalline domains.

While SEM, XRD, W–H, and EDX analyses do not directly separate nucleation from growth, they reveal how thermal history governs the balance between nucleation, grain growth, and coarsening. Intermediate heating rates provide conditions for well-developed grains, as seen in more distinct faceting, higher crystal density, lower lattice strain, and a more homogeneous microstructure. These results demonstrate the strong influence of heating rate on NaSICON microstructure and the value of multi-scale characterization for process optimization.

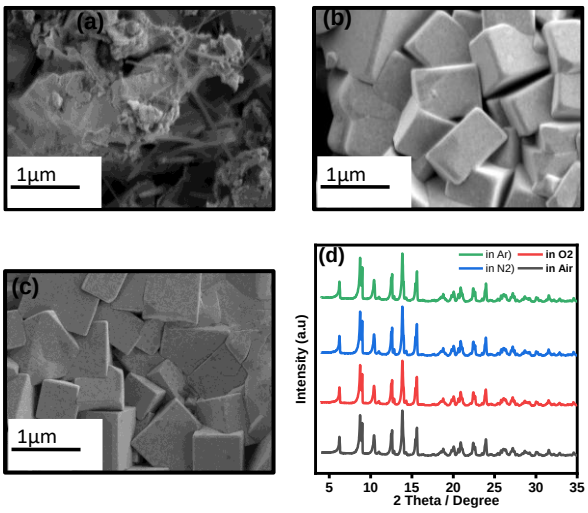

Fig.5.7: Effect of sintering environment on microstructure and structure. (a) SEM of NZSP in Argon, (b) SEM of NZSP in Oxygen, (c) SEM of NZSP in Nitrogen, (d) XRD pattern in Argon, Oxygen, Nitrogen and air.

The influence of sintering atmosphere on microstructure and structure was investigated at a fixed heating and cooling rate of 180 °C/h in argon, nitrogen, oxygen, and ambient air. SEM micrographs (Fig.5.7) show distinct morphological differences. In argon (Fig.5.7a), the microstructure appears as dense, irregularly shaped aggregates with poor grain visibility and surface coverage, likely due to slow diffusion and suppressed grain growth. In contrast, samples sintered in oxygen (Fig.5.7b) exhibit well-faceted, cubic-like grains with sharp edges and smooth surfaces, suggesting enhanced grain development. Nitrogen-sintered samples (Fig.5.7c) also show faceted grains but with less uniformity and occasional surface coverings, implying slower kinetics or partial amorphous retention.

Despite the cubic like morphology in oxygen and nitrogen samples, all samples were confirmed to crystallize in the monoclinic C2/c structure by Rietveld refinement using ICSD 38057. This is supported by the overlapping XRD patterns in Fig.5.8 a and the zoomed-in views (Fig.5.8 b–e), which show sharp reflections and peak splitting, consistent with a monoclinic phase. The observed cubic-like grain shapes can be rationalized by noting that grain morphology is not always a direct representation of internal symmetry. In systems like NaSICON, which possess a pseudo-cubic substructure, minor distortions from the idealized framework can still yield faceted grains with near-cubic external morphology. The well-defined, low-strain grains in oxygen (Fig.5.7b) likely

formed under favorable conditions for isotropic growth and surface energy minimization, resulting in the observed morphology.

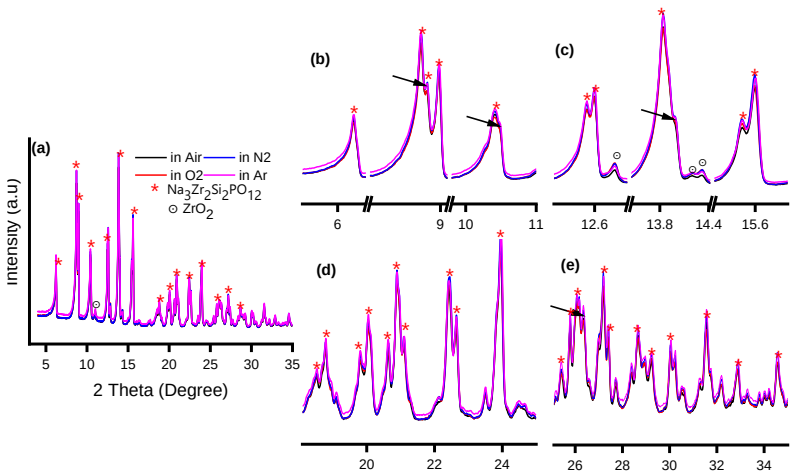

Fig.5.8: Overlapped XRD patterns in different sintering environment, b,c,d,e are zoomed in images of a, black arrows indicates reflections with peak splitting.

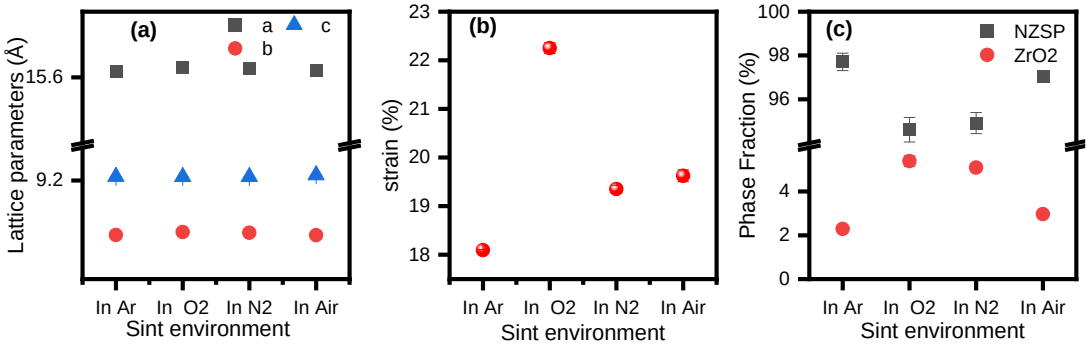

Fig.5.9:. Structure modelling parameters in different sintering environment, a) lattice parameter, b) strain, c) phase fraction.

XRD patterns (Fig.5.8) are sharp and largely overlapping, showing that high crystallinity was retained across all atmospheres. However, samples sintered in air and oxygen exhibit slightly stronger intensities and more defined peak splitting, possibly reflecting better ordering or domain coherence. The high overlap and minimal differences support the conclusion that the monoclinic framework is retained regardless of gas atmosphere, but the microstructural quality and strain state are atmosphere-dependent.

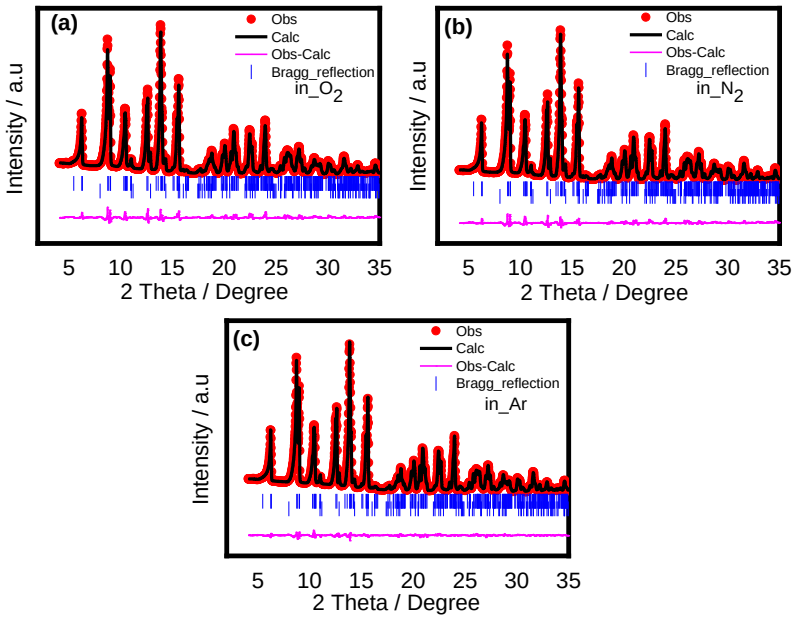

Fig.5.10: Rietveld refinement plots data for different samples sintering environments (a) Oxygen (b) Nitrogen, and (c) Argon sintering environment respectively.

Structural parameters extracted from Rietveld refinement (Fig.5.9) further support SEM grain shape interpretation. The lattice parameters (Fig.5.9 a) show subtle but consistent variations across sintering atmospheres, particularly in the a- and c-axes, suggesting slight lattice distortions likely influenced by differences in gas composition and partial pressures. The lattice strain (Fig.5.9 b) is lowest in the oxygen-sintered sample, indicating reduced internal stresses, which may facilitate more regular grain faceting. Phase fractions (Fig.5.9 c) reveal that the NaSICON phase predominates in all samples, with minor variations in ZrO_2 content. The highest ZrO_2 fraction is observed in the argon-sintered sample, potentially due to incomplete NaSICON crystallization or surface segregation under inert conditions.

Although the applied techniques (SEM, XRD, strain analysis) do not allow a strict separation of nucleation and growth, the data provide meaningful insight into the impact of thermal and environmental history on microstructure evolution. The well-developed, low-strain, and faceted grains in oxygen highlight the importance of atmosphere in promoting effective grain growth and phase purity. Conversely, the irregular morphology and higher ZrO_2 content in argon suggest inhibited sintering dynamics and possible phase instability. This signifies the role of the sintering atmosphere in tuning grain development, stress relaxation, and impurity segregation in NaSICON electrolytes.

The influence of quenching media—air, nitrogen, and water—on the microstructure and structure of NaSICON was evaluated after sintering at 1100 °C for 12 h and 1280 °C for 6 h at a heating rate of 180 °C/h. Following sintering, the samples were rapidly quenched by transferring the closed crucibles into ambient air, distilled water, or a nitrogen-filled chamber, without the use of sealed ampules. Representative SEM micrographs are shown in (Fig.5.11a–c), while structural insights are presented in Fig.5.12–5.13.

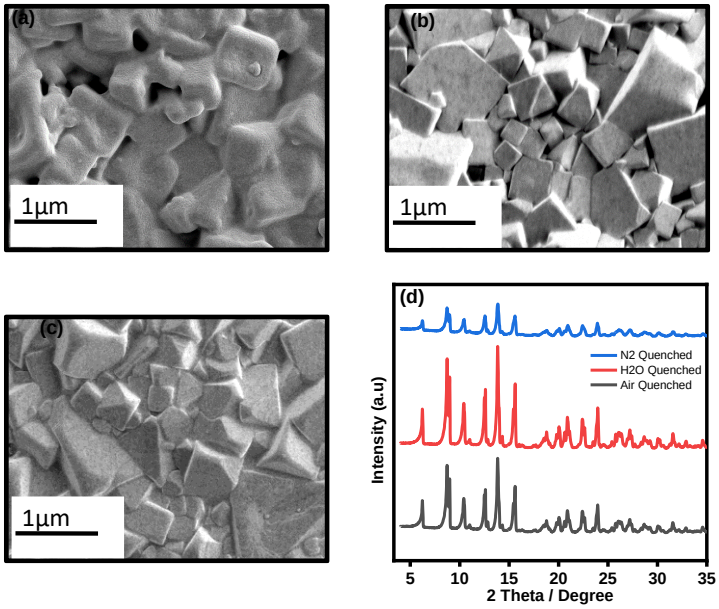

Fig.5.11: Effect of quenching media on microstructure and structure. (a) SEM of quenching in Air, (b) SEM of quenching in Nitrogen, (c) SEM of quenching in Water, (d) XRD data collected on Mo Xrd λ = 0.709patterns for quenching in Air, Nitrogen and Water.

Air quenching (Fig.5.11a) produced well-defined equiaxed grains with moderate faceting and visible intergranular phases, reflecting cooling conditions that permitted uniform grain development and partial relaxation of high-temperature strain. The microstructure indicates that moderate cooling under oxidizing conditions supported recovery and relaxation of thermal stresses, yielding lower refined microstrain values. In contrast, nitrogen quenching (Fig.5.11b) generated a heterogeneous microstructure consisting of abnormally large grains embedded in a finer-grained matrix. This grain size distribution reflects the combined influence of faster cooling and reduced oxygen partial pressure, which froze oxygen-deficient defect structures and inhibited full recovery. Rietveld refinement confirmed this condition exhibited the highest microstrain, consistent with the broadened diffraction peaks observed in the XRD patterns. Water quenching (Fig.5.11c) produced irregular morphologies characterized by small, strained grains with poor faceting embedded with large grains. The high cooling rate suppressed coarsening and recovery while introducing thermal-shock stresses, giving rise to intermediate strain values. (Fig.5.11b,c) exhibited microstructural heterogeneity, with large irregular grains embedded within a finer-grained matrix. This morphology indicates rapid thermal contraction and localized stresses during quenching, which disrupted uniform growth and promoted uneven grain coarsening.

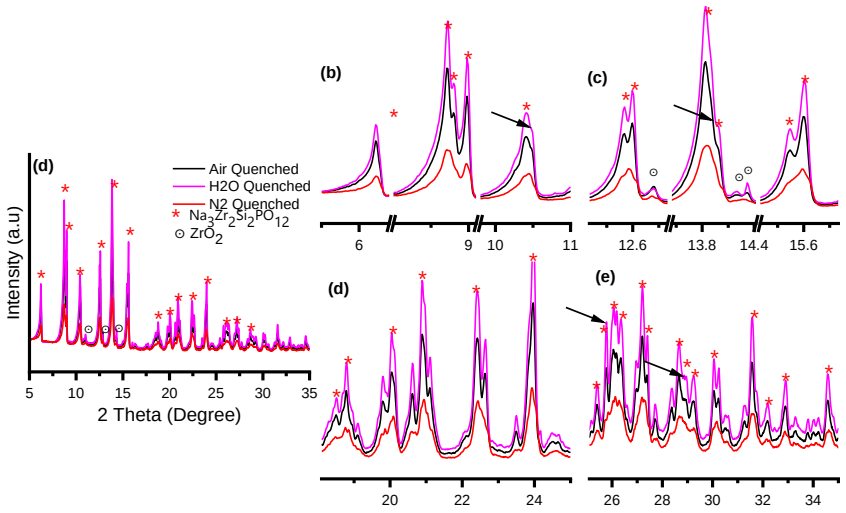

Fig.5.12: Overlapped XRD patterns in different quenching media, b,c,d,e are zoomed in images of a, black arrows indicates reflections with peak splitting.

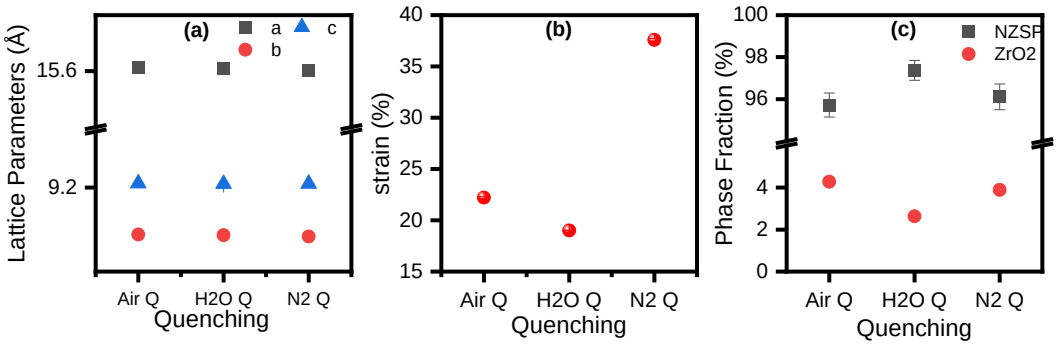

Fig.5.13: Structure modelling parameters in different quenching medium, a) lattice parameter, b) strain, c) phase fraction.

XRD patterns (Fig.5.12) confirm that the NaSICON framework was retained across all quenching media. Air and water quenching yielded sharp reflections consistent with high crystallinity, while nitrogen quenching showed broader, less intense peaks at lower angles, consistent with increased lattice strain and partial disorder. Rietveld refinement (Fig.5.13, Fig.5.14) further supports these trends: lattice parameters (Fig.5.13a) remained nearly constant, though subtle changes in the a- and c-axis indicate minor structural distortions. Strain values (Fig.5.13b) were lowest for air quenching and markedly higher for nitrogen, correlating with the observed peak broadening. Phase analysis (Fig.5.13c) showed the lowest ZrO_2 fraction in air-quenched samples, while both nitrogen and water quenches retained higher ZrO_2 contents, suggesting that faster cooling restricted diffusion and preserved high-temperature heterogeneity before complete Zr incorporation into the NaSICON lattice.

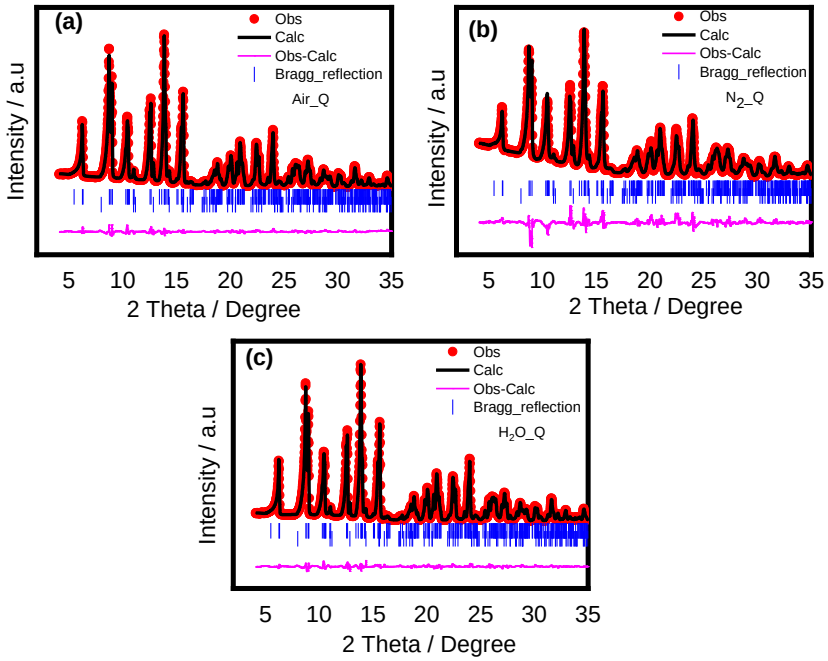

Fig. 5.14: Rietveld refinement plots for different quenching media (a) Air, (b) Nitrogen, and (c) Water.

These results show that while all quenching routes preserved the primary NaSICON phase, the microstructural and structural quality varied with medium. Air quenching produced the most balanced outcome, combining good crystallinity, reduced strain, and minimal secondary phases. Water and nitrogen quenching, by contrast, introduced irregular grain morphologies, higher ZrO_2 retention, and increased strain, outcomes likely to reduce ionic transport by disrupting grain boundary pathways. Although quenching does not disentangle nucleation from growth, it reveals how cooling dynamics directly shape grain coarsening, phase stability, and lattice relaxation.

To evaluate the influence of initial particle size on the final structure and microstructure, powders were sieved after calcination into two size fractions: –45 µm and –75+45 µm, using the smallest available mesh sieves in the laboratory. A third sample combining both fractions was also evaluated as a mixed particle size reference. The resulting samples were subjected to under identical combined sintering conditions and analyzed via SEM, XRD, and Rietveld refinement. Fig.5.15 presents SEM images of the sintered microstructures revealing distinct differences in the final microstructure. The –45 µm fraction (Fig.5.15a) produced compact, homogeneous grains with well-faceted cubic-like morphologies. The –75+45 µm sample (Fig.5.15b) showed less uniformity, with some grains partially embedded in a glassy matrix. The mixed powder (Fig.5.15c) exhibited pronounced heterogeneity, with irregular grain sizes and local non-uniformity.

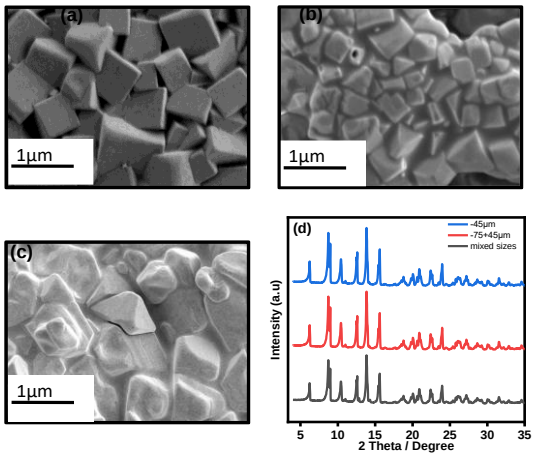

Fig.5.15: Effect of powder particle size range on microstructure and structure. (a) SEM of –45µm, (b) SEM of –75+45µm, (c) SEM of mixed particles sizes, (d) XRD patterns data collected on Mo Xrd λ = 0.709 for –45µm, –75+45µm and mixed particles sizes.

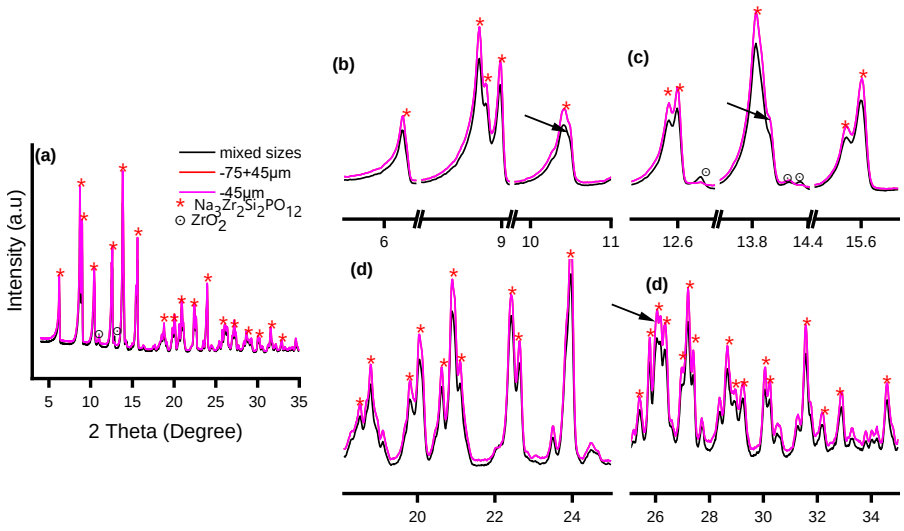

Fig.5.16: Overlapped XRD at varied HEM powder size ranges b,c,d,e are zoomed in images of (a) black arrows indicating reflections with peak splitting.Fig. 2.1

The XRD patterns (Fig.5.16) revealed sharp reflections across all samples, suggesting high crystallinity. The NaSICON phase crystallized in the monoclinic C2/c structure.

Rietveld refinement (Fig.5.17, Fig.5.18) indicated only small differences in lattice parameters and densities. The –45 µm fraction yielded the highest crystal density (3.273 gcm^{-3}), whereas the –75+45 µm (3.252 gcm^{-3}) and mixed powders (3.267 gcm^{-3}) were slightly lower. These variations lie within refinement scatter but align with the more uniform densification of the fine powder.

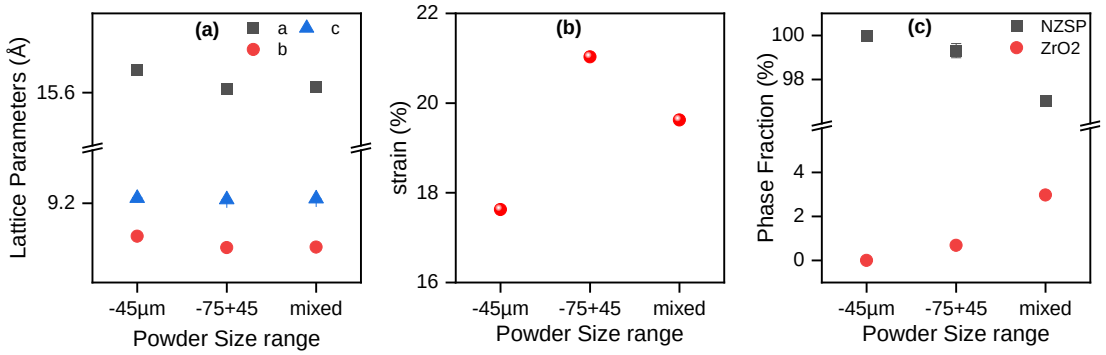

Fig.5.17: Structure modelling parameters for HEM powder size range, a) lattice parameter, b) strain, c) phase fraction.

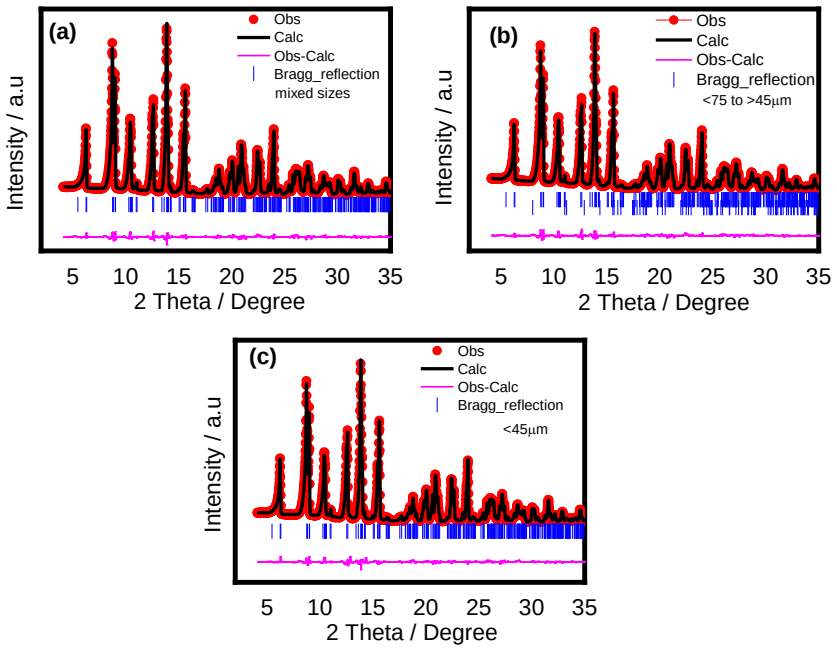

Fig.5.18: Rietveld refinement plots for different particle sizes (a) mixed particle sizes, (b) "–75+45 µm" (c) "–45 µm".

Secondary ZrO_2 was undetectable in the –45 µm sample, while traces (<1%) appeared in the –75+45 µm and mixed samples (Fig.5.17). Given the low magnitude, these are close to the detection/uncertainty limit of refinement, but their presence may reflect incomplete reaction or segregation at particle interfaces for the coarser fractions.

Lattice strain followed a similar trend: lowest for the –45 µm sample and slightly higher for the coarser and mixed fractions (Fig.5.17b), consistent with residual stress from larger particle sintering and possible distortions from intergranular glassy regions.

Overall, the –45 µm fraction provided the most favorable outcome, with dense and homogeneous grains, minimal secondary phases, and reduced lattice strain. Coarser or mixed powders introduced microstructural heterogeneity, minor ZrO_2 presence, and slightly elevated strain, though all samples maintained the NaSICON structure with high crystallinity.

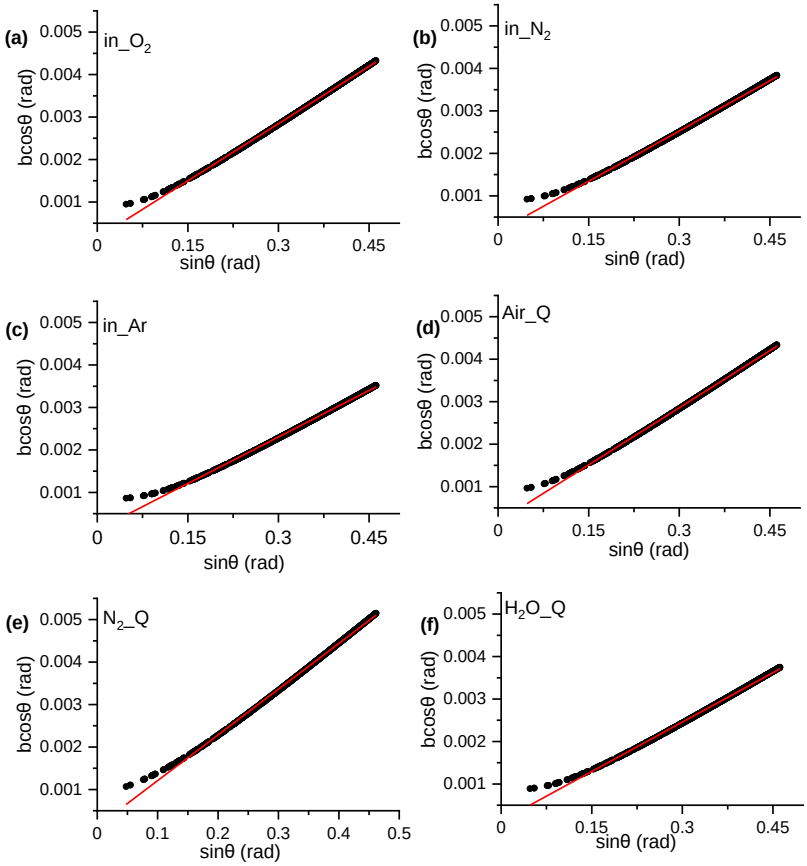

Fig. 5.19: Williamson-Hall plots for samples treated at different temperatures. The trend of increasing intercept and decreasing slope with temperature suggests a systematic reduction in lattice strain and growth in crystallite size.

To complement the structural interpretation based on microstructure and Rietveld refinement, Williamson–Hall (W-H) analysis was carried out to assess the evolution of crystallite size in NaSICON samples under different atmospheric conditions. The apparent crystallite sizes derived from W–H analysis (Fig5.19) range between ~250 and ~700 nm across different conditions. These values exceed the reliable detection limit of XRD-based line broadening (typically <100–150nm), and should therefore be considered as qualitative indicators rather than absolute values. Nonetheless, the relative trends are consistent: O_2 and air-processed samples yield the largest apparent crystallites, while nitrogen and water quenching result in smaller apparent sizes. Argon samples occupy an intermediate position.

These trends can be rationalized by considering the combined effects of thermal history and atmosphere. The long dwell at 1100 °C for 12 h followed by 1280 °C for 6 h ensured substantial grain growth and coarsening before quenching. Thus, the observed differences primarily reflect the extent of defect recovery and structural relaxation, rather than fresh nucleation events during cooling.

Oxidizing conditions (O_2, air) provide sufficient oxygen chemical potential to heal oxygen vacancies and support lattice recovery, resulting in larger equiaxed grains, reduced lattice strain, and more complete incorporation of Zr into the NaSICON structure. This is consistent with W–H results showing lower microstrain and larger apparent crystallite sizes.

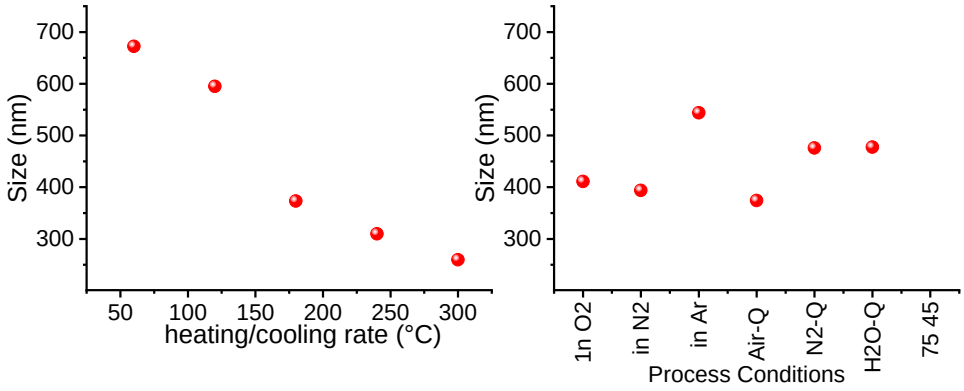

Fig. 5.20: Apparent crystallite size extracted from W-H analysis as a function of (a) heating/cooling rate and (b) processing atmosphere. Though values exceed XRD resolution limits, relative trends highlight the impact of processing conditions on microstructural evolution

Quenched environments disrupt this recovery. Nitrogen quenching combines low oxygen potential with rapid cooling, freezing oxygen-deficient defect structures and yielding the highest refined microstrain alongside bimodal, irregular grain morphologies. Water quenching, with the fastest cooling rate, further suppresses recovery and coarsening, producing finer apparent sizes but at the expense of irregular morphology and intermediate strain. In contrast, air quenching provides the most balanced outcome, with equiaxed grains, lower microstrain, and reduced ZrO_2 content, reflecting slower cooling and the stabilizing influence of higher oxygen potential.

Overall, the combined SEM, XRD, Rietveld, and W–H analyses demonstrate that oxidizing conditions favor coarsening and structural relaxation, while inert or quenched environments preserve smaller crystalline domains but freeze in higher strain and defect content. This highlights the crucial role of the cooling atmosphere in governing the balance between recovery, defect annihilation, and defect freeze-in after high-temperature sintering of NaSICON electrolytes

The impedance spectroscopy (Fig.5.21) was used to study the effects of the various conditions on ionic conductivity. For the different heating/cooling rates, an increase in conductivity was observed from 2.7×10^{-5} Scm^{-1} at 300°C/h to 1.8×10^{-4} Scm^{-1} at 60°C/h. This could be attributed to the increase in particle size, decrease in grain boundary resistance and increase in compactness.

Further, by changing the sintering atmosphere and sintering at 180°C/h, an increase in conductivity compared to sintering in air at 180°C/h was observed. Conductivities of 1.4×10^{-5} Scm^{-1}, 2.4×10^{-5} Scm^{-1}, and 3.5×10^{-4} Scm^{-1} were obtained in argon, nitrogen and oxygen, respectively. In the quenching media, conductivities of 1.4×10^{-5} Scm^{-1}, 5.4×10^{-5} Scm^{-1}, 1.4×10^{-4} Scm^{-1} were obtained in air, nitrogen and H_2O medium respectively. For particle size, conductivities of 1.4×10^{-5} Scm^{-1} and 2.2×10^{-3} Scm^{-1} were obtained for –75+45µm' and –45µm, respectively. Slower heating/cooling rates are associated with larger particle sizes, well-defined grains, and reduced grain boundaries. This should lead to enhanced ionic conductivity due to the favourable microstructure and decreased resistance to ion migration. Sintering in oxygen-rich atmospheres, where well-defined crystal structures are promoted, resulted in higher conductivity compared to inert atmospheres. The oxygen atmosphere facilitates the formation of ordered crystal structures, favouring ion conduction. The choice of quenching media influences the final microstructure. If a particular quenching medium promotes homogeneous grain growth and minimizes the formation of secondary phases, it is expected to contribute to higher ionic conductivity. Smaller particle sizes exhibited higher conductivity due to increased surface area and reactivity. While smaller particle sizes enhance reactivity during the early stages of sintering promoting densification and phase formation the final ionic conductivity is more closely linked to the resulting microstructure after sintering.

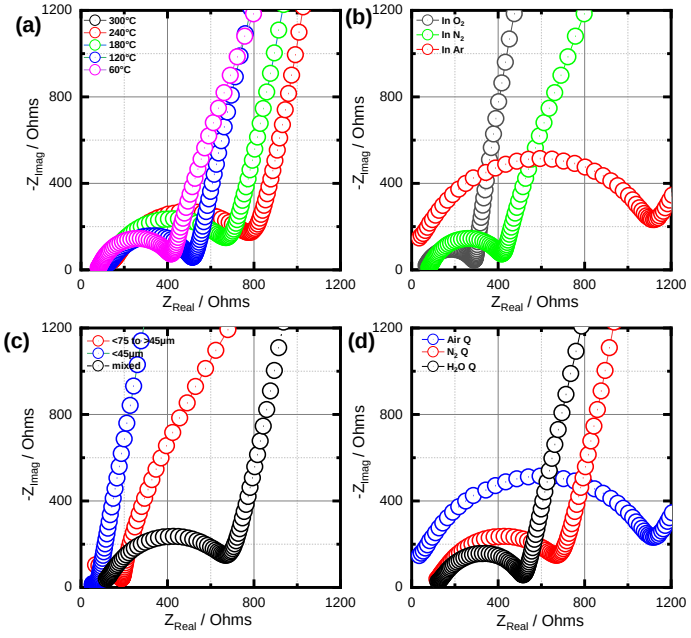

Fig.5.21: Influence of processing conditions on the ionic conductivities (a, b, c, d) electrochemical impedance plots for or the heating rates, the sintering environments, the particle size, and quenching media, respectively.

In particular, processing conditions that lead to larger, well-defined grains with fewer grain boundaries and reduced defect concentrations tend to favour higher bulk ionic conductivity.

Therefore, although small initial particle size can aid in achieving desirable sintered microstructures, the key determinant of conductivity is the quality and connectivity of the final grain structure. Well-defined grains with fewer defects and boundaries should facilitate ion movement. Consistent with previous studies the observed trends in microstructure and crystal properties align with expected conductivity variations. This agreed with earlier studies that attributed differences in conductivity and micro-structure to variations in sintering conditions[102],[110],[159],[143]. The processing conditions favouring larger, well-defined grains with reduced defects and boundaries will contribute to higher ionic conductivity. The relationship between microstructure and conductivity highlights the importance of carefully optimizing processing parameters for the desired electrochemical performance in NaSICON solid electrolytes.

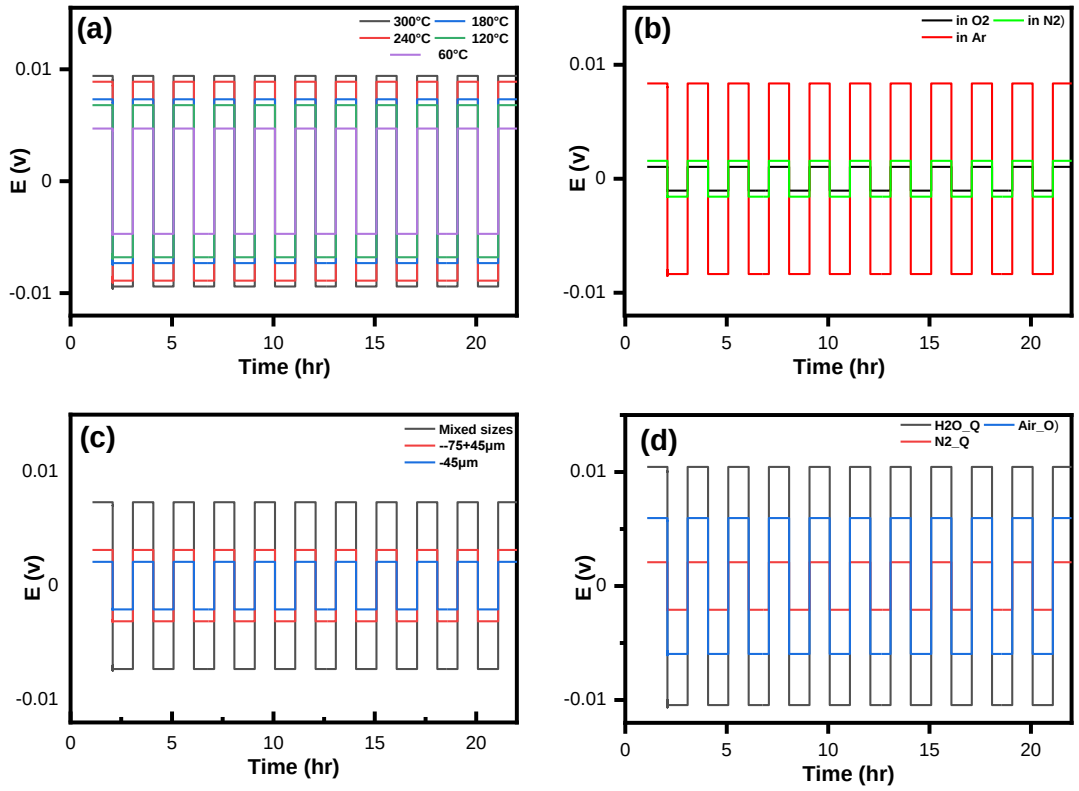

Fig.5.22: Influence of processing conditions on the overpotential (a, b, c, d) corresponding stripping and plating curves for the heating rates, the sintering environments, the particle size and quenching media, respectively.

The cycling performance of the NaSICON solid electrolyte was systematically assessed through galvanostatic cycling with potential limitation (GCPL). Symmetric cells, subjected to a current density of 0.1 $mAcm^{-1}$ for 1 hour per charge/discharge cycle at 60°C were employed to evaluate 10 cycles. Remarkably, all tested conditions exhibited commendable cycling stability, showcasing plateaus indicative of stable cycling. An increase in overpotential was observed across the cycles, aligning with the observed trend in ionic conductivity. There is a decrease in over-potential with a decreasing heating/cooling rate. This could also be related to micro-structural effects such

as porosity and tortuosity[162],. Sintering in oxygen and nitrogen reduces the over-potential; the –45μm led to low over-potential. The microstructural variations, particularly those induced by different heating/cooling rates and sintering atmospheres, played a crucial role in shaping the overpotential behaviour during cycling. Notably, a consistent decrease in overpotential was evident with decreasing heating/cooling rates, suggesting a favourable impact of slower processing on the electrochemical performance. Sintering in oxygen and nitrogen further contributed to reduced overpotential, with the condition involving finer particles (–45 μm) displaying particularly low overpotential.

This observation showed that varying the micro-structure through the different treatments could enhance ionic conductivity as well as cycling stability. The observed correlation between microstructure, overpotential, and cycling stability highlights the interplay of processing conditions and electrochemical performance. Amorphous content, variations in porosity and tortuosity, linked to microstructural differences, were considered as potential factors influencing the observed overpotential trends. Considering that the reported good performance for the material[149],[150] so far went through long processing times and the overarching aim of simplifying the synthesis process, the observed stabilities are quite promising. Despite the low ionic conductivities observed for some samples, the applied temperature of 60°C enhanced stable cycling within the number of cycles studied. The promising cycling stability observed, even with variations in ionic conductivity, suggests that the single double-step treatment could be further optimized for the synthesis of NaSICON solid electrolytes. This is particularly encouraging in the context of simplifying the synthesis process, as the reported good performance thus far required extensive processing times. The findings highlight the potential for achieving both improved synthesis procedures and enhanced electrochemical performance.

5.3 Effect of Mg and Mo Doping on Structure, Morphology and Ionic Conductivity

The impact of Mg and Mo doping on the structure, microstructure, and ionic conductivity of NaSICON solid electrolytes was studied using a consistent heating/cooling rate of 180 °C/h. Dopants were selected based on ionic radius and oxidation state Mg^{2+} (0.72 Å) for potential Zr-site substitution, and Mo^{4+} (0.46 Å) for P-site substitution. Doped compositions outlined in Table3.3 were studied. Fig.5.23 shows SEM images across these compositions. At lower Mg content (0.1), compact, irregular grains are observed. Increasing Mg to 0.2 results in more uniform, cubic-like grains.

XRD patterns (Fig. 5.24a) confirm rhombohedral symmetry (R–3c), consistent with literature[163]. Rietveld refinement supports the incorporation of Mg into the lattice, no evidence of Mg in the Na_3PO_4 secondary phase was found. Densities were 3.241, 3.285, 3.248, and 3.244 g/cm³ for $Mg_{0.1}Si_2$, $Mg_{0.1}Si_{2.2}$, $Mg_{0.2}Si_2$, and $Mg_{0.2}Si_{2.2}$, respectively. Slight fluctuations in ZrO_2 fraction (4.99–5.74%) and strain could be related to Mg content and Si/P ratio influence lattice distortion and packing or data scatter. The refinement also indicates that strain and lattice parameters shift with composition, consistent with local distortions from dopant incorporation.

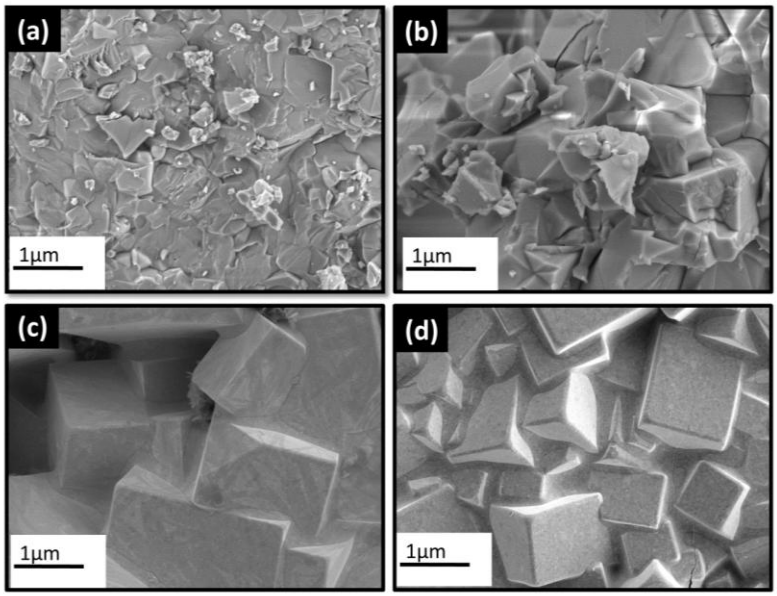

Fig.5.23: Effect of Mg doping on morphology doping and impedance. (a, b, c, d) SEM images of $Mg_{0.1}Si_2$, $Mg_{0.1}Si_{2.2}$, $Mg_{0.2}Si_2$ and $Mg_{0.2}Si_{2.2}$, respectively.

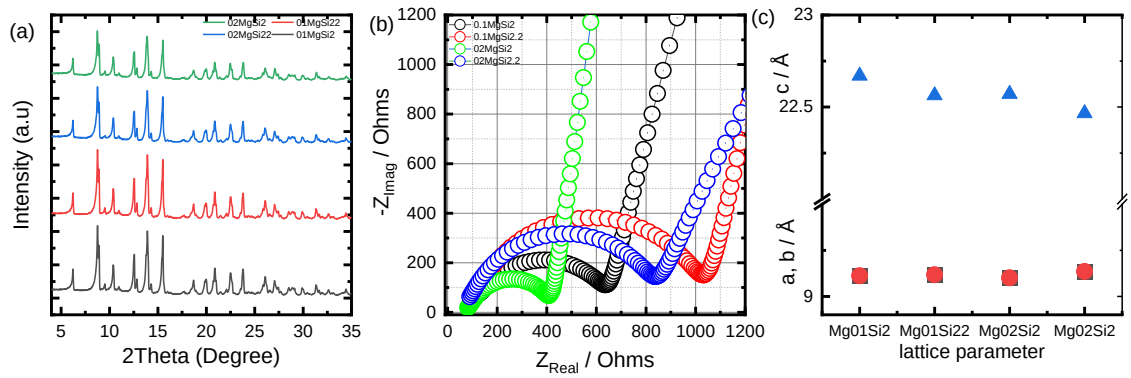

Fig.5.24: Effect of Mg doping on structure and ionic conductivity. (a) XRD patterns and (b) EIS spectra of Mg doping.(c) Lattice parameter of Mg doped NaSICON

EIS analysis (Fig. 5.24b) shows enhanced conductivity in $Mg_{0.1}Si_2$, $Mg_{0.1}Si_{2.2}$, and $Mg_{0.2}Si_2$, possibly due to improved packing and chemistry. A drop in conductivity in $Mg_{0.2}Si_{2.2}$ is likely linked to reduced Na-vacancy concentration due to increased Na content.

With Mo doping, the observed crystallization of the samples in the monoclinic C2/c phase suggests a low solubility of Mo in the lattice. This limitation is likely attributed to the large ionic radius of Mo compared to P, causing structural distortions, which are manifested in peak splitting during XRD analysis (Fig. 5.27).

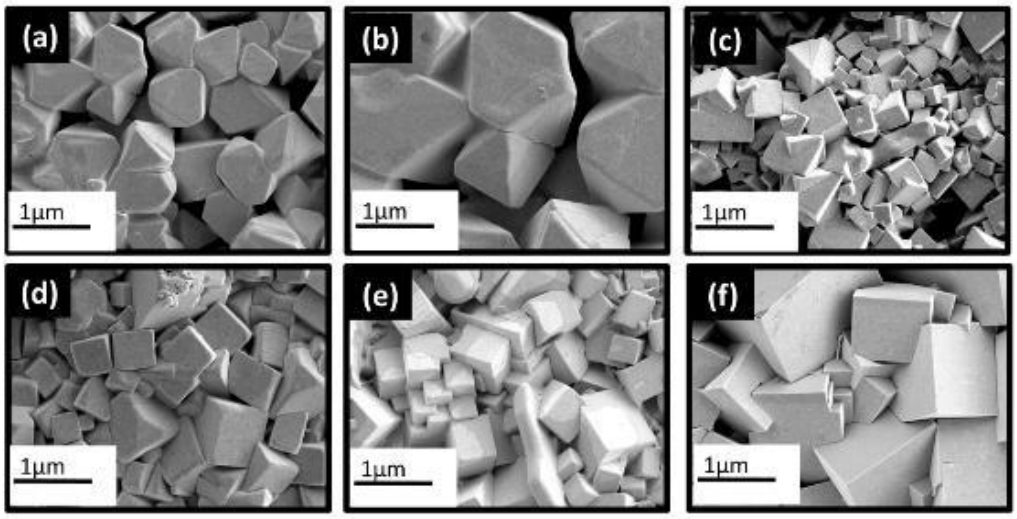

Fig.5.25 Morphological evolution with Mo doping of (a) 0.025, (b) 0.05, (c) 0.075, (d) 0.1, e) 0.2, (f) 0.4 respectively.

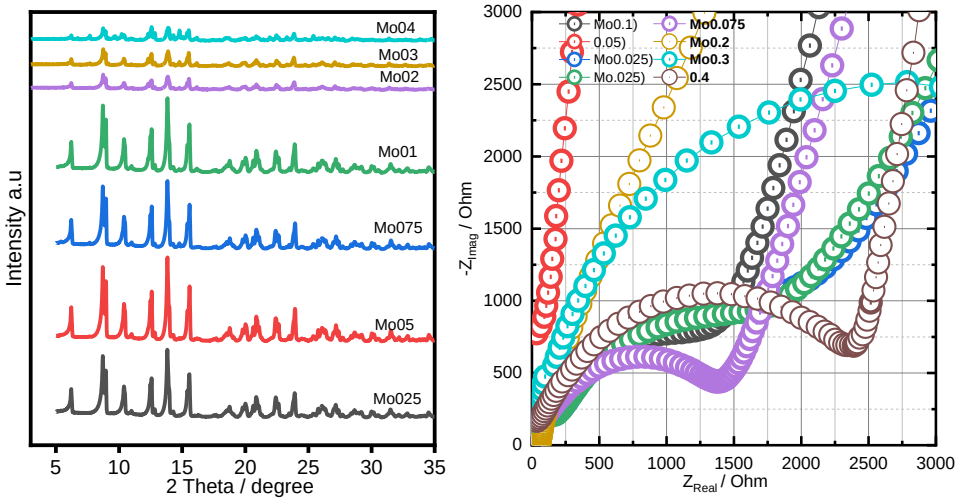

Fig.5.26 (a) Structure evolution (overlapping plot below) with Mo (b) Variations in Impedance with Mo doping.

An increase in lattice parameters, as revealed by Rietveld refinement, further supports Mo-induced alterations in the crystal lattice. Distinct variations in crystal densities, lattice strain, ZrO_2 fractions, and lattice parameters were observed for different Mo doping levels. Crystal densities of 3.247, 3.246, 3.251, 3.249 g/cm³ indicate changes in the packing of atoms within the crystal lattice. ZrO_2 fractions (3.01%, 2.36%, 1.26%, 2.47%) reflect the influence of Mo on secondary phases in the material. 'a' lattice parameter (15.64453Å, 15.62944 Å, 15.62789 Å, 15.6382Å) and 'c' lattice parameters (9.21281Å, 9.21104 Å, 9.21122 Å, 9.21031 Å) showcase the dimensional changes in the crystal lattice. The introduction of Mo (Fig.5.25) resulted in grain refinement, especially evident in the well-defined monoclinic grains observed in 0.025Mo. As the Mo content was increased, grain refinement persisted, and the samples transitioned to more cubic like grains with larger sizes, it also leads to inhomogeneous grain growth.

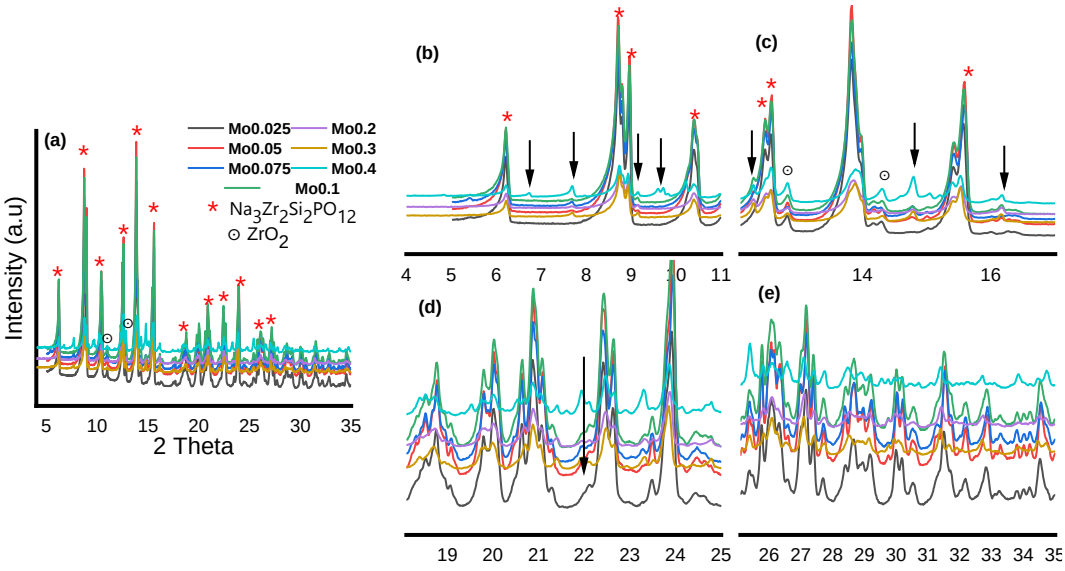

Fig. 5.27: Overlapped XRD patterns of Mo doped compostions, b,c,d,e are zoomed in images a. black arrows indicate peak splitting.

The analysis of XRD, coupled with observations of grain characteristics, suggests that Mo and Mg doping induces structural changes in the NaSICON lattice, impacting both primary and secondary phases within the material. The interplay between Mo/Mg and the host lattice elements contributes to variations in crystal properties and ultimately influences the microstructural evolution of the material. For the Mg-doped samples ($Mg_{0.1}Si_2$, $Mg_{0.1}Si_{2.2}$, $Mg_{0.2}Si_2$), an increase in conductivity is observed. This enhancement can be attributed to chemistry optimization and improved compactness. The incorporation of Mg seems to positively influence the chemistry of the material, leading to enhanced conductivity, while improved compactness supports more efficient ion migration through the material. However, an interesting observation is noted for $Mg_{0.2}Si_{2.2}$, where a decrease in conductivity is observed. This reduction is likely due to an increase in Na content, resulting in fewer available vacancies for Na migration. The excess Na might introduce more resistive pathways, hindering the efficient movement of ions and leading to a decline in overall conductivity. The trends in ionic conductivity with varying Mo doping levels are examined. The increase in conductivity from 0.025 to 0.05 Mo content is attributed to a combination of chemistry optimization and an increase in the size of the bottleneck in the structure. The optimized chemistry likely facilitates ion movement, and the enlarged bottleneck provides a more favourable environment for efficient ionic conductivity. However, a decrease in ionic conductivity is observed from 0.075 Mo content. This decrease is linked to the limited solubility of Mo in the lattice, potentially causing severe distortion and anisotropic grain growth. The distortion, induced by the large ionic radius of the dopant, creates resistance to ion migration, leading to a decrease in overall conductivity.

6 Effect of Processing Route on the Structure and Dynamics of $Na_3Zr_2Si_2PO_{12}$

A systematic investigation of the structural complexities within NaSICON and the effects of processing and composition was carried out to gain insight into structure and sodium ion dynamics in NaSICON solid electrolytes. $Na_3Zr_2Si_2PO_{12}$ was synthesized through three distinct processing routes (the samples were named NZSP, SS_NCO, and SS_NHP) and slight compositional variations with $Na_{3.4}Zr_2Si_{2.4}PO_{12}$ (NZS24P) explored. To characterize these materials, high-temperature X-ray diffraction (HTXRD) data and nuclear magnetic resonance (NMR) techniques were employed.

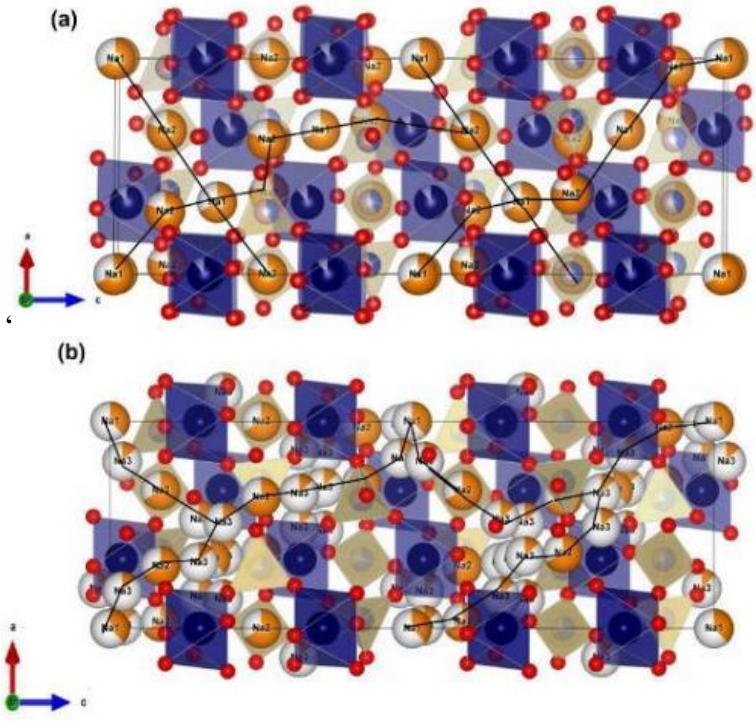

Fig.6.1: Crystal structure of $Na_3Zr_2Si_2PO_{12}$ in R-3c (167) for (a) 2 Na positions configuration (b) 3 Na positions, The diffusion paths are indicated by black lines (Images drawn on Vesta using ICSD cif files).

Due to significant controversy regarding the sodium sub-lattice within NaSICON, with multiple models[81,82,86] proposing different sodium configurations, including 2Na and 3Na in the rhombohedral phase, and 3Na, 4Na, and 5Na in the monoclinic phase, each offering distinct diffusion pathways for sodium ions as shown in Fig.6.1: and Fig.6.2:. A systematic approach was adopted,

employing FullProf Rietveld refinement using R-3c, 3Na, C2/c and 4Na C2/c, and correlating our observations with NMR and EIS data.

Fig.6.1: provide visual representations of the crystal structure in the R-3c configuration, showing both 2Na and 3Na arrangements. The black lines in both figures indicate the pathways along which sodium ions diffuse within the NaSICON structure. In the 2Na R-3c configuration (Fig.6.1:a), sodium ions are located in the interstitial spaces between ZrO_2 octahedra and SiO_4/PO_4 tetrahedra. The primary diffusion pathway in this configuration is Na1-Na2-Na1-Na2, with jump distances of 3.4498 Å for Na1-Na2 and 3.450 Å for Na2-Na1.

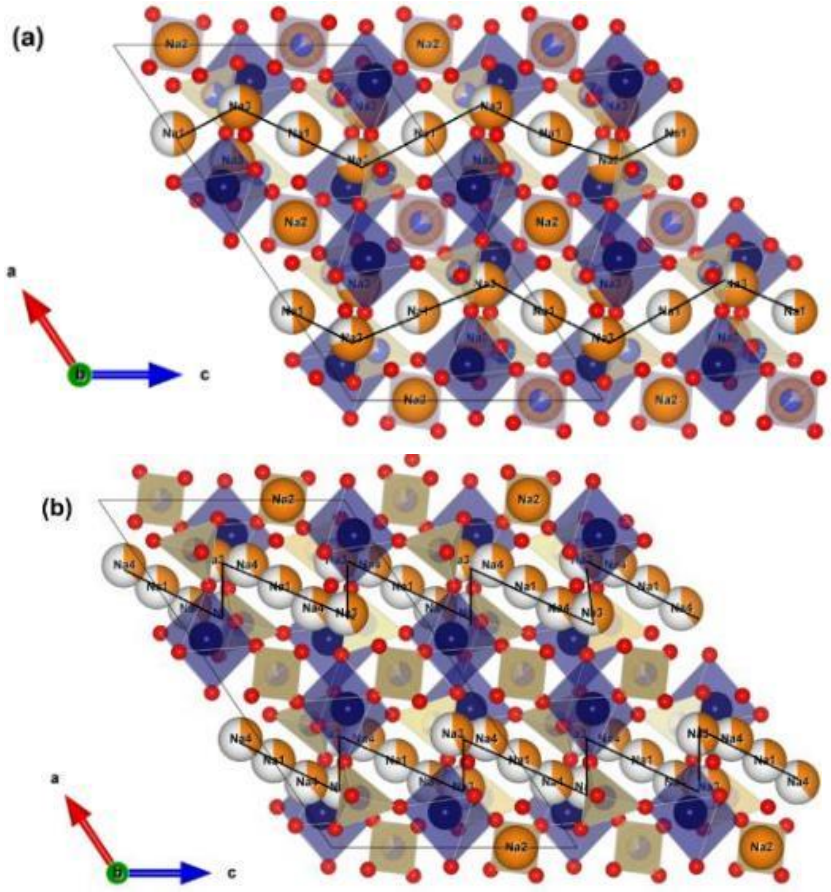

Fig.6.2: Crystal structure of $Na_3Zr_2Si_2PO_{12}$ in C2/c (15) for (a) 3 Na positions configuration (b) 4 Na positions, The diffusion paths are indicated by black lines (Images drawn on Vesta using ICSD cif files).

However, transitioning to the 3Na R-3c configuration (Fig.6.1:b), a new Na3 position occupies the interstitial regions between Na1 and Na2, giving rise to a potential new diffusion path, Na1-Na3-Na2 and Na3-Na2-Na3. Although the jump distances for these paths are shorter, with Na1-Na3 = 1.75 Å, Na2-Na3 = 1.88 Å, Na3-Na1 = 1.83 Å, and Na3-Na2 = 1.80 Å, note that these closer proximities also result in higher electrostatic repulsion, which may affect the rate of diffusion.

In the 3Na C2/c configuration (Fig.6.2:a), distinct diffusion paths, include Na1-Na3-Na1 and Na1-Na2-Na1, having jump distances (Na1-Na3 = 3.519 Å, Na3-Na1 = 3.519 Å, and Na2-Na1 = 3.71 Å). The 4Na C2/c (Fig.6.2:b) configuration introduces a new Na4 position between Na1 and Na3 and gives rise to a new diffusion route Na4-Na1-Na4-Na3-Na4: where, Na1-Na4 = 1.8 Å, Na3-Na4 = 1.4 Å, Na4-Na3 = 1.4 Å, Na2-Na1 = 3.5 Å, and Na2-Na4 = 3.5 Å. While the reduction in distance in this new configuration may suggest closer proximity between ions, such proximity also results in significant electrostatic repulsion. The introduction of new positions and the potential for increased electrostatic repulsion are shared characteristics of both 3Na R-3c and 4Na C2/c configurations. To address the model claims in the literature regarding the placement of sodium ions and space group configurations, a systematic approach was adopted during the refinement of high temperature structure. This involved applying the 3Na R-3c, 3Na C2/c, and 4Na C2/c models[81,82,86] to assess their suitability for the dataset and identify the most suitable model for gaining understanding of the mechanistic insights underlying the relationship between structural characteristics and dynamic behaviour.

Another common hypothesis in the existing literature[81,92] is that there is a transition from a monoclinic phase at room temperature to a rhombohedral phase at elevated temperatures within the 3Na configuration. In order to gain clarity on this matter, this assertion was examined through the refinement process of high-temperature X-ray diffraction data. Specifically, the room temperature C2/c refinement covered the temperature range from 25°C to 350°C. While the refinement of the R-3c configuration, was done from 350°C down to 25°C. The goodness of fit, lattice parameter, volume, Na occupancies (linear equations were used to fix the amount of Na), atomic displacement parameters, were analysed. The systematic analysis aimed to determine the presence or absence of this transition, and to contribute to a more comprehensive understanding of the structural behaviour within the 3Na and 4Na configurations as a function of temperature.

6.1 3Na Monoclinic / Rhombohedral Model Refinement

The high-temperature XRD data for all four samples were collected between 25°C and 350°C. The long-range average structure of the samples was characterised by Rietveld refinement using X-ray powder diffraction data. The NaSICON structure models ICSD473[81] and ICSD 62383[82] were used as a starting model for Rietveld refinement of the 3Na C2/c and 3Na R-3c respectively. In the refinement procedure, restraints were imposed on the atomic displacement parameter for atoms occupying identical positions or sharing the same nuclei, while constraints were placed on their occupancies. The lattice parameters, occupancies, phase fractions and volumes were analysed. The NZSP, NZS24P and SS_NCO samples crystallized in the monoclinic C2/c phase, and SS_NHP crystallized in the rhombohedral R-3c phase. The probable mixing of Na and Zr, and the probable changes in P/Si, were checked.

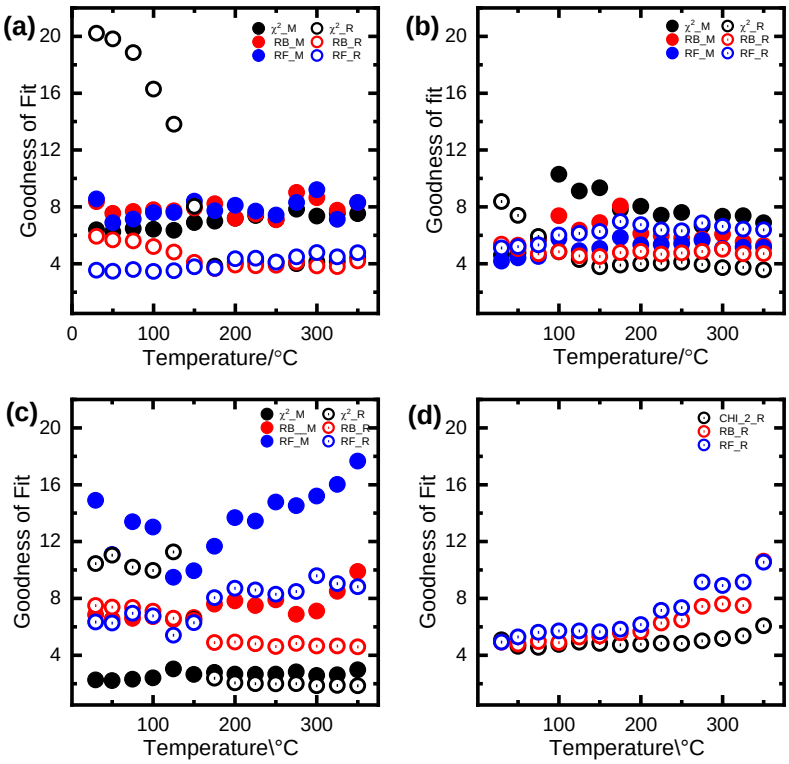

Fig.6.3: Goodness of fit plot showing statistical parameters for 3Na monoclinic and 3Na rhombohedral modelling of (a) NZSP, (b) NZS24P, (c) SS_NCO and (d) SS_NHP (the scale of the axis was kept same to make visible the deviations)

Fig.6.3: illustrates the variations in goodness of fit parameters from modelling with 3Na R-3c and 3Na C2/c. For NZSP (Fig.6.3:a), the two crystallographic structures, 3Na R-3c and 3Na C2/c, displayed distinct behaviours. In the monoclinic phase, the chi-square values were high at room temperature. However, as the temperature increased from approximately 150°C, these values escalated even further. The rhombohedral phase, on the other hand, showed a different trend. At 350°C, chi-square values were low (2.03) and increased as the refinement progressed from high temperature downwards to room temperature (9.08 at 150°C). This behavior hints at temperature-dependent changes in the crystal structure, which is likely associated with phase transition. The results for NZS24P (Fig.6.3:b) mirrored those of NZSP, with variations in the goodness of fit parameter based on the chosen crystallographic structure. In the 3Na C2/c structure, the chi-square values decreased from 14 at room temperature to 9.18 at 350°C, indicating reduced reliability in agreement factors which might be related to structural changes. Conversely, in the 3Na R-3c structure, the chi-square was 3.54 at 350°C, increasing to 8.14 at 25°C. These fluctuations in chi-square values suggest a structural response to temperature changes. The SS_NCO (Fig.6.3:c) material exhibited stability in chi-square values at 25°C, with a slight deviation around 150°C. It was only at 350°C that a sharp increase occurred, signaling a notable structural transformation at high temperatures. In the case of SS_NHP (Fig.6.3:d), the 3Na R-3c structure was the only one that could be successfully modeled. The chi-square value was high at 350°C and decreases to lower values at 25°C. However, a significant change in chi-square values was observed around 150°C, indicating a critical temperature point for structural changes.

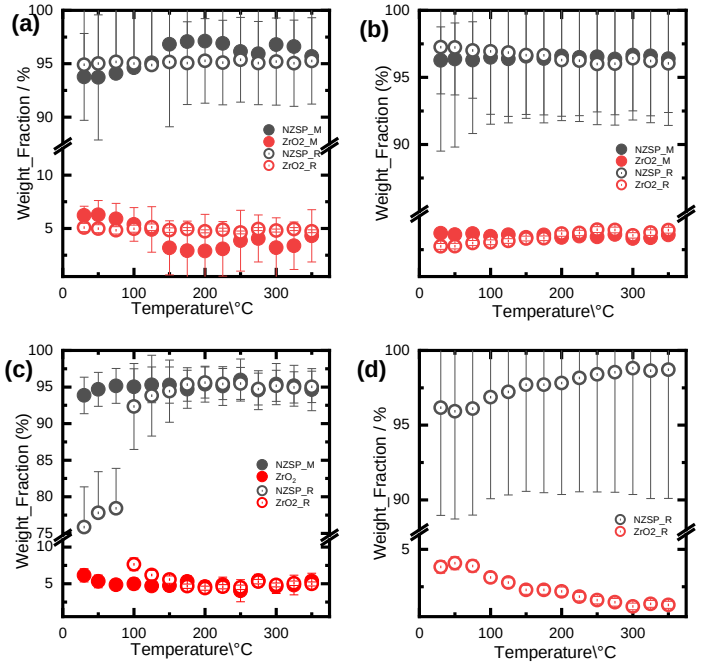

Fig.6.4: Trends in phase fraction with the R-3c and C2/c 3Na model at different temperatures for (a, b) NZSP and NZS24P and (c, d) SS_NCO and SS_NHP. The large error bars increased uncertainty in the 3Na refinement, partly due to peak overlap and model limitations.

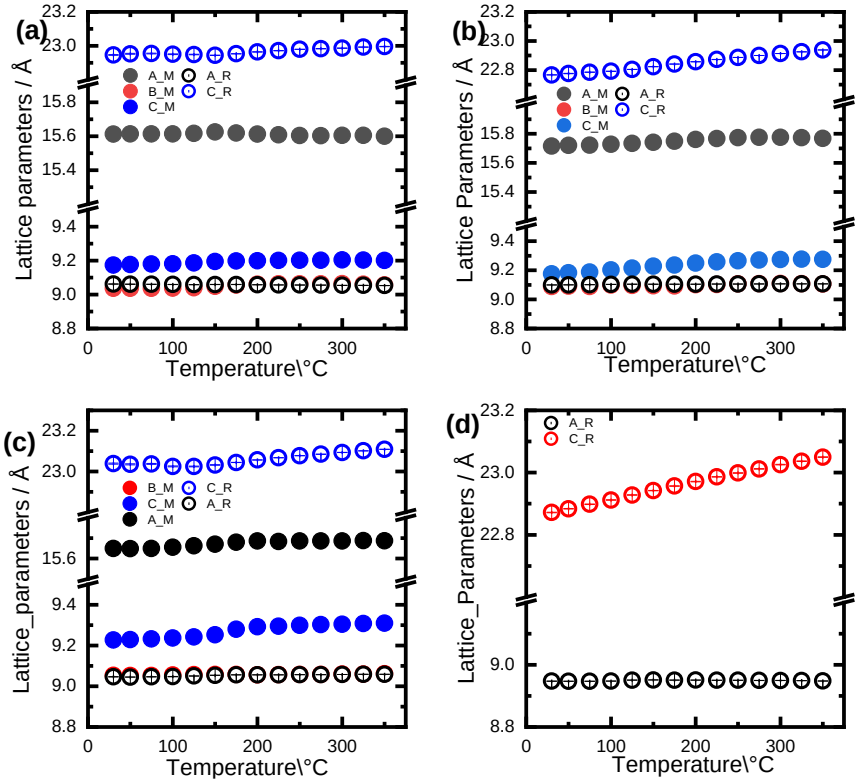

Fig.6.5: Trends in Lattice parameters with the R-3c and C2/c 3Na model at different temperatures for (a, b) NZSP and NZS24P and (c, d) SS_NCO and SS_NHP

The reliability of the refinement was further assessed by examining the changes in weight fractions (Fig.6.4:) in both the forward direction (25°C to 350°C with 3Na C2/c) and the reverse direction (350°C to 25°C with 3Na R-3c). It was assumed that if a true phase transition had occurred, there should be no significant differences in weight fractions, indicating the stability and reversibility of the refinement process. However, our observations revealed significantly high error margins in the weight fractions of NZSP, NZS24P, SS_NCO, and SS_NHP. These error margins indicate the potential instability of the selected crystallographic model. In light of these findings, questions emerged regarding the existence of a genuine phase transition to a rhombohedral structure at high temperature, as the observed discrepancies cast doubt on the stability of the model.

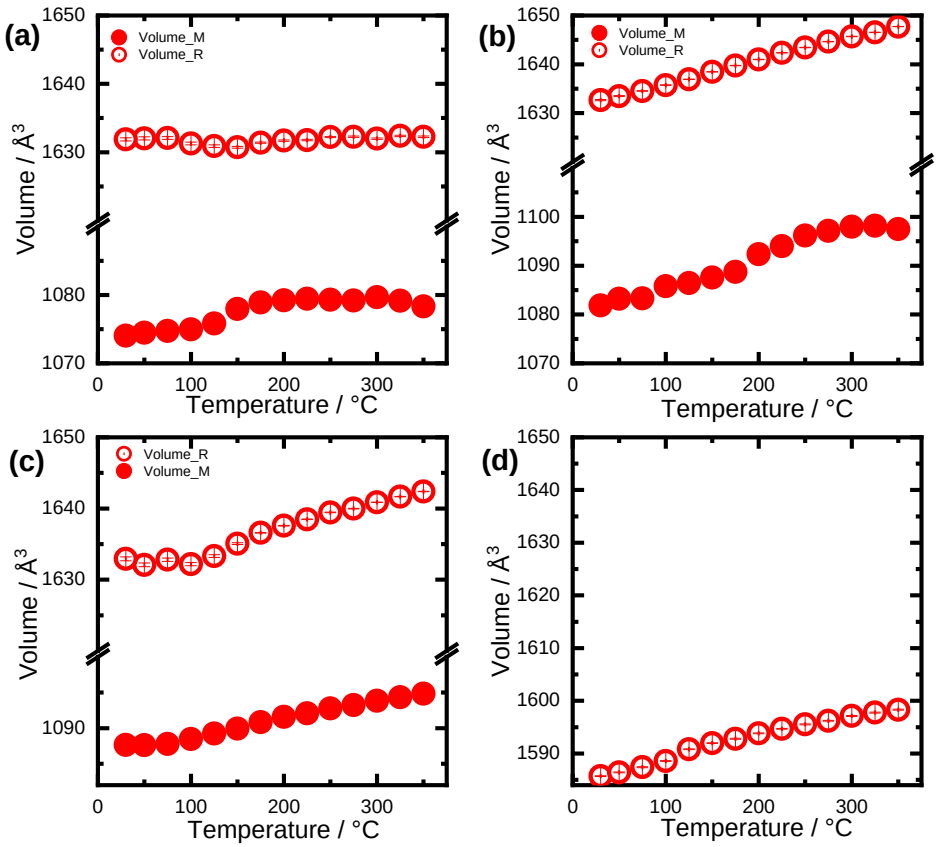

Fig.6.6: Trends in volumes with the R-3c and C2/c 3Na model at different temperatures for (a, b) NZSP and NZS24P and (c, d) SS_NCO and SS_NHP

To understand the origin of the observed mid-temperature changes, an examination of lattice parameters, volume, and sodium (Na) occupancy as functions of temperature was conducted. These additional investigations aimed to provide insights into the underlying mechanisms responsible for the variations in the crystallographic properties, shedding light on the nature of the structural changes observed during the refinements.

In all samples, a small increase in both the 'a' and 'c' lattice parameters, and the lattice volume (Fig.6.6:), was observed both before and after the region of structural alteration. For instance, in

the case of NZSP, the 'a' parameter exhibited a slight increase from 15.687 to 15.690 Å, while the 'b' parameter experienced a slight reduction from 9.079 to 9.076 Å. Concurrently, the 'c' parameter expanded slightly, progressing from 9.218 to 9.246 Å. Similarly, the rhombohedral R-3c phase showed a marginal enlargement of the 'a' and 'b' parameters from 9.075 to 9.084 Å, while the 'c' parameter increased from 23.02 to 23.08 Å. The lattice volume also underwent a minute rise, shifting from 1089.57 to 1091.93 Å³ in C2/c and from 1639.95 to 1646.3 Å³ in the rhombohedral phase.

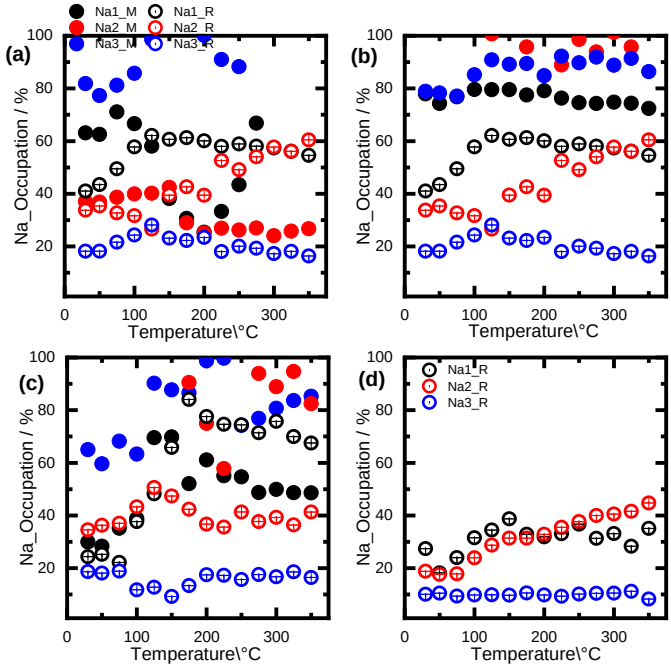

Fig.6.7: Trends in Na occupancies with the R-3c and C2/c 3Na model at different temperatures for (a, b) NZSP and NZS24P and (c, d) SS_NCO and SS_NHP

These observed trends of slight increment in the lattice parameters and volume extend the observation from the analysis of goodness of fit parameters, emphasizing a correlation within this specific region. However, the small increases in the 'a', 'c' parameters and volume do not constitute the primary driving force behind this phenomenon, rather they indicate small thermal expansion.

The variations in sodium (Na) occupancy at different temperatures were examined (Fig.6.7:). For both NZSP (Fig.6.7:a) and SS_NCO(Fig.6.7:c) cases, the occupancies of the Na1 and Na3 sites displayed an increase within the mid-temperature range, while Na2 exhibited a decrease during the same temperature interval. These findings could be attributed to a dynamic and temperature-dependent redistribution of sodium ions within the crystal structure. In contrast, in NZS24P (Fig.6.7:b), all three Na positions exhibited an increase in occupancy around the mid-temperature region. Since the stoichiometric content in the unit cell is fixed, the observed trend indicates the material-specific nature of ion redistribution phenomena.

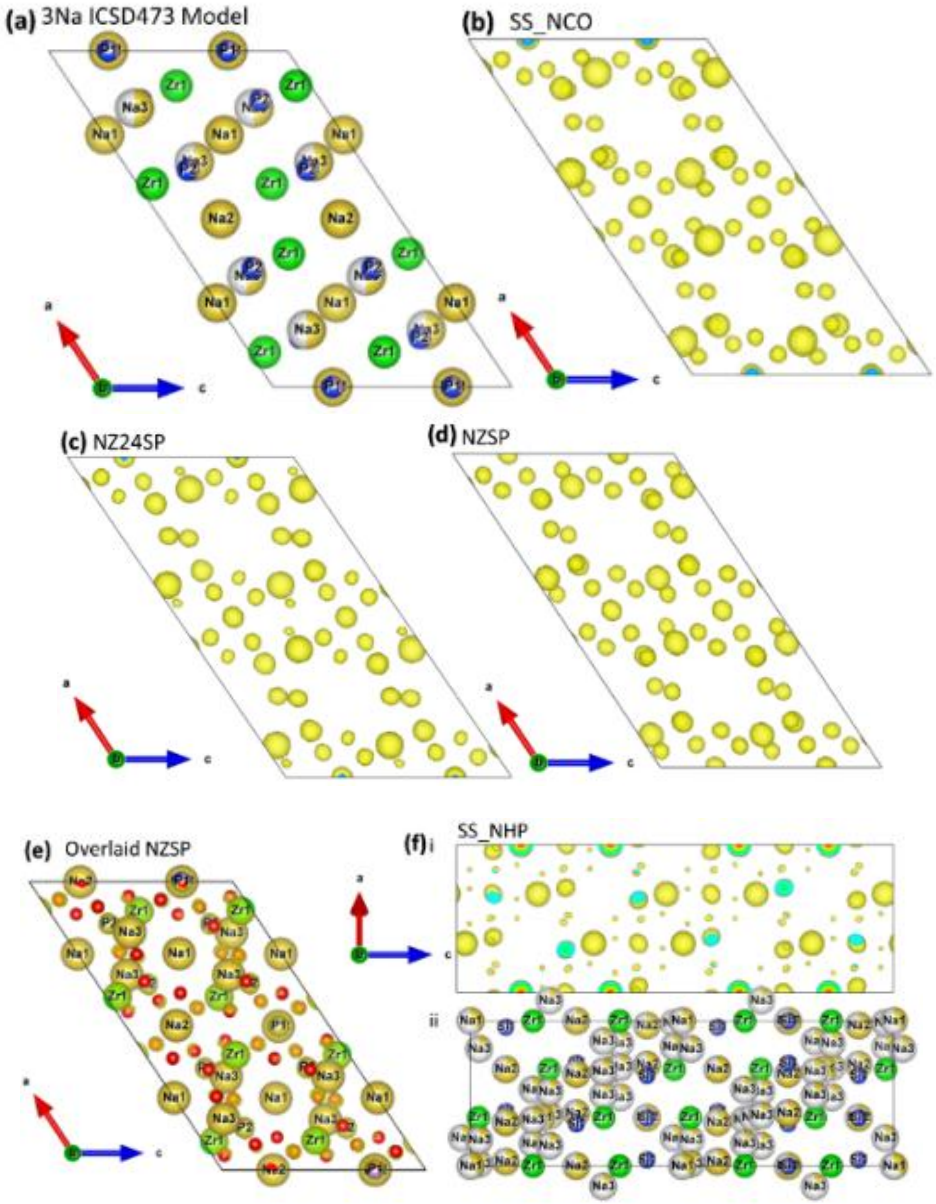

Fig.6.8: (a) Crystal structure of the ICSD473 3Na model used for refinement. The effective scattering-length-density map of the X-ray diffraction data at room temperature for (b) SS_NCO, (c) NZS24P, (d) NZSP at a different isostructural level showing no negative scattering-density of Na5 on the Zr site, (e) NZSP (f) (i), Scattering-length-density map of SS_NHP and (ii) the ICSD62383 model used for the high-temperature rhombohedral phase refinement. The negative scattering-density is in turquoise and the positive scattering-length-density is in yellow.

It should also be mentioned that the presence of unidentified impurity phases in SS_NHP (Fig.6.7:d) which were added to the background led to reduced reliability of observation. Additionally, focus was placed on investigating the potential intermixing of Na and Zr ions on the Zr sites within the C2/c 3Na model. Interestingly, it was observed that a minor fraction of Na ions infiltrated the Zr site in NZSP for some temperature ranges. However, for certain temperatures, this behaviour was deemed unreliable and thus was not considered for precise quantification. In

contrast, this observation did not hold in the reverse scenario with the rhombohedral configuration refinement from high temperature to room temperature.

Furthermore, an examination was conducted using an effective x-ray scattering-density map, to gain more insights into the site occupancies, as visually represented in Fig.6.8:. This map, resulting from the Fourier transform of the diffracted signal, which combines the intensity data acquired from measurements with the phase information derived from the theoretical model. No negative scattering was observed around some of the Zr atoms, hence, the possibility of the intermixing of Zr and Na was not reliably established the negative scattering cannot be linked to this.

The observations from analyses of the parameter, provide insights into the dynamics governing the behaviour of these materials. However, the high chi-square values and fluctuations/error margins associated with the refinement process introduce uncertainty and lower the reliability of the observations for the two models. A. Consequently, the samples were modelled using the 4Na C2/c configuration. This alternative modelling strategy seek to check the challenges posed by high chi-square values error margins and hoped provide a more reliable framework for interpreting the intricate interplay of factors influencing the observed structural changes in the mid temperature region.

6.2 4Na Model Refinement

The high-temperature XRD data for all four samples were collected between 25°C and 350°C, and they were characterized by Rietveld refinement using 4Na C2/c ICSD38057[85] (4Na positions) as the starting model. In the refinement procedure, restraints were imposed on the atomic displacement parameter for atoms occupying identical positions or sharing the same nuclei, while constraints were placed on their occupancies (Na stoichiometry was fixed using a linear equation). The lattice parameters, occupancies, phase fractions and volumes were analysed. The probable mixing of Na and Zr, and the probable changes in P/Si, were checked.

When the 4Na C2/c (Fig.6.9:) model was employed in comparison to the 3Na C2/c model, a remarkable difference was observed in the chi-square values for NZSP, NZS24P, and SS_NCO. Specifically, the chi square values exhibited a consistent reduction from room temperature to high temperatures, with notable variations in the mid-temperature range, signifying the occurrence of structural alterations within these materials at those temperatures. This observation signifies the fit of the model, highlighting its high reliability in characterizing the structural properties of these materials. It indicates that the 4Na C2/c model continues to provide a more dependable representation of the materials' structural behaviour, even as the temperature extends beyond the mid-temperature structural alteration zone.

Using the 4Na C2/c model for the refinement of SS_NHP was not successful, rendering it unsuitable for this particular process route. Nonetheless, to enhance the comprehensiveness of the analysis, plots generated from the R-3c 3Na model refinement of the SS_NHP were incorporated into the figures.

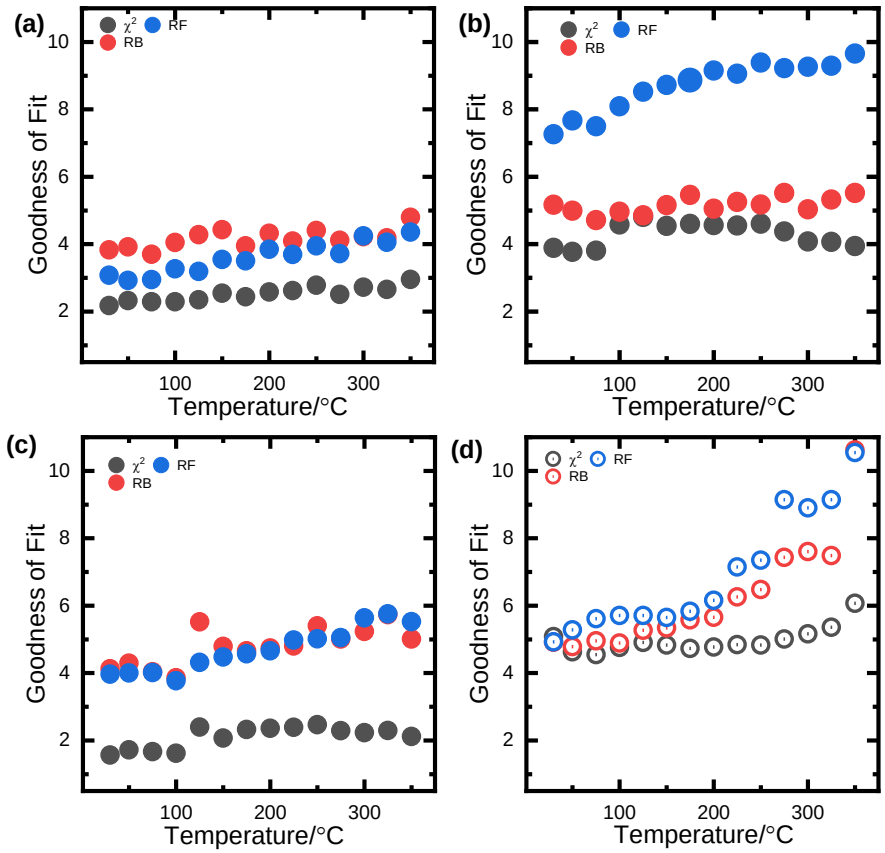

Fig.6.9: Trends in 4Na model Rietveld refinement empirical data of phase fraction, Na and Si/P occupancy at different temperatures for (a) NZSP (b) NZS24P and (c) SS_NCO and (d) SS_NHP refined using 3Na R-3c section added for comparison.

The decrease in chi-square values observed in the refinement using the 4Na C2/c (Fig.6.9:a,b,c) model beyond the mid-temperature range, which is typically associated with the transition from monoclinic to rhombohedral phases, suggests that the Structure might be better described with a 4 Na monoclinic model. To gain better understanding of the structural alterations when using this model, parameters such as weight fractions, lattice parameters, volume changes, and sodium occupancies were examined.

The refinement process using the 4Na C2/c configuration displayed remarkable stability and reliability, as evidenced by the minimal error margins in weight fractions across all three samples, as depicted in Fig.6.10:

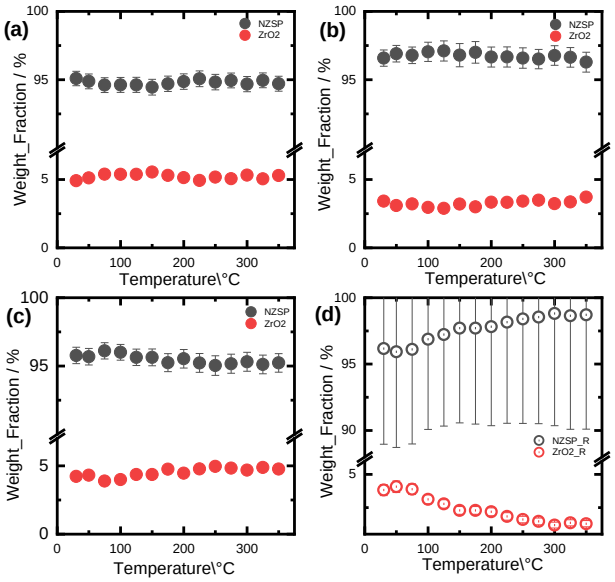

Fig.6.10: Trends in weight fractions with the C2/c 4Na model at different temperatures for (a, b) NZSP and NZS24P and (c, d) SS_NCO and SS_NHP

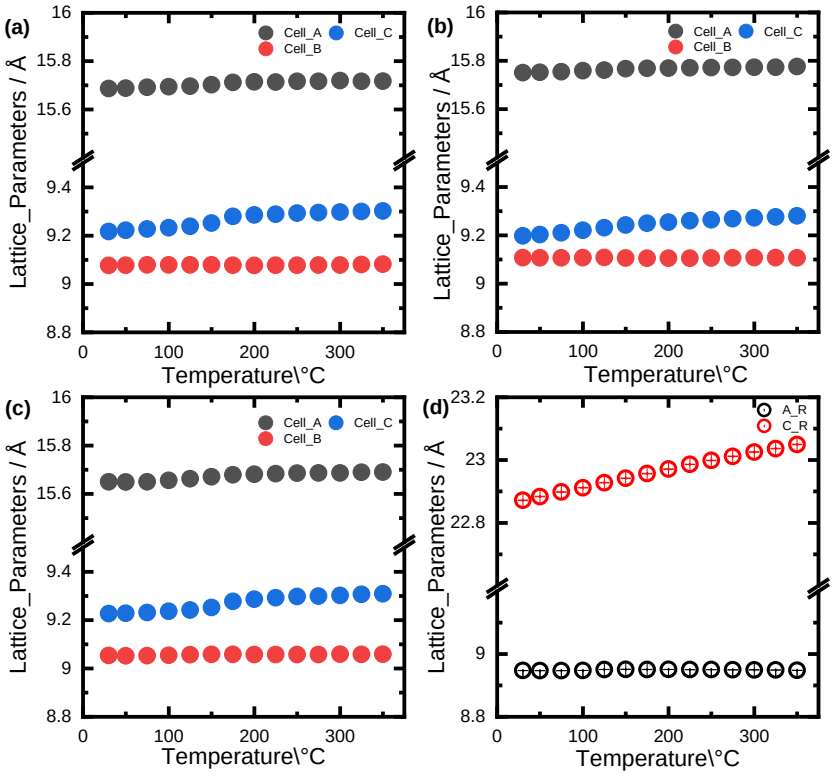

Fig.6.11: Trends in lattice parameters with the C2/c 4Na model at different temperatures for (a, b) NZSP and NZS24P and (c, d) SS_NCO and SS_NHP

This consistent stability was observed from 25°C to 350°C, suggesting the robustness of the 4Na C2/c model. The three samples exhibited a subtle increase in their lattice parameters (Fig.6.11:) 'a,' 'b,' and 'c' both before and after the mid temperature region. Additionally, the lattice volume in Fig.6.12:, exhibited a steady increase in all three samples. While these alterations in weight fractions, volume, and lattice parameters demonstrated a consistent trend of increase around the region where structural changes were anticipated, they cannot be definitively attributed as the driving forces behind the observed structural modifications.

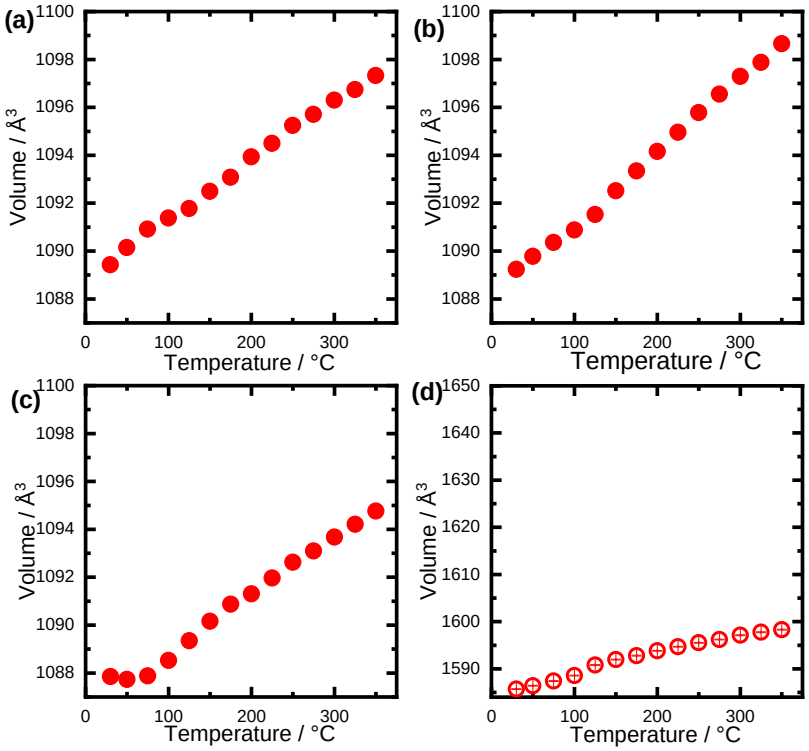

Fig.6.12: Trends in volumes with the C2/c 4Na model at different temperatures for (a, b) NZSP and NZS24P and (c, d) SS_NCO and SS_NHP

Furthermore, the Na occupancies (Fig.6.13:) were analysed For NZSP and SS_NCO, the occupancy of Na2 (4e) was initially full (100%) at 25°C. However, as the temperature increased, there was a noticeable decline in the occupancy of Na2, decreasing to approximately 70% in NZSP and around 65% in SS_NCO. Na3 (8f) increased from around 40% at room temperature to almost 80% at 350°C in NZSP and SS_NCO. On the other hand, Na1 (4d) and Na4, which initially had lower occupancies, displayed a gradual reduction, with fluctuations in the mid-temperature regions, presumably corresponding to potential structural changes. Conversely, in the case of NZS24P, Na4 (8f) exhibited an initial occupancy of approximately 60%, and this occupancy gradually increased with rising temperatures. Meanwhile, Na2, initially almost fully occupied, showed a consistent decrease with temperature, and Na1 also exhibited a gradual decrease.

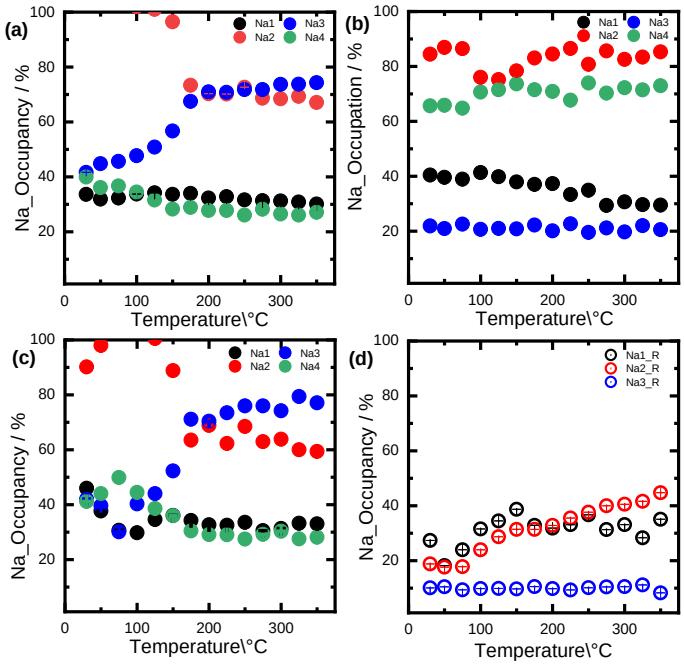

Fig.6.13: Trends in Na occupancies with the C2/c 4Na model at different temperatures for (a, b) NZSP and NZS24P and (c, d) SS_NCO and SS_NHP

Furthermore, the potential mixing of sodium (Na) and zirconium (Zr) ions on the Zr site was investigated. Although the 4Na model indicated that a small quantity of Na may have infiltrated the Zr site within the NZSP sample for some temperature conditions, the refinement process was unable to confirm this mixing with certainty. Further, the effective X-ray scattering density map, depicted in Fig.6.16: provided insights into site occupancies. The map was generated through the Fourier transformation of the diffracted signal, incorporating the intensity data obtained from measurements and the phase information extracted from the model. No residual energy densities were observed, but more negative scatterings were observed. This phenomenon may be attributed, in part, to the signs of the coherent scattering associated with Na and Zr, as seen in the effective scattering-density maps (Fig.6.14: d). A negative scattering implies that the X-rays scattered from Na and Zr on the same site interfere destructively, resulting in decreased site scattering, which is factored into the site occupancy. Furthermore, the presence of an additional Na4 site near Na3 and the Zr site on 8f significantly contributed to this destructive interference, potentially causing the effective scattering to approach zero.

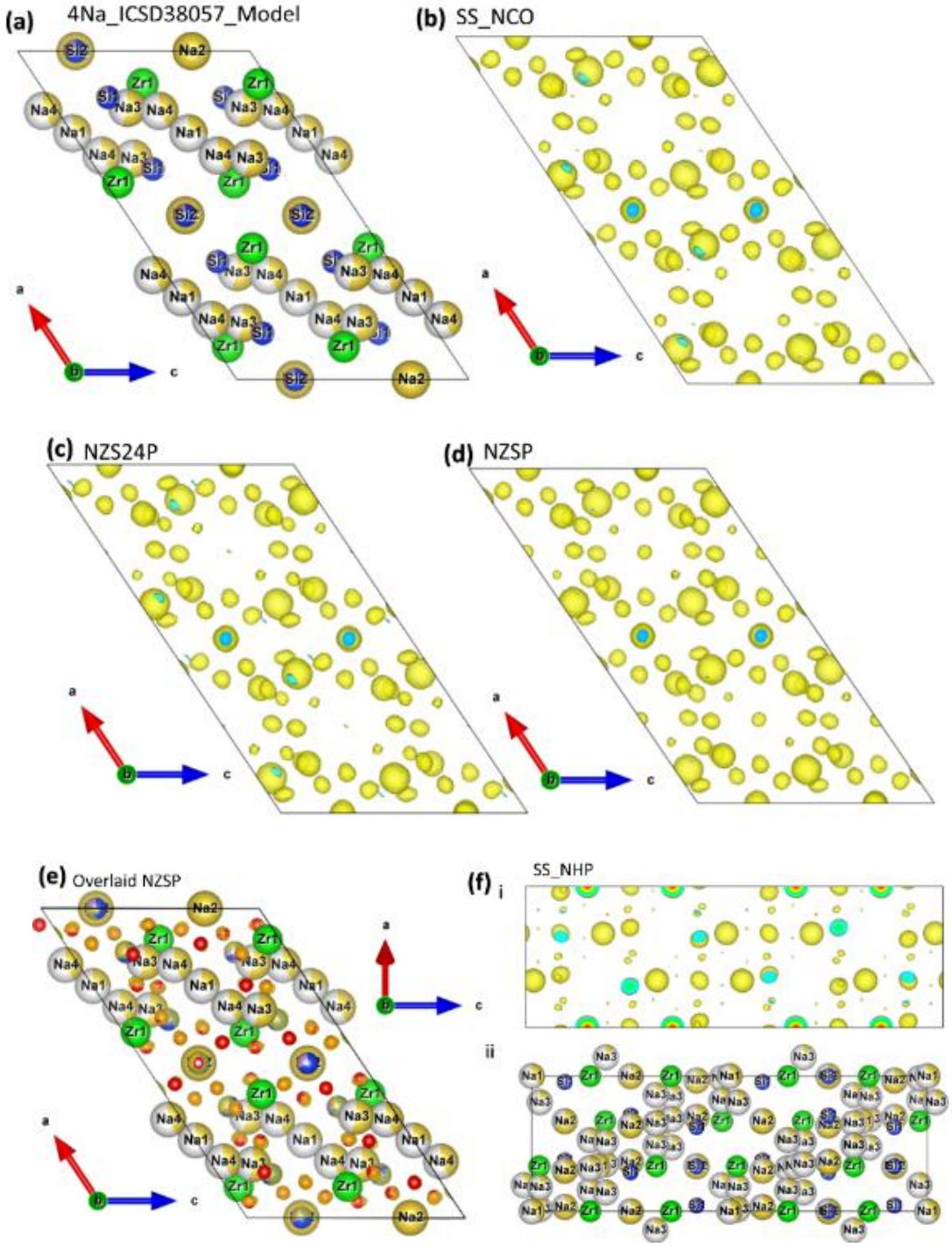

Fig. 6.14: (a) Crystal structure of the ICSD38057 4Na model used for refinement. The effective scattering-length-density map of the X-ray diffraction data at room temperature for (b) SS_NCO, (c) NZS24P, (d) NZSP at a different isostructural level showing negative scattering-length-density of Na5 on the Zr site, (e) NZSP (f) scattering-length-density map of SS_NHP.

An attempt was made to establish a correlation between the random distribution of Si/P occupancy, and the observed changes in Na occupancy within the monoclinic phase. However, these

efforts were unsuccessful due to the instability of the refinement process. The shifts in Na occupancies were particularly prominent, emphasizing their role in the observed structural changes. In samples with lower Na composition, such as NZSP and SS_NCO, a significant proportion of Na migrated into the Na3 positions as the temperature increased. Conversely, in samples with increased Na content, as observed in NZS24P, the Na4 position exhibited increased activity, attracting a greater quantity of sodium at elevated temperatures. This could probably be attributed to a decrease in the energy of the site due to an increase in amount of sodium. Though regions of marked structural changes were observed in the mid temperature regions for all parameters. The observed changes could not be attributed to a transition from monoclinic to rhombohedral phase due to the reliability of the refinement with the 4Na C2/c beyond this region as well as the irreversibility of the refinement parameters obtained in the forward and backward direction with monoclinic and rhombohedral phases, respectively. Probably the observed structural changes could be attributed to the changing centre of gravity of the atomic position/coordinates due to the combined effect of anisotropic lattice expansion/distortion in the x and z direction as well as the electrostatic repulsion promoted by the proximity of the Na positions.

6.3 Visualizing Structural Discrepancy Variations with Temperature between 4Na and 3Na Model Refinement

6.3.1 NZSP

As seen inFig.6.15:, the primary diffusion pathways identified in 3Na C2/c NZSP are Na3-Na1-Na3 and Na1-Na2-Na1. An elevation in temperature from 25 to 350°C resulted in noticeable alterations in the size of the bottleneck (estimated by measuring the dimension of the bonds around Na1) and the displacement of Na3. This displacement of Na3 exhibits a proportional increase with rising temperatures.

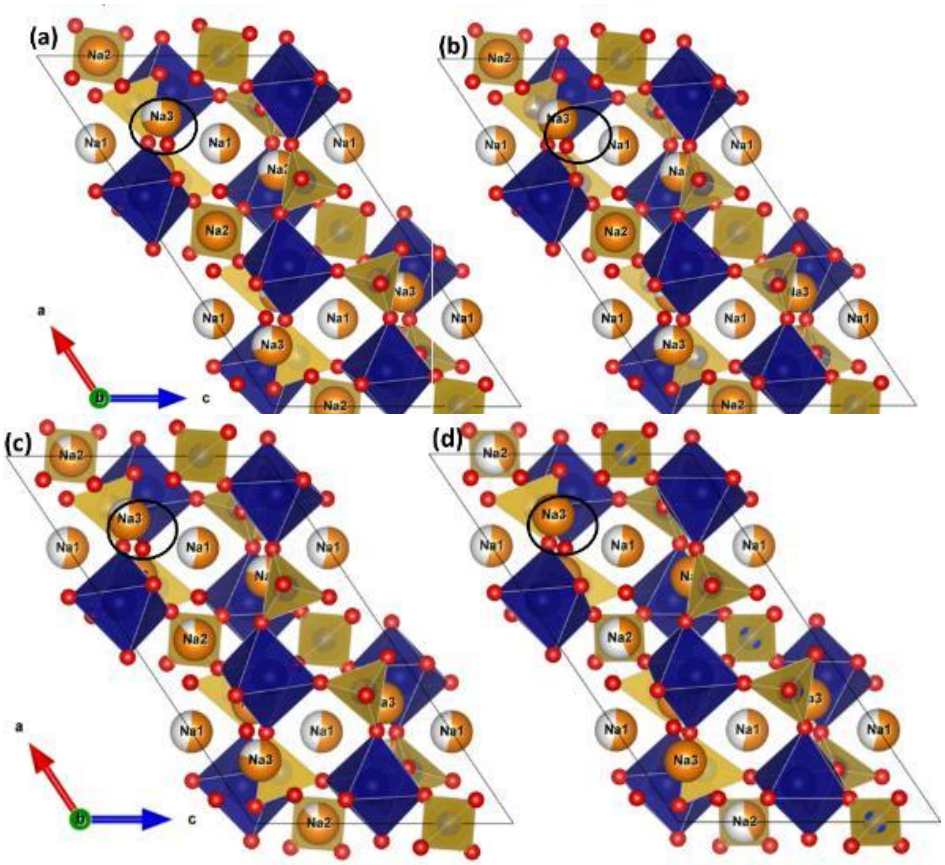

Fig.6.15: Crystal structure of refined NZSP 3Na C2/c at a) 25°C b) 100°C c)150°C and d) 350°C (Images drawn on Vesta using refinement crystallographic information- files)

In contrast, Fig.6.16:, depicting the 4Na model, reveals larger bottlenecks within the structure. In this model, the diffusion paths Na3-Na1-Na3 include an additional Na4 atom, forming a sequence of Na4-Na1-Na4-Na3, along with the pathway Na1-Na2-Na1. Notably, Na1 and Na4 are in close proximity, reducing the likelihood of both positions being occupied simultaneously due to strong electrostatic repulsion forces. The increased electrostatic repulsion not only encourages correlated migration by enabling Na1 or Na4 to be available for diffusion within the pathway at any given time but also promotes the displacement of Na3. This displacement is particularly significant because Na3 is typically located at a short distance from Na4, facilitating efficient ion diffusion.

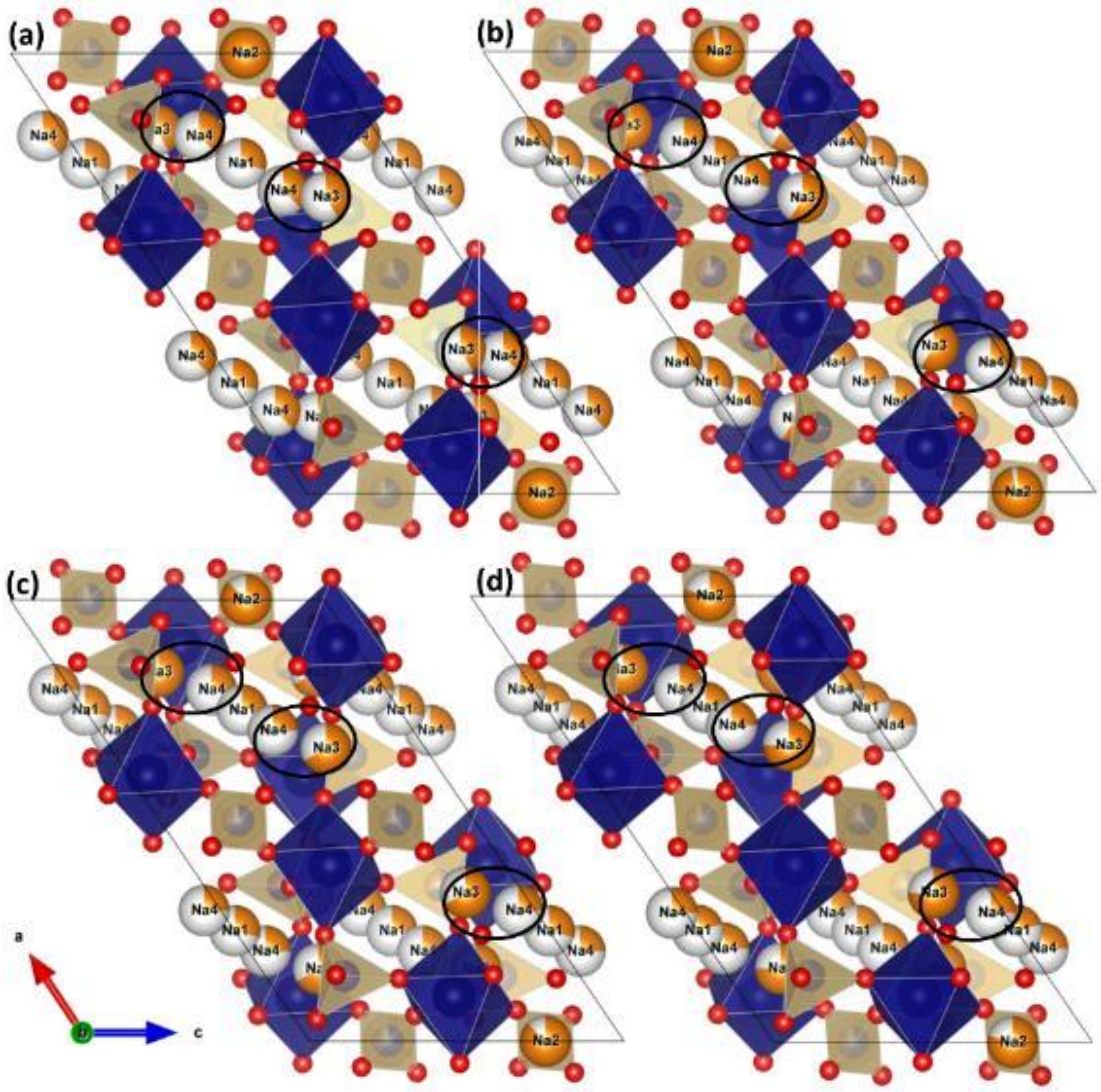

Fig.6.16: Crystal structure of refined NZSP 4Na C2/c at a) 25°C b) 100°C c)150°C and d) 350°C (Images drawn on Vesta using refinement cif files)

Furthermore, the degree of displacement of Na3 increases with the increase in temperature, from 25 to 350°C. This elevation in temperature not only intensifies the electrostatic repulsion but also leads to an alteration in the size of the bottleneck within the structure.

6.3.2 NZS24P

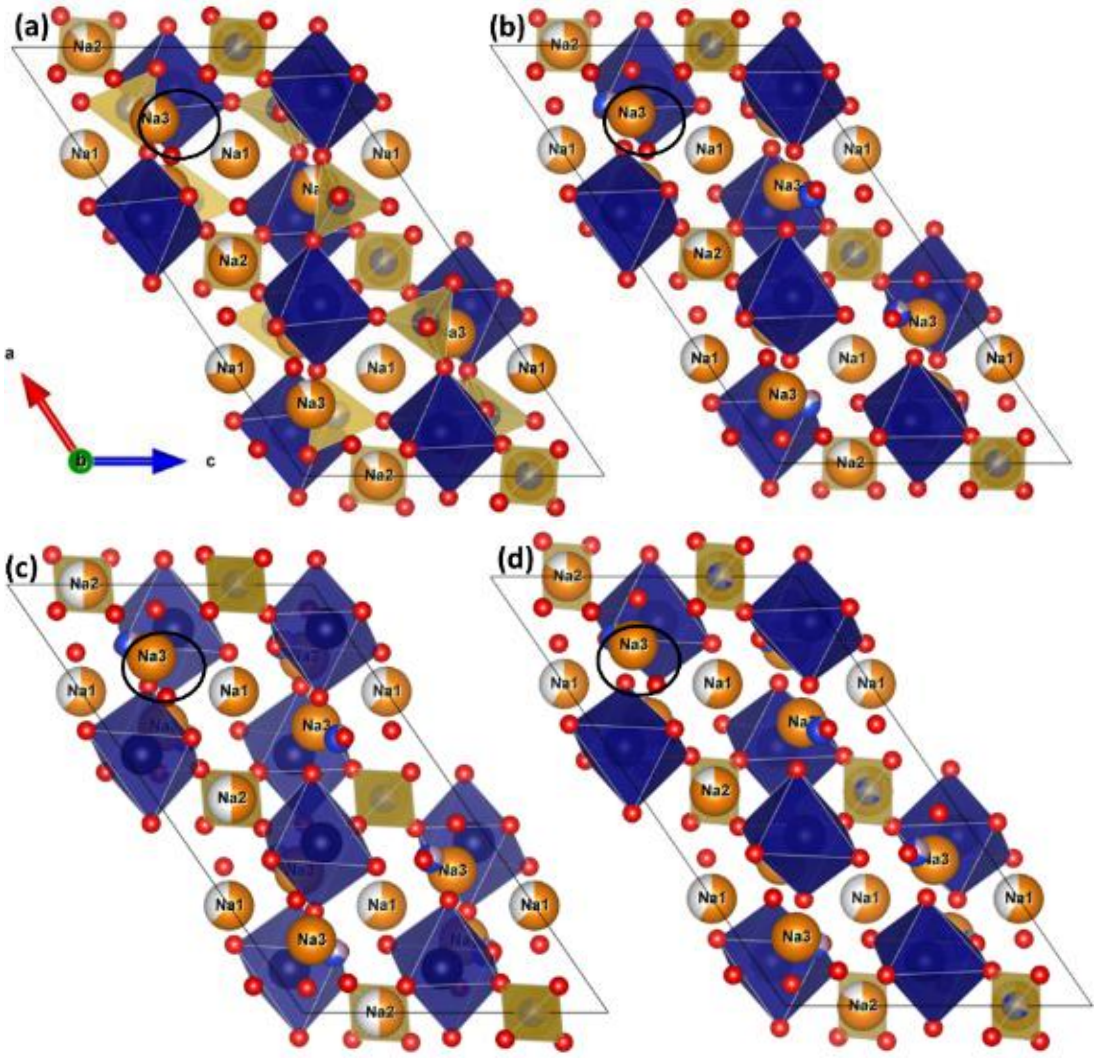

Fig.6.17: Crystal structure of refined NZS24P 3Na C2/c at a) 25°C b) 100°C c) 150°C and d) 350°C (Images drawn on Vesta using refinement cif files)

For the 3Na C2/c modelling of NZS24P (Fig.6.17:), a pattern analogous to the previously seen Na3 displacement was observed. However, at 100°C, certain SiO_4/PO_4 tetrahedra vanished from the structure, casting doubts on the model's reliability.

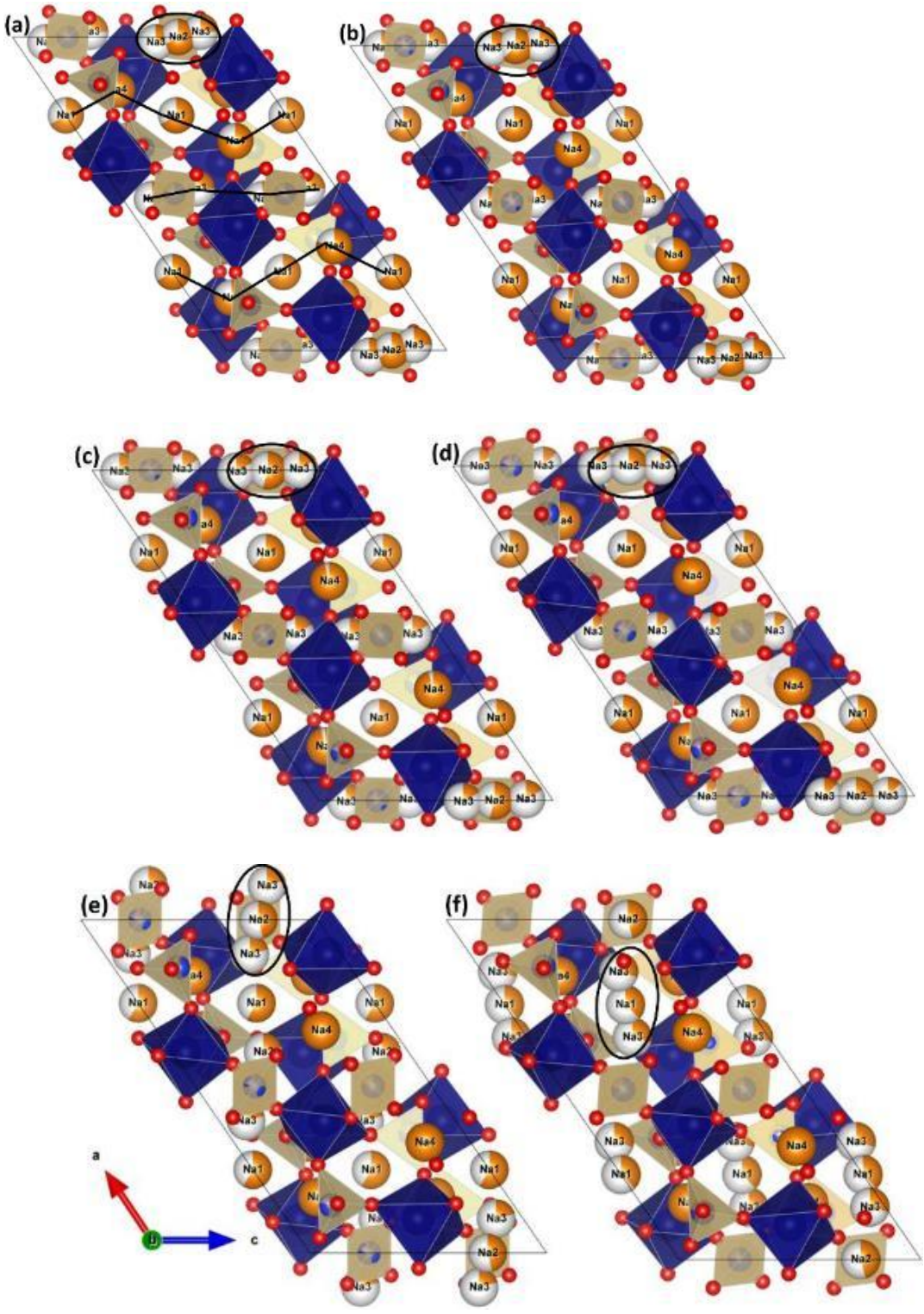

Fig.6.18: Crystal structure of refined NZS24P 4Na C2/c at a) 25°C b) 100°C c) 125°C d)150°C, e) 175°C and d) 350°C (Images drawn on Vesta using refinement cif files)

Fig.6.18: showed the 4Na model for NZS24P, which exhibits a distinct diffusion pathway, Na4-Na1-Na4, and accompanying atomic arrangement modifications across a range of temperatures.

Unlike the 3Na model, no vanishing tetrahedral structures were observed in this model. The introduction of a higher sodium content had a significant impact on the activity of the Na4 site, leading to modifications in the diffusion pathway, as demonstrated in the shifting Na ion placement depicted in

Fig.6.18: (e) and (f). However, these significant alterations in sodium diffusion and ion arrangements did not compromise the structural integrity of the SiO_4/PO_4 and ZrO_6 skeletal framework, which remained robust throughout the experimental temperature variations. Making the 4Na a more reliable model for the structure.

6.3.3 SS_NCO

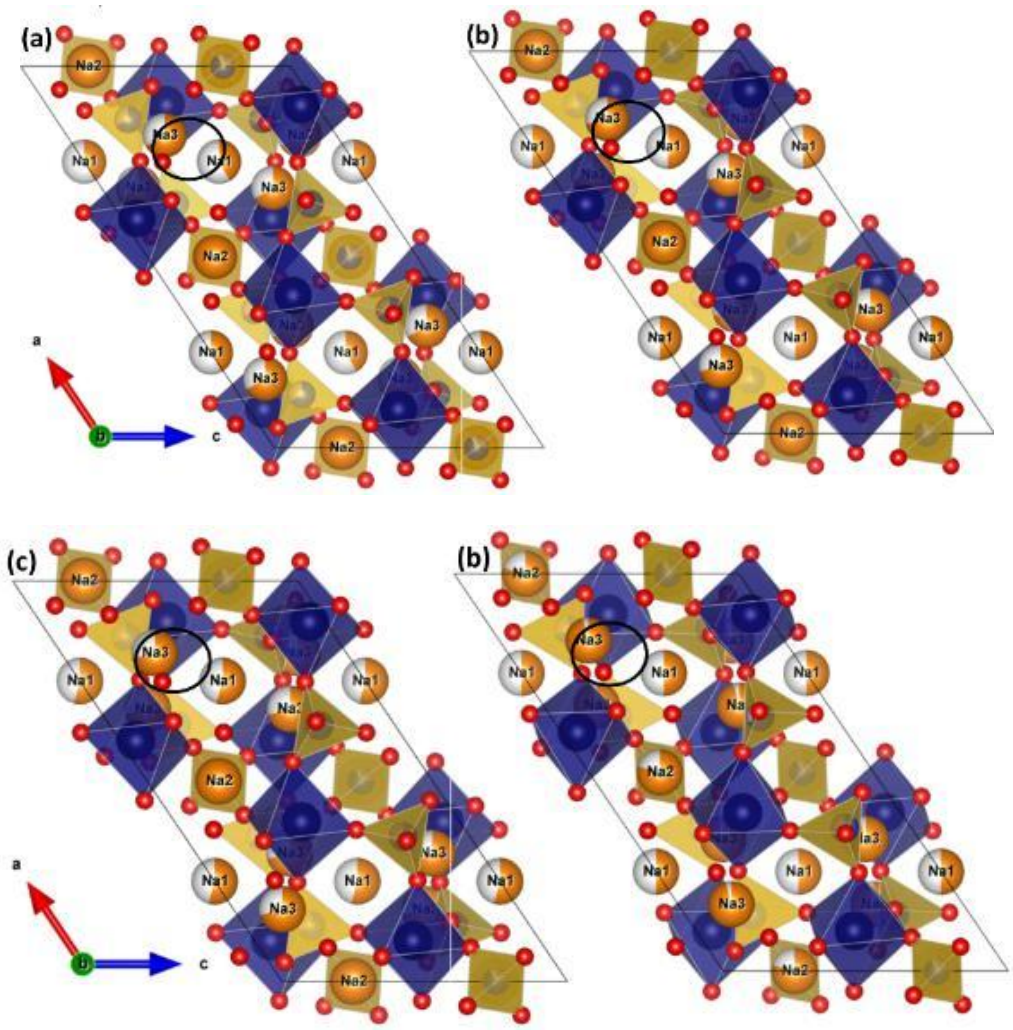

Fig.6.19: Crystal structure of refined SS_NCO 3Na C2/c at a) 25°C b) 100°C c)150°C and d) 350°C (Images drawn on Vesta using refinement cif files)

SS_NCO demonstrates a pattern similar to that observed in NZSP. As depicted in

Fig.6.19:, the main diffusion routes identified are Na3-Na1-Na3 and Na1-Na2-Na1. When the temperature is raised from 25 to 350°C, significant changes become apparent in both the dimensions of the bottleneck and the movement of Na3 within the crystal lattice. The displacement of Na3 increases with temperatures.

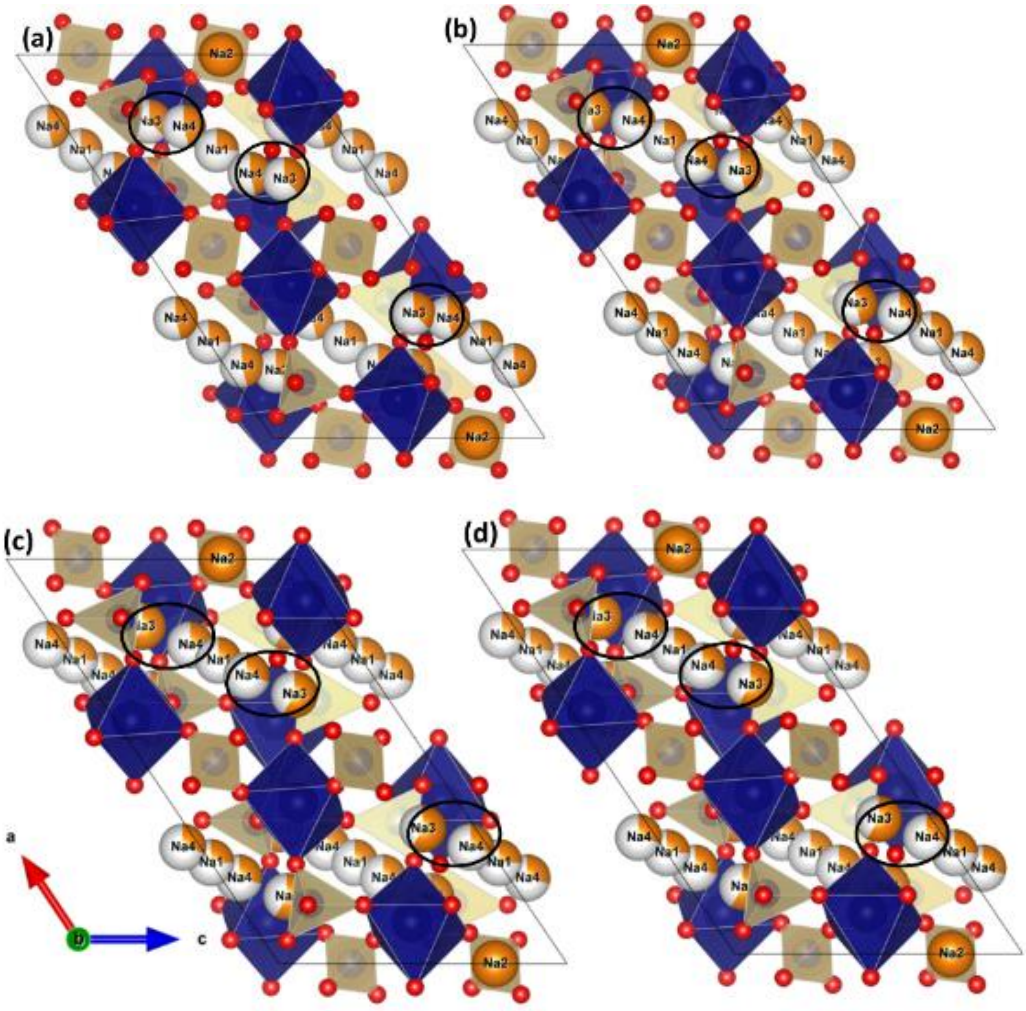

Fig.6.20: Crystal structure of refined SS_NCO 4Na C2/c at a) 25°C b) 100°C c)150°C and d) 350°C (Images drawn on Vesta using refinement cif files)

Fig.6.20: shows the structures of 4Na SS_NCO, which is similar to that of 4Na NZSP. This model depicts wider bottlenecks within the crystal structure. In this configuration, the diffusion pathways follow the sequence Na3-Na1-Na3, with the inclusion of an additional Na4 atom, resulting in the sequential arrangement of Na4-Na1-Na4-Na3, also the pathway Na1-Na2-Na1. The close proximity of Na1 and Na4, reduces the likelihood of simultaneous occupancy due to high electrostatic repulsion forces. The increased electrostatic repulsion in this scenario serves two purposes. Firstly, it promotes correlated migration by ensuring that either Na1 or Na4 is readily available

for diffusion within the pathway at any given time. Secondly, it propels the displacement of Na3, which is of particular significance given Na3's typically close proximity to Na4 and its contribution to the efficient diffusion of ions.

6.4 Local Dynamics

Insights into the local dynamics of Na^+ was drawn using ^{23}Na NMR line shape and motional narrowing and the ^{23}Na NMR spin lattice relaxometry. The temperature-dependent quadrupolar echo experiment serves as a method for analysing motion processes taking place within millisecond timescales[118]. Motions occurring during these periods result in the progressive narrowing of the central transition. This broadening is particularly notable at the "rigid-lattice" limit (at low temperatures) due to both dipolar interaction and chemical shift anisotropy. With a rise in temperature, the accelerated motion of Na+ ions, and consequently, Na nuclei, averages out the distribution of these interactions, leading to the emergence of a more focused signal[118].

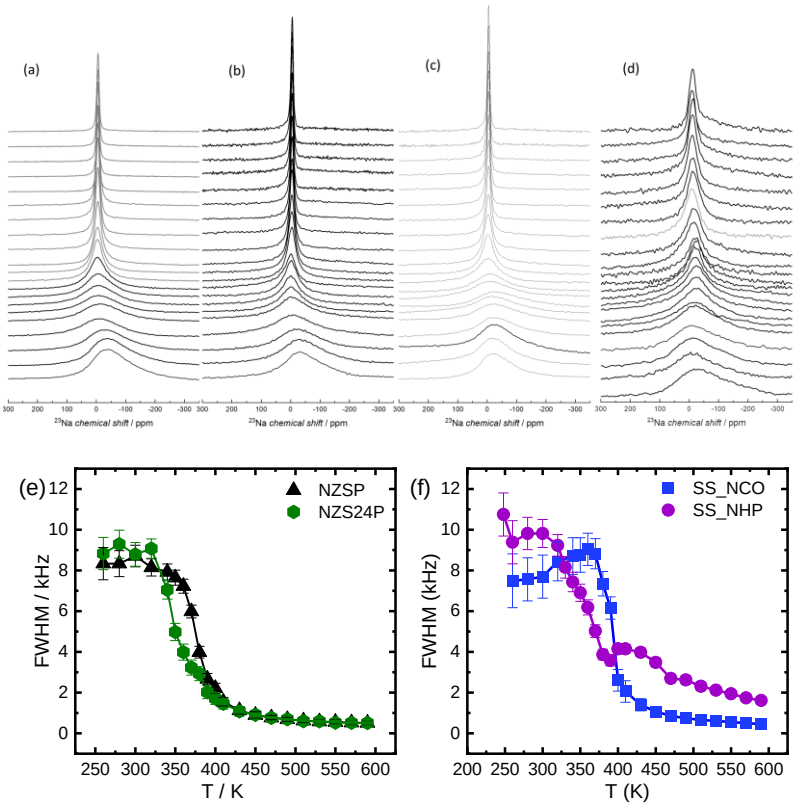

Fig.6.21: line shape evolution of a) NZSP, b) NZS24P, c) SS_NCO , d) SS_NHP and FWHM showing the motion narrowing in e) NZSP, NZS24P, and f) SS_NCO and SS_NHP

The temperature-dependent static ^{23}Na NMR spectra were collected between 260 and 595 K for the 4 samples. Fig.6.21: displays the FWHM evolution with temperature of the line shape. NZSP

and NZS24P showed a similar trend followed closely by SS_NCO, and SS_NHP showed a different trend. The line shapes for the spectra of NZSP, SS_NCO, and NZS24P contain a broad line with a full width at half maximum (FWHM) above 8 kHz at 260 K and the peaks become narrower and are shifted to lower ppm values above 400 K, in SS_NHP the FWHM values observed around 400K were not as low as in the other samples. Additionally, a shoulder at the right side of the resonance is formed. At elevated temperatures, the faster motion of the Na^+ ions result in an averaging of the local sodium environments and causes the motional narrowing of the line shapes which makes the FWHM decrease to lower values at 595 K.

The temperature-dependent results also display a shift to lower ppm of the resonance. On the contrary, for SS_NHP, narrowing begins earlier (~350 K) but proceeds more gradually, which shows a sharper drop. This gradual change may suggest differences in activation energy for ion hopping, or the influence of unidentified secondary phase/phase transition affecting local environments. The difference is more pronounced above ~400 K. The evolution of the linewidth as a function of temperature in a large temperature range, could be described by 3 distinct regions[118]: (i) A level plateau observed at lower temperatures, representing the rigid-lattice limit and highlighting the structural characteristics of the material. (ii) A temperature-driven, gradual narrowing of the width initiated when the motion rate matches the low-temperature width of the signal. (iii) The high-temperature plateau characterized by rapid motions, where only the field inhomogeneity plays a role in determining the line width[118].

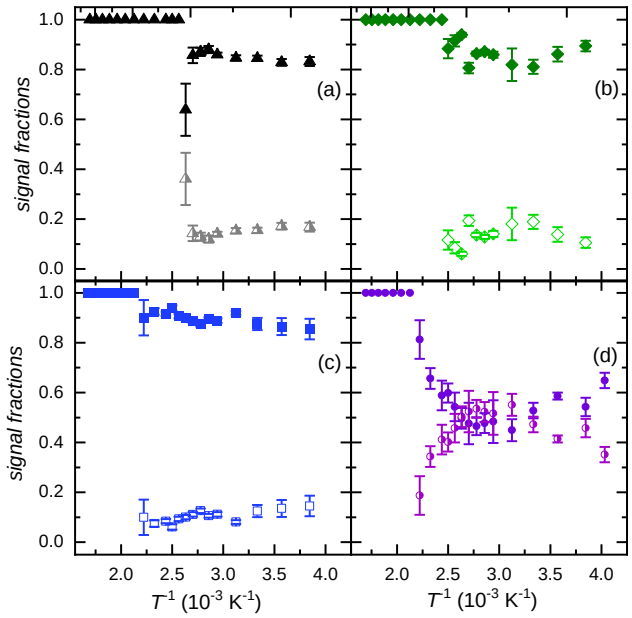

Fig.6.22: Signal Fraction evolution of a) NZSP, b) NZS24P, c) SS_NCO, d) SS_NHP

When all regions are present, it becomes feasible to determine the activation energy (E_a) of the motion based on the experimentally observed initiation of the narrowing. While this 3 region description applies to NZSP, NZS24P, and SS_NCO, SS_NHP shows a more gradual decrease in linewidth starting already at ~300 K and no well-defined low-temperature plateau. The absence

of a sharp inflection point suggests that multiple processes contribute to Na mobility in SS_NHP, potentially including the influence of secondary phase or broadened phase transition. Consequently, the standard three-region model was cautiously applied to SS_NHP, and activation energy extraction based on the onset of narrowing is less reliable for this sample. Various methods exist for quantifying these experimental findings, and one such approach is the phenomenological method developed by Bloembergen-Purcell Pound theory (BPP theory).

The local hopping of the Na^+ ions was evaluated from the relaxation times T1 using an inversion recovery pulse sequence. These relaxation times are sensitive to motions on time scales τ of the order of the inverse Larmor frequency (ωL^{-1} ~ few ns)[164]. The temperature dependence of the relaxation rate T_1^{-1} according to the Bloembergen-BPP theory) is given by eqn 2.20. The temperature-dependent signal fractions and results of the relaxation rates T_1^{-1} are shown in Fig.6.22: and Fig.6.23:.

At lower temperatures, two distinct relaxation components are observed, which merge into a single component at higher temperatures. This behaviour likely reflects Na^+ ions in different dynamic or structural environments, such as variations in site occupancy, short-range ordering, or correlated hopping, which become indistinguishable once thermal motion increases. The relative weights of the two components are similar for NZSP, NZS24P, and SS_NCO, whereas SS_NHP shows a different distribution.

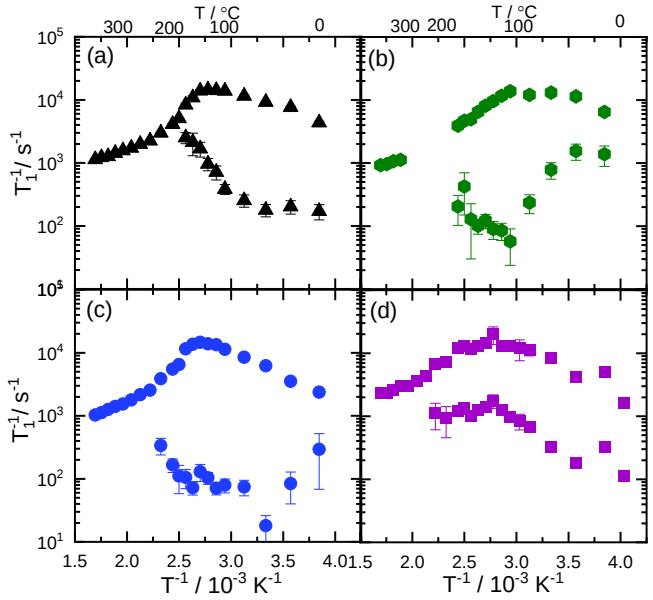

Fig.6.23: NMR lattice relaxation showing the two motions in (a) NZSP (b) NZS24P (c) SS_NCO (d) SS_NHP

The log T_1^{-1} versus T^{-1} curves show broad maxima, consistent with thermally activated Na^+ motion. In an ideal BPP-type process, symmetry of the log (T_1^{-1}) versus T^{-1} plot curve about the peak would indicate identical activation energies for the processes on both the low- and high-temperature sides. In the present case, the peaks are not perfectly symmetric, indicating that different correlation times or overlapping motional processes dominate in the two regimes. This asymmetry

suggests that Na^+ dynamics are influenced by more than one hopping process or by variations in local structural environments, rather than a single uniform activation barrier governing the entire temperature range.

From 260 K, two relaxation rates are observed in NZSP, NZS24P, and SS_NCO, which collapse into one around ~393 K, ~413 K, and ~473 K, respectively. SS_NHP maintains two components up to ~473 K but with a different relative weighting (~50% each) compared to ~80% for the faster component in the other samples. Above the collapse temperature, only a single relaxation rate is observed.This behaviour indicates that Na^+ ions experience at least two different dynamic or structural environments at low temperatures, which become dynamically averaged at higher temperatures.

While this does not conclusively prove the presence of two separate diffusive mechanisms, comparison with Na site occupancy trends from the variable-temperature diffraction refinements (Fig.6.13:) reveals a correlation: the temperature range over which the relaxation components merge coincides with significant redistribution of Na^+ among the Na1, Na2, and Na3 sites. For NZSP, NZS24P, and SS_NCO, the collapse temperature corresponds to an increase in Na3 occupancy at the expense of Na1 and Na2 sites, consistent with increased mobility via a common conduction pathway. SS_NHP, by contrast, shows a slower and more gradual change in site occupancies, which may explain its broader two-component regime in T_1^{-1} relaxometry. This combined structural and NMR evidence supports the interpretation that the merging of relaxation components reflects thermally driven homogenisation of Na^+ dynamics through site redistribution, although other effects such as correlated hopping or microstructural heterogeneity cannot be excluded.

The faster relaxation components were fitted with the BPP and Arrhenius models, yielding temperature-dependent activation energies (Fig.6.24:). These values agree with the activation energies from high-temperature conductivity, whereas the higher activation energies from low-temperature conductivity measurements indicate additional grain-boundary contributions not probed by NMR relaxometry, which is sensitive to local motions in the sub-μs regime.

6.5 Correlation between XRD, NMR and EIS

The activation energy obtained from the EIS and NMR are shown in Fig.6.24:, and a good agreement is observed between the two methods. The EIS values of activation energies were higher, which is attributable to the great influence of composition and sintering temperature on the conductivity of the NaSICON samples.

The activation energies obtained from EIS and NMR for the investigated samples are compared in Fig. 6.24. While both techniques show the same relative trend across the compositions—SS_NCO having the lowest values and SS_NHP the highest—there is a difference in magnitude. In all cases, the activation energies from EIS are higher than those from NMR. This discrepancy is expected because the two techniques probe ion dynamics on different timescales and length scales. NMR T_1^{-1} relaxometry is sensitive to local Na^+ hopping in the sub-microsecond regime,

while EIS measures long-range charge transport over macroscopic distances, which is additionally influenced by microstructural features such as grain boundaries and secondary phases. Consequently, EIS captures additional resistive contributions absent in the NMR, leading to higher apparent activation energies.

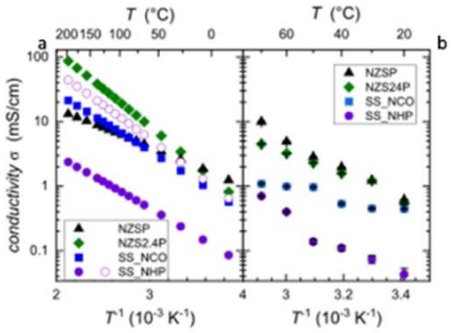

	$E_{a,NMR}$ / eV	$E_{a,EIS}$ / eV
NZSP	0.15 ± 0.02	0.57 ± 0.03
NZS24P	0.26 ± 0.02	0.32 ± 0.03
SS_NCO	0.21 ± 0.02	0.18 ± 0.08
SS_NHP	0.20 ± 0.02 0.24 ± 0.04	0.61 ± 0.04

Fig.6.24: Arrhenius plots obtained from (a) NMR and (b) EIS with corresponding activation energies for the samples from the two techniques.

In the NMR analysis, two distinct relaxation components were observed at low temperatures, which merge into a single component upon heating. These components likely correspond to Na^+ ions residing in different local structural or dynamic environments rather than proving the existence of two separate diffusive mechanisms. The temperature range over which this merging occurs correlates with significant changes in Na site occupancies determined from variable-temperature XRD refinements using the 4Na model.

At low temperatures, Na1 occupancy is low, with Na2 populated, while Na3 and Na4 occupancies are comparatively low. As temperature increases, Na1 and Na2 occupancies decrease, accompanied by a pronounced increase in Na3 and a more gradual increase in Na4 occupancy. This redistribution becomes most pronounced in NZSP, NZS24P, and SS_NCO near the temperatures at which their NMR relaxation components merge, suggesting that site exchange and dynamic averaging are closely linked. SS_NHP, which maintains higher Na1/Na2 occupancies and shows slower Na3/Na4 population growth over the same temperature range, also displays a broader two-component regime in the NMR data and the highest activation energies from both techniques.

This correlation indicates that the onset of enhanced long-range Na^+ mobility is associated with thermally activated occupation of Na3 and Na4 sites, which likely participate in interconnected conduction pathways.

7 Summary and Outlook

In this study, a high- energy milling method was introduced to synthesize the NaSICON solid electrolyte. First, the method was compared with conventional solid-state and sol–gel methods, and it shows high potential for control, optimization and scaling up in NaSICON synthesis. Through a comparative study between the commonly reported methods with high-energy ball milling (HEM), it was observed that by initiating reactions during the milling stage, the use of high-energy milling improved the NaSICON conversion process. Correspondingly, processing time and steps were successfully reduced: from a six-step conventional solid-state reaction to a three-step process and from 24 h milling to 3 h with HEM. The formation of a pure NaSICON structure with HEM at 900°C during the comparative analysis was attained. The pure monoclinic phase was formed when the calcination temperature was increased to 1100°C to improve densification. The high-energy pre-treatment by HEM enhanced the reactivity of ZrO_2, and a high-purity phase was obtained after sintering at 1280°C for 6 h. Furthermore, the NaSICON obtained via HEM exhibits promising cycling stability ($1mAcm^{-2}$) against sodium metal and has high potential for reproducibility. This opens an alternative route for NaSICON synthesis.

The potential of high-energy milling in starting nucleation of NaSICON due to a combined effect of impact and initial reaction was revealed by SEM. In summary, a facile synthesis technique was presented for the synthesis of NaSICON-type $Na_3Zr_2Si_2PO_{12}$ solid electrolytes. The HEM offers the advantage of initiating early reactions; this, coupled with the thermodynamic forces and kinetics of different sintering conditions, gave rise to different morphologies. To optimise the process further, a combined treatment schedule was studied under different conditions. The role of sintering conditions on micro-structure, density, phases and conductivity of the system were investigated. The dependence of the conductivity on the micro-structure, density and over-potential for the sintering conditions was also established. The effects of sintering with different heating/cooling rates, in air, in argon, in nitrogen, varying starting powder size and quenching in air, water and nitrogen were studied. The effect of large particle sizes in promoting amorphous phase was established. The −45μm NZSP sample sintered at 1280°C for 6 h was shown to exhibit the highest density and most compact micro-structure and it achieved a 22.2% increase in conductivity of ($\sim 2.2 \times 10^{-3} Scm^{-1}$). A composite of the NZSP membrane was developed and the NZSP membrane exhibited good electrochemical stability and good interfacial stability versus Na metal. These results indicate that HEM offers an easy and straightforward NaSICON processing route.

Furthermore, the effects of Mg and Mo dopants on HEM NaSICON were studied. Mo was found to have limited solubility and promote grain growth and densification, while Mg incorporate in the NaSICON phase not in the Na_3PO_4 phase, it also increased densification. Increasing the amount of sodium in the NaSICON structure through doping of the zirconium and phosphorus sites with Mg/Mo enhanced bulk conductivity. The increased number of sodium charge carriers in the lattice and a charge imbalance of the zirconium site are directly related to improved ionic

mobility. The presence of Mo in the lattice increased the size of the structural bottleneck; however, because of its limited solubility in the phase and the large ionic radius compared to P, the highest conductivity was observed for Mo0.05. Mo and Mg doping led to slight increase in conductivity.

High-temperature XRD and lattice spin NMR relaxometry were used to study the dynamics of Na in NaSICON ($Na_3Zr_2Si_2PO_{12}$) synthesised through different routes and $Na_{3.4}Zr_2Si_{2.4}P_{0.6}O_{12}$ using HEM. NZSP, NZS24P, SS_NCO crystallized in the monoclinic C2/c phase and SS_NHP in the rhombohedral. Due to the controversy surrounding the number of Na positions in the sodium sub lattice of the Monoclinic NaSICON, the 3Na C2/c and 4Na C2/c Models were used for Full-Prof Rietveld refinement. A mid temperature (100°C-200°C) region of structural alteration characterised by increasing values of all parameters was observed. The existence of the purported high temperature monoclinic to rhombohedral phase transition within this region was checked by probing the reliability and reversibility (of parameters when modelled with the two structures in opposite directions) of refinement with the monoclinic phase from room temperature to high temperature and the rhombohedral 3Na R-3c from high temperature to room temperature. Though The 3Na C2/c and 3Na R-3c show similar trends in opposite direction of low reliability parameters at the start of refinement which increases around the regions of observed structural alteration, the irreversibility of the parameters in both direction and the stability of the 4Na C2/c beyond the region casts a doubt on the purported transition. The Rietveld refinement showed better fitting of the data with the 4Na C2/c model than with the 3Na model. With the C2/c and R-3c increase in lattice parameters with temperature was observed. A corresponding increase in the volume of the unit cell was observed. The fractions of the phases were similar in all models and pronounced changes in the refinement parameters in the intermediate (100–200°C) were observed. Through visualisation, displacement of the Na positions and position rearrangements were observed. Thus, the observed structure alteration could be attributed to lattice distortion, high electrostatic repulsion due to proximity of the atom positions. The NMR showed a similar trend of structural alterations observed on the HT_XRD. Two Na motions one fast and the second slow having an 80:20 ratio and attributed to the diffusion paths were observed. The fast motion was attributed to the main diffusion path and the slow motion to the path influenced by the local compositional variation.

To dig deeper into the origin of the second diffusion path, the existence or not of a phase transition in the 4 Na C 2/c and the mid temperature structure alteration region it was planned to investigate a wider range of compositions. Six samples $Na_{1+x}Zr_2Si_xP_{3-x}O_{12}$ x = 1.8, 2, 2.2, 2.4, 2.6 and 2.8 were prepared and the analysis is ongoing. The sintering/formation mechanisms for the different compositions will be analysed. Porosimetry will be used to study the distribution of pores with composition and correlate it with the motion process at low temperature from impedance. The use of TEM to study the local compositions, atomic, electronic, crystal structure as well as space charge distribution is being explored. In the pursuit of future research endeavours, the transformative potential of thin sodium NaSICON solid electrolytes is being considered. It is anticipated that these slender electrolytes could play a pivotal role in crafting high-energy, all-solid-state batteries, promising enhanced safety, increased energy density, design flexibility and prolonged cycle life. A future where these materials contribute significantly to energy storage technology is envisioned, offering efficiency, sustainability, and readiness to meet the challenges of tomorrow.

The commitment is to uncover the untapped possibilities that thin sodium NaSICON electrolytes hold for the future of energy solutions.

References

[1] Kim H, Kim H, Ding Z, Lee MH, Lim K. Recent Progress in Electrode Materials for Sodium-Ion Batteries 2016:1–38. https://doi.org/10.1002/aenm.201600943.

[2] Melot BC, Tarascon JM. Design and preparation of materials for advanced electrochemical storage. Acc Chem Res 2013;46:1226–38. https://doi.org/10.1021/ar300088q.

[3] Karabelli D, Singh S, Kiemel S, Koller J, Konarov A. Sodium-Based Batteries : In Search of the Best Compromise Between Sustainability and Maximization of Electric Performance 2020;8:1–16. https://doi.org/10.3389/fenrg.2020.605129.

[4] Vasudevan S, Dwivedi S, Balaya P. Overview and perspectives of solid electrolytes for sodium batteries. International Journal Applied Ceramic Technology 2023;20:563–84. https://doi.org/10.1111/ijac.14267.

[5] Hou W, Guo X, Shen X, Amine K, Yu H, Lu J. Solid electrolytes and interfaces in all-solid-state sodium batteries: Progress and perspective. Nano Energy 2018;52:279–91. https://doi.org/10.1016/j.nanoen.2018.07.036.

[6] Qiao L, Judez X, Rojo T, Armand M, Zhang H. Review—Polymer Electrolytes for Sodium Batteries. J Electrochem Soc 2020;167:070534. https://doi.org/10.1149/1945-7111/ab7aa0.

[7] Vineeth SK, Tebyetekerwa M, Liu H, Soni CB, Sungjemmenla N, Zhao XS, et al. Progress in the development of solid-state electrolytes for reversible room-temperature sodium-sulfur batteries. Mater Adv 2022;2:6415–40. https://doi.org/10.1039/d2ma00428c.

[8] Tuo K, Sun C, Liu S. Recent Progress in and Perspectives on Emerging Halide Superionic Conductors for All-Solid-State Batteries. vol. 6. Springer Nature Singapore; 2023. https://doi.org/10.1007/s41918-023-00179-5.

[9] Slater MD, Kim D, Lee E, Johnson CS. Sodium-ion batteries. Adv Funct Mater 2013;23:947–58. https://doi.org/10.1002/adfm.201200691.

[10] Ellis BL, Nazar LF. Sodium and sodium-ion energy storage batteries. Curr Opin Solid State Mater Sci 2012;16:168–77. https://doi.org/10.1016/j.cossms.2012.04.002.

[11] Deng J, Luo W Bin, Chou SL, Liu HK, Dou SX. Sodium-Ion Batteries: From Academic Research to Practical Commercialization. Adv Energy Mater 2018;8. https://doi.org/10.1002/aenm.201701428.

[12] Murat Yavuz. Investigation of local and Average structure in Li-ion battery electrode materials by x ray diffraction. Technische Universität Darmstadt doi: 10.26083/tuprints-00005271 2016 .

[13] Masoumi M. Thermochemical and electrochemical investigations of Li (Ni,Mn,Co)O_2 (NMC) as positive electrode material for lithium-ion batteries. Karlsruher Instituts für Technologie doi: 10.5445/IR/1000126623 2020;2.

[14] Lin Z, Liu T, Ai X, Liang C. Aligning academia and industry for unified battery

performance metrics. Nat Commun 2018:8–12. https://doi.org/10.1038/s41467-018-07599-8.

[15] Bublil S, Peta G, Fayena-Greenstein M, Alon-Yehezkel H, Raskin O, Elias Y, et al. Electrochemical Methods of Transference Number Determination for Polymer Electrolyte Systems: A Comparative Study. J Electrochem Soc 2022;169:110523. https://doi.org/10.1149/1945-7111/ac9f75.

[16] Shao Y, Gudla H, Brandell D, Zhang C. Transference Number in Polymer Electrolytes: Mind the Reference-Frame Gap. J Am Chem Soc 2022;144:7583–7. https://doi.org/10.1021/jacs.2c02389.

[17] Adelhelm P, Hartmann P, Bender CL, Busche M, Eufinger C, Janek J. From lithium to sodium: Cell chemistry of room temperature sodium-air and sodium-sulfur batteries. Beilstein J Nanotechnol 2015;6:1016–55. https://doi.org/10.3762/bjnano.6.105.

[18] Bauer A, Song J, Vail S, Pan W, Barker J, Lu Y. The Scale-up and Commercialization of Nonaqueous Na-Ion Battery Technologies. Adv Energy Mater 2018;8. https://doi.org/10.1002/aenm.201702869.

[19] Delmas C. Sodium and Sodium-Ion Batteries: 50 Years of Research. Adv Energy Mater 2018;8. https://doi.org/10.1002/aenm.201703137.

[20] Yung-Fang Yu Yao, Kummer JT. Ion exchange properties of and rates of ionic diffusion in beta-alumina. J Inorg Nucl Chem 1967;29. https://doi.org/10.1016/0022-1902(67)80301-4.

[21] Zhu W, Akbar SA. Mixed conduction in β-alumina type materials: a critical review. J Mater Process Tech 1993;38:15–27. https://doi.org/10.1016/0924-0136(93)90182-6.

[22] Zyl A Van. Review of the zebra battery system development. Solid State Ionics 1996;86–88:883–9.

[23] Tang K, Ren Y. Practical Application of Room Temperature Na-Ion Batteries. Sodium-Ion Batter 2022:531–49. https://doi.org/10.1002/9783527825769.ch16.

[24] Sayahpour B, Hirsh H, Parab S, Nguyen LHB, Zhang M, Meng YS. Perspective: Design of cathode materials for sustainable sodium-ion batteries. MRS Energy Sustain 2022;XX:1–15. https://doi.org/10.1557/s43581-022-00029-9.

[25] https://northvolt.com/articles/northvolt-sodium-ion/.

[26] Kanwade A, Gupta S, Kankane A, Srivastava A, Yadav SC, Shirage PM. Phosphate-based cathode materials to boost the electrochemical performance of sodium-ion batteries. Sustain Energy Fuels 2022;6:3114–47. https://doi.org/10.1039/d2se00475e.

[27] Oh JAS, He L, Plewa A, Morita M, Zhao Y, Sakamoto T, et al. Composite NaSICON ($Na_3Zr_2Si_2PO_{12}$) Solid-State Electrolyte with Enhanced Na+ Ionic Conductivity: Effect of Liquid Phase Sintering. ACS Appl Mater Interfaces 2019;11:40125–33. https://doi.org/10.1021/acsami.9b14986.

[28] Hwang JY, Myung ST, Sun YK. Sodium-ion batteries: Present and future. Chem Soc Rev 2017;46:3529–614. https://doi.org/10.1039/c6cs00776g.

[29] Gupta P, Pushpakanth S, Haider MA, Basu S. Understanding the Design of Cathode

Materials for Na-Ion Batteries. ACS Omega 2022;7:5605–14. https://doi.org/10.1021/acsomega.1c05794.

[30] Zhang J, Li J, Wang H, Wang M. Research progress of organic liquid electrolyte for sodium ion battery. Front Chem 2023;11:1–22. https://doi.org/10.3389/fchem.2023.1253959.

[31] Klemens J, Wurba AK, Burger D, Müller M, Bauer W, Büchele S, et al. Challenges and Opportunities for Large-Scale Electrode Processing for Sodium-Ion and Lithium-Ion Battery. Batter Supercaps 2023;202300291. https://doi.org/10.1002/batt.202300291.

[32] Shi C, Wang L, Chen X, Li J, Wang S, Wang J, et al. Challenges of layer-structured cathodes for sodium-ion batteries. Nanoscale Horizons 2021;7:338–51. https://doi.org/10.1039/d1nh00585e.

[33] Akçay T, Häringer M, Pfeifer K, Anhalt J, Binder JR, Dsoke S, et al. $Na_3V_2(PO_4)_3$-A Highly Promising Anode and Cathode Material for Sodium-Ion Batteries. ACS Appl Energy Mater 2021;4:12688–95. https://doi.org/10.1021/acsaem.1c02413.

[34] Shraer SD, Luchinin ND, Trussov IA, Aksyonov DA, Morozov A V., Ryazantsev S V., et al. Development of vanadium-based polyanion positive electrode active materials for high-voltage sodium-based batteries. Nat Commun 2022;13:1–10. https://doi.org/10.1038/s41467-022-31768-5.

[35] Lv Z, Ling M, Yue M, Li X, Song M, Zheng Q, et al. Vanadium-based polyanionic compounds as cathode materials for sodium-ion batteries: Toward high-energy and high-power applications. J Energy Chem 2021;55:361–90. https://doi.org/10.1016/j.jechem.2020.07.008.

[36] Maddar FM, Walker D, Chamberlain TW, Compton J, Menon AS, Copley M, et al. Understanding dehydration of Prussian white: from material to aqueous processed composite electrodes for sodium-ion battery application. J Mater Chem A 2023;11:15778–91. https://doi.org/10.1039/d3ta02570e.

[37] Insinna T, Bassey EN, Märker K, Collauto A, Barra AL, Grey CP. Graphite Anodes for Li-Ion Batteries: An Electron Paramagnetic Resonance Investigation. Chem Mater 2023;35:5497–511. https://doi.org/10.1021/acs.chemmater.3c00860.

[38] Perveen T, Siddiq M, Shahzad N, Ihsan R, Ahmad A, Shahzad MI. Prospects in anode materials for sodium ion batteries - A review. Renew Sustain Energy Rev 2020;119:109549. https://doi.org/10.1016/j.rser.2019.109549.

[39] Au H, Alptekin H, Jensen ACS, Olsson E, O'Keefe CA, Smith T, et al. A revised mechanistic model for sodium insertion in hard carbons. Energy Environ Sci 2020;13:3469–79. https://doi.org/10.1039/d0ee01363c.

[40] Pereira da Silva JG, Bram M, Laptev AM, Gonzalez-Julian J, Ma Q, Tietz F, et al. Sintering of a sodium-based NASICON electrolyte: A comparative study between cold, field assisted and conventional sintering methods. J Eur Ceram Soc 2019;39:2697–702. https://doi.org/10.1016/j.jeurceramsoc.2019.03.023.

[41] Hasa I, Mariyappan S, Saurel D, Adelhelm P, Koposov AY, Masquelier C, et al. Challenges of today for Na-based batteries of the future: From materials to cell metrics. J Power Sources 2021;482. https://doi.org/10.1016/j.jpowsour.2020.228872.

[42] Thompson M, Xia Q, Hu Z, Zhao XS. A review on biomass-derived hard carbon materials for sodium-ion batteries. Mater Adv 2021;2:5881–905. https://doi.org/10.1039/d1ma00315a.

[43] Mittal U, Djuandhi L, Sharma N, Andersen HL. Structure and function of hard carbon negative electrodes for sodium-ion batteries. JPhys Energy 2022;4. https://doi.org/10.1088/2515-7655/ac8dc1.

[44] Ponrouch A, Marchante E, Courty M, Tarascon JM, Palacín MR. In search of an optimized electrolyte for Na-ion batteries. Energy Environ Sci 2012;5:8572–83. https://doi.org/10.1039/c2ee22258b.

[45] Lu Y, Li L, Zhang Q, Niu Z, Chen J. Electrolyte and Interface Engineering for Solid-State Sodium Batteries. Joule 2018;2:1747–70. https://doi.org/10.1016/j.joule.2018.07.028.

[46] Armand M, Endres F, MacFarlane DR, Ohno H, Scrosati B. Ionic-liquid materials for the electrochemical challenges of the future. Nat Mater 2009;8:621–9. https://doi.org/10.1038/nmat2448.

[47] Niu Y Bin, Yin YX, Guo YG. Nonaqueous Sodium-Ion Full Cells: Status, Strategies, and Prospects. Small 2019;15:1–27. https://doi.org/10.1002/smll.201900233.

[48] Sawicki M, Shaw LL. Advances and challenges of sodium ion batteries as post lithium ion batteries. RSC Adv 2015;5:53129–54. https://doi.org/10.1039/c5ra08321d.

[49] Wang J, Lu H, Zhang J, Li S. Improved Interfacial Property of $Na_3V_2(PO_4)_3$@C Cathode: Application of NaODFB-Based Ether Electrolyte in Sodium-Ion Batteries. J Electrochem Energy Convers Storage 2023;20. https://doi.org/10.1115/1.4054389.

[50] Xu K. Electrolytes and interphases in Li-ion batteries and beyond. Chem Rev 2014;114:11503–618. https://doi.org/10.1021/cr500003w.

[51] Wang E, Niu Y, Yin YX, Guo YG. Manipulating Electrode/Electrolyte Interphases of Sodium-Ion Batteries: Strategies and Perspectives. ACS Mater Lett 2021;3:18–41. https://doi.org/10.1021/acsmaterialslett.0c00356.

[52] Zhang SS. A review on electrolyte additives for lithium-ion batteries. J Power Sources 2006;162:1379–94. https://doi.org/10.1016/j.jpowsour.2006.07.074.

[53] Goodenough JB, Kim Y. Challenges for rechargeable Li batteries. Chem Mater 2010;22:587–603. https://doi.org/10.1021/cm901452z.

[54] Zhu Y, Luo X, Zhi H, Yang X, Xing L, Liao Y, et al. Structural Exfoliation of Layered Cathode under High Voltage and Its Suppression by Interface Film Derived from Electrolyte Additive. ACS Appl Mater Interfaces 2017;9:12021–34. https://doi.org/10.1021/acsami.7b00032.

[55] Ponrouch A, Monti D, Boschin A, Steen B, Johansson P, Palacín MR. Non-aqueous electrolytes for sodium-ion batteries. J Mater Chem A 2015;3:22–42. https://doi.org/10.1039/c4ta04428b.

[56] Benchakar M, Naéjus R, Damas C, Santos-Peña J. Exploring the use of EMImFSI ionic liquid as additive or co-solvent for room temperature sodium ion battery electrolytes. Electrochim Acta 2020;330. https://doi.org/10.1016/j.electacta.2019.135193.

[57] Egashira M, Tanaka T, Yoshimoto N, Morita M. Influence of ionic liquid species in non-aqueous electrolyte on sodium insertion into hard carbon. Electrochemistry 2012;80:755–8. https://doi.org/10.5796/electrochemistry.80.755.

[58] Liu X, Jiang X, Zeng Z, Ai X, Yang H, Zhong F, et al. High Capacity and Cycle-Stable Hard Carbon Anode for Nonflammable Sodium-Ion Batteries. ACS Appl Mater Interfaces 2018;10:38141–50. https://doi.org/10.1021/acsami.8b16129.

[59] Wang Y, Song S, Xu C, Hu N, Molenda J, Lu L. Development of solid-state electrolytes for sodium-ion battery–A short review. Nano Mater Sci 2019;1:91–100. https://doi.org/10.1016/j.nanoms.2019.02.007.

[60] Deng Y, Eames C, Nguyen LHB, Pecher O, Griffith KJ, Courty M, et al. Crystal Structures, Local Atomic Environments, and Ion Diffusion Mechanisms of Scandium-Substituted Sodium Superionic Conductor (NaSICON) Solid Electrolytes. Chem Mater 2018;30:2618–30. https://doi.org/10.1021/acs.chemmater.7b05237.

[61] Guin M. Chemical and physical properties of sodium ionic conductors for solid-state batteries. vol. 373. n.d.

[62] Lalère F, Leriche JB, Courty M, Boulineau S, Viallet V, Masquelier C, et al. An all-solid state NaSICON sodium battery operating at 200°C. J Power Sources 2014;247:975–80. https://doi.org/10.1016/j.jpowsour.2013.09.051.

[63] Vignarooban K, Kushagra R, Elango A, Badami P, Mellander BE, Xu X, et al. Current trends and future challenges of electrolytes for sodium-ion batteries. Int J Hydrogen Energy 2016;41:2829–46. https://doi.org/10.1016/j.ijhydene.2015.12.090.

[64] Famprikis T, Canepa P, Dawson JA, Islam MS, Masquelier C. Fundamentals of inorganic solid-state electrolytes for batteries. Nat Mater 2019. https://doi.org/10.1038/s41563-019-0431-3.

[65] Lan T, Tsai CL, Tietz F, Wei XK, Heggen M, Dunin-Borkowski RE, et al. Room-temperature all-solid-state sodium batteries with robust ceramic interface between rigid electrolyte and electrode materials. Nano Energy 2019;65:104040. https://doi.org/10.1016/j.nanoen.2019.104040.

[66] Squires AG, Davies DW, Kim S, Scanlon DO, Walsh A, Morgan BJ. Low electronic conductivity of $Li_7La_3Zr_2O_{12}$ solid electrolytes from first principles. Phys Rev Mater 2022;6:1–12. https://doi.org/10.1103/PhysRevMaterials.6.085401.

[67] Francisco BE, Stoldt CR, M'Peko JC. Lithium-ion trapping from local structural distortions in sodium super ionic conductor (NaSICON) electrolytes. Chem Mater 2014;26:4741–9. https://doi.org/10.1021/cm5013872.

[68] Gebert F, Knott J, Gorkin R, Chou SL, Dou SX. Polymer electrolytes for sodium-ion batteries. Energy Storage Mater 2021;36:10–30. https://doi.org/10.1016/j.ensm.2020.11.030.

[69] Yang J, Zhang H, Zhou Q, Qu H, Dong T, Zhang M, et al. Safety-Enhanced Polymer Electrolytes for Sodium Batteries: Recent Progress and Perspectives. ACS Appl Mater Interfaces 2019;11:17109–27. https://doi.org/10.1021/acsami.9b01239.

[70] Yin H, Han C, Liu Q, Wu F, Zhang F, Tang Y. Recent Advances and Perspectives on the

Polymer Electrolytes for Sodium/Potassium-Ion Batteries. Small 2021;17:1–23. https://doi.org/10.1002/smll.202006627.

[71] Mohan VM, Raja V, Sharma AK, Narasimha Rao VVR. Ion transport and battery discharge characteristics of polymer electrolyte based on PEO complexed with NaFeF4 salt. Ionics (Kiel) 2006;12:219–26. https://doi.org/10.1007/s11581-006-0035-1.

[72] Peta G, Alon-Yehezkel H, Bublil S, Penki TR, Breuer O, Elias Y, et al. Influence of Salt Anions on the Reactivity of Polymer Electrolytes in All-Solid-State Sodium Batteries. J Electrochem Soc 2022;169:070530. https://doi.org/10.1149/1945-7111/ac8241.

[73] Xu X, Wang Y, Yi Q, Wang X, Paredes Camacho RA, Kungl H, et al. Ion Conduction in Composite Polymer Electrolytes: Potential Electrolytes for Sodium-Ion Batteries. ChemSusChem 2023;16. https://doi.org/10.1002/cssc.202202152.

[74] Chintapalli M, Timachova K, Olson KR, Mecham SJ, Devaux D, Desimone JM, et al. Relationship between Conductivity, Ion Diffusion, and Transference Number in Perfluoropolyether Electrolytes. Macromolecules 2016;49:3508–15. https://doi.org/10.1021/acs.macromol.6b00412.

[75] Kwak H, Wang S, Park J, Liu Y, Kim KT, Choi Y, et al. Emerging Halide Superionic Conductors for All-Solid-State Batteries: Design, Synthesis, and Practical Applications. ACS Energy Lett 2022;7:1776–805. https://doi.org/10.1021/acsenergylett.2c00438.

[76] Wan H, Mwizerwa JP, Qi X, Liu X, Xu X, Li H, et al. Core-Shell $Fe_{1-x}S@Na_{2.9}PS_{3.95}Se_{0.05}$ Nanorods for Room Temperature All-Solid-State Sodium Batteries with High Energy Density. ACS Nano 2018;12:2809–17. https://doi.org/10.1021/acsnano.8b00073.

[77] Hayashi A, Noi K, Tanibata N, Nagao M, Tatsumisago M. High sodium ion conductivity of glass-ceramic electrolytes with cubic Na_3PS_4. J Power Sources 2014;258:420–3. https://doi.org/10.1016/j.jpowsour.2014.02.054.

[78] Tatsumisago M, Nagao M, Hayashi A. Recent development of sulfide solid electrolytes and interfacial modification for all-solid-state rechargeable lithium batteries. J Asian Ceram Soc 2013;1:17–25. https://doi.org/10.1016/j.jascer.2013.03.005.

[79] Smith JG, Siegel DJ. Ion Migration Mechanisms in the Sodium Sulfide Solid Electrolyte $Na_{3-x}Sb_{1-x}W_xS_4$. Chem Mater 2022;34:4166–71. https://doi.org/10.1021/acs.chemmater.2c00526.

[80] Hayashi A, Masuzawa N, Yubuchi S, Tsuji F, Hotehama C, Sakuda A, et al. A sodium-ion sulfide solid electrolyte with unprecedented conductivity at room temperature. Nat Commun 2019;10. https://doi.org/10.1038/s41467-019-13178-2.

[81] Hong HY. Mat. Res. Bull. Vol. II, pp. 173-182 , Printed in the United States. Pergamon Crystal structures and crystal chemistry in the system $N_{l+x}Zr_2Si_xP_{3-x}O_{12}$ Lincoln Laboratory, Massachusetts Insti 1976;I:173–82.

[82] Boilot JP, Collin G, Colomban P. Relation structure-fast ion conduction in the NaSICON solid solution. J Solid State Chem 1988;73:160–71. https://doi.org/10.1016/0022-4596(88)90065-5.

[83] Li C, Li R, Liu K. NaSICON : A promising solid electrolyte for solid - state sodium batteries 2022:396–416. https://doi.org/10.1002/idm2.12044.

[84] Collin G, Comes R, Boilot JP, Colomban P. Disorder of tetrahedra in Nasicon-type structure—I. J Phys Chem Solids 1986;47:843–54. https://doi.org/10.1016/0022-3697(86)90055-7.

[85] Zhang Z, Zou Z, Kaup K, Xiao R, Shi S, Avdeev M, et al. Correlated Migration Invokes Higher Na^+-Ion Conductivity in NaSICON-Type Solid Electrolytes. Adv Energy Mater 2019;9. https://doi.org/10.1002/aenm.201902373.

[86] Zhang Z, Zou Z, Kaup K, Xiao R, Shi S, Avdeev M, et al. Correlated Migration Invokes Higher Na^+-Ion Conductivity in NaSICON-Type Solid Electrolytes. Adv Energy Mater 2019;9:1–14. https://doi.org/10.1002/aenm.201902373.

[87] Park H, Jung K, Nezafati M, Kim CS, Kang B. Sodium Ion Diffusion in Nasicon ($Na_3Zr_2Si_2PO_{12}$) Solid Electrolytes: Effects of Excess Sodium. ACS Appl Mater Interfaces 2016;8:27814–24. https://doi.org/10.1021/acsami.6b09992.

[88] Guin M, Tietz F. Survey of the transport properties of sodium superionic conductor materials for use in sodium batteries. J Power Sources 2015;273:1056–64. https://doi.org/10.1016/j.jpowsour.2014.09.137.

[89] Rao YB, Bharathi KK, Patro LN. Review on the synthesis and doping strategies in enhancing the Na ion conductivity of $Na_3Zr_2Si_2PO_{12}$ (NaSICON) based solid electrolytes. Solid State Ionics 2021;366–367:115671. https://doi.org/10.1016/j.ssi.2021.115671.

[90] Guin M, Tietz F, Guillon O. New promising NASICON material as solid electrolyte for sodium-ion batteries: Correlation between composition, crystal structure and ionic conductivity of $Na_{3+x}Sc_2Si_xP_{3-x}O_{12}$. Solid State Ionics 2016;293:18–26. https://doi.org/10.1016/j.ssi.2016.06.005.

[91] Yang J, Wan HL, Zhang ZH, Liu GZ, Xu XX, Hu YS, et al. NASICON-structured $Na_{3.1}Zr_{1.95}Mg_{0.05}Si_2PO_{12}$ solid electrolyte for solid-state sodium batteries. Rare Met 2018;37:480–7. https://doi.org/10.1007/s12598-018-1020-3.

[92] Jolley AG, Taylor DD, Schreiber NJ, Wachsman ED. Structural Investigation of Monoclinic-Rhombohedral Phase Transition in $Na_3Zr_2Si_2PO_{12}$ and doped NaSICON. J Am Ceram Soc 2015;98:2902–7. https://doi.org/10.1111/jace.13692.

[93] Samiee M, Radhakrishnan B, Rice Z, Deng Z, Meng YS, Ong SP, et al. Divalent-doped $Na_3Zr_2Si_2PO_{12}$ natrium superionic conductor: Improving the ionic conductivity via simultaneously optimizing the phase and chemistry of the primary and secondary phases. J Power Sources 2017;347:229–37. https://doi.org/10.1016/j.jpowsour.2017.02.042.

[94] Song S, Duong HM, Korsunsky AM, Hu N, Lu L. A Na+ Superionic Conductor for Room-Temperature Sodium Batteries. Sci Rep 2016;6:1–10. https://doi.org/10.1038/srep32330.

[95] Lu Y, Alonso JA, Yi Q, Lu L, Wang ZL, Sun C. A High-Performance Monolithic Solid-State Sodium Battery with Ca^{2+} doped $Na_3Zr_2Si_2PO_{12}$ electrolyte. Adv Energy Mater 2019;9. https://doi.org/10.1002/aenm.201901205.

[96] Jolley AG, Cohn G, Hitz GT, Wachsman ED. Improving the ionic conductivity of NaSICON through aliovalent cation substitution of $Na_3Zr_2Si_2PO_{12}$ 2015:3031–8. https://doi.org/10.1007/s11581-015-1498-8.

[97] Ma Q, Guin M, Naqash S, Tsai CL, Tietz F, Guillon O. Scandium-substituted

$Na_3Zr_2(SiO_4)_2(PO_4)$ prepared by a solution-assisted solid-state reaction method as sodium-ion conductors. Chem Mater 2016;28:4821–8. https://doi.org/10.1021/acs.chemmater.6b02059.

[98] Yan Z, Yang QW, Wang Q, Ma J. Nitrogen doped porous carbon as excellent dual anodes for Li- and Na-ion batteries. Chinese Chem Lett 2020;31:583–8. https://doi.org/10.1016/j.cclet.2019.11.002.

[99] Boilot JP, Salanié JP, Desplanches G, Le Potier D. Phase transformation in $Na_{1+x}Si_xZr_2P_{3-x}O_{12}$ compounds. Mater Res Bull 1979;14:1469–77. https://doi.org/10.1016/0025-5408(79)90091-6.

[100] Park H, Jung K, Nezafati M, Kim CS, Kang B. Sodium Ion Diffusion in NaSICON ($Na_3Zr_2Si_2PO_{12}$) Solid Electrolytes: Effects of Excess Sodium. ACS Appl Mater Interfaces 2016;8:27814–24. https://doi.org/10.1021/acsami.6b09992.

[101] Morgan EE, Evans HA, Pilar K, Brown CM, Clément RJ, Maezono R, et al. Lattice Dynamics in the NaSICON $NaZr_2(PO_4)_3$Solid Electrolyte from Temperature-Dependent Neutron Diffraction, NMR, and Ab Initio Computational Studies. Chem Mater 2022;2. https://doi.org/10.1021/acs.chemmater.2c00212.

[102] Jalalian-Khakshour A, Phillips CO, Jackson L, Dunlop TO, Margadonna S, Deganello D. Solid-state synthesis of NaSICON ($Na_3Zr_2Si_2PO_{12}$) using nanoparticle precursors for optimisation of ionic conductivity. J Mater Sci 2020;55:2291–302. https://doi.org/10.1007/s10853-019-04162-8.

[103] Naqash S, Ma Q, Tietz F, Guillon O. $Na_3Zr_2(SiO_4)_2(PO_4)$ prepared by a solution-assisted solid state reaction. Solid State Ionics 2017;302:83–91. https://doi.org/10.1016/j.ssi.2016.11.004.

[104] Aguilar DH, Torres-Gonzalez LC, Torres-Martinez LM, Lopez T, Quintana P. A study of the crystallization of ZrO_2 in the sol-gel system: ZrO_2-SiO_2. J Solid State Chem 2001;158:349–57. https://doi.org/10.1006/jssc.2001.9126.

[105] Zhang Z, Zhang Q, Shi J, Chu YS, Yu X, Xu K, et al. A Self-Forming Composite Electrolyte for Solid-State Sodium Battery with Ultralong Cycle Life. Adv Energy Mater 2017;7. https://doi.org/10.1002/aenm.201601196.

[106] Fuentes RO, Marques FMB, Franco JI. Cerámica y Vidrio Synthesis and properties of nasicon prepared from different zirconia-based precursors. Bol Soc Esp Cerám Vidr 1999:631–4.

[107] Yadav P, Bhatnagar MC. Structural studies of NaSICON material of different compositions by sol-gel method. Ceram Int 2012;38:1731–5. https://doi.org/10.1016/j.ceramint.2011.09.022.

[108] Naqash S. Sodium Ion Conducting Ceramics for Sodium Ion Batteries. vol. 451. n.d.

[109] Wang H, Okubo K, Inada M, Hasegawa G, Enomoto N, Hayashi K. Low temperature-densi fi ed NaSICON-based ceramics promoted by Na_2O- Nb_2O_5 -P_2O_5 glass additive and spark plasma sintering. Solid State Ionics 2018;322:54–60. https://doi.org/10.1016/j.ssi.2018.04.025.

[110] Lee JS, Chang CM, Lee Y Il, Lee JH, Hong SH. Spark Plasma Sintering (SPS) of

NASICON Ceramics. J Am Ceram Soc 2004;87:305–7. https://doi.org/10.1111/j.1551-2916.2004.00305.x.

[111] Wang X, Liu Z, Tang Y, Chen J, Wang D, Mao Z. Low temperature and rapid microwave sintering of $Na_3Zr_2Si_2PO_{12}$ solid electrolytes for Na-Ion batteries. J Power Sources 2021;481:228924. https://doi.org/10.1016/j.jpowsour.2020.228924.

[112] Ermrich M, Opper D. X-RAY POWDER DIFFRACTION nλ = 2d sin θ The Analytical X-ray Company. 2013.

[113] Rodríguez-Carvajal J. Recent advances in magnetic structure determination by neutron powder diffraction. Phys B Phys Condens Matter 1993;192:55–69. https://doi.org/10.1016/0921-4526(93)90108-I.

[114] Paszkowicz W. Ninety Years of Powder Diffraction: from Birth to Maturity. Synchrotron Radiat Nat Sci 2006;5:115–26.

[115] Kaus M, Guin M, Yavuz M, Knapp M, Tietz F, Guillon O, et al. Fast Na+ ion conduction in NaSICON-type $Na_{3.4}Sc_2(SiO_4)_{0.4}(PO_4)_{2.6}$ observed by ^{23}Na NMR relaxometry. J Phys Chem C 2017;121:1449–54. https://doi.org/10.1021/acs.jpcc.6b10523.

[116] Rao BDN. Relaxation effects in nuclear magnetic double resonance. Phys Rev 1965;137. https://doi.org/10.1103/PhysRev.137.A467.

[117] Stanje B, Rettenwander D, Breuer S, Uitz M, Berendts S, Lerch M, et al. Solid Electrolytes: Extremely Fast Charge Carriers in Garnet-Type $Li_6La_3ZrTaO_{12}$ Single Crystals. Ann Phys 2017;529:1–9. https://doi.org/10.1002/andp.201700140.

[118] Zinkevich T, Fiedler A, Guin M, Tietz F, Guillon O, Ehrenberg H, et al. Na+ ion mobility in $Na_{3+x}Sc_2(SiO_4)_x(PO_4)_{3-x}$ ($0.1<x<0.8$) observed by ^{23}Na NMR spectroscopy. Solid State Ionics 2020;348. https://doi.org/10.1016/j.ssi.2020.115277.

[119] Lgps SEL, Untersuchungen N, Paulus MC. NMR-Investigations on the Lithium Solid Eidesstattliche Erklärung 2019;12.

[120] Boyce JB, Huberman BA. Superionic conductors: Transitions, structures, dynamics. Phys Rep 1979;51:189–265. https://doi.org/10.1016/0370-1573(79)90067-X.

[121] Perkin Elmer. A Beginner's Guide Introduction. Perkin Elmer 2004:3–19.

[122] Nixon WC. Scanning electron microscopy. Contemp Phys 1969;10:71–96. https://doi.org/10.1080/00107516908204564.

[123] Zhou W, Apkarian R, Wang ZL, Joy D. Fundamentals of scanning electron microscopy (SEM). Scanning Microsc Nanotechnol Tech Appl 2007:1–40. https://doi.org/10.1007/978-0-387-39620-0_1.

[124] Orlando A, Franceschini F, Muscas C, Pidkova S, Bartoli M, Rovere M, et al. A comprehensive review on Raman spectroscopy applications. Chemosensors 2021;9:1–28. https://doi.org/10.3390/chemosensors9090262.

[125] Xu Z, He Z, Song Y, Fu X, Rommel M, Luo X, et al. Topic review: Application of raman spectroscopy characterization in micro/nano-machining. Micromachines 2018;9. https://doi.org/10.3390/mi9070361.

[126] Greczynski G, Hultman L. A step-by-step guide to perform x-ray photoelectron spectroscopy. J Appl Phys 2022;132. https://doi.org/10.1063/5.0086359.

[127] Loveday D, Peterson P, Rodgers B. Evaluation of organic coatings with electrochemical impedance spectroscopy: Part 1: Fundamentals of electrochemical impedance spectroscopy. CoatingsTech 2004;1:46–52.

[128] Lazanas AC, Prodromidis MI. Electrochemical Impedance Spectroscopy─A Tutorial. ACS Meas Sci Au 2023;3:162–93. https://doi.org/10.1021/acsmeasuresciau.2c00070.

[129] Meddings N, Heinrich M, Overney F, Lee JS, Ruiz V, Napolitano E, et al. Application of electrochemical impedance spectroscopy to commercial Li-ion cells: A review. J Power Sources 2020;480. https://doi.org/10.1016/j.jpowsour.2020.228742.

[130] Techni- GIT, Intermittent P, Techniques T, Spectro- SPE. EC-Lab – Application Note # 01 Protocols for studying intercalation electrodes materials : Part I : Galvanostatic cycling with potential limitation (GCPL) I – Introduction EC-Lab – Application Note # 01 II – Galvanostatic Cycling with Potential Limitati 2005:31–4.

[131] Roisnel T, Rodríguez-Carvajal J. WinPLOTR: A windows tool for powder diffraction pattern analysis. Mater Sci Forum 2001;378–381:118–23. https://doi.org/10.4028/www.scientific.net/msf.378-381.118.

[132] Gebi AI, Dolokto O, Mereacre L, Geckle U, Radinger H, Knapp M, et al. Characterization and Comparative Study of Energy Efficient Mechanochemically Induced NaSICON Sodium Solid Electrolyte Synthesis. ChemSusChem 2024;17. https://doi.org/10.1002/cssc.202300809.

[133] Bukun NG, Moskvina EI. The effect of ion substitution in sodium-conducting solid electrolytes on the reversibility of the electrode-solid electrolyte interface. Solid State Ionics 1996;86–88:107–11. https://doi.org/10.1016/0167-2738(96)00101-4.

[134] Kim Y, Kim H, Park S, Seo I, Kim Y. Na ion- Conducting Ceramic as Solid Electrolyte for Rechargeable Seawater Batteries. Electrochim Acta 2016;191:1–7. https://doi.org/10.1016/j.electacta.2016.01.054.

[135] Tiliakos A, Iordache M, Marinoiu A. Ionic conductivity and dielectric relaxation of nasicon superionic conductors at the near-cryogenic regime. Appl Sci 2021;11. https://doi.org/10.3390/app11188432.

[136] Feist T, Davies PK, Vogel E. The energetics of phase transitions in the system $N_{1+x}Zr_2Si_xP_{3-x}O_{12}$, ($1.9 \leq x \leq 2.5$). Thermochim Acta 1986;106:57–61.

[137] Barj M, Lucazeau G, Delmas C. Raman and infrared spectra of some chromium Nasicon-type materials: Short-range disorder characterization. J Solid State Chem 1992;100:141–50. https://doi.org/10.1016/0022-4596(92)90164-Q.

[138] Giarola M, Sanson A, Tietz F, Pristat S, Dashjav E, Rettenwander D, et al. Structure and Vibrational Dynamics of NaSICON-Type $LiTi_2(PO_4)_3$. J Phys Chem C 2017;121:3697–706. https://doi.org/10.1021/acs.jpcc.6b11067.

[139] Greczynski G, Hultman L. The same chemical state of carbon gives rise to two peaks in X-ray photoelectron spectroscopy. Sci Rep 2021;11:1–5. https://doi.org/10.1038/s41598-021-90780-9.

[140] Wang S, Xu H, Li W, Dolocan A, Manthiram A. Interfacial Chemistry in Solid-State Batteries: Formation of Interphase and Its Consequences. J Am Chem Soc 2018;140:250–7. https://doi.org/10.1021/jacs.7b09531.

[141] Azdad Z, Marot L, Moser L, Steiner R, Meyer E. Valence band behaviour of zirconium oxide, Photoelectron and Auger spectroscopy study. Sci Rep 2018;8:1–6. https://doi.org/10.1038/s41598-018-34570-w.

[142] Vadhva P, Hu J, Johnson MJ, Stocker R, Braglia M, Brett DJL, et al. Electrochemical Impedance Spectroscopy for All-Solid-State Batteries: Theory, Methods and Future Outlook. ChemElectroChem 2021;8:1930–47. https://doi.org/10.1002/celc.202100108.

[143] Naqash S, Sebold D, Tietz F, Guillon O. Microstructure–conductivity relationship of $Na_3Zr_2(SiO_4)_2(PO_4)$ ceramics. J Am Ceram Soc 2019;102:1057–70. https://doi.org/10.1111/jace.15988.

[144] Hanaor DAH, Xu W, Ferry M, Sorrell CC. Abnormal grain growth of rutile TiO_2 induced by $ZrSiO_4$. J Cryst Growth 2012;359:83–91. https://doi.org/10.1016/j.jcrysgro.2012.08.015.

[145] Narayanan S, Reid S, Butler S, Thangadurai V. Sintering temperature, excess sodium, and phosphorous dependencies on morphology and ionic conductivity of NaSICON $Na_3Zr_2Si_2PO_{12}$. Solid State Ionics 2019;331:22–9. https://doi.org/10.1016/j.ssi.2018.12.003.

[146] Ma Q, Tsai CL, Wei XK, Heggen M, Tietz F, Irvine JTS. Room temperature demonstration of a sodium superionic conductor with grain conductivity in excess of $0.01 Scm^{-1}$ and its primary applications in symmetric battery cells. J Mater Chem A 2019;7:7766–76. https://doi.org/10.1039/c9ta00048h.

[147] Lee SM, Lee ST, Lee DH, Lee SH, Han SS, Lim SK. Effect of particle size on the density and ionic conductivity of $Na_3Zr_2Si_2PO_{12}$ NaSICON. J Ceram Process Res 2015;16:49–53.

[148] Lu Y, Zhao CZ, Yuan H, Cheng XB, Huang JQ, Zhang Q. Critical Current Density in Solid-State Lithium Metal Batteries: Mechanism, Influences, and Strategies. Adv Funct Mater 2021;31. https://doi.org/10.1002/adfm.202009925.

[149] Ma Q, Ortmann T, Yang A, Sebold D, Burkhardt S, Rohnke M, et al. Enhancing the Dendrite Tolerance of NaSICON Electrolytes by Suppressing Edge Growth of Na Electrode along Ceramic Surface. Adv Energy Mater 2022;12. https://doi.org/10.1002/aenm.202201680.

[150] Zhou W, Li Y, Xin S, Goodenough JB. Rechargeable Sodium All-Solid-State Battery. ACS Cent Sci 2017;3:52–7. https://doi.org/10.1021/acscentsci.6b00321.

[151] Querel E, Seymour I, Cavallaro A, Ma Q, Tietz F, Aguadero A. Chemical Tuning of NaSICON Surfaces for Fast-Charging Na Metal Solid-State Batteries 2021:5–9.

[152] Yang J, Liu G, Avdeev M, Wan H, Han F, Shen L, et al. Ultrastable all-solid-state sodium rechargeable batteries. ACS Energy Lett 2020;5:2835–41. https://doi.org/10.1021/acsenergylett.0c01432.

[153] Ma T, Xu GL, Li Y, Song B, Zeng X, Su CC, et al. Insights into the Performance Degradation of Oxygen-Type Manganese-Rich Layered Oxide Cathodes for High-Voltage

Sodium-Ion Batteries. ACS Appl Energy Mater 2018;1:5735–45. https://doi.org/10.1021/acsaem.8b01325.

[154] Nieto-Muñoz AM, Ortiz-Mosquera JF, Rodrigues ACM. The impact of heat-treatment protocol on the grain size and ionic conductivity of NaSICON glass-ceramics. J Eur Ceram Soc 2020;40:5634–45. https://doi.org/10.1016/j.jeurceramsoc.2020.05.026.

[155] Gautam A, Sadowski M, Prinz N, Eickhoff H, Minafra N, Ghidiu M, et al. Rapid Crystallization and Kinetic Freezing of Site-Disorder in the Lithium Superionic Argyrodite Li_6PS_5Br. Chem Mater 2019;31:10178–85. https://doi.org/10.1021/acs.chemmater.9b03852.

[156] Chaim R, Levin M, Shlayer A, Estournes C. Sintering and densification of nanocrystalline ceramic oxide powders: A review. Adv Appl Ceram 2008;107:159–69. https://doi.org/10.1179/174367508X297812.

[157] Heo TW, Grieder A, Wang B, Wood M, Hsu T, Akhade SA, et al. Microstructural impacts on ionic conductivity of oxide solid electrolytes from a combined atomistic-mesoscale approach. Npj Comput Mater 2021;7. https://doi.org/10.1038/s41524-021-00681-8.

[158] Wang J, He T, Yang X, Cai Z, Wang Y, Lacivita V, et al. Design principles for NaSICON super-ionic conductors. Nat Commun 2023;14. https://doi.org/10.1038/s41467-023-40669-0.

[159] Dubey BP, Vinodhkumar A, Sahoo A, Thangadurai V, Sharma Y. Microstructural Tuning of Solid Electrolyte $Na_3Zr_2Si_2PO_{12}$ by Polymer-Assisted Solution Synthesis Method and Its Effect on Ionic Conductivity and Dielectric Properties. ACS Appl Energy Mater 2021;4:5475–85. https://doi.org/10.1021/acsaem.1c00107.

[160] Oh SA, Aroh JW, Lamprinakos NL, Chuang CA, Bucsek AN, Rollett AD. Martensite decomposition during rapid heating of Ti-6Al-4V studied via in situ synchrotron X-ray diffraction. Commun Mater 2024;5:2–11. https://doi.org/10.1038/s43246-024-00492-6.

[161] Cullity BD. Elements of X ray DIFFRACTION.

[162] Horii M, Christianson RJ, Mutha H, Bachman JC. Modeling the effect of electrolyte microstructure on conductivity and solid-state Li-ion battery performance. J Power Sources 2022;528:231177. https://doi.org/10.1016/j.jpowsour.2022.231177.

[163] Leng H, Huang J, Nie J, Luo J. Cold sintering and ionic conductivities of $Na_{3.256}Mg_{0.128}Zr_{1.872}Si_2PO_{12}$ solid electrolytes. J Power Sources 2018;391:170–9. https://doi.org/10.1016/j.jpowsour.2018.04.067.

[164] Yang A, Yao K, Schaller M, Dashjav E, Li H, Zhao S, et al. Enhanced room-temperature Na+ ionic conductivity in $Na_{4.92}Y_{0.92}Zr_{0.08}Si_4O_{12}$. EScience 2023;3:100175. https://doi.org/10.1016/j.esci.2023.100175.

APPENDIX

Table A.1 Structural parameters for SS_NCO $Na_3Zr_2Si_2PO_{12}$ refined with space group C12/c1 (no. 15) using Rietveld analysis. Cell parameters a = 15.67584(30) Å, b = 9.06901(18) Å, c = 9.21373(16) Å, β = 123.9257(10) and volume = 1087.17(4) Å3

Atom	Wyckoff site	X	Y	z	Occupancy	Biso, Å2
Na1	4d	¼	¼	½	0.25(2)	3.815(13)
Na2	4e	0	0.39405(9)	¼	0.8940(10)	3.815(13)
Na3	8f	0.3299(11)	0.5214(2)	0.4379(3)	0.714(7)	3.815(13)
Zr	8f	0.10081(7)	0.24735(3)	0.05616(4)	1	0.505(15)
Si1	4e	0	0.04354(7)	¼	⅔	0.493(5)
P1	4e	0	0.04354(7)	¼	⅓	0.493(5)
Si2	8f	0.35671(3)	0.11116(6)	0.25914(5)	⅔	0.493(5)
P2	8f	0.35671(3)	0.11116(6)	0.25914(5)	⅓	0.493(5)
O1	8f	0.15052(6)	0.43693(9)	0.22489(7)	1	1.371(6)
O2	8f	0.43874(5)	0.45019(9)	0.08771(8)	1	1.371(6)
O3	8f	0.25321(5)	0.17985(9)	0.21194(7)	1	1.371(6)
O4	8f	0.37773(5)	0.13569(8)	0.10770(9)	1	1.371(6)
O5	8f	0.55565(5)	0.18592(8)	0.06213(7)	1	1.371(6)
O6	8f	0.08620(5)	0.14390(8)	0.14390(8)	1	1.371(6)

Rexp: 0.96, Rwp: 5.6, Rp: 4.28, $\chi 2 = 2.38$

Weight ratio of phase 1 (NaSICON): 98 (1.6) %, ZrO_2 = 2 (0.03) %.

Table A.2 Structural parameters for SS_NHP $Na_3Zr_2Si_2PO_{12}$ refined with space group C12/c1 (no. 15) using Rietveld analysis. Cell parameters a = 15.67584(30) Å, b = 9.06901(18) Å, c = 9.21373(16) Å, β = 123.9257(10) and volume = 1086.17(4) Å3

Atom	Wyckoff site	X	Y	z	Occu-pancy	Biso, Å2
Na1	4d	¼	¼	½	0.19(2)	2.815(15)
Na2	4e	0	0.39405(9)	¼	0.890(10)	2.815(15)
Na3	8f	0.3299(11)	0.4214(2)	0.3379(3)	0.274(7)	2.815(15)
Zr	8f	0.10081(7)	0.24735(3)	0.05616(4)	1	0.405(15)
Si1	4e	0	0.04354(7)	¼	⅔	0.393(5)
P1	4e	0	0.04354(7)	¼	⅓	0.393(5)
Si2	8f	0.35671(3)	0.11116(6)	0.25914(5)	⅔	0.393(5)
P2	8f	0.35671(3)	0.11116(6)	0.25914(5)	⅓	0.393(5)
O1	8f	0.15052(6)	0.43693(9)	0.22489(7)	1	1.471(6)
O2	8f	0.43874(5)	0.45019(9)	0.08771(8)	1	1.471(6)

O3	8f	0.25321(5)	0.17985(9)	0.21194(7)	1	1.471(6)
O4	8f	0.37773(5)	0.13569(8)	0.10770(9)	1	1.471(6)
O5	8f	0.55565(5)	0.18592(8)	0.06213(7)	1	1.471(6)
O6	8f	0.08620(5)	0.14390(8)	0.14390(8)	1	1.471(6)

Rexp: 2.51, Rwp: 5.98, Rp: 4.66, $\chi 2 = 2.38$

Weight ratio of phase 1 (NaSICON): 99 (2.3) %.

Table A.3 Structural parameters for SOL $Na_3Zr_2Si_2PO_{12}$ refined with space group C12/c1 (no. 15) using Rietveld analysis. Cell parameters a = 15.6545(31) Å, b = 9.0568(19) Å, c = 9.21744(16) Å, β = 123.735(10) and volume = 1085.17(4) Å3

Atom	**Wyckoff site**	**X**	**Y**	**Z**	**Occu-pancy**	**Biso, Å2**
Na1	4d	¼	¼	½	0.23(2)	1.815(13)
Na2	4e	0	0.39405(9)	¼	0.910(10)	1.815(13)
Na3	8f	0.2299(11)	0.4731(2)	0.2379(3)	0.717(7)	1.815(13)
Zr	8f	0.10081(7)	0.24735(3)	0.0/5616(4)	1	0.505(15)
Si1	4e	0	0.04354(7)	¼	⅔	0.593(5)
P1	4e	0	0.04354(7)	¼	⅓	0.593(5)
Si2	8f	0.39671(3)	0.11116(6)	0.25914(5)	⅔	0.593(5)
P2	8f	0.49671(3)	0.11116(6)	0.25914(5)	⅓	0.593(5)
O1	8f	0.25052(6)	0.48693(9)	0.21489(7)	1	1.523(6)
O2	8f	0.48743(5)	0.42019(9)	0.08771(8)	1	1.523(6)
O3	8f	0.29321(5)	0.21985(9)	0.19194(7)	1	1.523(6)
O4	8f	0.9 773(5)	0.15569(8)	0.10770(9)	1	1.523(6)
O5	8f	0.52165(5)	0.18592(8)	0.06213(7)	1	1.523(6)
O6	8f	0.08620(5)	0.14390(8)	0.14390(8)	1	1.523(6)

Rexp: 2.51, Rwp: 7.55, Rp: 5.59, $\chi 2 = 10.5$

Phase fraction NaSICON: 98 (1.05)%, ZrO_2 = 2 (0.08)%

Table A.4 Structural parameters for SP_NH4 $Na_3Zr_2Si_2PO_{12}$ refined with space group C2/c (no. 15) using Rietveld analysis. Cell parameters a = 15.7009(34) Å, b = 9.08359(19) Å, c = 9.204134(16) Å, β = 124.0757(10) and volume = 1088.17(4) Å3.

Atom	**Wyckoff site**	**X**	**y**	**Z**	**Occupancy**	**Biso, Å2**
Na1	4d	¼	¼	½	0.27(2)	2.732(13)
Na2	4e	0	0.39405(9)	¼	0.840(10)	2.732(13)
Na3	8f	0.3299(11)	0.4214(2)	0.3379(3)	0.723(7)	2.732(13)
Zr	8f	0.10081(7)	0.24735(3)	0.05616(4)	1	0.505(15)
Si1	4e	0	0.04354(7)	¼	⅔	0.593(5)
P1	4e	0	0.04354(7)	¼	⅓	0.593(5)
Si2	8f	0.35671(3)	0.11116(6)	0.25914(5)	⅔	0.593(5)

P2	8f	0.35671(3)	0.11116(6)	0.25914(5)	⅓	0.593(5)
O1	8f	0.15052(6)	0.43693(9)	0.22489(7)	1	1.471(6)
O2	8f	0.43874(5)	0.45019(9)	0.08771(8)	1	1.471(6)
O3	8f	0.25321(5)	0.17985(9)	0.21194(7)	1	1.471(6)
O4	8f	0.37773(5)	0.13569(8)	0.10770(9)	1	1.471(6)
O5	8f	0.55565(5)	0.18592(8)	0.06213(7)	1	1.471(6)
O6	8f	0.08620(5)	0.14390(8)	0.14390(8)	1	1.471(6)

Rexp: 1.26, Rwp: 4.29, Rp: 3.22, $\chi 2 = 11.5$

Phase fraction NaSICON: 100%

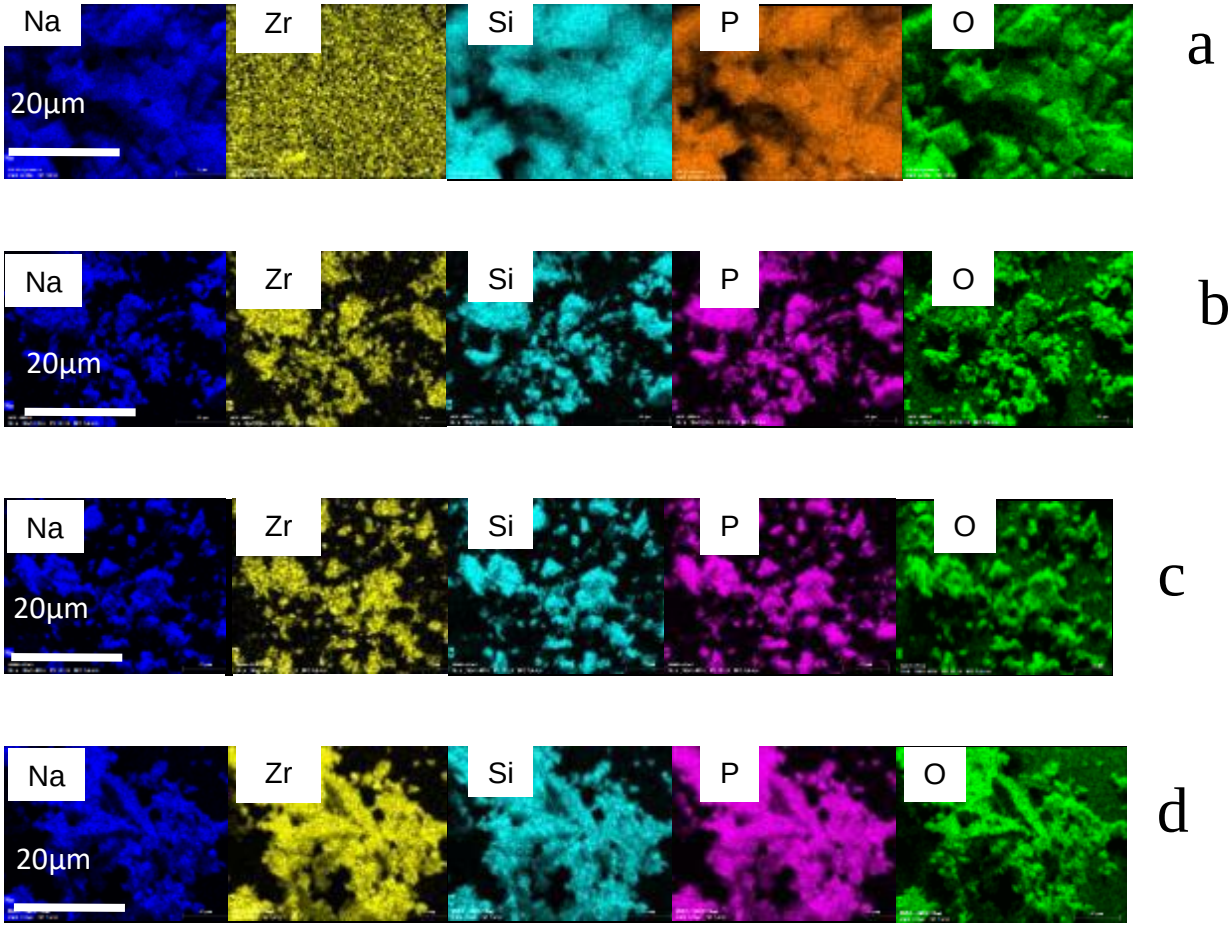

Fig. A. 1 Elemental distribution maps in (a) SP_NC, (b) SP_NOH, (c) SP_NO and (d) SP_ZNO

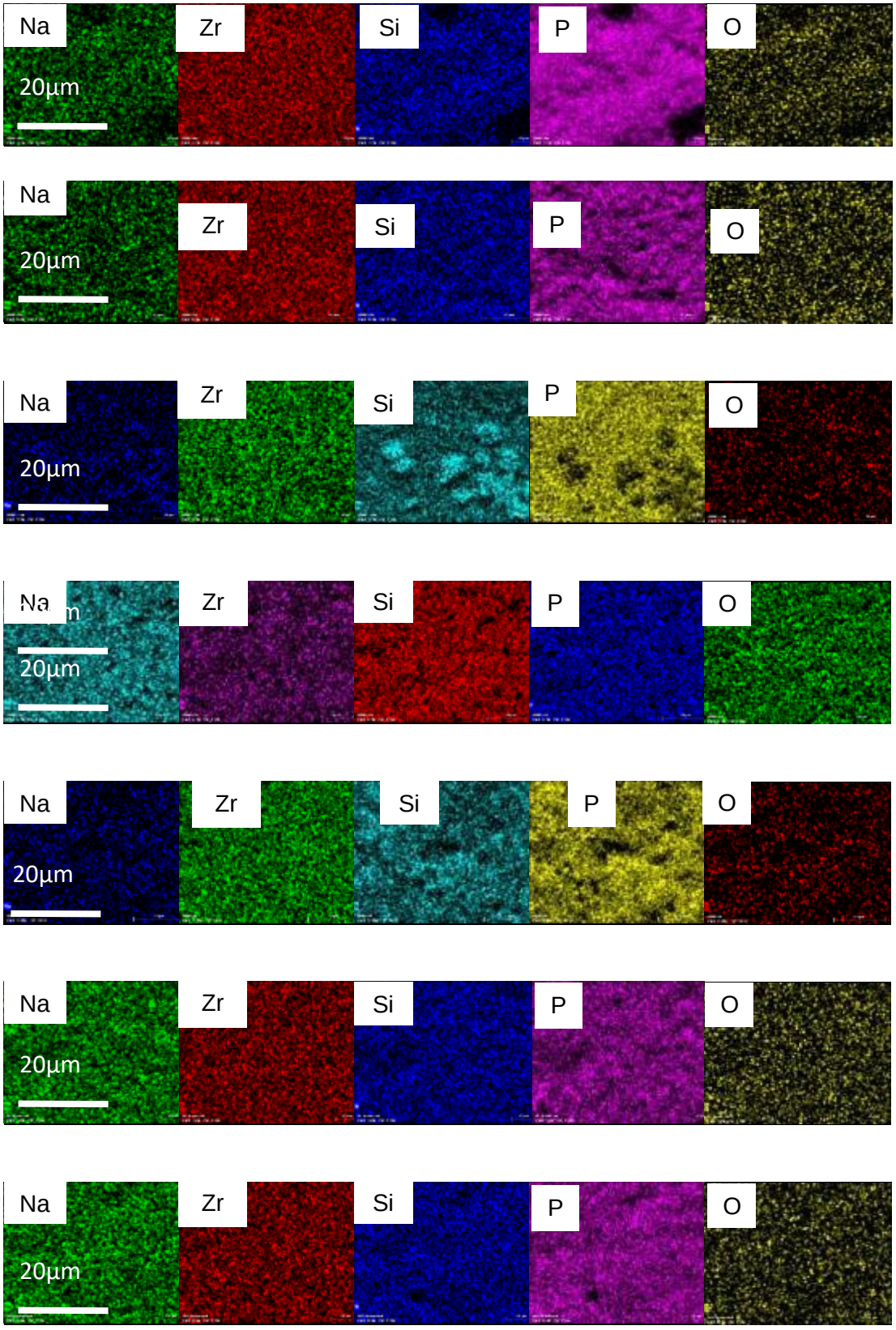
Na
Zr
Si
P
O
20µm
a
b
c
d
e
f
g

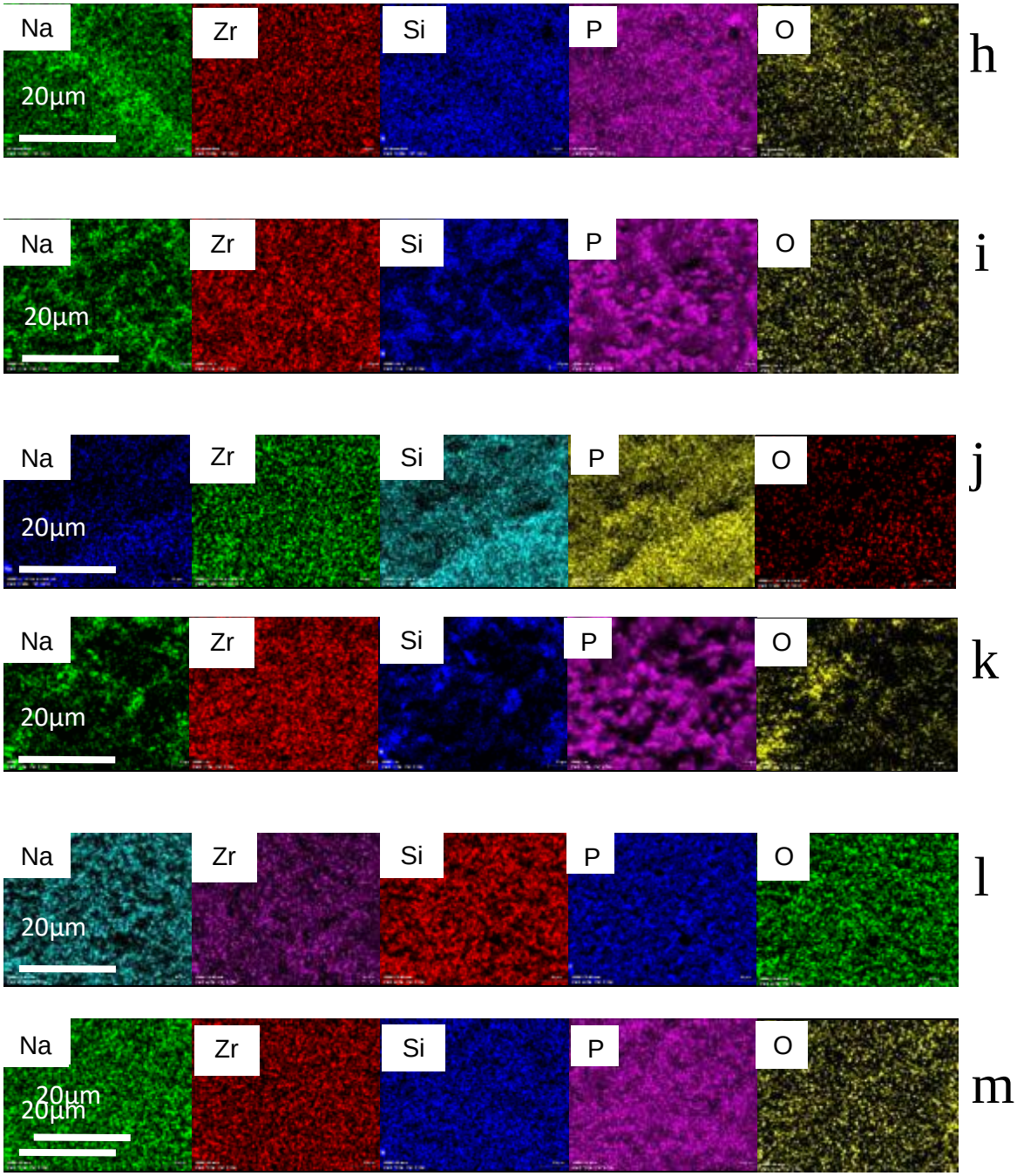

Fig. A. 2 Element distribution of different sintering conditions (a, b, c, d, e) for the heating rates 300°C/h, 240°C/h, 180°C/h, 120°C/h, 60°C/h respectively (f, g) -45µm, -75+45µm particle sizes respectively (h, i, j) in air, H2O, nitrogen, quenching media respectively (k, l, m) in nitrogen, argon and oxygen sintering environments respectively

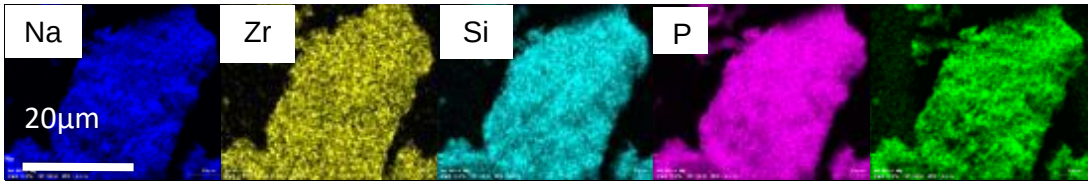
Na
Zr
Si
P
20µm

a

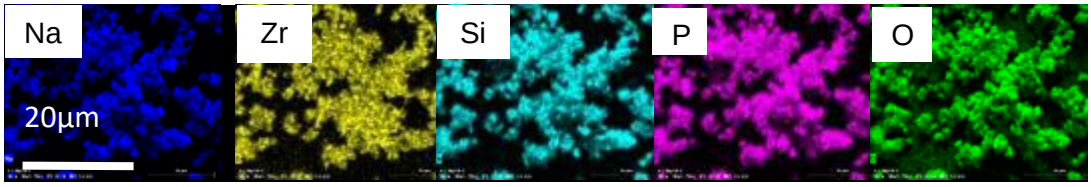
Na
Zr
Si
P
O
20µm

b

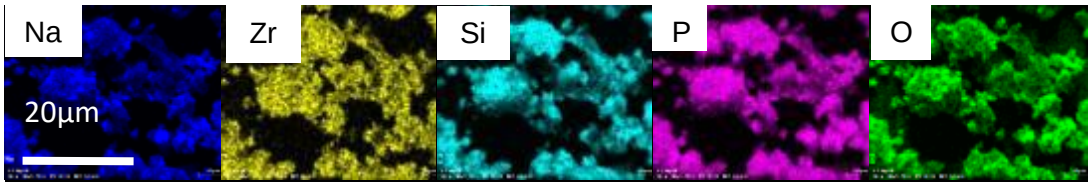
Na
Zr
Si
P
O
20µm

c

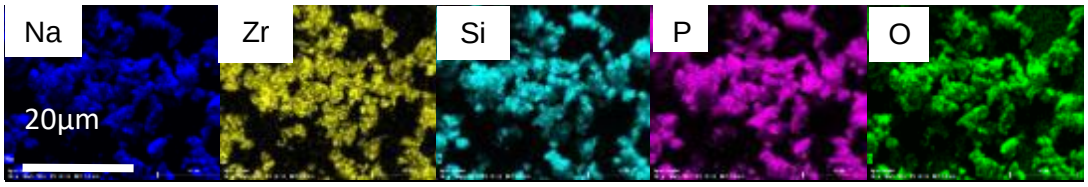
Na
Zr
Si
P
O
20µm

d

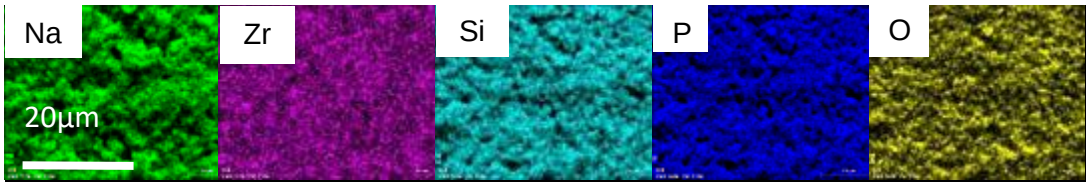
Na
Zr
Si
P
O
20µm

e

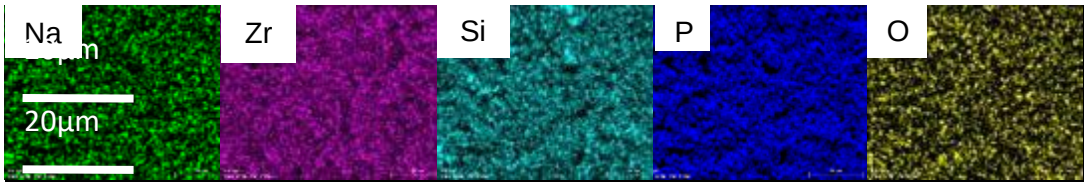
Na
Zr
Si
P
O
20µm

f

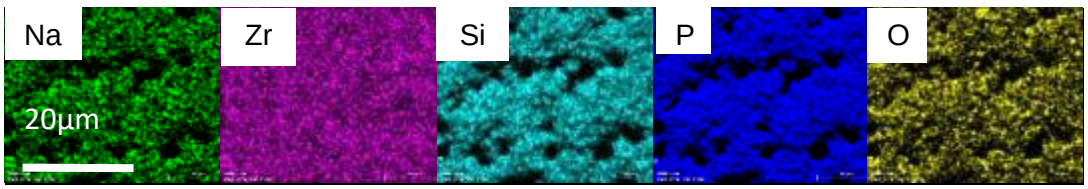
Na
Zr
Si
P
O
20µm

g

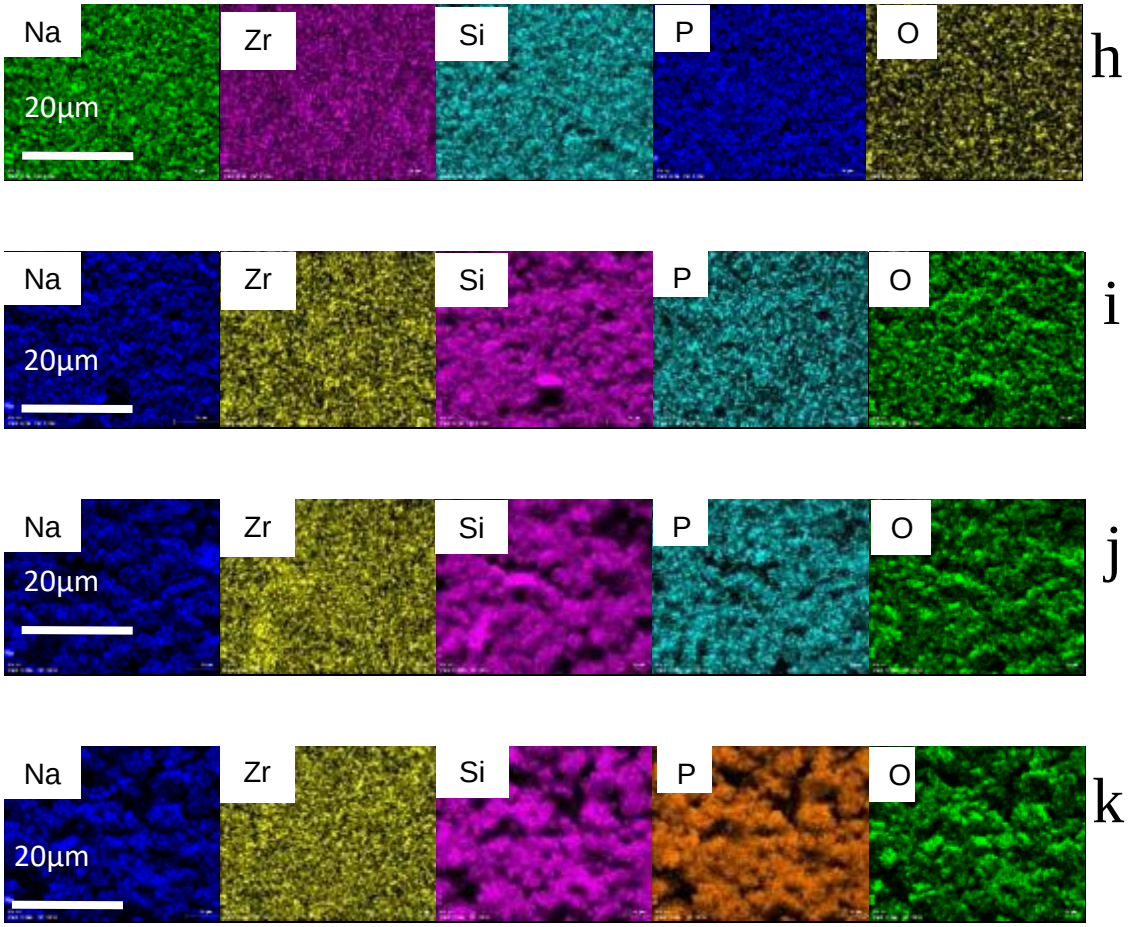

Fig. A. 3 Elemental distribution in the doped compositions (a) 1MgSi2 (b) 1MgSi2.2 (c) 2MgSi2 (d) 2MgSi2.2 (e) 0.25Mo (f) 0.05Mo (g) 0.075Mo (h) 0.1Mo (i) 0.2Mo (j) 0.3Mo (k) 0.4Mo

Table A.5 Structural parameters for 300°C/h heating/cooling rate $Na_3Zr_2Si_2PO_{12}$ refined with space group C2/c (No15) using Rietveld analysis.

Atom	x	y	Z	B	Occ.	Wyckoff
O1	0.14770	0.06180	0.21900	1.482(159)	1	8f
Na2	0	0.09761(0.02)	$^1/_4$	5.050(484)	0.548(15)	4d
Na1	$^1/_4$	$^1/_4$	$^1/_2$	5.050(484)	0.091(10)	4e
Na3	0.32902(312)	0.07965(534)	0.33530(575)	5.050(484)	0.430(27)	8f
Na4	0.31329(251)	0.12995(374)	0.43893(449)	5.050(484)	0.539(23)	8f
Zr1	0.10059(26)	0.25046(105)	0.05561(31)	1.439(61)	1	8f
Si1	0.35708(96)	0.38997(184)	0.25967(157)	1.546(154)	$^2/_3$	8f

Si2	0	0.45633(244)	1/4	1.546(154)	2/3	4e
P1	0.35708(96)	0.38997(184)	0.25967(157)	1.546(154)	1/3	8f
P2	0	0.45633(244)	1/4	1.546(154)	1/3	4e
O2	0.43852	0.05414	0.08663	1.482(159)	1	8f
O3	0.25279	0.31542	0.20711	1.482(159)	1	8f
O4	0.38133	0.36103	0.11456	1.482(159)	1	8f
O5	0.05271	0.18436	0.56468	1.482(159)	1	8f
O6	0.08220	0.35847	0.24259	1.482(159)	1	8f

Table 7.6 Structural parameters for 240°C heating/cooling rate refined with space group C2/c (No15) using Rietveld analysis.

Atom	**x**	**y**	**z**	**B**	**Occ.**	**Wyckoff**
O1	0.14770	0.06180	0.21900	2.089(141)	1	8f
Na2	0	0.09656(268)	1/4	5.781(371)	0.543	4d
Na1	1/4	1/4	1/2	5.781(371)	0.120	4e
Na3	0.32262(232)	0.07935(408)	0.31837(378)	5.781(371)	0.462	8f
Na4	0.31226(214)	0.13471(311)	0.43218(355)	5.781(371)	0.488	8f
Zr1	0.10154(21)	0.24973(88)	0.05653(24)	2.010(61)	1	8f
Si1	0.35763(79)	0.38597(154)	0.25883(135)	2.483(145)	2/3	8f
Si2	0	0.45303(181)	1/4	2.483(145)	2/3	4e
P1	0.35763(79)	0.38597(154)	0.25883(135)	2.483(145)	1/3	8f
P2	0	0.45303(181)	1/4	2.483(145)	1/3	4e
O2	0.43210	0.05390	0.07670	2.089(141)	1	8f
O3	0.25210	0.31390	0.20540	2.089(141)	1	8f
O4	0.38670	0.35970	0.12410	2.089(141)	1	8f
O5	0.05220	0.18890	0.55910	2.089(141)	1	8f
O6	0.08060	0.35580	0.24160	2.089(141)	1	8f

Table A.7 Structural parameters for 180°C heating/cooling rate refined with space group C2/c (No15) using Rietveld analysis.

atom	x	Y	z	B	Occ.	Wyckoff
O1	0.14770	0.06180	0.21900	0.692	1	8f
Na2	0	0.10256(118)	1/4	5.260(156)	0.516(7)	4d
Na1	1/4	1/4	1/2	5.260(156)	0.130(3)	4e
Na3	0.32713(109)	0.07618(183)	0.31024(188)	5.260(156)	0.439(9)	8f
Na4	0.31144(91)	0.13086(130)	0.42712(165)	5.260(156)	0.519(7)	8f
Zr1	0.10083(7)	0.25082(31)	0.05627(10)	0.715(19)	1	8f
Si1	0.35903(29)	0.38944(55)	0.25916(47)	0.982(51)	2/3	8f
Si2	0	0.45483(63)	1/4	0.982(51)	2/3	4e
P1	0.35903(29)	0.38944(55)	0.25916(47)	0.982(51)	1/3	8f
P2	0	0.45483(63)	1/4	0.982(51)	1/3	4e
O2	0.43210	0.05390	0.07670	0.692(52)	1	8f
O3	0.25210	0.31390	0.20540	0.692(52)	1	8f
O4	0.38670	0.35970	0.12410	0.692(52)	1	8f
O5	0.05220	0.18890	0.55910	0.692(52)	1	8f
O6	0.08060	0.35580	0.24160	0.692(52)	1	8f

Table A.8 Structural parameters for 120°C heating/cooling rate $Na_3Zr_2Si_2PO_{12}$ refined with space group C2/c (No15) using Rietveld analysis.

Atom	x	y	z	B	Occ.	Wyckoff
O1	0.14770	0.06180	0.21900	0.468(54)	1.000	8f
Na2	0	0.10366(112)	1/4	5.329(153)	0.524(7)	4d
Na1	1/4	1/4	1/2	5.329(153)	0.126(3)	4e
Na3	0.32878(109)	0.07658(181)	0.31053(185)	5.329(153)	0.426(8)	8f
Na4	0.31345(84)	0.13092(119)	0.42830(158)	5.329(153)	0.525(6)	8f
Zr1	0.10090(7)	0.25165(31)	0.05644(10)	0.524(25)	1	8f
Si1	0.35897(29)	0.38879(56)	0.25849(48)	0.781(56)	2/3	8f
Si2	0	0.45439(64)	1/4	0.781(56)	2/3	4e

P1	0.35897(29)	0.38879(56)	0.25849(48)	0.781(56)	$^1/_3$	8f
P2	0	0.45439(64)	$^1/_4$	0.781(56)	$^1/_3$	4e
O2	0.43210	0.05390	0.07670	0.468(54)	1	8f
O3	0.25210	0.31390	0.20540	0.468(54)	1	8f
O4	0.38670	0.35970	0.12410	0.468(54)	1	8f
O5	0.05220	0.18890	0.55910	0.468(54)	1	8f
O6	0.08060	0.35580	0.24160	0.468(54)	1	8f

Table A.9 Structural parameters for 60˚C heating/cooling rate $Na_3Zr_2Si_2PO_{12}$ refined with space group C2/c (No15) using Rietveld analysis.

Name	**x**	**Y**	**Z**	**B**	**Occ.**	**Wyckoff**
O1	0.14770	0.06180	0.21900	0.988(75)	1	8f
Na2	0	0.10339(163)	$^1/_4$	5.339(223)	0.515(9)	4d
Na1	$^1/_4$	$^1/_4$	$^1/_2$	5.339(223)	0.127(5)	4e
Na3	0.32895(160)	0.07773(269)	0.31328(278)	5.339(223)	0.417(13)	8f
Na4	0.31536(119)	0.12909(168)	0.43312(218)	5.339(223)	0.541(9)	8f
Zr1	0.10000(0)	0.25061(46)	0.05586(13)	0.904(32)	1	8f
Si1	0.35871(41)	0.38993(80)	0.25868(68)	0.856(76)	$^2/_3$	8f
Si2	0	0.45522(91)	$^1/_4$	0.856(76)	$^2/_3$	4e
P1	0.35871(41)	0.38993(80)	0.25868(68)	0.856(76)	$^1/_3$	8f
P2	0	0.45522(91)	$^1/_4$	0.856(76)	$^1/_3$	4e
O2	0.43210	0.05390	0.07670	0.988(75)	1	8f
O3	0.25210	0.31390	0.20540	0.988(75)	1	8f
O4	0.38670	0.35970	0.12410	0.988(75)	1	8f
O5	0.05220	0.18890	0.55910	0.988(75)	1	8f
O6	0.08060	0.35580	0.24160	0.988(75)	1	8f

Table A.10 Structural parameters for –45µm $Na_3Zr_2Si_2PO_{12}$ refined with space group C2/c (No15) using Rietveld analysis.

Name	x	Y	z	B	Occ.	Wyckoff
O1	0.14770	0.06180	0.21900	0.659(58)	1	8f
Na2	0.00000(0)	0.10714(120)	$^1/_4$	4.650(157)	0.512(7)	4d
Na1	$^1/_4$	$^1/_4$	$^1/_2$	4.650(157)	0.112(4)	4e
Na3	0.33452(116)	0.07361(184)	0.32758(200)	4.650(157)	0.438(9)	8f
Na4	0.31326(93)	0.12982(130)	0.42846(164)	4.650(157)	0.538(7)	8f
Zr1	0.10070(8)	0.25129(33)	0.05589(11)	0.646(23)	1	8f
Si1	0.35882(32)	0.38884(57)	0.25838(51)	0.682(62)	$^2/_3$	8f
Si2	0	0.45428(64)	$^1/_4$	0.682(62)	$^2/_3$	4e
P1	0.35882(32)	0.38884(57)	0.25838(51)	0.682(62)	$^1/_3$	8f
P2	0	0.45428(64)	$^1/_4$	0.682(62)	$^1/_3$	4e
O2	0.44156	0.04984	0.08889	0.659(58)	1	8f
O3	0.25465	0.31842	0.21237	0.659(58)	1	8f
O4	0.38037	0.36354	0.11311	0.659(58)	1	8f
O5	0.04975	0.18504	0.55919	0.659(58)	1	8f
O6	0.08619	0.35839	0.24702	0.659(58)	1	8f

Table A.11 Structural parameters for '–75 +45µm' $Na_3Zr_2Si_2PO_{12}$ based on lab XRD (λ = 0.70932), data collected at room temperature refined with space group C2/c (No15) using Rietveld analysis.

Name	X	y	Z	B	Occ.	Wyckoff
O1	0.14770	0.06180	0.21900	0.811(49)	1	8f
Na2	0	0.10227(94)	$^1/_4$	3.603(179)	0.510(6)	4d
Na1	$^1/_4$	$^1/_4$	$^1/_2$	3.603(179)	0.112(3)	4e
Na3	0.32475(98)	0.07897(157)	0.31593(163)	3.603(179)	0.397(7)	8f
Na4	0.31075(80)	0.13437(117)	0.43047(147)	3.603(179)	0.469(7)	8f
Zr1	0.10087(7)	0.25059(29)	0.05629(9)	0.686(19)	1	8f
Si1	0.35859(27)	0.38955(50)	0.25940(43)	0.827(47)	$^2/_3$	8f
Si2	0	0.45618(63)	$^1/_4$	0.827(47)	$^2/_3$	4e

P1	0.35859(27)	0.38955(50)	0.25940(43)	0.827(47)	$^1/_3$	8f
P2	0	0.45618(63)	$^1/_4$	0.827(47)	$^1/_3$	4e
O2	0.43210	0.05390	0.07670	0.811(49)	1	8f
O3	0.25210	0.31390	0.20540	0.811(49)	1	8f
O4	0.38670	0.35970	0.12410	0.811(49)	1	8f
O5	0.05220	0.18890	0.55910	0.811(49)	1	8f
O6	0.08060	0.35580	0.24160	0.811(49)	1	8f

Table A.12 Structural parameters for Air quenched $Na_3Zr_2Si_2PO_{12}$ refined with space group C2/c (No15) using Rietveld analysis.

Name	**x**	**y**	**z**	**B**	**Occ.**	**Wyckoff**
O1	0.14770	0.06180	0.21900	1.104(80)	1	8f
Na2	0	0.09834(150)	$^1/_4$	4.217(217)	0.529(9)	4d
Na1	$^1/_4$	$^1/_4$	$^1/_2$	4.217(217)	0.092(5)	4e
Na3	0.32666(146)	0.07966(240)	0.32398(259)	4.217(217)	0.433(13)	8f
Na4	0.31347(116)	0.13014(168)	0.43996(203)	4.217(217)	0.549(10)	8f
Zr1	0.10091(12)	0.25129(47)	0.05626(15)	1.033(32)	1	8f
Si1	0.35847(44)	0.38952(84)	0.25924(72)	0.935(76)	$^2/_3$	8f
Si2	0	0.45606(98)	$^1/_4$	0.935(76)	$^2/_3$	4e
P1	0.35847(44)	0.38952(84)	0.25924(72)	0.935(76)	$^1/_3$	8f
P2	0	0.45606(98)	$^1/_4$	0.935(76)	$^1/_3$	4e
O2	0.43210	0.05390	0.07670	1.104(80)	1	8f
O3	0.25210	0.31390	0.20540	1.104(80)	1	8f
O4	0.38670	0.35970	0.12410	1.104(80)	1	8f
O5	0.05220	0.18890	0.55910	1.104(80)	1	8f
O6	0.08060	0.35580	0.24160	1.104(80)	1	8f

Table A.13 Structural parameters for Nitrogen quenched $Na_3Zr_2Si_2PO_{12}$ refined with space group C2/c (No15) using Rietveld analysis (negative thermal displacement parameters do not have a direct physical meaning but may appear as artefacts, indicating residual electron density).

Atoms	x	y	z	B	Occ.	Wyckoff
O1	0.14770	0.06180	0.21900	–0.642(107)	1	8f
Na2	0	0.10236(658)	$^1/_4$	2.608(394)	0.242(7)	4d
Na1	$^1/_4$	$^1/_4$	$^1/_2$	2.608(394)	0.242(7)	4e
Na3	0.33444(193)	0.08768(260)	0.30736(297)	2.608(394)	0.654(18)	8f
Na4	0.32125(270)	0.12713(396)	0.43946(489)	2.608(394)	0.368(9)	8f
Zr1	0.10011(21)	0.25027(94)	0.05639(23)	–0.293(31)	1	8f
Si1	0.35836(84)	0.40056(162)	0.24764(145)	0.369(108)	$^2/_3$	8f
Si2	0	0.45916(196)	$^1/_4$	0.369(108)	$^2/_3$	4e
P1	0.35836(84)	0.40056(162)	0.24764(145)	0.369(108)	$^1/_3$	8f
P2	0	0.45916(196)	$^1/_4$	0.369(108)	$^1/_3$	4e
O2	0.43210	0.05390	0.07670	–0.642(107)	1	8f
O3	0.25210	0.31390	0.20540	–0.642(107)	1	8f
O4	0.38670	0.35970	0.12410	–0.642(107)	1	8f
O5	0.05220	0.18890	0.55910	–0.642(107)	1	8f
O6	0.08060	0.35580	0.24160	–0.642(107)	1	8f

Table A.14 Structural parameters for H_2O quenched $Na_3Zr_2Si_2PO_{12}$ refined with space group C2/c (No15) using Rietveld analysis.

Atoms	x	y	z	B	Occ.	Wyckoff
O1	0.14770	0.06180	0.21900	1.046(64)	1	8f
Na2	0	0.10114(123)	$^1/_4$	3.683(229)	0.498(8)	4d
Na1	$^1/_4$	$^1/_4$	$^1/_2$	3.683(229)	0.098(4)	4e
Na3	0.32419(127)	0.07935(201)	0.31764(219)	3.683(229)	0.396(10)	8f
Na4	0.31344(94)	0.12926(134)	0.43433(171)	3.683(229)	0.524(10)	8f
Zr1	0.10000	0.25155(37)	0.05577(11)	0.788(24)	1	8f
Si1	0.35916(34)	0.38853(62)	0.26054(54)	0.831(63)	$^2/_3$	8f

Si2	0	0.45484(77)	$^1/_4$	0.831(63)	$^2/_3$	4e
P1	0.35916(34)	0.38853(62)	0.26054(54)	0.831(63)	$^1/_3$	8f
P2	0	0.45484(77)	$^1/_4$	0.831(63)	$^1/_3$	4e
O2	0.43210	0.05390	0.07670	1.046(64)	1	8f
O3	0.25210	0.31390	0.20540	1.046(64)	1	8f
O4	0.38670	0.35970	0.12410	1.046(64)	1	8f
O5	0.05220	0.18890	0.55910	1.046(64)	1	8f
O6	0.08060	0.35580	0.24160	1.046(64)	1	8f

Table A.15 Structural parameters for $Na_3Zr_2Si_2PO_{12}$ in Argon refined with space group C2/c (No15) using Rietveld analysis.

Atoms	**x**	**y**	**z**	**B**	**Occ.**	**Wyckoff**
O1	0.14770	0.06180	0.21900	0.968(59)	1	8f
Na2	0.00000(0)	0.10066(115)	$^1/_4$	4.574(161)	0.527(7)	4d
Na1	$^1/_4$	$^1/_4$	$^1/_2$	4.574(161)	0.101(4)	4e
Na3	0.32644(116)	0.07698(192)	0.31722(202)	4.574(161)	0.422(9)	8f
Na4	0.31269(88)	0.13049(126)	0.43231(161)	4.574(161)	0.550(7)	8f
Zr1	0.10082(8)	0.25093(34)	0.05636(11)	0.818(23)	1	8f
Si1	0.35881(31)	0.38858(56)	0.25990(50)	0.892(57)	$^2/_3$	8f
Si2	0	0.45461(67)	$^1/_4$	0.892(57)	$^2/_3$	4e
P1	0.35881(31)	0.38858(56)	0.25990(50)	0.892(57)	$^1/_3$	8f
P2	0	0.45461(67)	$^1/_4$	0.892(57)	$^1/_3$	4e
O2	0.43210	0.05390	0.07670	0.968(59)	1	8f
O3	0.25210	0.31390	0.20540	0.968(59)	1	8f
O4	0.38670	0.35970	0.12410	0.968(59)	1	8f
O5	0.05220	0.18890	0.55910	0.968(59)	1	8f
O6	0.08060	0.35580	0.24160	0.968(59)	1	8f

Table A.16 Structural parameters for $Na_3Zr_2Si_2PO_{12}$ in Nitrogen refined with space group C2/c (No15) using Rietveld analysis.

Atoms	x	y	z	B	Occ.	Wyckoff
O1	0.14770	0.06180	0.21900	1.059(78)	1	8f
Na2	0	0.10008(147)	$^1/_4$	4.229(211)	0.540(9)	4d
Na1	$^1/_4$	$^1/_4$	$^1/_2$	4.229(211)	0.121(5)	4e
Na3	0.32548(142)	0.07575(233)	0.31526(246)	4.229(211)	0.439(12)	8f
Na4	0.31437(119)	0.13207(180)	0.43769(217)	4.229(211)	0.507(9)	8f
Zr1	0.10082(12)	0.25022(46)	0.05625(15)	1.010(29)	1	8f
Si1	0.35841(43)	0.39069(79)	0.25970(71)	0.907(74)	$^2/_3$	8f
Si2	0	0.45774(99)	$^1/_4$	0.907(74)	$^2/_3$	4e
P1	0.35841(43)	0.39069(79)	0.25970(71)	0.907(74)	$^1/_3$	8f
P2	0	0.45774(99)	$^1/_4$	0.907(74)	$^1/_3$	4e
O2	0.43210	0.05390	0.07670	1.059(78)	1	8f
O3	0.25210	0.31390	0.20540	1.059(78)	1	8f
O4	0.38670	0.35970	0.12410	1.059(78)	1	8f
O5	0.05220	0.18890	0.55910	1.059(78)	1	8f
O6	0.08060	0.35580	0.24160	1.059(78)	1	8f

Table A.17 Structural parameters for $Na_3Zr_2Si_2PO_{12}$ in Oxygen based on lab XRD (λ = 0.70932), data collected at room temperature refined with space group C2/c (No15) using Rietveld analysis.

Atoms	x	y	z	B	Occ.	Wyckoff
O1	0.14770	0.06180	0.21900	1.166(95)	1.000(0)	8f
Na2	0	0.09889(163)	$^1/_4$	3.436(321)	0.519(10)	4d
Na1	$^1/_4$	$^1/_4$	$^1/_2$	3.436(321)	0.130(6)	4e
Na3	0.32514(149)	0.08169(241)	0.32379(259)	3.436(321)	0.454(14)	8f
Na4	0.31251145)	0.13357(222)	0.44259(243)	3.436(321)	0.459(13)	8f
Zr1	0.10087(14)	0.25017(54)	0.05620(17)	1.038(35)	1	8f
Si1	0.35752(51)	0.39139(96)	0.25924(84)	0.850(87)	$^2/_3$	8f

Si2	0	0.45889(122)	$^{1}/_{4}$	0.850(87)	$^{2}/_{3}$	4e
P1	0.35752(51)	0.39139(96)	0.25924(84)	0.850(87)	$^{1}/_{3}$	8f
P2	0	0.45889(122)	$^{1}/_{4}$	0.850(87)	$^{1}/_{3}$	4e
O2	0.43210	0.05390	0.07670	1.166(95)	1	8f
O3	0.25210	0.31390	0.20540	1.166(95)	1	8f
O4	0.38670	0.35970	0.12410	1.166(95)	1	8f
O5	0.05220	0.18890	0.55910	1.166(95)	1	8f
O6	0.08060	0.35580	0.24160	1.166(95)	1	8f